AGE AND THERMAL HISTORY OF THE PORT MOUTON PLUTON, SOUTHWEST NOVA SCOTIA: A COMBINED U-Pb, $^{40}Ar/^{39}Ar$ AGE SPECTRUM, AND $^{40}Ar/^{39}Ar$ LASERPROBE STUDY

Raymond Patrick Fallon

Submitted in Partial Fulfillment of the Requirements
for the Degree of Master of Science
Department of Earth Sciences
Dalhousie University, Halifax, Nova Scotia
August 1998

DALHOUSIE UNIVERSITY

DEPARTMENT OF EARTH SCIENCES

The undersigned hereby certify that they have read and recommend to the Faculty of Graduate Studies for acceptance a thesis entitled, "Age and Thermal History of the Port Mouton Pluton, southwest Nova Scotia: a combined U-Pb, $^{40}Ar/^{39}Ar$ Age Spectrum, and $^{40}Ar/^{39}Ar$ Laserprobe study", by Raymond Patrick Fallon, in partial fulfillment of the requirements for the degree of Master of Science.

Dated: _____

Examining Committee:

(External Examiner)

(Co-Supervisor)

(Co-Supervisor)

(Departmental Reader)

(Chair)

DALHOUSIE UNIVERSITY

DATE: AUGUST 25TH 1998

AUTHOR: Raymond Patrick Fallon

TITLE: Age and Thermal History of the Port Mouton Pluton, southwest Nova Scotia: a combined U-Pb, $^{40}Ar/^{39}Ar$ Age Spectrum, and $^{40}Ar/^{39}Ar$ Laserprobe study

DEPARTMENT OR SCHOOL: Earth Sciences

DEGREE: M.Sc. CONVOCATION: Fall YEAR: 1998

Permission is herewith granted to Dalhousie University to circulate and to have copied for non-commercial purposes, at its discretion, the above title upon the request of individuals or institutions.

Signature of Author

TABLE OF CONTENTS

LIST OF FIGURES

CHAPTER 1

CHAPTER 2

CHAPTER 3

CHAPTER 4

CHAPTER 5

LIST OF TABLES

CHAPTER 1

CHAPTER 2

CHAPTER 3

CHAPTER 4

Abstract

Previous $^{40}Ar/^{39}Ar$ geochronology indicates a complex post-intrusion thermal history for the Port Mouton Pluton (PMP) with most ages lying between ca. 350-310 Ma, suggesting either Carboniferous plutonism, slow cooling, or subsequent resetting of an older crystallization age. New U-Pb data for monazite and titanite, and new $^{40}Ar/^{39}Ar$ incremental heating data for muscovite and K-feldspar, coupled with the first reported laserprobe data (total fusion and spot analysis of muscovite) from Meguma Zone plutons, provide clarification of the age and thermal history of the PMP. U-Pb dating of monazite constrains the crystallization age of the main intrusive units to 373 ± 1 Ma. Magmatic muscovite ages of ca. 373 Ma ($^{40}Ar/^{39}Ar$ laserprobe) from undeformed samples suggest rapid post-crystallization cooling. Laserprobe muscovite ages of ca. 360 Ma to 345 Ma (with core ages generally older than rim ages) reflect partial loss of accumulated argon from muscovite between ca. 330-300 Ma. Recrystallized grain margins and core-rim element variation suggest that argon loss from deformed samples occurred by a combination of reaction and deformation mechanisms. Ages of ca. 360-345 Ma from some undeformed samples suggest that other mechanisms may have contributed to argon loss from these samples. Muscovite incremental heating spectra generally yield ages of ca. 360-350 Ma and do not show the apparent age gradients revealed by laserprobe spot fusion analysis. Total fusion ages from all samples are highly variable, possibly reflecting the complex age gradients preserved within PMP muscovite. The oldest ages recorded in the highest-temperature increments of K-feldspar spectra suggest a distinct argon loss event between ca. 280-260 Ma. A U-Pb titanite age of ca. 260 Ma may record this event. Younger ages recorded in low-temperature increments suggest reheating events at ca. 230-210 Ma and ca. 200 Ma. The incremental heating spectra from a sample of pegmatite suggests that argon loss from the least retentive K-feldspar domains occurred fairly recently probably at ambient temperatures. The muscovite laserprobe data presented here are compatible with an argon loss event at ca. 330-300 Ma, a result consistent with previous studies in southwestern Nova Scotia. However, no clear distinction exists between possible separate argon loss events at ca. 330-315 Ma and 300 Ma, a single protracted event lasting ca. 30 Ma, or a single argon loss event at ca. 300 Ma. Argon loss at ca. 330-300 Ma may reflect Alleghanian deformation in the Meguma Zone. Although K-feldspar ages ca. 280 Ma could record cooling following thermal resetting at ca. 300 Ma, similar K-feldspar ages from several other plutons in the southwestern Meguma Zone suggest that argon loss was widespread in this part of the Meguma Zone at this time. Feldspar ages of ca. 230-200 Ma correlate well with the timing of mafic magmatism in Nova Scotia associated with North Atlantic rifting and elevated temperatures during intrusion could have reset feldspar ages. This study demonstrates the value of integrated geochronological studies involving several techniques on a variety of minerals in elucidating complex thermal histories. In particular, $^{40}Ar/^{39}Ar$ laserprobe studies are more effective than conventional incremental heating analysis in revealing complex age gradients in minerals from complex geological regions.

ACKNOWLEDGEMENTS

I would like to extend my sincere thanks and gratitude to Professor D. Barrie Clarke and Professor P. H. Reynolds for bringing me to Dalhousie and Canada, and giving me the opportunity (with the help of a Dalhousie Graduate Scholarship) to experience the ups and downs of graduate research. Both DBC and PHR were most generous with their time and resources. I would like to give praise to Keith Taylor without whom this thesis would not have been possible. I thank Professor Larry Heaman for inviting me to Edmonton and sharing his insights into U-Pb geochronology. I thank Melissa Polloway and Kim Toope for expert assistance in the U-Pb geochronology lab at the University of Alberta.

I must thank Tom Duffet for his endless assistance with computers and graphics. I acknowledge Bob MacKay and Gordon Brown for assistance with microprobe analysis and thin-section preparation respectively. Thanks to Norma Keeping and Darlene Van De Rijt for administrative stuff. Thanks to Dirk van Loon for allowing access to the Port Joli pegmatite. Thanks to Dan Kontak, Marcos Zentilli, and Becky Jamieson for reviewing this work. A big thanks to everyone I met and had a good time with. Thank you Nicole for supreme assistance in the field.

CHAPTER 1

INTRODUCTION, GEOLOGICAL SETTING, AND PURPOSE

1.1 Introduction

Orogenic cycles last tens of millions of years and inherently involve several phases of superimposed deformation, metamorphism, and magmatism. An important goal of tectonic studies is to determine the rates and duration of processes that operate during orogenesis; this knowledge is essential for constructing the long-term tectonic history of an orogen or modelling the geodynamic history of the crust. Processes such as heat transfer, crustal anatexis, metamorphic mineral growth, and ductile deformation, operate over millions of years, and absolute ages with uncertainties of ± 1 million years are required to resolve their timing (Hawkins and Bowring 1997).

Radiogenic isotope geochronology is key to unravelling the sequence of deformational, metamorphic, and plutonic events responsible for producing the complex geotectonic histories we seek to understand. By exploiting the temperature-dependent nature of radiogenic isotope diffusion within rocks and minerals, geochronologists provide insights into processes that operate over the entire temperature range of an orogenic cycle. Minerals with a high retention temperature for daughter isotopes provide information on high temperature processes such as mineral growth during prograde metamorphism, whereas minerals with progressively lower retention temperatures yield detailed temperature information on post-metamorphic/plutonic cooling histories (Zeitler 1989).

In general, uranium-bearing accessory minerals such as zircon and monazite exhibit relatively strong retention of lead making it possible to date events that occurred during and before high grade metamorphism (ca. 650°- 800°C). Zircon, monazite, and xenotime can date the age of protolith rocks, the formation of prograde metamorphic isograds in middle-upper amphibolite facies conditions, the time of leucosome formation in migmatites, and emplacement ages for granitoid plutons and pegmatites that place constraints on the timing of deformation (Heaman and Parrish 1991).

With a range of retention temperatures (ca. 500°- 200°C) for the common potassium-bearing minerals hornblende, mica, and K-feldspar, the K-Ar system (and the $^{40}Ar/^{39}Ar$ variant) is critical for providing information on post-peak plutonic-metamorphic conditions. In regions where cooling is not prolonged, hornblende and mica ages may approximate the age of crystallization or peak metamorphism (Zeitler 1989; Hanes 1991). Integrated geochronological studies using different dating methods on a variety of minerals with different retention temperatures, can produce detailed (although admittedly simplistic) pressure-temperature-time histories for orogenic belts (Daly et al. 1989; Brown 1993).

1.2 Regional geotectonic setting

The Appalachian Orogen of eastern North America represents the eroded remnant of a Lower Paleozoic mountain belt formed from the closure of the Late Proterozoic-Ordovician Iapetus Ocean and the resulting collision between Laurentian and Gondwanan continents (Windley 1995). The collage of terranes that make up the

Appalachians in Canada and the United States represents the multitude of island arcs, ocean crust fragments, continental margins, and microcontinental fragments, caught up in the collision. Considerable debate exists regarding the relative timing of major periods of deformation along the Appalachian belt (Windley 1995) and a single unified tectonic model incorporating the entire orogen is not yet possible. This orogen-wide debate is mirrored by the continuing uncertainty regarding timing of events within individual terranes.

The Meguma Zone of Nova Scotia is the most outboard terrane in the Canadian Appalachians. The Cobequid-Chedabucto fault defines the northern boundary of the Meguma Zone and separates it from the adjacent Avalon Zone (Fig. 1.1). The Meguma Zone consists of two main lithological components: (i) Cambrian-Ordovician Meguma Supergroup, a thick succession of metamorphosed sandstone and shale, interpreted as a deep-sea turbidite fan complex deposited on the Gondwanan passive margin and unconformably overlain by Silurian-Early Devonian metasedimentary and metavolcanic rocks (Shenk 1995); and (ii) voluminous Late Devonian peraluminous granitoid plutons (Fig. 1.1). This superficially simplistic geology masks a complicated thermal history that, despite thirty years of intense geochronological investigations, has yet to be adequately resolved.

The Meguma Group and overlying units were deformed and variably metamorphosed during the Devonian Acadian Orogeny during accretion with the

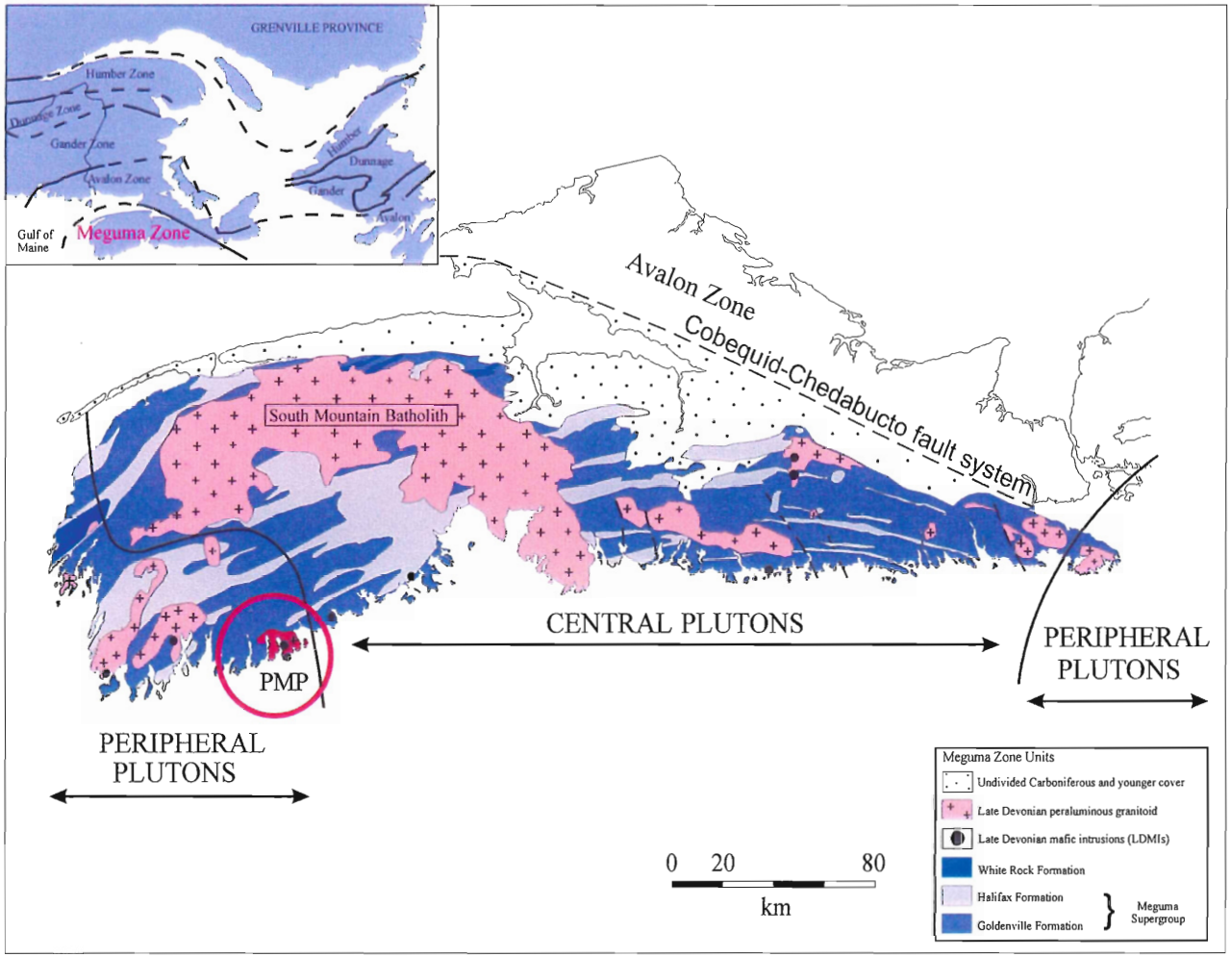

Figure 1.1. Geological map of the Meguma Zone showing division of Central and Peripheral plutons. The location of the PMP is indicated.

adjacent Avalon Zone (Keppie 1993). Toward the end of the Acadian Orogeny, the Meguma crust was intruded by a suite of dominantly peraluminous Late Devonian granitoid plutons and syn-plutonic mafic dykes (Clarke et al. 1997). Following Meguma-Avalon collision, the Meguma Zone was variably affected by the Carboniferous-Permian Alleghanian Orogeny (Muecke at al. 1988). Although the effects of this event were much more significant in the central and southern Appalachians (Windley 1995), localized deformation, mineralization, and minor plutonism in the Meguma Zone appear to belong to this orogeny, which probably reflects reactivation of Acadian structures (Keppie and Dallmeyer 1995; Culshaw and Liesa 1997; Culshaw and Reynolds 1997; Kontak et al. 1998).

1.3 Port Mouton Pluton: a complex Peripheral Pluton

The Meguma Zone is host to a large number of Late Devonian (375-372 Ma), late- to post-tectonic peraluminous granitoid intrusions (Fig. 1.1). The Port Mouton Pluton (PMP), the focus of this study, belongs to a group of several small plutons of weakly peraluminous tonalitic to granodioritic and monzogranitic compositions which contrast with the more voluminous peraluminous plutons of the Meguma Zone such as the South Mountain Batholith (SMB). These small plutons, including the Barrington Passage Pluton, Shelburne Pluton, and Canso Plutons, have been termed Peripheral Plutons by Tate (1995); the SMB and Musquodoboit Batholith constitute the Central Plutons (Tate 1995). Distinct chemical and isotopic differences between the Central and Peripheral Plutons suggest different sources and processes were involved in their

formation (Tate et al. 1997). In particular, mantle-derived magmas appear to have played a crucial role (as a source of heat and material) in the origin of several Peripheral Plutons, including the PMP (Clarke et al. 1997).

The PMP is a complex, multiple intrusion of elliptical shape, that crops out in southwest Nova Scotia (Fig. 1.1). The PMP is distinct from other Late Devonian peraluminous granitoid intrusions in the Meguma Zone in its lithological heterogeneity, extensive interaction with country rock, evidence for mingling and mixing with mafic magmas, and abundant pegmatites (Clarke et al. in prep.). On the basis of cross-cutting relationships, Woodend-Douma (1988) defined ten lithological units within the PMP which can be assigned to three intrusive cycles (Fig. 2.1): Early Stage, Middle Stage, and Late Stage (Clarke et al., in prep.) (Table 1.1). Early Stage tonalite-granodiorite occurs as a continuous body along the southern contact of the PMP, as a discontinuous body along the northern contact, and as detached blocks in the Middle-Stage granodiorite-monzogranite (Woodend-Douma 1988). Middle Stage granodiorite-monzogranite occupies a large part of the interior of the PMP and is the most abundant phase. Late Stage bodies, ranging in composition from tonalite to aplite-pegmatite granite, occur as numerous small intrusions cutting all earlier units (Woodend-Douma 1988).

Table 1.1. Summary of Field and Lithological Characteristics of the Port Mouton Pluton, from Clarke et al. (in prep.).

	Main lithologies	Description	Chemical group
Early Stage	biotite tonalite, biotite granodiorite; minor tonalite breccia, trondhjemite, and shoshonitic lamprophyre	incorporates map Units 1, 2, and 5 of Douma (1988, 1992), and comprises about 15% of the PMP; coarse-grained, equigranular to sub-porphyritic, foliated (110-140°) granitoids (colour index 10-26) occur discontinuously around outer margin of PMP, as thick sheets in the south and as intimate injections along bedding in migmatites in the north; locally abundant enclaves of partially melted and ductily deformed country rock; several small tonalitic breccia pipes, with abundant rounded granitoid and metasedimentary inclusions, occur near the southern contact; two irregular synplutonic lamprophyric dykes and mingled pillows intrude the tonalite near the southern contact (Tate and Clarke 1995)	1 Rb/Sr<0.55 Eu/Eu*>0.40
Middle Stage	biotite-muscovite granodiorite, biotite-muscovite monzogranite; minor muscovite-biotite leucomonzogranite with related aplites and pegmatites	incorporates map Units 3, 4, and 6 of Douma (1988, 1992), and comprises more than 50% of the PMP; equigranular, medium- to coarse-grained, weakly foliated (ca. 020-040°) granitoids (colour index 1-16) containing enclaves of both country rock and Early Stage granitoids; cut by minor related leucomonzogranite and associated aplite-pegmatite dykes	2 Rb/Sr>0.55 Eu/Eu*<0.40
Late Stage	biotite-muscovite tonalite and granodiorite	approximately equivalent to map Unit 7 of Douma (1988, 1992), and comprises about 10% of the PMP; dykes up to 25 m wide and small irregular bodies of fine- to medium-grained, unfoliated granitoids (colour index 5-16)	≡ 1
	two-mica monzogranite and leucomonzogranite with associated aplites and pegmatites	incorporates map Units 8 and 9 of Douma (1988, 1992), and comprises up to 25% of the PMP; subhorizontal and subvertical sheets of fine- to medium-grained, equigranular monzogranites and leucomonzogranites (colour index < 6) closely associated with garnet-rich zoned aplites, and texturally variable garnet-tourmaline-fluorapatite-beryl pegmatites	≡ 2

1.4 Meguma Zone geochronology

Geochronological investigations in the Meguma Zone have focused on resolving the various phases of deformation, metamorphism, and plutonism, but resetting by later thermal events has made resolving the absolute timing and duration of events difficult (e.g., Muecke et al. 1988). Tables 1.2 and 1.3 present important geochronological results from the last 20 years.

Whole-rock slate/phyllite and muscovite ages ca. 390 Ma record Devonian Acadian deformation in the Meguma Zone (Hicks et al. 1998). U-Pb and $^{40}Ar/^{39}Ar$ dating of granitoids constrains their intrusion to ca. 372 Ma. A U-Pb zircon age of 378.5 ± 2 Ma from the North Forest Hills Pluton (Hill 1991) and a maximum apparent age of 385 Ma for hornblende from a marginal tonalite phase of the Barrington Passage Pluton (Reynolds et al. 1987), suggest the possibility that initial crystallization began several million years earlier, possibly during the waning stages of Acadian deformation. Mica $^{40}Ar/^{39}Ar$ ages between 380-370 Ma from the Meguma Supergroup in the vicinity of the Late Devonian plutons are attributed to thermal resetting associated with intrusion (Keppie and Dallmeyer 1987; Muecke et al. 1988).

The recent hypothesis (Benn et al. 1997) that the South Mountain Batholith was intruded during the waning stages of Acadian deformation implies that deformation occurred during the interval 390-370 Ma. Consequently, some ages of ca. 370 Ma from the Meguma Supergroup may record Acadian deformation and not thermal resetting associated with pluton intrusion. The idea that Acadian deformation extended over a ca. 20 My period is not unrealistic considering that accretion of adjacent terranes is unlikely

to be a distinct event. Ages of ca. 370 Ma from dynamically recrystallized micas in rocks adjacent to the Cobequid-Chedabucto fault in the eastern Meguma Zone date movement along the terrane boundary associated with continued convergence and the initial stages of tectonic uplift (Keppie and Dallmeyer 1987).

The close agreement of U-Pb, Rb-Sr, and $^{40}Ar/^{39}Ar$ ages (ca. 372 Ma) from central and eastern plutons implies rapid post-crystallization cooling through respective retention temperatures (Keppie and Dallmeyer 1987; Clarke et al. 1993). Rapid cooling was possibly associated with rapid uplift and unroofing as indicated by the overlying Late Devonian-Early Carboniferous sediments (Martel et al. 1993). Mica ages between ca. 370 and 360 Ma suggest the possibility of less rapid cooling for some plutons. The large number of $^{40}Ar/^{39}Ar$ determinations between 360 and 220 Ma (with most lying between 350-300 Ma) from granitoids and host rocks in the southwestern Meguma Zone are variably interpreted (Reynolds et al. 1987; Muecke et al. 1988; Keppie and Dallmeyer 1995). Clearly resetting has occurred, but how many episodes and at what times is currently unclear. The virtual absence of $^{40}Ar/^{39}Ar$ mica ages < 365 Ma from the central and eastern Meguma Zone, implies that these regions went largely unaffected.

Reynolds et al. (1987) and Muecke et al. (1988) identified resetting events at ca. 320-300 Ma (mica ages) and ca. 230-220 Ma (K-feldspar ages) associated with Alleghanian deformation and Atlantic rifting respectively. These authors interpret all $^{40}Ar/^{39}Ar$ ages < 370 Ma as reset. In contrast, Dallmeyer and Keppie (1987), Keppie and Dallmeyer (1987, 1995), Kontak and Cormier (1991), and Kontak et al. (1995) identified several distinct resetting events at various times between ca. 340-254 Ma.

Keppie and Dallmeyer (1995) interpreted mica ages between ca. 360-340 Ma from plutons in the southwestern Meguma Zone as retention ages following relatively rapid post-crystallization cooling. Corresponding ages in nearby country rocks (ca. 350-340 Ma) date contact metamorphism associated with intrusion. These authors attribute the disparity in mica ages between central and eastern parts of the Meguma Zone (ca. > 360 Ma) and the southwestern Meguma Zone (ca. 340-360 Ma) to diachronistic cooling following intrusion at ca. 372 Ma. Younger plateau ages and low-temperature increments of older (ca. 360-340 Ma) plateau ages record resetting events at ca. 331, 320-314, 302, and 287-281 Ma (Keppie and Dallmeyer 1995).

Keppie and Dallmeyer (1995) associated resetting with infusion of hot magmatic fluids along shear zones; however, post-370 Ma magmatism within the Meguma Zone has only been documented by the relatively minor Wedgeport Pluton (316 ± 5 Ma; Cormier et al. 1988). Kontak and Cormier (1991) and Kontak et al. (1995) interpreted complex $^{40}Ar/^{39}Ar$ and Rb-Sr data from the Davis Lake Pluton (East Kemptville area) as evidence for local resetting at ca. 344, 330-320, and 254 Ma. These authors also invoked a similar mechanism involving migration of heated fluids along shear zones to explain their data.

1.5 Port Mouton Pluton: a geochronological enigma?

Previous attempts to date the PMP have produced variable results and many hypotheses (Fig. 1.2). Reynolds et al. (1981, 1987), and Woodend-Douma (1988), attributed $^{40}Ar/^{39}Ar$ apparent ages ca. 343-300 Ma for hornblende, muscovite, and biotite from various intrusive phases and two synplutonic mafic dykes to thermal resetting. Keppie and Dallmeyer (1995) presented a 340 ± 1 Ma plateau age from a sample of Middle Stage monzogranite and plateau ages of 343 ± 1 and 347 ± 1 Ma from the adjacent Meguma Supergroup, as evidence for moderately rapid post-crystallization cooling following intrusion, with subsequent thermal resetting between ca. 330-310 Ma.

In the absence of reliable crystallization ages for the main intrusive phases of the PMP it is difficult to test these competing hypotheses and to evaluate the relative roles of slow cooling versus reheating. Carboniferous-Permian Alleghanian overprinting has obliterated much of the original post-intrusive cooling history in the southwestern Meguma Zone. The two or three mica plateau ages ca. 370 that exist for granitoid intrusions and mafic dykes in this region suggest the possibility that rapid cooling may have been a terrane-wide phenomenon.

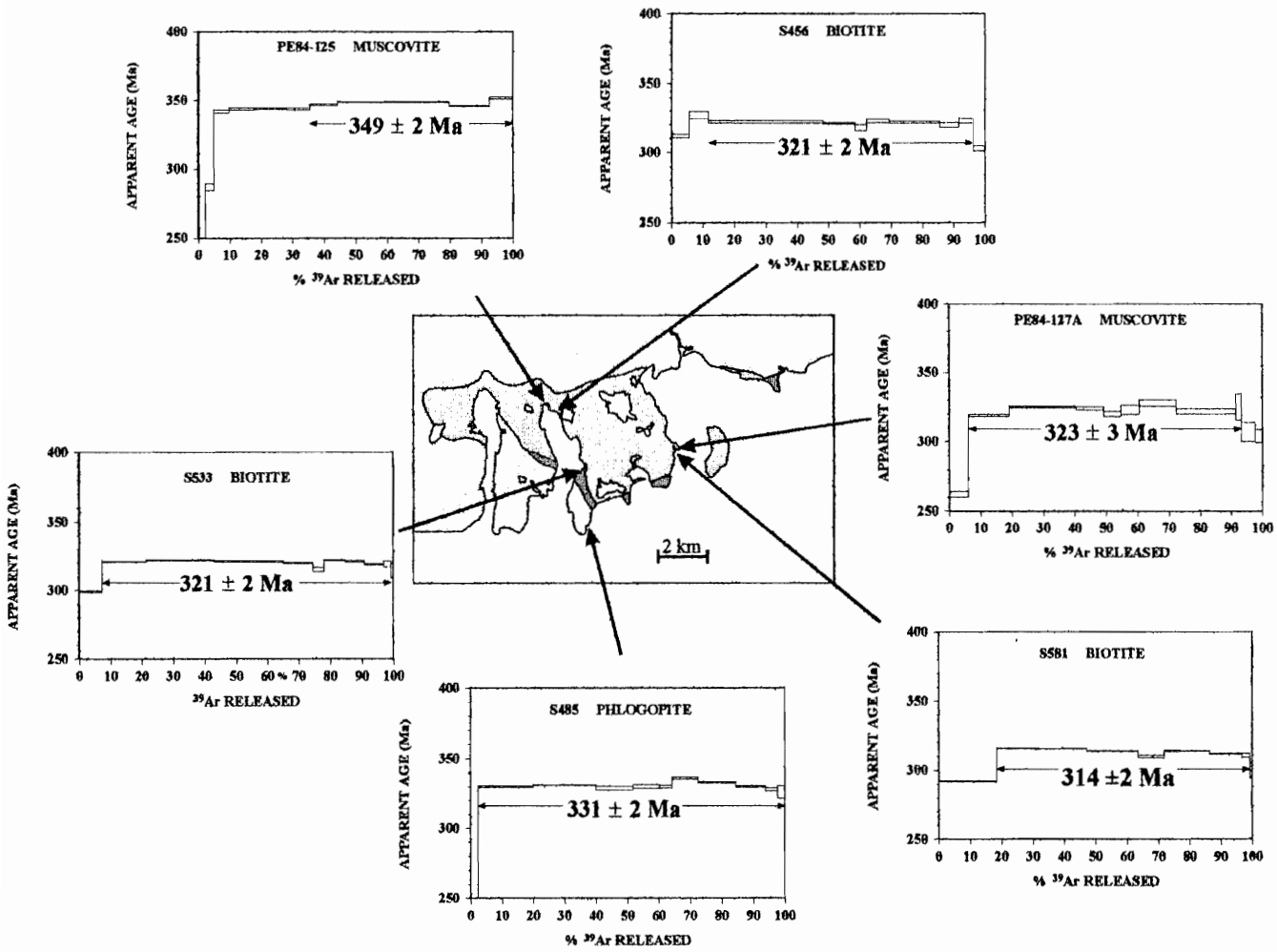

Figure 1.2. Previous $^{40}Ar/^{39}Ar$ ages for the Port Mouton Pluton (Reynolds et al. 1987; Woodend-Douma 1988). Ages indicated are mean apparent ages. This diagram does not include the 340 ± 1 Ma plateau age of Keppie and Dallmeyer (1995).

1.6 Current analytical techniques

Conventional U-Pb geochronology using thermal ionization mass spectrometry (TIMS) is currently the only method that can produce high precision crystallization ages for granitoid rocks (e.g., Tomascak et al. 1996). Recent advances in $^{40}Ar/^{39}Ar$ analytical procedures (Lee at al. 1990; Hodges et al. 1994; Hodges and Bowring 1995; Hodges 1996; Hames and Cheney 1997) have shown that laser-based studies could potentially provide an alternative mechanism for seeing through complex post-intrusive histories.

Laserprobe studies show that single mineral grains can contain large gradients in radiogenic ^{40}Ar concentrations and, thus, apparent age (e.g., Hodges et al. 1994). Prior to the development of high-resolution laserprobes, geochronologists deduced the nature of ^{40}Ar gradients in minerals from the morphology of incremental release spectra (e.g., Hanes 1991). West and Lux (1993) and Heizler et al. (1997) used this method to show that muscovite in rocks penetratively deformed at low temperatures can experience substantial loss of radiogenic ^{40}Ar, yet porphyroclasts can retain accumulated ^{40}Ar and yield ages older than the timing of their deformation.

In contrast, other studies (e.g., Lee et al. 1990; Hodges et al. 1994) have demonstrated that the morphologies of many incremental release spectra do not provide accurate information on the distribution of ^{40}Ar within minerals and, therefore, cannot be used to deduce thermal histories. Hodges et al. (1994) and Hodges and Bowring (1995) obtained flat incremental release spectra from micas suggesting a uniform distribution of radiogenic ^{40}Ar within grains; however, laserprobe studies on micas from the same

samples revealed complex age gradients that suggested a very different thermal history. Such studies illustrate the importance of combining laserprobe and incremental heating techniques in the study of regions where complex thermal histories are suspected, e.g., southwest Meguma Zone and the PMP.

1.7 Purpose and objectives

The purpose of this study is to apply current geochronology techniques in unraveling the complex thermal history of the Port Mouton Pluton. The objectives of this thesis are:

1) To obtain precise U-Pb crystallization ages for the main intrusive phases of the Port Mouton Pluton. Precise crystallization ages will provide a benchmark for interpreting subsequent $^{40}Ar/^{39}Ar$ ages.
2) To clarify the post-crystallization thermal history of the Port Mouton Pluton. Conventional incremental heating (spectrum) analysis of muscovite and feldspar will be combined with high-resolution laserprobe $^{40}Ar/^{39}Ar$ dating of single muscovite grains. The combination of conventional and new techniques allows comparisons with previous $^{40}Ar/^{39}Ar$ studies of the PMP, and may offer new insights into the factors influencing previous $^{40}Ar/^{39}Ar$ results.

Table 1.2. Geochronology of Central Meguma Zone plutons.

METHOD	MINERAL	AGE (Ma)	REFERENCE	COMMENTS
		SOUTH MOUNTAIN BATHOLITH		
U-Pb	Monazite	374 ± 2, 373 ± 2	Harper 1988	Crystallization age
Pb-Pb	Whole rock	373 ± 4	Chatterjee & Ham 1991	
$^{40}Ar/^{39}Ar$	Muscovite	372 ± 3 plateau	Clarke et al. 1993	Average of 13 plateau ages (369 ± 2 – 375 ± 4) from leucogranites
		377 ± 6, 373 ± 6, 370 ± 6 plateaus	Keppie et al .1993	Millet Brook biotite granodiorite
		368 ± 8 plateau	Keppie et al. 1993	Westfield altered porphyry
	Biotite	368 plateau	Reynolds et al. 1981	Average of 10 plateau ages
	K-feldspar	352-343 total gas	Reynolds et al. 1987	High temperature ages (356-371 Ma) suggest rapid cooling following intrusion; low temperature ages imply resetting at ca. 300Ma and ca. 220 Ma
		MUSQUODOBOIT BATHOLITH		
$^{40}Ar/^{39}Ar$	Muscovite	372 ± 1 plateau	Keppie & Dallmeyer 1987	Crystallization age
	Biotite	370 ± 2 plateau	Keppie & Dallmeyer 1987	
		362 plateau	Reynolds et al. 1981	
		KINSAC PLUTON		
$^{40}Ar/^{39}Ar$	Muscovite	363 plateau	Reynolds et al. 1981	
	Biotite	373, 362 plateaus	Reynolds et al. 1981	Crystallization age
		LISCOMB COMPLEX GRANITES		
$^{40}Ar/^{39}Ar$	Muscovite	373 ± 4, 372 ± 5, 370 ± 3, 369 ± 3 plateaus	Kontak & Reynolds 1994	Crystallization age; Associated mafic intrusions: 371 ± 4-373 ± 3 Ma.; associated high-grade gneisses: 367 ± 3-377 ± 3 Ma.
	Biotite	368 ± 3 total gas		

Table 1.2. continued. Geochronology of Central Meguma Zone plutons.

METHOD	MINERAL	AGE (Ma)	REFERENCE	COMMENTS
		EASTERN PLUTONS		
U-Pb	Zircon	378.5 ± 2	Hill 1991	North Forest Hills Pluton; crystallization age
$^{40}Ar/^{39}Ar$	Muscovite	364 ± 1 plateau	Keppie & Dallmeyer 1987	
	Biotite	368 ± 2 plateau	Keppie & Dallmeyer 1987	
$^{40}Ar/^{39}Ar$	Muscovite	362 ± 2 plateau	Keppie & Dallmeyer 1987	South Forest Hills Pluton
	Biotite	362 ± 2 plateau	Keppie & Dallmeyer 1987	
U-Pb	Monazite	375 ± 1	Keppie et al. 1985	Sangster Lake Pluton; crystallization age
$^{40}Ar/^{39}Ar$	Muscovite	365 ± 1 plateau	Keppie & Dallmeyer 1987	
	Biotite	366 ± 2 plateau	Keppie & Dallmeyer 1987	
U-Pb	Monazite	372 ± 1	Keppie et al. 1985	Larry's River Pluton; crystallization age
$^{40}Ar/^{39}Ar$	Muscovite	365 ± 2 plateau	Keppie & Dallmeyer 1987	
	Biotite	364 ± 2 plateau	Keppie & Dallmeyer 1987	
U-Pb	Monazite	373 ± 1	Keppie et al. 1985	Halfway Cove Pluton; crystallization age
$^{40}Ar/^{39}Ar$	Muscovite	360 ± 1 plateau	Keppie & Dallmeyer 1987	
U-Pb	Monazite	375 ± 2	Keppie et al. 1985	Queensport Pluton; crystallization age
$^{40}Ar/^{39}Ar$	Muscovite	360 ± 2 plateau	Keppie & Dallmeyer 1987	
	Biotite	362 ± 2 plateau	Keppie & Dallmeyer 1987	
$^{40}Ar/^{39}Ar$	Muscovite	367 ± 2 plateau	Keppie & Dallmeyer 1987	Sherbrooke Pluton; crystallization age
	Biotite	364 ± 2 plateau	Keppie & Dallmeyer 1987	
$^{40}Ar/^{39}Ar$	Muscovite	367 ± 1, 370 ± 2 plateaus	Keppie & Dallmeyer 1987	Bull Ridge Pluton; crystallization age
	Biotite	364 ± 1 plateau	Keppie & Dallmeyer 1987	

Table 1.3. Geochronology of Peripheral Meguma Zone plutons.

METHOD	MINERAL	AGE (Ma)	REFERENCE	COMMENTS
Eastern Meguma Zone				
			CANSO PLUTONS	
U-Pb	Monazite	371 ± 2	Hill 1991	Whitehaven Pluton; crystallization age
$^{40}Ar/^{39}Ar$	Muscovite	364 ± 2 plateau	Keppie & Dallmeyer 1987	
		368 ± 2 plateau	Reynolds et al. 1981	
	Biotite	364 ± 2 plateau	Keppie & Dallmeyer 1987	
$^{40}Ar/^{39}Ar$	Muscovite	359 ± 3, 362 ± 2 plateaus	Keppie & Dallmeyer 1987	Durrell Island Pluton
	Biotite	366 ± 2 plateau	Keppie & Dallmeyer 1987	
Southwestern Meguma Zone				
			SOUTH MOUNTAIN BATHOLITH (DAVIS LAKE PLUTON)	
U-Pb	Whole rock	367 ± 10	Kontak & Chatterjee 1992	East Kemptville; Concordia plot of 10 samples; crystallization age
Pb-Pb	Whole rock	366 ± 4	Kontak & Chatterjee 1992	East Kemptville; Isochron age (34 samples)
$^{40}Ar/^{39}Ar$	Muscovite	361 ± 2, 358 ± 1 plateaus	Keppie & Dallmeyer 1995	East Kemptville area; discordant age ranges from 300-360 Ma and 340-358 Ma
		(ca. 300-ca. 330)	Kontak et al. 1995	East Kemptville; age range (seven spectra)
		338 ± 2	Kontak & Cormier 1991	East Kemptville
		350, 300 plateaus	Zentilli & Reynolds 1985	East Kemptville
		366 plateau	Reynolds et al. 1981	Near mineralized zone
	Biotite	372 plateau	Reynolds et al. 1981	Outside mineralized zone
		317 plateau	Reynolds et al. 1981	Near mineralized zone
Rb-Sr	Whole rock	374 ± 5	Chatterjee & Cormier 1991	
	Whole rock	334 ± 5	Kontak & Cormier 1991	East Kemptville
	Muscovite-WR	(361-311Ma)	Kontak & Cormier 1991	East Kemptville; age range (seven samples)
	Feldspar-WR	(240-276 Ma)	Kontak & Cormier 1991	Range of ages

Table 1.3 continued. Geochronology of Peripheral Meguma Zone plutons.

METHOD	MINERAL	AGE (Ma)	REFERENCE	COMMENTS
		PORT MOUTON PLUTON		
$^{40}Ar/^{39}Ar$	Muscovite	340 ± 1 plateau	Keppie & Dallmeyer 1995	
		343 total gas	Reynolds et al. 1987	discordant spectrum (340-350 Ma)
		325 plateau		
	Biotite	321 total gas	Reynolds et al. 1987	
		300 plateau	Reynolds et al. 1981	
	K-feldspar	255 total gas	Reynolds et al. 1987	discordant spectrum (230-275 Ma)
	Hornblende	324 total gas	Woodend-Douma 1988	Age of two synplutonic mafic dykes
		SHELBURNE PLUTON		
U-Pb	Monazite	371 ± 2	Keppie et al. 1985	
	Zircon	376 ± 2	Tate et al. 1997	Crystallization age of tonalite and diorite
$^{40}Ar/^{39}Ar$	Muscovite	350, 340 plateaus	Reynolds et al. 1987	discordant spectra (335-360 Ma)
		324 ± 1	Keppie & Dallmeyer 1987	
	Biotite	350 total gas	Reynolds et al. 1987	
		310 plateau	Reynolds et al. 1987	
		302 plateau	Reynolds et al. 1981	
		309 ± 1 plateau	Keppie & Dallmeyer 1987	
		371 plateau	Reynolds et al. 1987	Synplutonic diorite
	K-feldspar	(230-275 Ma)	Reynolds et al. 1987	Discordant age range

Table 1.3 continued Geochronology of Peripheral Meguma Zone plutons.

METHOD	MINERAL	AGE (Ma)	REFERENCE	COMMENTS
		BARRINGTON PASSAGE PLUTON		
U-Pb	Monazite	375 ± 2	Keppie et al. 1985	Crystallization age
$^{40}Ar/^{39}Ar$	Hornblende	372 plateau	Reynolds et al. 1987	Synplutonic gabbronorite; 330 & 340 Ma biotite plateau ages from same sample
		370 plateau	Reynolds et al. 1987	Synplutonic gabbronorite; 345 Ma biotite plateau
	Muscovite	347 plateau	Reynolds et al. 1987	
		320 ± 1 plateau	Keppie & Dallmeyer 1987	
	Biotite	plateau ages from 319-350	Reynolds et al. 1987	
		313 plateau	Dallmeyer & Keppie 1987	
		306 plateau	Reynolds et al 1981	
	K-feldspar	(220-290 Ma)	Reynolds et al 1987	Discordant age range
		BALD MOUNTAIN PLUTON		
$^{40}Ar/^{39}Ar$	Muscovite	370, 340 plateaus	Reynolds et al. 1981	
		BRENTON PLUTON		
$^{40}Ar/^{39}Ar$	Muscovite	322 ± 1 plateau	Dallmeyer & Keppie 1987	
		318 plateau	Reynolds et al. 1981	
	Biotite	316-328 total gas	Reynolds et al. 1981	
		WEDGEPORT PLUTON		
U-Pb	Zircon	316 ± 5	Cormier et al. 1988	Crystallization age
$^{40}Ar/^{39}Ar$	Biotite	258 ± 8 plateau	Reynolds et al. 1981	

1.8 Organization of this thesis

Chapter 2 describes the samples selected for this study and discusses the paragenesis of muscovite used for $^{40}Ar/^{39}Ar$ geochronology. Chapter 3 presents the results of monazite and titanite U-Pb geochronology. Chapter 4 presents the results of conventional incremental heating (spectrum) analysis of muscovite and feldspar and high-resolution laserprobe $^{40}Ar/^{39}Ar$ dating of single muscovite grains. Chapter 5 combines U-Pb and $^{40}Ar/^{39}Ar$ results in discussing the thermal history of the PMP and suggests implications for the geological evolution of the southwestern Meguma Zone. Chapter 5 also includes recommendations for future work.

CHAPTER 2

SAMPLE SELECTION, PETROGRAPHY, AND MUSCOVITE CHEMISTRY

2.1 Introduction

This chapter discusses the selection of samples, primarily for $^{40}Ar/^{39}Ar$ muscovite geochronology. Following a detailed description of sample petrography, I discuss the chemical and textural characteristics of muscovite dated in this study in terms of magmatic versus non-magmatic origin.

2.2 Sample selection

A variety of rock types was selected for U-Pb and $^{40}Ar/^{39}Ar$ geochronology (Table 2.1). Several factors influenced sample selection. The sample set reflects the extreme lithological variation of the PMP, ranging from biotite-tonalite to muscovite-garnet pegmatite. I attempted to sample compositions from the three main intrusive stages, at the same time covering as much of the exposed pluton as possible (Fig. 2.1). An inevitable bias toward Middle Stage compositions resulted because these rocks are the most abundant within the PMP, and thus cover the widest geographical area.

More significantly, Middle Stage rocks have high muscovite contents, making them ideal candidates for $^{40}Ar/^{39}Ar$ geochronology. Muscovite contents of Early Stage tonalites are typically <5%, whereas the very coarse grain size of most Late Stage pegmatites makes them unsuitable for laserprobe or furnace experiments, especially if one wishes to work with single crystals. For these reasons, the majority of samples used in this study are Middle Stage granodiorites and monzogranites (Table 2.1).

Table 2.1. Samples dated in this study.

Sample number	Lithology	Intrusive Stage	Location	Technique
96-1	muscovite-biotite monzogranite	Middle Stage	Wobamkek Beach	U-Pb titanite; $^{40}Ar/^{39}Ar$ muscovite
96-2	biotite tonalite	Early Stage	St Catherine's River road	U-Pb monazite
96-3	muscovite-garnet pegmatite	Late Stage	Sandy Bay Beach	$^{40}Ar/^{39}Ar$ muscovite, K-feldspar
97-3	muscovite monzogranite	Middle Stage	Hwy 103, north of Robertson's Lake	$^{40}Ar/^{39}Ar$ muscovite
97-4	muscovite pegmatite	Late Stage	Hwy 103, north of Robertson's Lake	$^{40}Ar/^{39}Ar$ K-feldspar
97-9	biotite-muscovite granodiorite	Middle Stage	St Catherine's River road	U-Pb monazite; $^{40}Ar/^{39}Ar$ muscovite
97-14	biotite-muscovite granodiorite	Middle Stage	Summerville Beach	U-Pb monazite; $^{40}Ar/^{39}Ar$ muscovite
97-16a	muscovite-biotite monzogranite	Middle Stage	Wobamkek Beach	$^{40}Ar/^{39}Ar$ muscovite
97-17	muscovite-biotite monzogranite	Middle Stage	Wobamkek Beach	$^{40}Ar/^{39}Ar$ muscovite
98-4	muscovite pegmatite	Late Stage	Summerville Beach	$^{40}Ar/^{39}Ar$ K-feldspar
477	biotite-muscovite monzogranite	Middle Stage	On road through Goose Hills	$^{40}Ar/^{39}Ar$ muscovite
484	biotite-muscovite granodiorite	Early Stage	MacLeods Cove	$^{40}Ar/^{39}Ar$ muscovite
487	Biotite-muscovite tonalite	Early Stage	MacLeods Cove	$^{40}Ar/^{39}Ar$ muscovite
556	biotite-muscovite monzogranite	Middle Stage	Port Mouton Head	$^{40}Ar/^{39}Ar$ muscovite

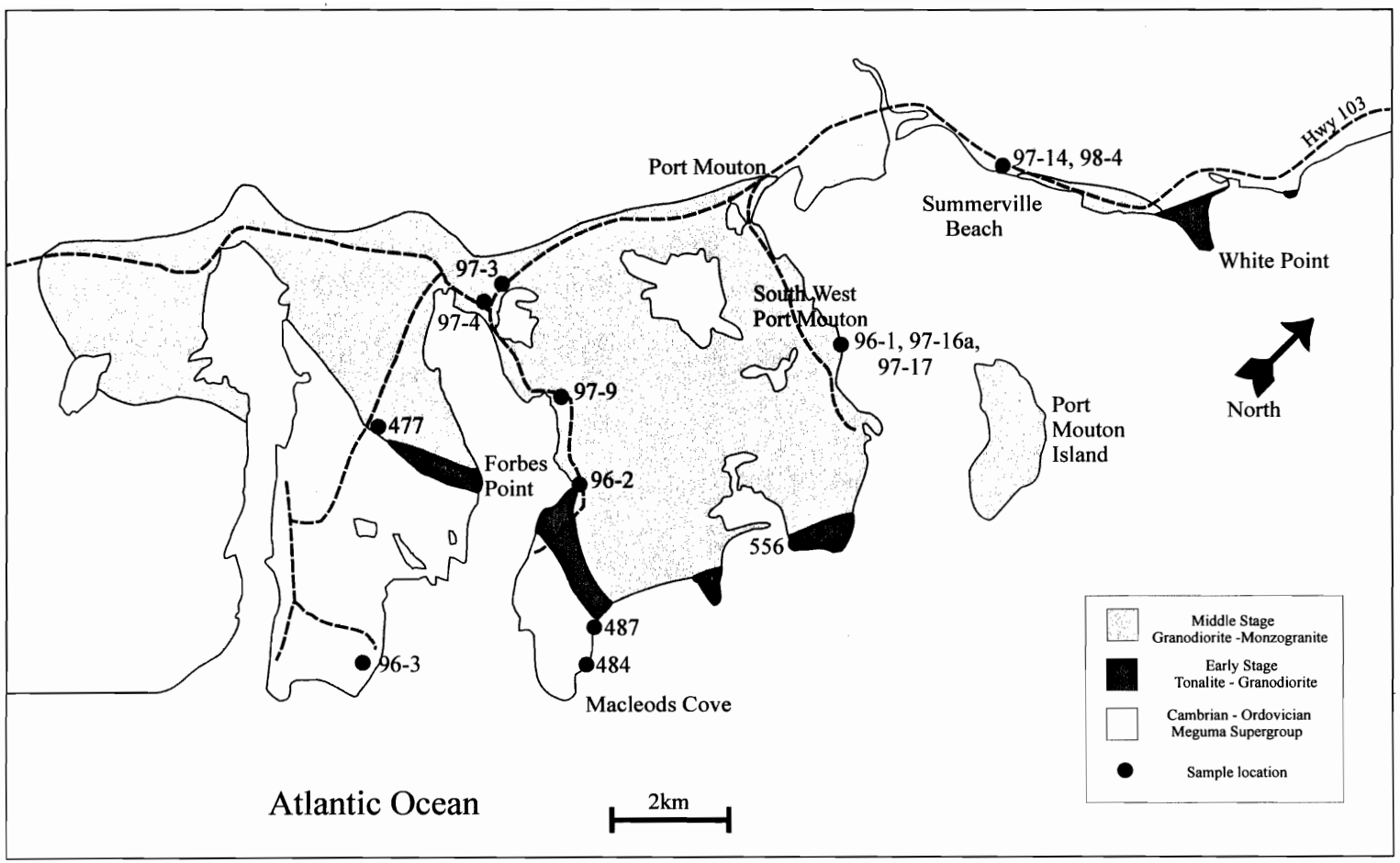

Figure 2.1. Simplified geological map of the Port Mouton Pluton, southwest Nova Scotia. The map omits the complex cross-cutting relationships and abundant Late Stage sheets for simplicity. Locations of samples used for U-Pb and $^{40}Ar/^{39}Ar$ geochronology are shown. After Woodend-Douma (1988) and Clarke et al. (in prep.)

Previous studies (e.g., West and Lux 1993; Hames and Cheney 1997; Heizler et al. 1997), including several from southwestern Nova Scotia (e.g., Dallmeyer and Keppie 1987; Kontak et al. 1995; Culshaw and Reynolds 1997), have described the important role that deformation plays in influencing the distribution of argon isotopes in rocks and minerals. To understand the role deformation played in resetting $^{40}Ar/^{39}Ar$ ages from the PMP, samples displaying several degrees of deformation were selected for $^{40}Ar/^{39}Ar$ geochronology. This sample set can be conveniently grouped into undeformed and deformed samples. The petrographic characteristics of these two sample sets are described in detail in the following section.

In the field, undeformed samples (Fig. 2.2) show only weak NE-striking fabrics, orientations consistent with previous observations (Woodend-Douma 1988). Four samples of variably deformed Middle Stage rocks were collected for $^{40}Ar/^{39}Ar$ geochronology. Sample 97-3 was collected close to the northern limit of the PMP, near the junction of Highway 103 and St. Catherine's River road (Fig. 2.1). Sample 97-3 is a fine-grained muscovite monzogranite. Outcrops display a weak NE-striking foliation, dipping steeply to the NW. Samples 96-1, 97-17, and 97-16a were collected from South West Port Mouton, in the vicinity of Wobamkek Beach (Fig. 2.1).

The intensity of deformation varies greatly in the vicinity of Wobamkek Beach, and some outcrops show well-developed mylonitic fabrics (Fig. 2.3d). Sample 96-1 is a medium-grained monzogranite. On fresh and weathered surfaces, a well-developed NE-striking (054-058) fabric defined by elongate micas and quartz dips steeply to the SE, although some outcrops dip to the NW.

Figure 2.2. Field relations of undeformed samples. a) Sample **96-2**, Early Stage tonalite cross-cut by Late Stage pegmatites, St. Catherine's River road. b) Sample **97-9**, fine-grained Middle Stage granodiorite showing weak NE-striking fabric (below hammer), St. Catherine's River road. c) Sample **97-14**, medium-grained Middle Stage granodiorite at northern contact of PMP, near Summerville Beach. d) Sample **98-4**, Late Stage pegmatite cross-cutting sample **97-14**, near Summerville Beach.

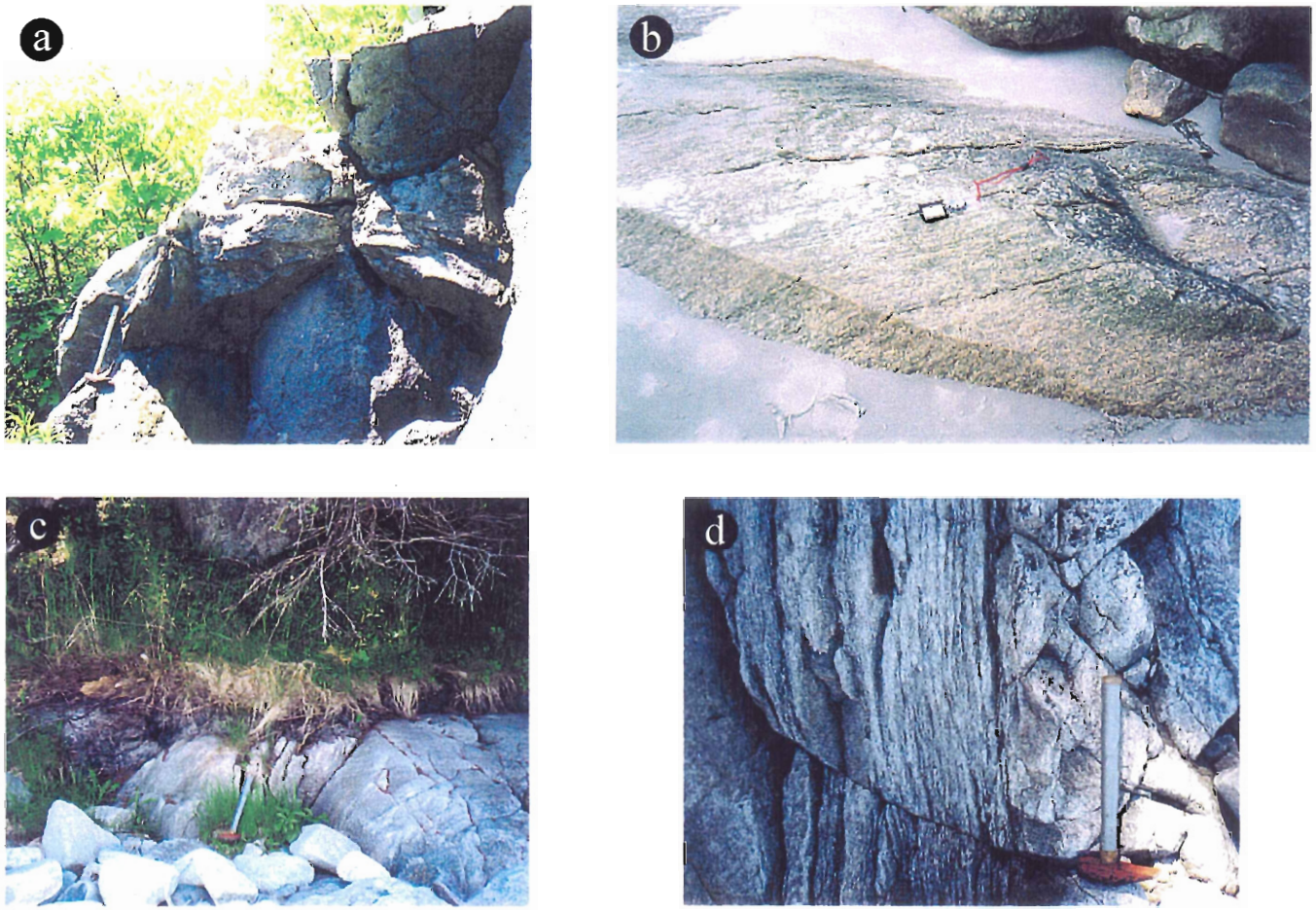

Figure 2.3. Field relations of deformed samples. a) Deformed sample **97-3**. b) Strongly foliated outcrop of sample **96-1**, Wobamkek Beach. c) Relatively undeformed outcrop of sample **97-17**, Wobamkek Beach. d) Well-developed shear zone (sample **97-16a**) in Middle Stage monzogranite, Wobamkek Beach.

Nearby, rocks of a similar composition (sample 97-17) display only weak NE-striking fabrics, and at first glance, appear totally undeformed (Fig. 2.3c). Ten to fifteen meters north of sample 97-17, the same outcrop is crossed by a narrow (<1m wide) NE-striking (052) shear zone (Fig. 2.3d). Rocks within the shear zone have a well-developed NE-NNE-striking (054-060) foliation that dips steeply (~80-near vertical) to the NW. Rocks immeadiately outside the shear zone are apparently undeformed (Fig. 2.3d).

2.3 Sample petrography

Tables 2.3 and 2.4 summarize important petrographic features of undeformed and deformed samples respectively. Figures 2.4 –2.7 illustrate important textural and mineralogical relationships. Undeformed samples (96-2, 97-9, 97-14, and 556) have typical hypidiomorphic granular textures and are distinguished from their deformed equivalents by the absence of significant grain size reduction of quartz and micas (Fig. 2.4). Deformation in these samples is restricted to undulose extinction of quartz and micas (Fig. 2.4b), and bending of mica cleavage planes. Grain-size reduction is restricted to rare mortar textures surrounding large quartz grains (Fig. 2.4b).

Muscovite in undeformed samples is present as euhedral-subhedral grains intergrown with biotite (Fig. 2.4d), and less commonly, as larger euhedral-subhedral interstitial grains (Fig. 2.8). Deformation affects most grains in the form of undulose extinction and bending of cleavage planes (Fig. 2.4d), but is rarely significant enough to induce grain size reduction of the micas. Muscovite is also present as a fine-grained

Table 2.2. Petrographic features of selected undeformed samples.

Quartz	Plagioclase	K-feldspar	Biotite	Muscovite	Deformation features
96-2, medium-coarse grained, Early Stage tonalite					
Anhedral grains, up to several mm, most 2-3mm; smaller (<1mm) interstitial grains; undulose extinction; sutured grain boundaries; minor sub-grain development; ~35%	Euhedral grains up to 6mm, most 2-3mm, ubiquitous albite twinning; diffuse oscillatory zoning common; minor sericitization; inclusions of quartz and mica; myrmekitic belbs at contacts with K-feldspar; no obvious undulose extinction; ~50%	Rare small (<1mm) anhedra of microcline; rare perthitic orthoclase (?); <1%	Subhedral-anhedral, grains, up to 3-4mm, smaller (≤ 1mm) interstitial grains; abundant inclusions of apatite and U-bearing accessories; minor chloritization; minor undulose extinction; some replacement by fine-grained muscovite along edges and cleavage; ~15%	Muscovite occurs in several habits: fine-grained intergrowth and replacement of biotite; fine-grained sericitic alteration of plagioclase; fine-grained aggregates at edges of felsic minerals; ~1%	Weak alignment of biotite in hand sample and thin section; undulose extinction of quartz and biotite
97-9, fine-medium grained, Middle Stage granodiorite					
Anhedral grains up to several mm; small (1mm) anhedral interstitial grains; variable undulose extinction; minor sub-grain development; sutured grain boundaries; ~30-40%	Euhedral-subhedral grains up to several mm, majority 2-3mm, many < 1mm; ubiquitous twinning, albite > Carlsbad; diffuse oscillatory zoning common; cloudy cores resulting from sericite alteration; abundant inclusions of prismatic muscovite; minor undulose extinction; ~30%	Small anhedral microcline, <1mm-3mm; some minor replacement of plagioclase(?); euhedral-subhedral perthitic orthoclase/, up to several mm, with inclusions of plagioclase, quartz, and biotite; undulose extinction; deformation lamellae(?) ~15-20%	Euhedral-subhedral, grains, in clusters or as interstitial grains; majority < 1mm, some up to 2mm; abundant inclusions of apatite and U-bearing accessories; undulose extinction, minor kinking of cleavage planes; ~10%	Muscovite occurs in several habits: Small (≤1mm) prismatic grains, with sharp or ragged terminations, associated with biotite, minor undulose extinction, kinking, no grain size reduction; rare inclusions of quartz; may be replacing biotite in some cases; rare large (>1mm) tabular grains, with minor undulose extinction; sericitized cores in plagioclase; prismatic inclusions in plagioclase; < 5%	Notable for fine grain size and lack of obvious deformation textures; weak alignment of biotite grains in hand sample and thin section; undulose extinction of quartz and micas only evidence of strain

Table 2.2 continued. Petrographic features of selected undeformed samples.

Quartz	Plagioclase	K-feldspar	Biotite	Muscovite	Deformation
97-14, medium grained, Middle Stage granodiorite					
Anhedral grains up to several mm very common; variable undulose extention in all grains, sub-grain development in most grains; polygoniaztion, of small (<1mm) interstitial grains; ~35%	Euhedral-subhedral grains, up to several mm; albite twinning; diffuse oscillatory zoning common; heavily sericitized cores in some grain; inclusions of small prismatic muscovite; undulose extinction in some grains, rare sub-grains; myrmekitic blebs at boundaries with K-feldspar; ~30%	Anhedral, poikilitic grains of perthitic orthoclase (?) up to several mm, some small (≤1mm) grains; large grains have inclusions of biotite and plagioclase; deformation lamellae; ~20%	Euhedral-subhedral, grains, in clusters or as interstitial grains; majority < 1 mm, some up to 2mm; abundant inclusions of apatite and U-bearing accessories; undulose extinction, kinking, and offset of cleavage planes; no significant grain size reduction; replacement by chlorite along margins and cleavage; fine-grained muscovite at margins; some relatively undeformed grains; < 10%	Muscovite occurs in several habits: small (≤1mm) prismatic grains, with sharp or ragged terminations, associated with biotite; variable but relatively minor undulose extinction, kinking, and no grain size reduction; rare inclusions of quartz; may be replacing biotite in some cases; rare larger (>1mm) tabular grains with minor undulose extinction; sericitized cores in plagioclase; prismatic inclusions in plagioclase; spongy replacement of plagioclase; fine-grained replacement along biotite margins < 5%	No obvious orientation of biotite in thin section, weak in hand sample; undulose extinction and kinking of micas and quartz more pronounced than 97-9; rare polygonization of quartz attests to increased strain
556, medium-coarse grained, Middle Stage monzogranite					
Anhedral grains up to several mm small (1mm) anhedral interstitial grains; variable undulose extinction; elongation of sub-grains; sutured grain boundaries; well-developed mortar texture around one large grain; ~35%	Euhedral-subhedral grains up to 4 mm, majority equant grains 1-2mm, many <1mm; ubiqitous twinning, albite > Carlsbad; diffuse oscillatory zoning common; sericitization less severe; cloudy cores in some grains; inclusions of biotite, quartz, and abundant prismatic muscovite; myrmekitic blebs at contacts with K-feldspar; minor undulose extinction; rare twin lamellae offset; ~30%	Small (~1-3mm) equant microlcline with well developed cross-hatch twins; large (up to several mm) perthitic feldspar with inclusions of quartz and biotite; undulose extinction common; minor kaolinization; no obvious grain-size reduction along margins; ~20%	Euhedral-subhedral, grains, in clusters or as interstitial grains; up to 5mm, majority 1-3mm; abundant inclusions of apatite and U-bearing accessories; chloritization common; ubiquitous undulose extinction, minor kinking of cleavage planes; some grain-size reduction along margins; ≤ 10%	Muscovite occurs in several habits: subhedral grains <1mm-2mm associated with or intergrown with biotite; in clusters or singly; undulose extinction, kinking common; small prismatic grains replacing (?) biotite ; prismatic inclusions in plagioclase; fine-grained aggregates at edges of felsic minerals; fine-grained aggregates or larger wholesale replacement of plagioclase and rarely microcline; <5%	Weak alignment of biotite and quartz in some hand samples samples; undulose extinction of feldspars, micas and quartz, kinking of micas, and mortar texture surrounding quartz

Table 2.2 continued. Petrographic features of selected undeformed samples.

Quartz	Plagioclase	K-feldspar	Biotite	Muscovite	Deformation
96-3, medium grained-pegmatitic, Late Stage pegmatite					
Complex intergrowths with plagioclase and microcline; minor undulose extinction; rare polygonization; grain size variable, but generally coarse; modal proportions variable	Coarse-grained intergrowth with quartz and K-feldspar; minor undulose extinction ; cloudy appearrance due in part to fine-grained muscovite replacement; modal proportions variable	Coarse-grained perthitic microcline; minor undulose extinction; modal proportions variable	Not present	Variable grain size; complex intergowths with quartz and feldspar; majority as large, prismatic clusters, typically several mm; minor undulose extinction in some grains; some kinking of planes; minor grain-size reduction along edges; fine-grained dark alteration along cleavage (?); also as clusters of dendritic grains, up to several mm long; modal proportions variable	Minor undulose extinction of quartz and muscovite

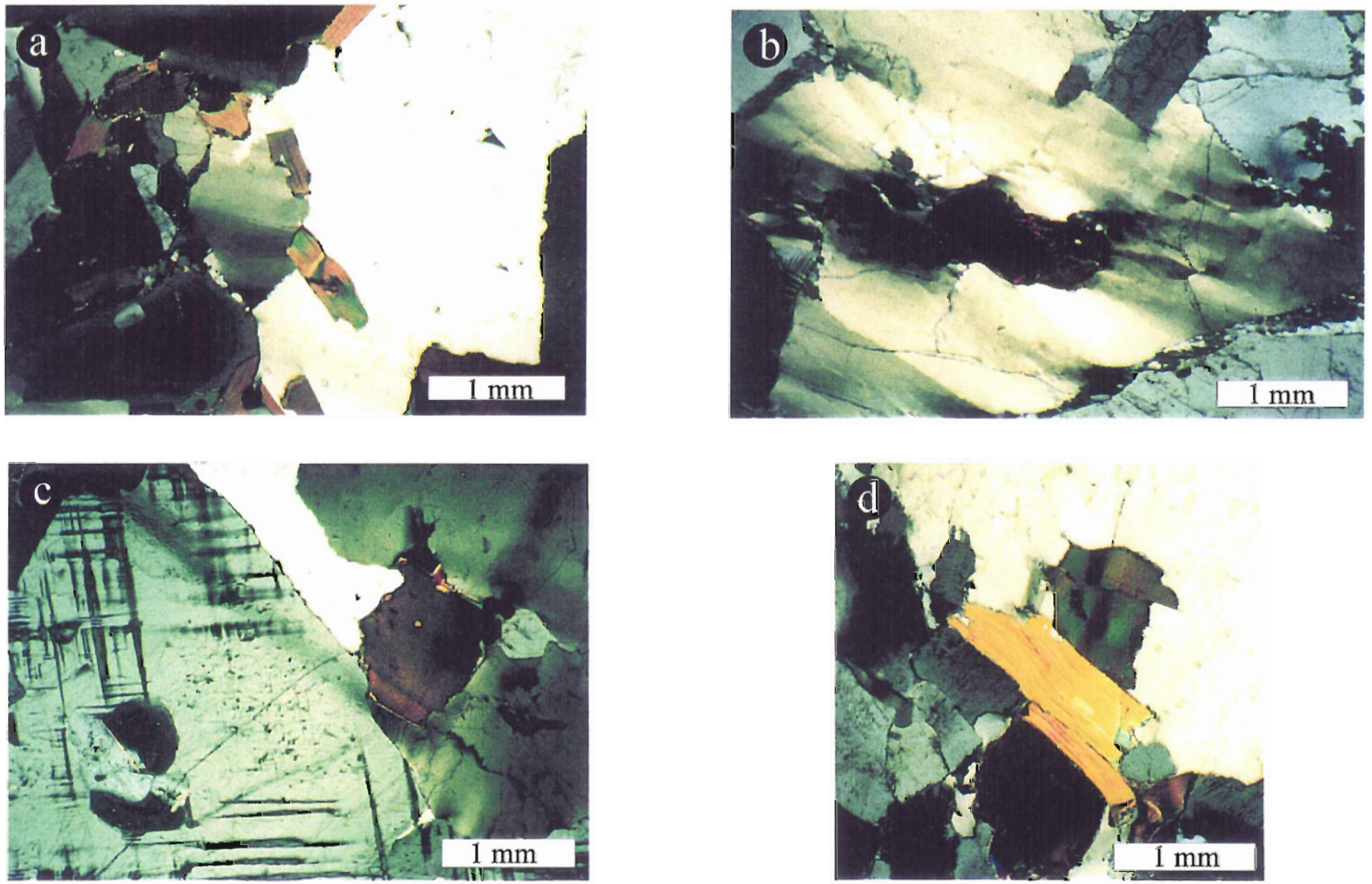

Figure 2.4. Petrographic features of undeformed samples. a) Sample **97-14**. Large anhedral quartz grain showing sutured grain boundaries and minor sub-grain development. Note the mildly deformed biotite. b) Sample **556**. Mortar texture surrounding large quartz grain. c) Sample **97-14**. Large undeformed microcline grain. d) Sample **97-14**. Intergrowth of biotite and subhedral muscovite. Both micas show evidence of mild deformation in the form of undulose extinction and kinking of cleavage planes.

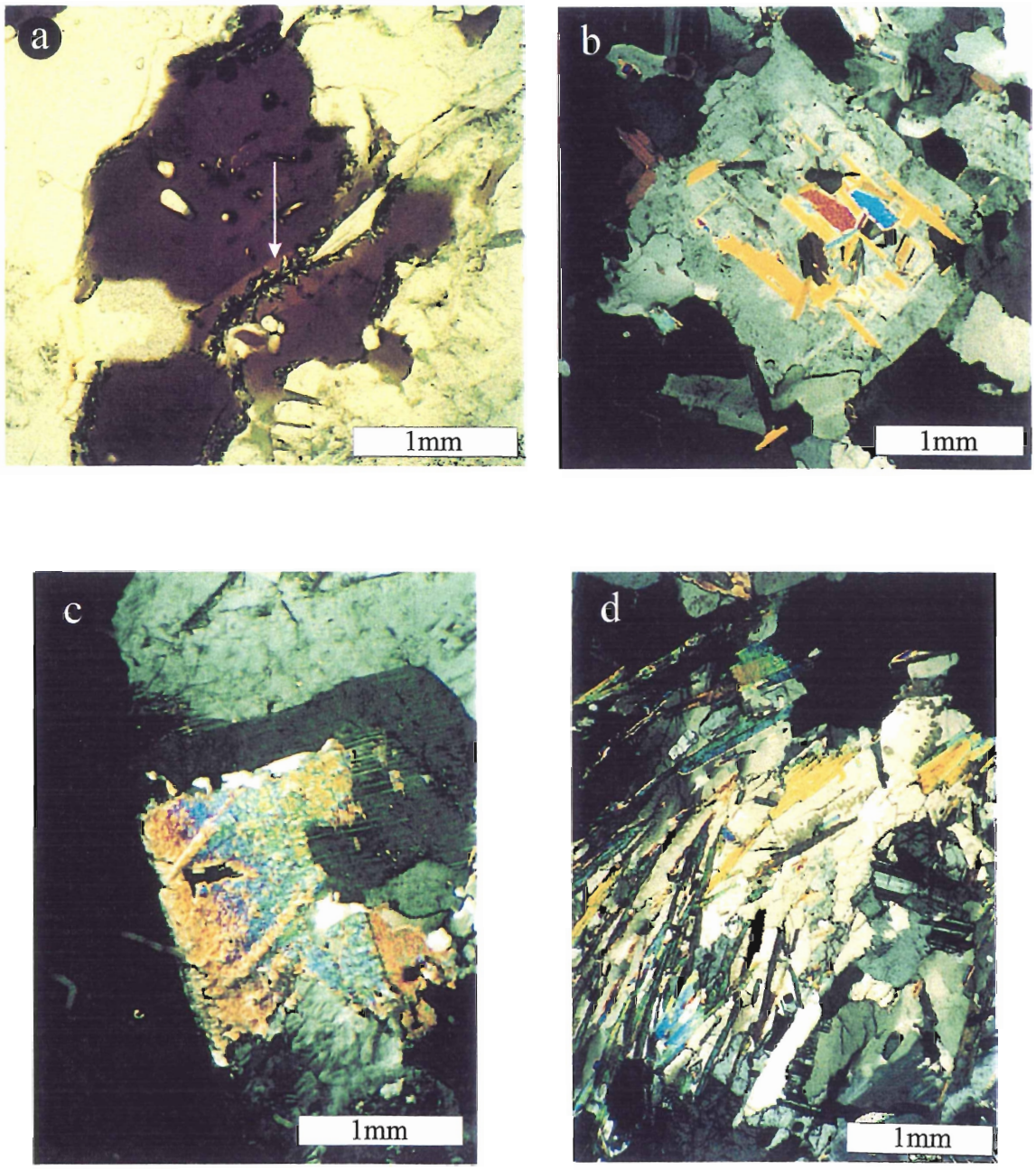

Figure 2.5. Muscovite types from undeformed samples. a) Sample **97-14**. Fine-grained muscovite replacing coarse biotite (arrow) b) Sample **97-9**. Euhedral muscovite replacing core of subhedral plagioclase. c) Sample **556**. Anhedral "spongy" muscovite replacing subhedral plagioclase. d) Sample **96-3**. Dendritic "plumose" muscovite intergrownwith quartz suggesting rapid growth from a magma.

replacement of biotite, along grain edges and cleavage planes (Fig. 2.5a), and as a fine-grained replacement of plagioclase (Fig. 2.5b), or as larger anhedral "spongy" grains replacing plagioclase (Fig. 2.5c).

Deformed samples are distinguished from their undeformed equivalents by significant grain size reduction of quartz and mica (Fig. 2.6a, b, i). Deformed samples contain numerous feldspar and muscovite porphyroclasts of various sizes preserved within a matrix of fine-grained micas, quartz, and feldspars (Fig. 2.6a). Sample 97-3 appears to have experienced more intense grain size reduction of feldspars (Fig. 2.6c) compared to samples 96-1, 97-16a, and 97-17, although the fine grain size of this sample may result from an original fine-grained protolith such as sample 97-9. Many porphyroclasts show evidence of deformation and recrystallization along their margins. In particular, muscovite grains are typically mantled along grain margins and tails, by fine-grained recrystallized muscovite (Fig. 2.6g), continuous with the mylonitic fabric in the matrix (Fig. 2.6i, j).

Deformed samples contain several textural varieties of muscovite not found in undeformed samples. Large (typically several mm) muscovite grains are a distinctive feature of deformed samples, in particular 96-1, 97-16a, and 97-17 (all from Wobamkek Beach). Large muscovite grains are typically anhedral, with irregular grain boundaries, and commonly, inclusions of quartz (Fig. 2.7g, h), display undulose extinction and bending of cleavage planes, and are typically mantled by fine-grained recrystallized muscovite (Fig. 2.7a-c). Rare, euhedral-subhedral, undeformed grains, with sharp

Table 2.3. Petrographic features of selected deformed samples.

Quartz	Plagioclase	K-feldspar	Biotite	Muscovite	Deformation features
96-1, medium-grained, Middle Stage, protomylonitic monzogranite					
Matrix of fine grained polygonal aggregates surrounding porpyroclasts of feldspar; larger (≥1mm) anhedral grains with undulose extinction and sub-grain development, typically mantled by fine-grained polygonal aggregates; ~35+%	Anhedral to rare subhedral grains, up to 3mm; ubiquitous albite twinning, rare Carlsbad twins; diffuse oscillatory zoning; undulose extinction with local sub-grain development; bending of twin planes common with offset resulting from fracturing; larger fractures filled with recrystallized quartz; sericitised cores commmon producing cloudy grains; replacement by K-feldspar; ~30%	Anhedral microcline up to 5mm, typically 1-2mm; undulose extinction and deformation lamellae common; fractures infilled with fine-grained muscovite; ~20%	Small, (≤1mm), ragged, anhedral grains, largely replaced by chlorite; complex intergrowths with fine-grained muscovite, replacing biotite in some cases; ~5%	Muscovite occurs in a variety of habits: Large (up to 3mm) euhedral-anhedral, sharp-ragged terminated grains, with minor undulose extinction, inclusions of quartz common, especially along edges; Large (up to 4mm) subhedral grains, sharp-ragged terminations, ubiquitous undulose extinction and kinking, distinctive mantle of fine-grained recrystallized muscovite; Smaller (≤1mm) grains similar to type 2, produced from the fragmentation of larger porphyroclasts, resulting in fine-grained aggregates that anastamose around more resistant feldspar grains; Small (≤1mm) euhedral-anhedral inclusions in plagioclase Fine-grained alteration of plagioclase (sericite); Fine-grained replacement of biotite along edges and as complex intergrowths; ≥5%	Weathered surfaces have obvious foliation defined by fine-grained elongate micas and quartz; larger resistant feldspars resemble augen; less obvious on fresh surfaces; large muscovite porphyroclasts define weak sub-vertical? lineation ("mica-fish")

Table 2.3 continued. Petrographic features of selected deformed samples.

Quartz	Plagioclase	K-feldspar	Biotite	Muscovite	Deformation
97-16a, fine-medium grained, protomylonitic, Middle Stage monzogranite					
Matrix of fine grained polygonal aggregates surrounding porpyroclasts of feldspar; some larger (up to 3mm) anhedral grains with undulose extinction and sub-grain development, mantled by finer grained polygonal aggregates; grain-size reduction more pronounced than 97-17, similar to 96-1; weak lineation defined in part by elongated polygonal aggregates; orientation of sub-grains, asymmetry of larger grains, and fracture orientaion suggest dextral movement, but ambiguities exist resulting from poorly developed mylonitic textures; also present in late thin veins that cross thin section; ~35+%	Anhedral- subhedral grains, typically 2-3mm, many <1mm, with ragged edges; albite twinning common,; diffuse oscillatory zoning; ubiquitous sericitization produces cloudy, dirty grains; inclusions of fine-grained muscovite; undulose extinction with local sub-grain development; bending of twin planes; fractures filled with recrystallized quartz; stair-step offset of albite twin planes suggests dextral shear; local replacement by K-feldspar; ~35%	Small (<1mm) anhedral microcline; perthitic grains; replacement of plagioclase; undulose extinction; ~10%	Ragged, chloritized grains up to 2mm, typically <1mm; associated apatite and U-bearing inclusions; complex intergrowths with muscovite define foliation; <5%	Muscovite occurs in a variety of habits: Large (up to 3-4mm) anhedral grains with irregular margins, inclusions of matriz grains common, especially along edges, variable undulose extinction and kinking, mantle of fine-grained recrystallized muscovite, less common than 96-1 or 97-17; Clusters of smaller (≤1mm) subhedral-anhedral grains with undulose extinction and kinking, well developed mantles of fine-grained recrystallized muscovite; produced from breakup of larger grains; Fine-grained replacement of biotite; Larger (≤1mm) intergrowths with biotite; Inclusions in plagioclase; Very fine- grained alteration of plagioclase (sericite); ≥5%	Apparently most deformed sample. Taken from small (<1 m wide maximum) shear zone 10-15 meters from 97-17. Well developed foliation on weathered surfaces defined by streaked out micas and quartz lenses, weak sub-vertical ? lineation defined by muscovite and biotite
97-3, fine-grained, Middle Stage monzogranite					
Matrix of fine grained-polygonal aggregates; larger (up to 2mm) elongate anhedral grains with undulose extinction, sub-grain development, and sutured grain boundaries typically mantled by finer grained polygonal aggregates; ~35+%	Small anhedral grains (≤1mm); larger anhedral porphyroclasts (up to 3mm); ubiquitous sericitization; Many larger grains appear to be shattered into smaller sub-grains, with fractures filled with fine-grained muscovite; ~25-30%	Small (≤1mm) anhedral matrix grains; some larger (>1mm) microcline with inclusion of quartz and plagioclase; simple and cross-hatch twins; undulose extinction; ≥15%	Small (<1mm) ragged, anhedral grains; undulose extinction, chloritization; associated with muscovite which replaces it in some cases; elongate anastamosing aggregates through matrix; <5%	Small (rarely >1mm), ragged, anhedral grains; undulose extinction, kinking of cleavage planes; fine-grained mantles not as obvious as 96-1; mildly deformed grains rare; also as fine-grained replacement of plagioclase and biotite; ≥5%	Fine grained, with moderate biotite-foliation

Table 2.3 continued. Petrographic features of selected deformed samples.

Quartz	Plagioclase	K-feldspar	Biotite	Muscovite	Deformation
97-17, medium-grained, Middle Stage monzogranite					
Grain-size reduction not as pronounced as 96-1; majority as fine- grained polygonal aggregates surrounding porpyroclasts of feldspar; many larger (up to 5 mm), elongate, anhedral grains with undulose extinction and sub-grain development, mantled by finer grained polygonal quartz; ~30+%	Anhedral to rare subhedral grains, up to 3mm, many <1mm; albite twinning common, rare Carlsbad twins; diffuse oscillatory zoning uncommon; ubiquitous sericitization producing cloudy, dirty grains; undulose extinction with local sub-grain development; bending of twin planes; local replacement by K-feldspar; ~35%	Small (<1mm) microcline, larger poikilitic grains (up to 4mm) present; fractures filled with quartz; undulose extinction; replacement of plagioclase; ≥15%	Ragged, chloritized grains up to 2mm, typically <1mm; associated apatite and U-bearing inclusions; complex intergrowths with muscovite define weak foliation; <5%	Muscovite occurs in a variety of habits: Large (up to 5mm) anhedral grains, sharp-ragged terminations , inclusions of matrix grains common, along edges, variable undulose extinction and kinking, mantle of fine-grained recrystallized muscovite; Clusters of smaller (≤1mm) subhedral-anhedral grains with undulose extinction and kinking, and typically well developed mantles of fine-grained recrystallized muscovite; produced from breakup of larger grains; Fine-grained replacement of biotite; Larger (≤1mm) intergrowths with biotite; Inclusions in plagioclase and microcline; Fine- grained alteration of plagioclase (sericite); ≥5%	Hand sample less deformed than 96-1; poorly developed foliation

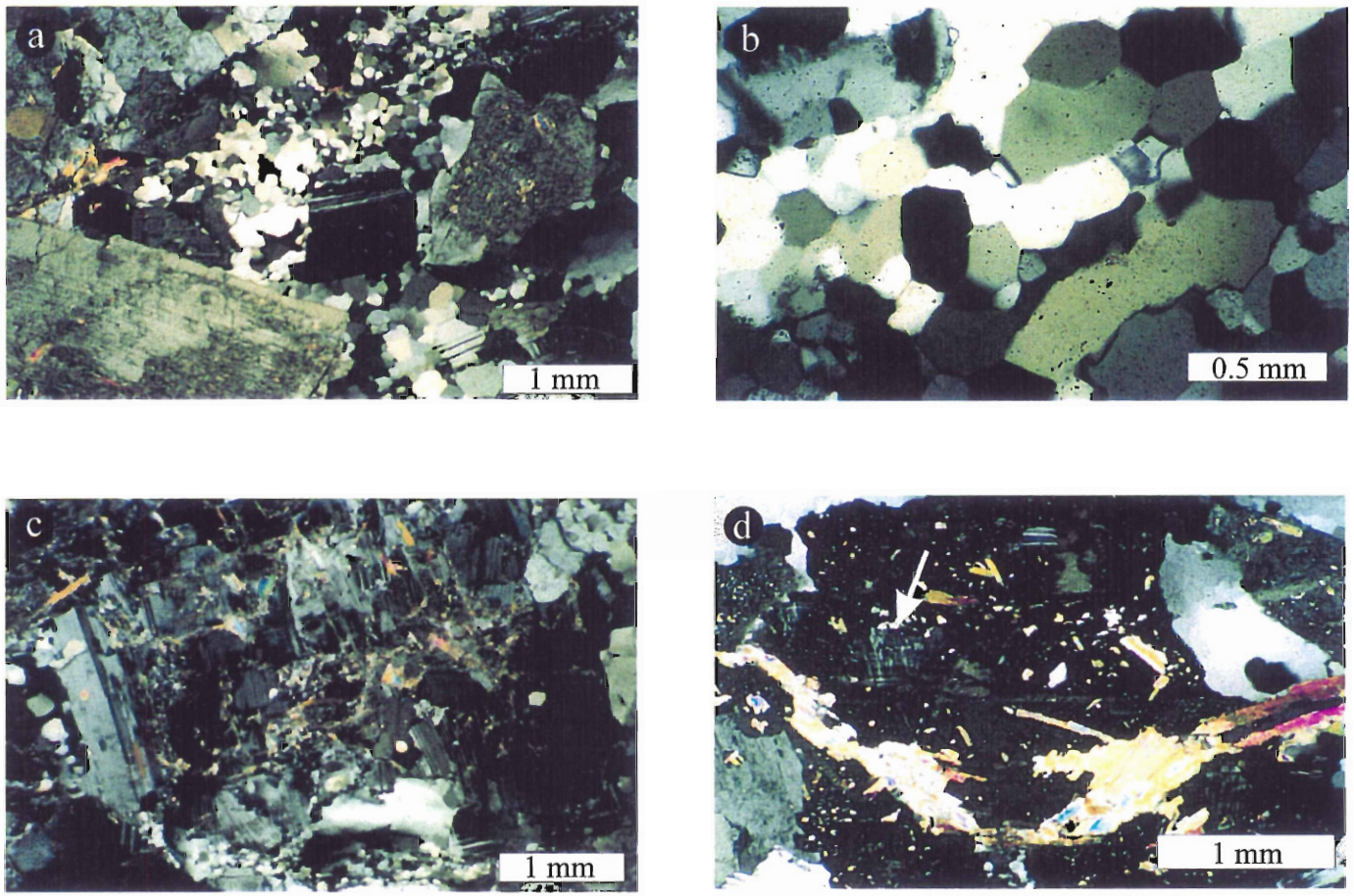

Figure 2.6. Petrographic features of deformed samples. a) Sample **97-16a**. Feldspar porphyroclasts in a fine-grained matrix of recrystallized quartz, feldspar, and mica. b) Sample **96-1**. Detail of fine-grained recrystallized (polygonal) quartz with high-angle grain boundaries. c) Sample **97-3**. Fragmentation of plagioclase porphyroclast; fractures are infilled? with fine-grained muscovite. d) Sample **97-17**. Replacement of plagioclase by a combination of fine-grained muscovite and microcline (arrow).

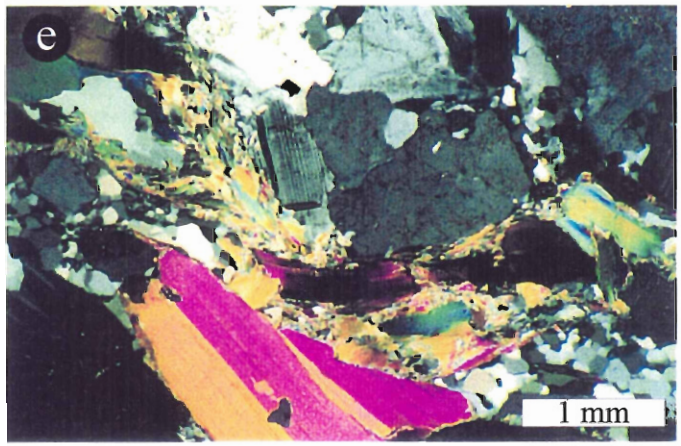

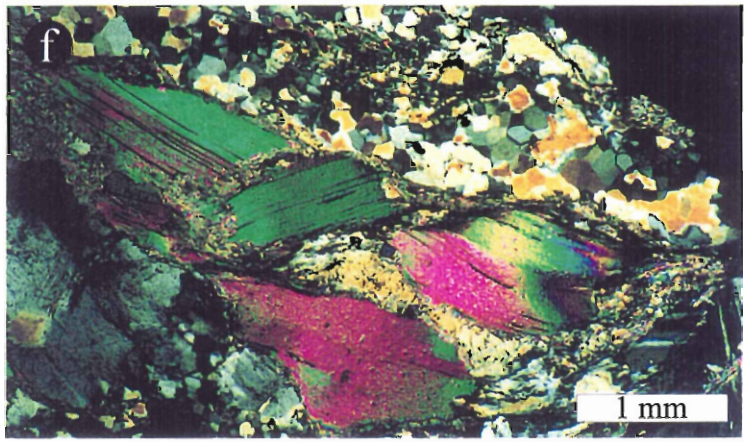

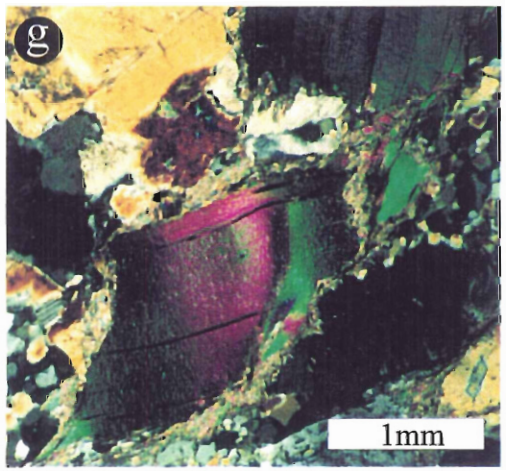

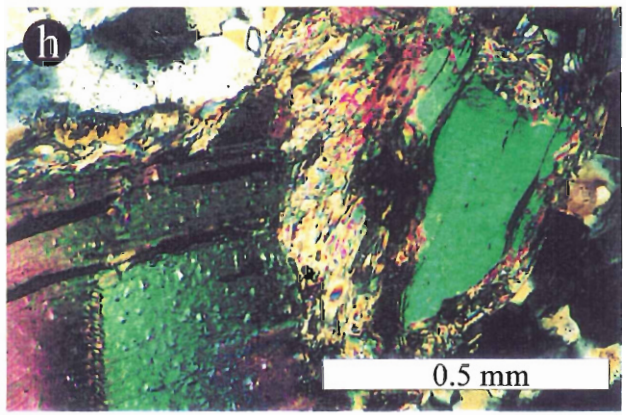

Figure 2.6. Continued. e) Sample **96-1**. Relatively undeformed muscovite porphyroclast adjacent to a cluster of intensely deformed muscovite. f) Sample **96-1**. Cluster of deformed muscovite mantled by fine-grained recrystallized muscovite; the three grains in the upper left were probably a single grain prior to breakup. g) Sample **96-1**. Fragmentation of large muscovite porphyroclast, mantled by fine-grained recrystallized muscovite. h) Sample **96-1**. Detail of muscovite breakup.

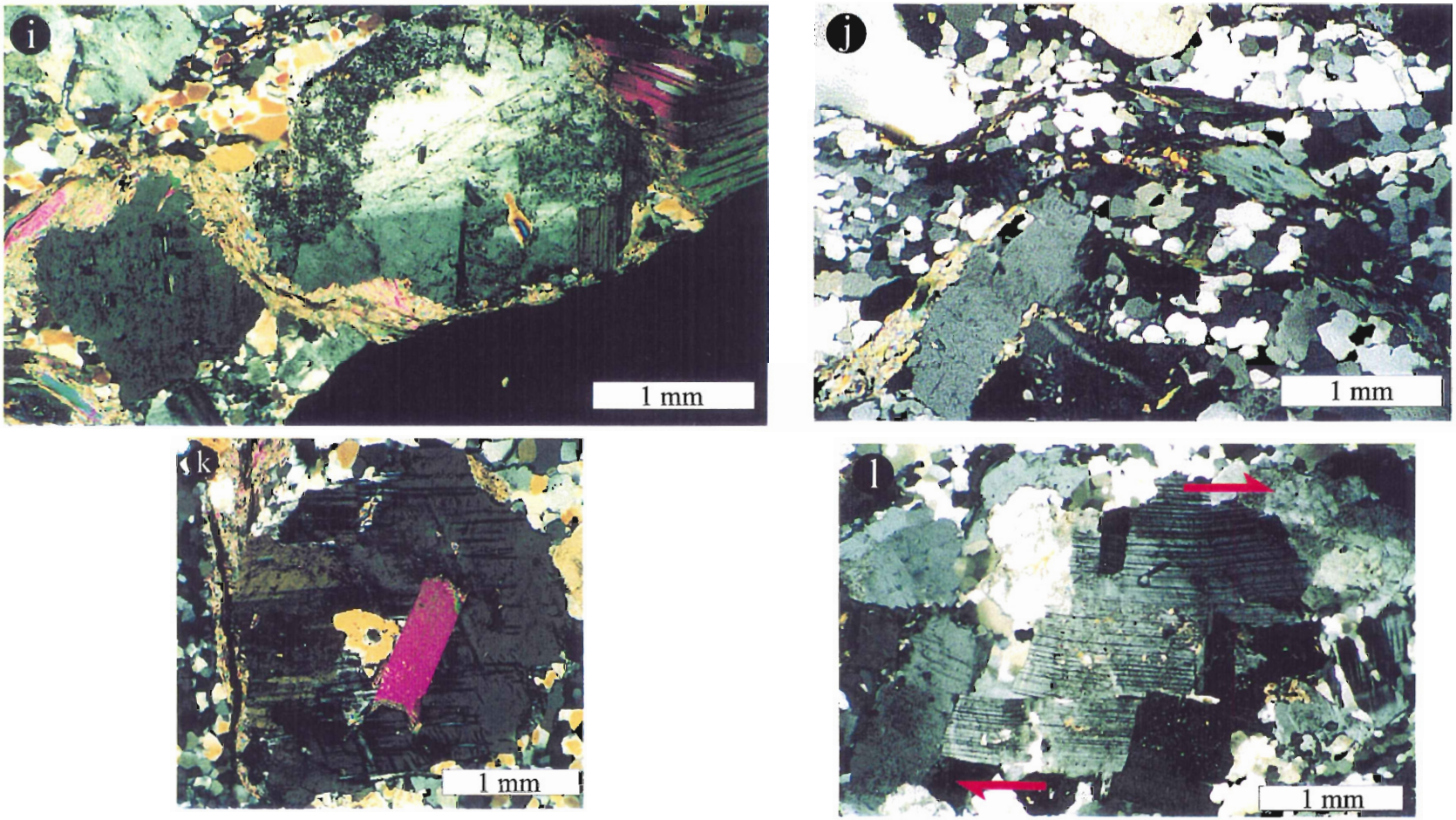

Figure 2.6 continued. i) Sample **96-1**. Feldspar porphyroclast mantled by fine-grained recrystallized muscovite, produced from the breakup of larger muscovite. The fine-grained muscovite is continuous with the weak fabric in the matrix. j) Sample **96-1**. Poorly developed shear bands. k) Sample **96-1**. Undeformed muscovite replacing feldspar?; the muscovite has been shielded from deformation in the matrix by the porphyroclast which encloses it. l) Sample **97-16a**. Stair-step fractured plagioclase indicating dextral (top-to-the-north) shear.

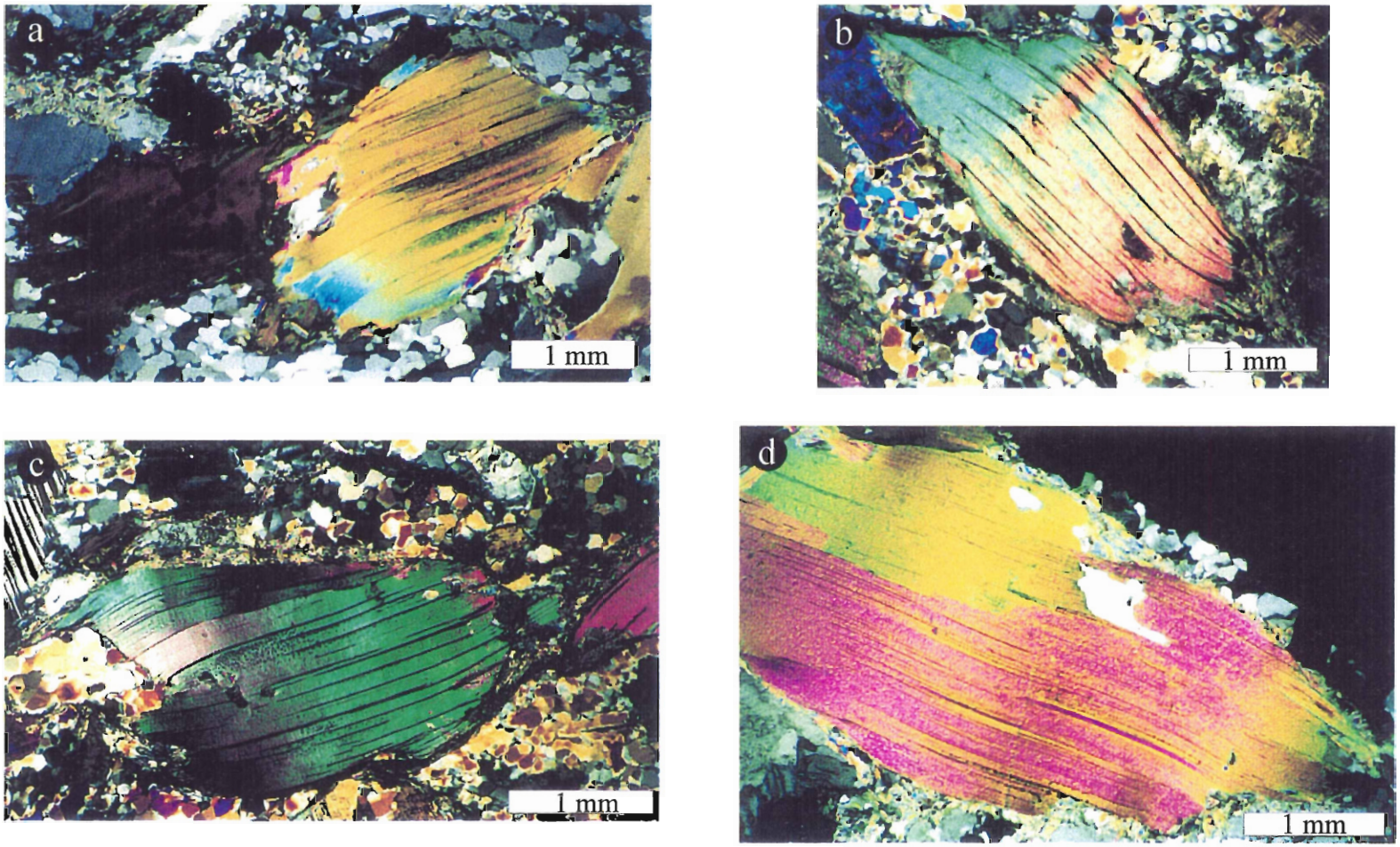

Figure 2.7. Distinctive muscovite textures from deformed samples. a) Sample **96-1**. Large deformed muscovite adjacent to ragged deformed biotite. b) Sample **96-1**. Large muscovite "fish" with fine grained tails and edges. c) Sample **96-1**. Large deformed muscovite mantled by fine-grained recrystallized muscovite. d) Sample **96-1**. Large muscovite with inclusions of quartz and distinctive ragged edges.

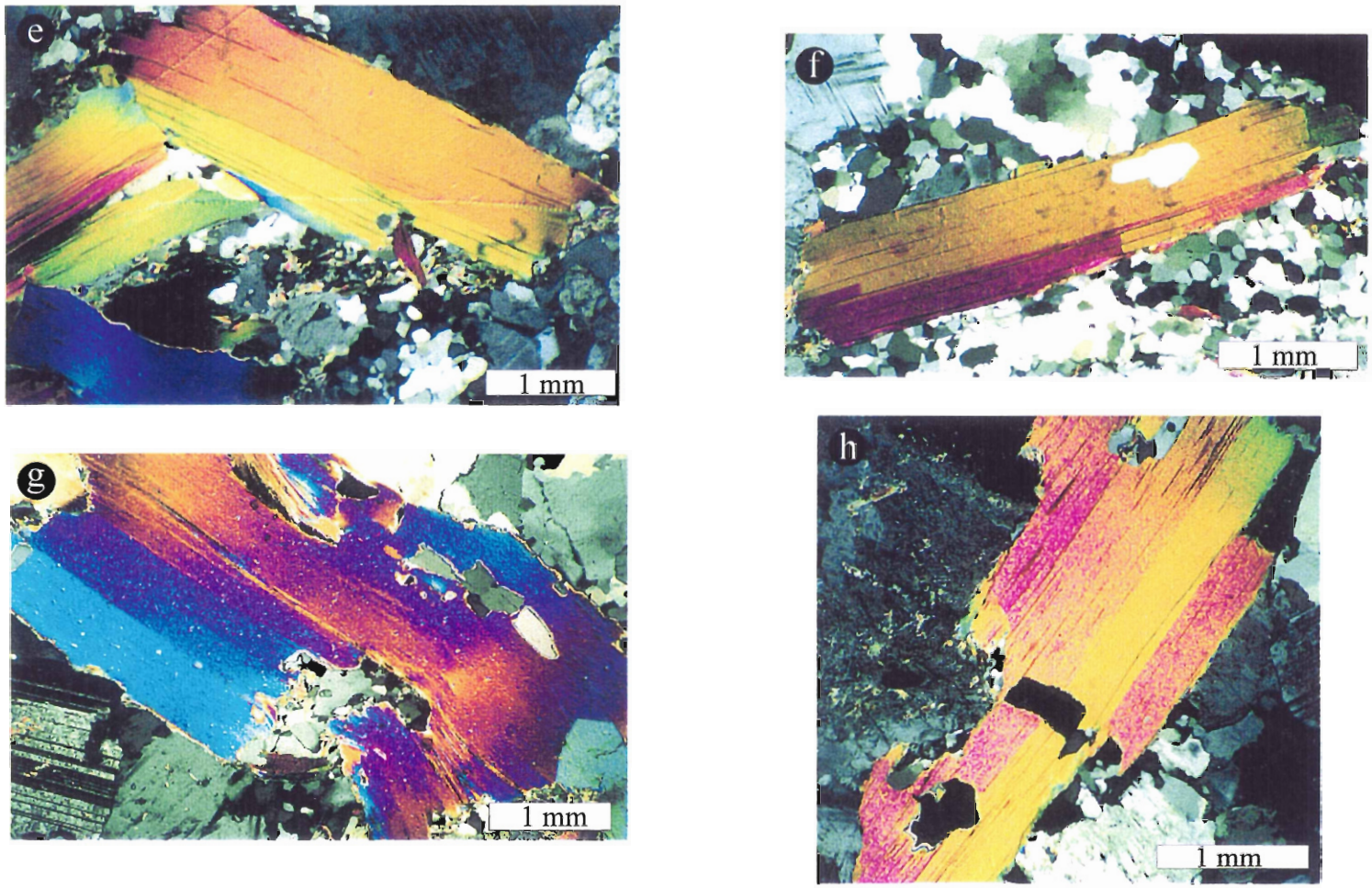

Figure 2.7 continued. Distinctive muscovite textures from deformed samples. e) Sample **96-1**. Large undeformed subhedral muscovite adjacent to deformed muscovite. f) Sample **96-1**. Euhedral undeformed muscovite with inclusions of quartz. g) Sample **97-17**. Very large anhedral muscovite overgrowing matrix. h) Sample **97-16a**. Ragged anhedral muscovite overgrowing matrix.

terminations and few inclusions are also present in close association with more deformed grains (Fig. 2.7e, f). Smaller (≤ 1mm) subhedral-anhedral muscovites are also present in abundance. Textural evidence suggests that the majority of muscovites <1mm were produced from the fragmentation of larger grains, and that the very fine-grained muscovite in the matrix was largely derived from the break-up of these large grains (Fig. 2.6e-h).

Although deformed samples have experienced more intense deformation than their undeformed equivalents, most samples do not contain well-developed mylonitic fabrics or shear-sense indicators. The most deformed samples, 96-1 and 97-16a, are protomylonites. Consequently, clearly defined shear sense indicators are rare. Those present (Fig. 2.6l) generally indicate a dextral shear sense (top-to-the-northwest) consistent with previous observations on similar structures from granitoid rocks in Nova Scotia (Dallmeyer and Keppie 1987). Textures such as fractured feldspars (Fig. 2.6l), and incomplete recrystallization of quartz, are considered typical of brittle-ductile deformation of granitoid rocks at relatively low temperatures (<400° C, i.e., lower greenschist facies) (Simpson 1985; West and Lux 1993; Heizler et al.1997).

2.4 Muscovite chemistry

Chemical analysis of muscovite revealed significant differences between undeformed and deformed samples. Several grains from each sample were analyzed and Tables 2.4 and 2.5 contain the mean chemical composition of muscovite from undeformed and deformed samples respectively.

Table 2.4. Microprobe data for muscovite from undeformed samples.

Sample	SiO_2	TiO_2	Al_2O_3	FeO	MnO	MgO	Na_2O	K_2O	Total
556									
CORES									
n=12	47.21±0.15	1.44±0.08	35.23±0.19	1.39±0.12	0.03±0.03	0.82±0.07	0.43±0.08	9.03±0.32	95.89
RIMS									
n=7	47.19±0.6	1.42±0.24	34.91±0.61	1.45±0.12	0.05±0.05	0.92±0.12	0.32±0.11	9.01±0.29	95.54
97-14									
CORES									
n=20	47.42±4.1	0.97±0.29	34.46±2.69	1.35±0.34	0.04±0.04	0.87±0.26	0.88±1.9	9.51±2.43	95.85
RIMS									
n=4	46.81±1.2	1.19±0.17	34.11±1.4	1.57±0.12	0.04±0.05	1.10±0.21	0.40±0.11	10.18±1.16	95.62
97-9									
CORES									
n=23	46.84±0.58	1.22±0.22	35.37±0.65	1.54±0.2	0.03±0.03	0.76±0.15	0.35±0.08	8.54±0.56	94.79
96-3									
CORES									
n=15	46.85±0.77	0.05±0.04	36.68±0.61	1.85±0.13	0.02±0.03	0.41±0.06	0.54±0.13	8.96±0.69	95.46
RIMS									
n=35	46.51±0.75	0.04±0.05	36.25±0.54	1.83±0.12	0.04±0.04	0.41±0.07	0.48±0.14	9.21±0.87	94.86

Table 2.5. Microprobe data for muscovite from deformed samples.

Samples	SiO_2	TiO_2	Al_2O_3	FeO	MnO	MgO	Na_2O	K_2O	Total
96-1									
CORES									
n=17	46.97±0.67	0.69±0.13	36.06±0.39	1.49±0.09	0.05±0.05	0.61±0.08	0.54±0.12	9.02±0.60	95.57
RIMS									
n=25	48.10±1.08	0.23±0.16	31.13±1.11	4.04±0.7	0.12±0.07	1.76±0.27	0.16±0.09	9.24±0.96	94.86
97-16a									
CORES									
n=10	47.01±0.42	0.77±0.11	35.31±1.28	1.78±0.56	0.05±0.05	0.71±0.18	0.49±0.13	8.56±0.2	94.95
RIMS									
n=10	48.00±1.27	0.44±0.15	32.61±2.37	2.92±1.07	0.08±0.07	1.33±0.54	0.23±0.11	8.41±0.91	94.35
97-17									
CORES									
n=6	46.97±0.3	0.55±0.12	35.84±0.26	1.47±0.14	0.05±0.04	0.59±0.05	0.57±0.11	9.04±0.12	95.32
RIMS									
n=11	48.05±1.11	0.41±0.1	33.54±2.89	2.53±1.15	0.08±0.08	1.20±0.6	0.30±0.17	9.00±0.27	95.83
97-3									
CORES									
n=7	47.27±0.66	1.19±0.08	35.38±0.36	1.45±0.15	0.00±0.01	0.85±0.06	0.48±0.12	8.49±1.0	95.28
RIMS									
n=16	47.72±0.91	0.96±0.11	34.23±1.82	2.02±0.82	0.04±0.05	1.10±0.38	0.37±0.21	8.91±1.06	95.49

Muscovite from undeformed rocks, both intergrown with biotite and as interstitial grains, is characterized by a relatively uniform composition among all samples (Table 2.4). Figure 2.8a shows a euhedral, cleanly terminated, muscovite from sample 556a. This grain is typical of muscovite from undeformed samples in that no significant major element variation exists between core and rim (Fig. 2.8b; Table 2.6). A distinctive feature of muscovite from undeformed samples is a high TiO_2 content, which is almost invariably >1 wt% (Table 2.4). The vast majority of grains analyzed from undeformed samples shows a similar pattern (Table 2.4), although some exceptions do occur.

Figure 2.9 shows a mildly deformed muscovite from sample 97-14. Unlike the majority of muscovite analyzed from undeformed samples, this grain does preserve a clear chemical zonation from core to rim (Fig. 2.9b; Table 2.7). Although core compositions are similar to those from other undeformed samples (Table 2.4), rim compositions are very different (Table 2.7), being depleted in TiO_2, Al_2O_3, and Na_2O, and enriched in SiO_2, FeO, and MgO relative to cores. Figure 2.10 and Table 2.8 suggest that muscovite replacing plagioclase has an average TiO_2 content less than muscovite from undeformed samples, although some overlap does occur.

A distinctive variety of low- TiO_2 muscovite characterizes muscovite from pegmatite sample 96-3 (Fig. 2.11). Muscovite from this sample has an average TiO_2 content <0.05 wt% (Table 2.9), and higher values for Al_2O_3, FeO, and Na_2O, and lower values for MgO than the majority of muscovites from Middle Stage rocks. Muscovite from pegmatite sample 96-3 also shows no chemical zonation from core to rim (Fig. 2.11b).

a)

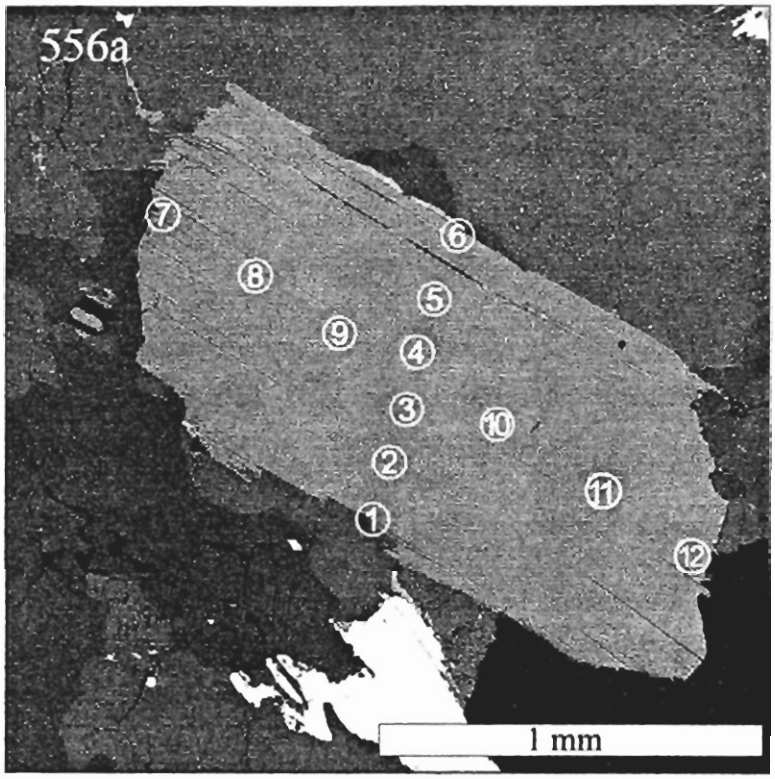

b)

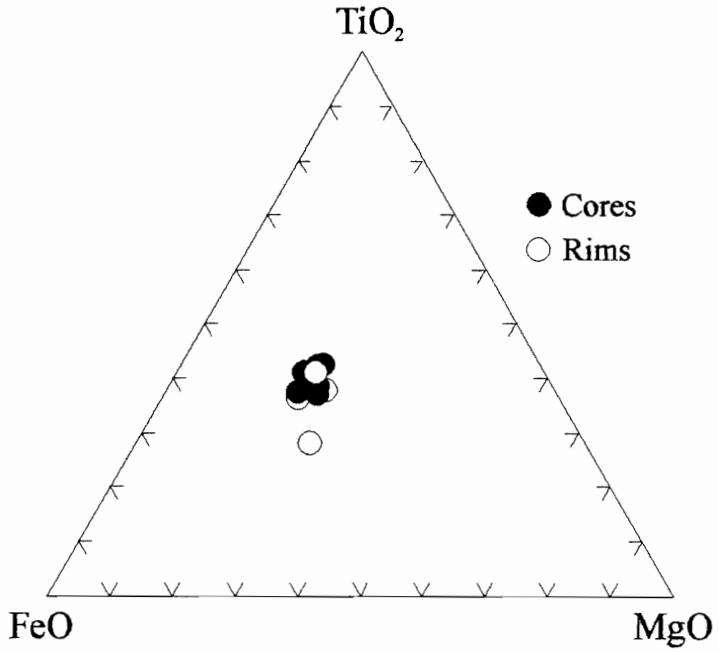

Figure 2.8. Sample **556.** a) Backscattered electron image of large, euhedral, undeformed muscovite. b) Ternary plot illustrating lack of significant core-rim variation. **Table 2.6** Contains the corresponding analytical data.

Table 2.6. Microprobe data for muscovite **556a**.

Analysis	SiO_2	TiO_2	Al_2O_3	FeO	MnO	MgO	CaO	Na_2O	K_2O	Total
CORES										
2	47.11	1.41	35.39	1.44	0.00	0.93	0.00	0.40	9.13	96.04
3	47.14	1.56	35.23	1.32	0.00	0.82	0.00	0.42	8.91	95.86
4	46.94	1.44	35.19	1.39	0.02	0.86	0.01	0.51	9.50	95.97
5	47.01	1.45	35.53	1.58	0.00	0.82	0.00	0.42	9.11	96.20
8	47.25	1.36	35.00	1.28	0.04	0.68	0.04	0.38	9.22	95.58
9	47.42	1.46	35.29	1.19	0.05	0.79	0.00	0.32	9.49	96.31
10	47.29	1.31	34.91	1.28	0.04	0.78	0.00	0.55	8.97	95.56
11	47.12	1.40	35.26	1.36	0.09	0.87	0.00	0.48	9.13	96.02
Average	47.16	1.42	35.22	1.36	0.03	0.82	0.01	0.44	9.18	95.94
RIMS										
1	47.32	1.69	35.41	1.50	0.13	0.93	0.01	0.47	9.04	96.56
6	47.16	1.29	35.42	1.25	0.05	0.88	0.00	0.43	9.18	96.01
7	47.79	1.33	35.73	1.52	0.08	0.80	0.00	0.23	9.13	97.24
12	47.85	1.00	34.89	1.57	0.00	1.00	0.04	0.29	9.42	96.35
Average	47.53	1.33	35.36	1.46	0.06	0.90	0.01	0.36	9.19	96.54

a)

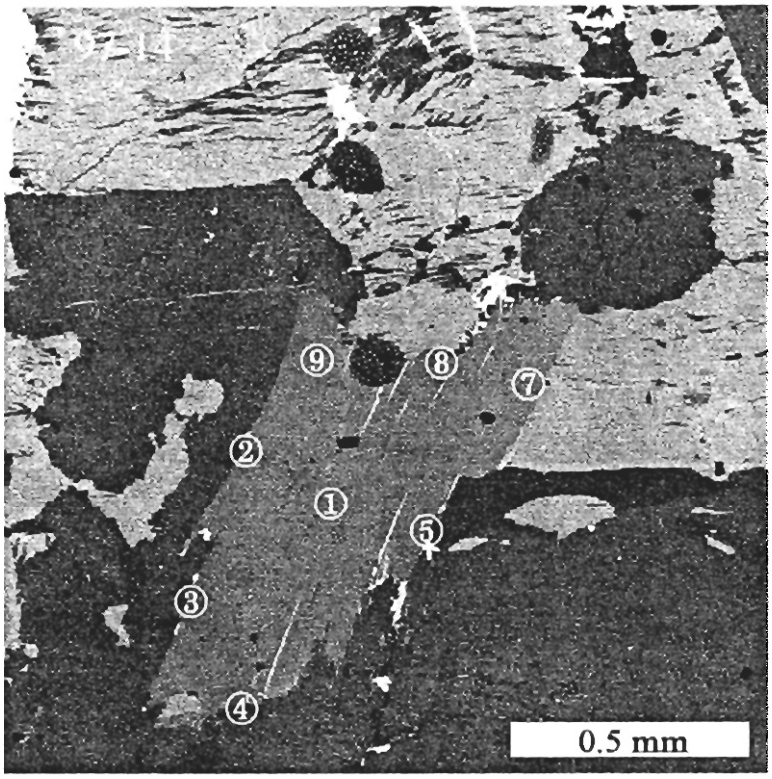

b)

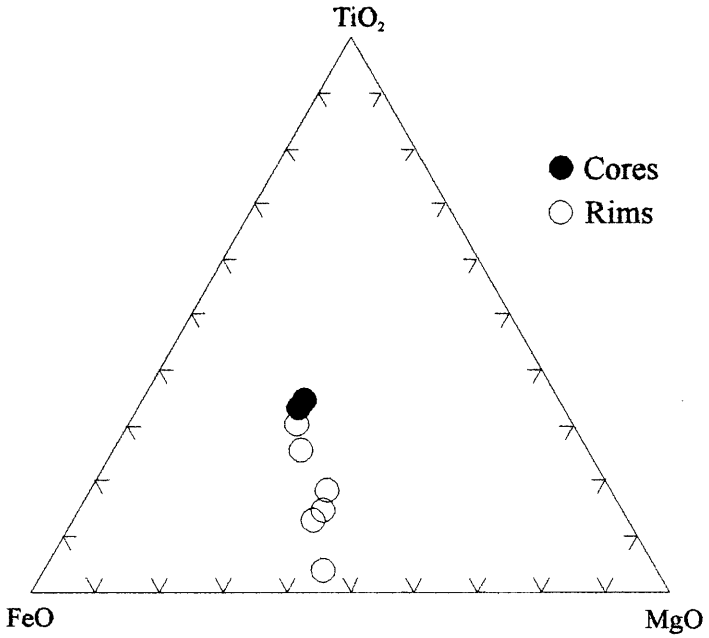

Figure 2.9. Undeformed sample **97-14**. a) Backscattered electron image of muscovite. b) Unlike most other muscovites from this sample, this grain exhibits major element variation from core to rim, similar to that shown by muscovites from deformed samples. **Table 2.7** contains the corresponding analytical data.

Table 2.7. Microprobe data for deformed muscovite from sample **97-14**.

Analysis	SiO_2	TiO_2	Al_2O_3	FeO	MnO	MgO	CaO	Na_2O	K_2O	Total
CORES										
1	48.08	1.12	35.99	1.39	0.00	0.85	0.00	0.50	8.90	97.19
9	47.77	1.14	35.52	1.30	0.02	0.84	0.05	0.41	9.00	96.34
Average	47.93	1.13	35.76	1.35	0.01	0.84	0.02	0.45	8.95	96.77
RIMS										
2	47.99	0.56	35.14	1.37	0.00	1.15	0.01	0.30	8.80	95.76
3	50.03	0.16	33.30	2.24	0.00	1.88	0.04	0.32	9.25	97.52
4	47.77	0.76	35.68	1.33	0.00	0.87	0.01	0.42	8.98	96.26
6	47.03	0.55	33.42	1.76	0.00	1.44	0.03	0.44	10.20	95.21
7	48.34	0.58	33.92	2.22	0.00	1.69	0.02	0.24	9.20	96.54
8	47.83	1.06	35.61	1.52	0.00	0.93	0.00	0.37	9.14	96.64
Average	48.16	0.61	34.51	1.74	0.00	1.33	0.02	0.35	9.26	96.32

a)

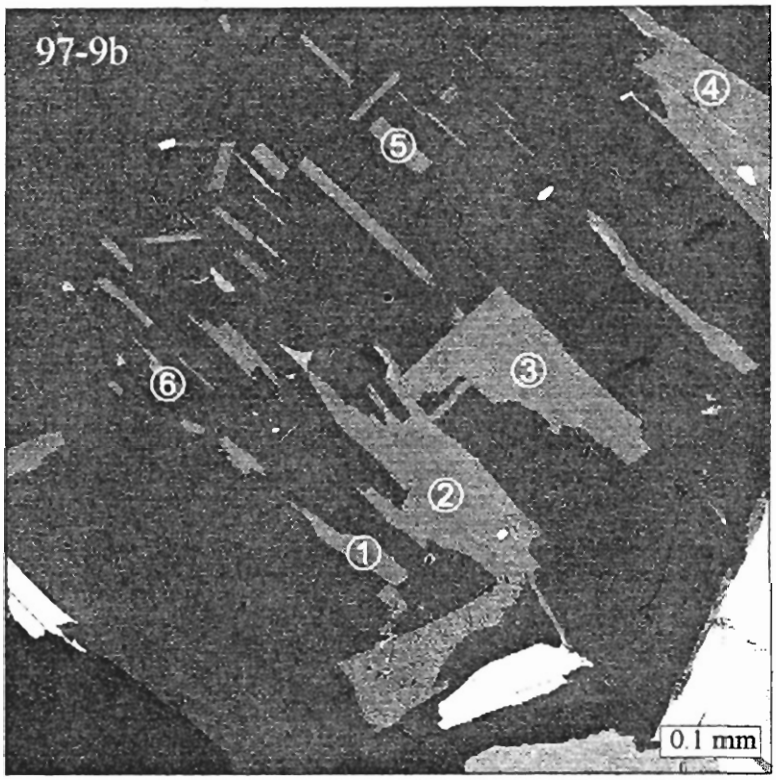

b)

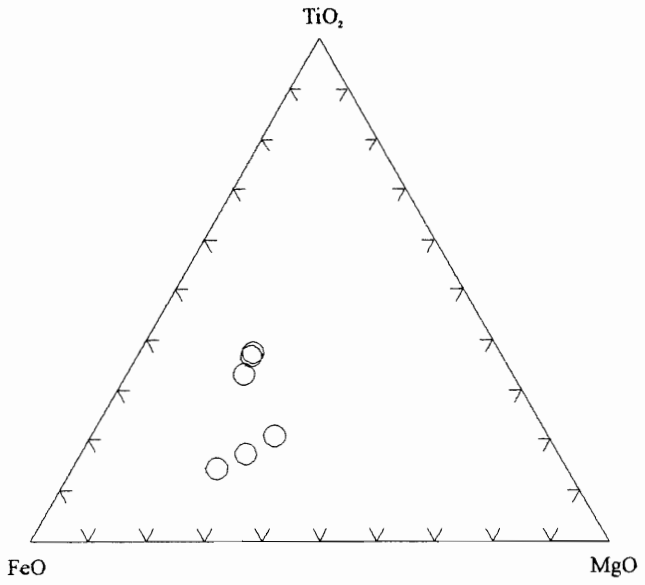

Figure 2.10. Undeformed sample **97-9**. a) Backscattered electron image of small subhedral inclusions of muscovite replacing plagioclase. b) Ternary plot illustrating variable Ti contents for apparently non-magmatic muscovite. **Table 2.8** contains the corresponding analytical data.

Table 2.8. Microprobe data for muscovite inclusions in plagioclase, sample **97-9**.

Analysis	SiO_2	TiO_2	Al_2O_3	FeO	MnO	MgO	CaO	Na_2O	K_2O	Total
1	47.93	0.53	36.80	1.21	0.00	0.82	0.04	0.26	8.45	96.14
2	47.21	0.40	36.43	1.26	0.00	0.67	0.04	0.27	8.52	94.99
3	47.42	1.36	35.56	1.60	0.00	0.73	0.05	0.22	8.36	95.38
4	47.50	1.35	35.19	1.53	0.00	0.71	0.01	0.33	8.22	94.93
5	47.07	1.02	36.22	1.43	0.00	0.63	0.00	0.29	8.63	95.42
6	48.29	0.31	36.85	1.32	0.12	0.55	0.01	0.54	8.86	96.99
Average	47.57	0.83	36.18	1.39	0.02	0.68	0.02	0.32	8.50	95.64

a)

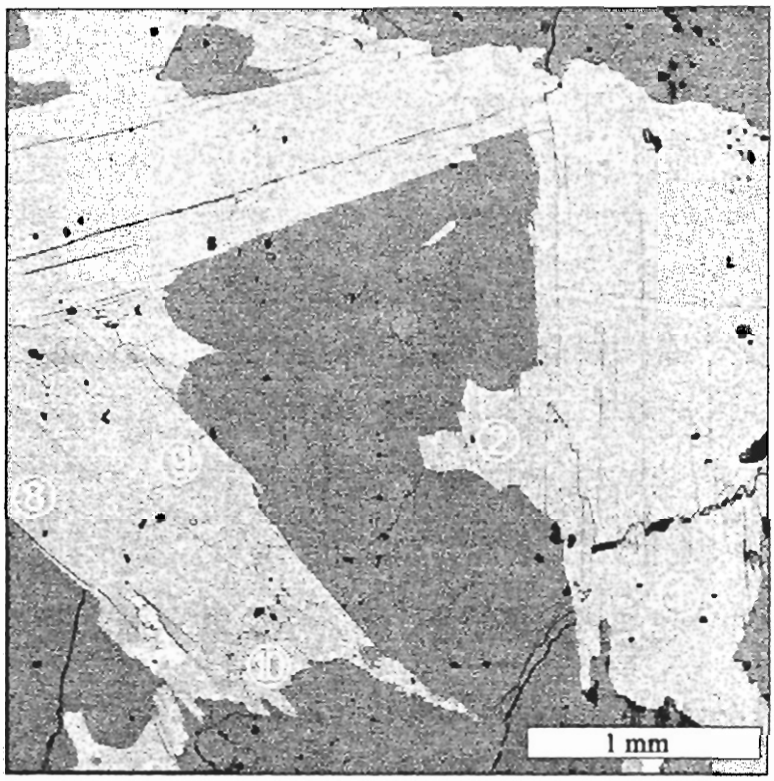

b)

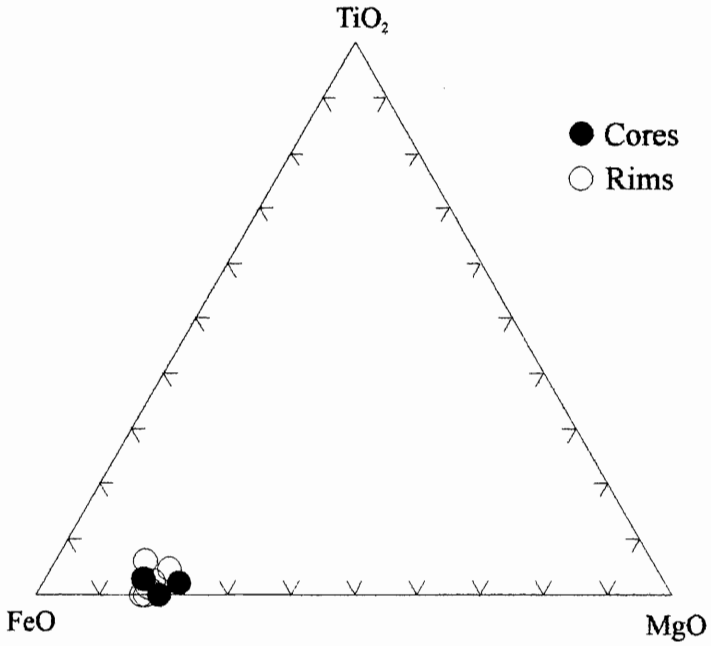

Figure 2.11. Undeformed pegmatite sample **96-3**. a) Backscattered electron image of muscovite. b) Ternary plot illustrating very low Ti contents of muscovite from this pegmatite. **Table 2.9** contains the corresponding analytical data.

Table 2.9. Microprobe data for muscovite from pegmatite sample **96-3**.

Analysis	SiO_2	TiO_2	Al_2O_3	FeO	MnO	MgO	CaO	Na_2O	K_2O	Total
CORES										
1	47.22	0.00	36.39	1.88	0.04	0.45	0.03	0.35	8.13	94.55
3	47.29	0.05	37.16	1.81	0.00	0.51	0.00	0.62	8.45	96.02
6	47.28	0.07	37.25	1.98	0.00	0.38	0.00	0.70	8.23	95.91
Average	47.26	0.04	36.93	1.89	0.01	0.45	0.01	0.56	8.27	95.49
RIMS										
2	47.32	0.06	36.45	1.99	0.00	0.43	0.03	0.30	8.20	94.78
4	47.45	0.12	36.69	2.06	0.00	0.50	0.00	0.55	8.68	96.07
5	47.32	0.03	37.42	1.76	0.10	0.36	0.01	0.58	8.57	96.26
7	47.63	0.14	36.65	1.84	0.02	0.33	0.00	0.29	8.83	95.74
8	46.75	0.00	36.34	1.83	0.12	0.38	0.00	0.27	8.54	94.35
9	46.63	0.04	36.07	1.95	0.05	0.41	0.00	0.35	8.18	93.72
10	46.79	0.00	36.47	1.61	0.00	0.32	0.00	0.43	7.61	93.22
Average	47.13	0.06	36.58	1.86	0.04	0.39	0.00	0.40	8.37	94.88

In contrast to muscovite from undeformed samples, muscovite from deformed samples has distinct core-rim chemical differences (Table 2.5). In all samples analyzed, muscovite rims contain higher values of SiO_2, FeO, and MgO, and lower values of TiO_2, Al_2O_3, and Na_2O, than cores, whereas K_2O contents remain relatively unchanged from core to rim (Table 2.5). Figure 2.12a shows a large deformed muscovite from sample 96-1. The core and rim of the muscovite have different colors resulting from differences in chemical composition (Fig. 2.12b; Table 2.10). Figure 2.13 shows a rare exception from the same sample. This grain does not show any chemical zoning, and was presumably shielded from deformation in the matrix by the large feldspar grain that encloses it (see also Fig. 2.6k). TiO_2 contents for this muscovite grain are similar to other muscovite from deformed samples (Table 2.11).

Core compositions of muscovite from deformed samples have similar values of SiO_2, Al_2O_3, FeO, MgO, and Na_2O to muscovite from undeformed samples. A notable exception is in TiO_2 content, which is <0.77 wt% for all samples. Sample 97-3 is an exception, and has core TiO_2 values >1 wt%, similar to muscovite from undeformed samples (Fig. 2.14).

2.5 Discussion

2.5.1 Muscovite in granitoid rocks

The question of muscovite paragenesis in plutonic rocks is a persistent problem in granite petrology (Zen 1988). The problem arises because muscovite can apparently form over a range of temperature conditions, incorporating magmatic (H_2O-undersaturated),

a)

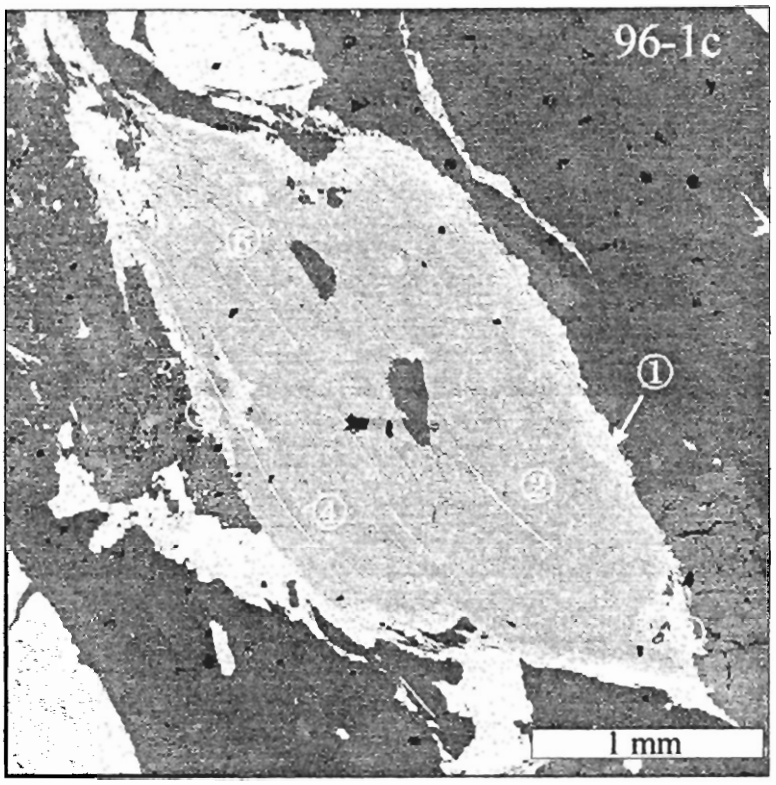

b)

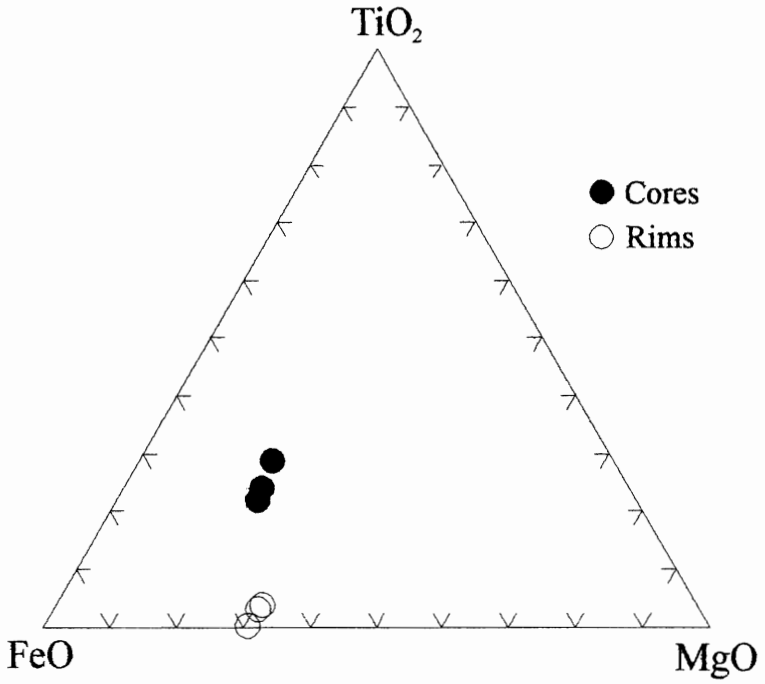

Figure 2.12. Deformed sample **96-1**. a) Backscattered electron image of large deformed muscovite. Note the thin zones of lighter color along the rims suggesting chemical zoning. b) Ternary plot illustrating marked core-rim variation in Fe and Mg contents. Cores have lower Ti vales than muscovite from undeformed samples. **Table 2.10** contains the corresponding analytical data.

Table 2.10. Microprobe data for large deformed muscovite **96-1c**, from sample **96-1**.

Analysis	SiO_2	TiO_2	Al_2O_3	FeO	MnO	MgO	CaO	Na_2O	K_2O	Total
CORES										
2	47.71	0.56	36.33	1.45	0.09	0.55	0.00	0.52	8.66	95.98
4	46.17	0.65	35.36	1.49	0.04	0.56	0.01	0.65	9.67	94.80
6	46.96	0.78	36.04	1.38	0.04	0.54	0.02	0.53	9.15	95.46
Average	46.94	0.66	35.91	1.44	0.06	0.55	0.01	0.57	9.16	95.41
RIMS										
1	48.77	0.16	32.74	3.35	0.06	1.55	0.00	0.22	8.62	95.60
3	48.40	0.22	31.69	3.89	0.12	1.84	0.05	0.18	8.81	95.24
5	48.17	0.02	30.53	4.13	0.18	1.83	0.03	0.14	9.95	95.00
Average	48.44	0.13	31.65	3.79	0.12	1.74	0.03	0.18	9.13	95.28

a)

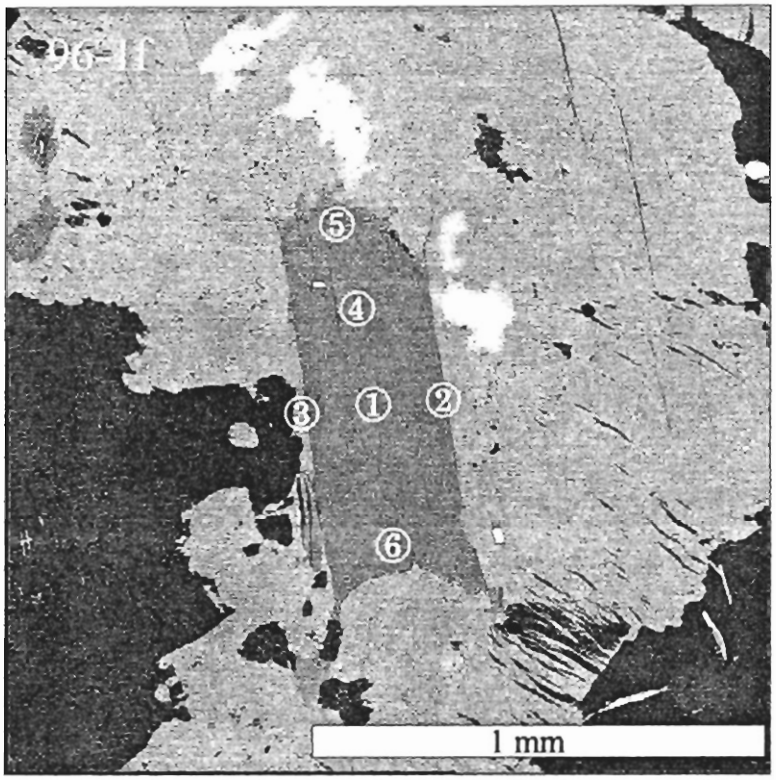

b)

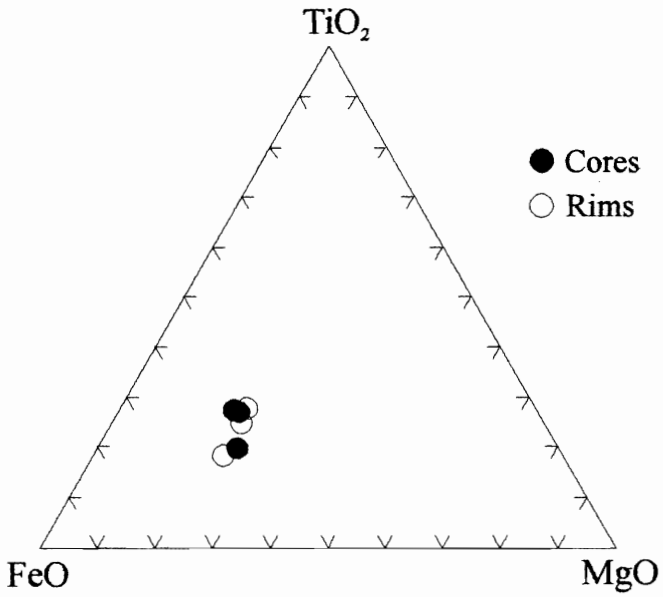

Figure 2.13. Deformed sample **96-1**. a) Backscattered electron image of euhedral muscovite replacing plagioclase? b) Unlike most muscovite from this sample, there is no significant chemical zoning between core and rim, suggesting that this grain was shielded from deformation in the matrix by the surrounding plagioclase. **Table 2.11** contains the corresponding analytical data.

Table 2.11. Microprobe data for muscovite **96-1f**.

Analysis	SiO_2	TiO_2	Al_2O_3	FeO	MnO	MgO	CaO	Na_2O	K_2O	Total
CORES										
1	47.37	0.84	35.79	1.60	0.07	0.61	0.00	0.51	9.24	96.21
4	47.51	0.79	36.13	1.50	0.04	0.62	0.00	0.43	8.99	96.28
6	48.04	0.53	36.39	1.49	0.10	0.66	0.04	0.48	9.10	97.13
Average	47.64	0.72	36.10	1.53	0.07	0.63	0.01	0.47	9.11	96.54
RIMS										
2	49.63	0.83	37.26	1.50	0.03	0.67	0.00	0.54	7.11	97.76
3	47.86	0.65	36.38	1.38	0.07	0.60	0.00	0.44	8.52	96.21
5	47.89	0.55	36.22	1.76	0.23	0.68	0.02	0.37	9.21	97.06
Average	48.46	0.68	36.62	1.55	0.11	0.65	0.01	0.45	8.28	97.01

a)

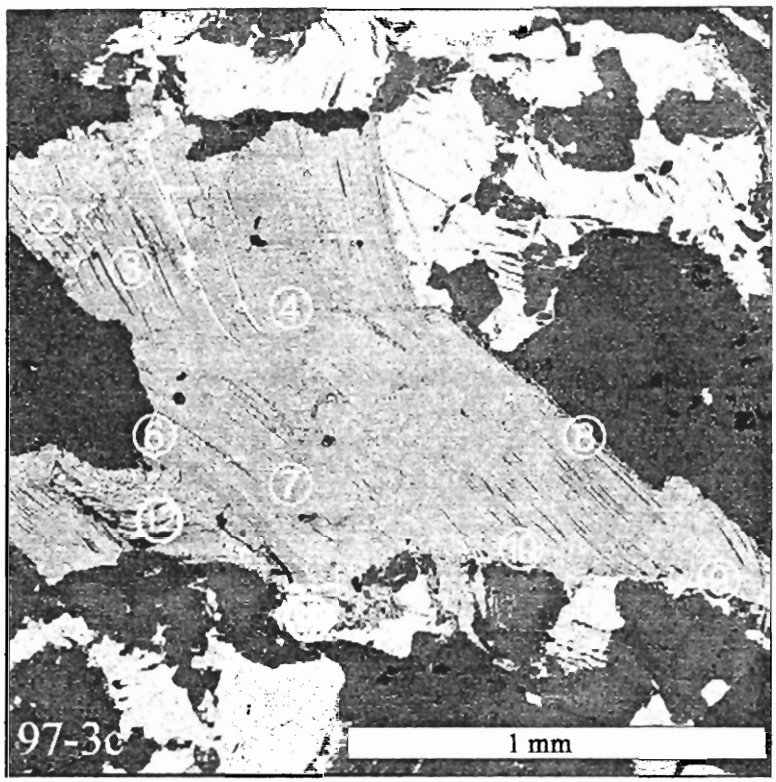

b)

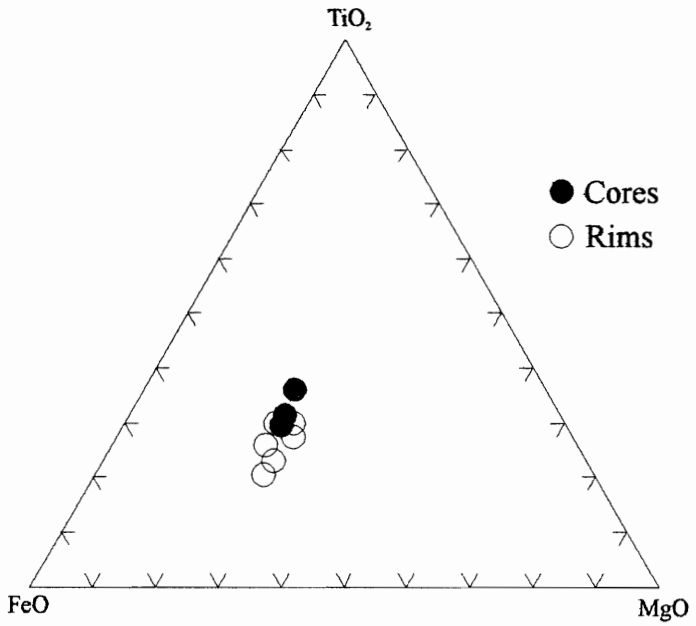

Figure 2.14. Deformed sample **97-3**. a) Backscattered electron image of deformed muscovite. b) Core-rim variation is less pronounced than deformed sample **96-1**. **Table 2.12** contains the corresponding analytical data.

Table 2.12. Microprobe data for deformed muscovite **97-3c**, from sample **97-3**.

Point	SiO_2	TiO_2	Al_2O_3	FeO	MnO	MgO	CaO	Na_2O	K_2O	Total
CORES										
3	47.92	1.08	35.66	1.64	0.00	0.92	0.01	0.36	7.79	95.54
4	48.21	1.10	35.95	1.53	0.00	0.88	0.00	0.55	7.65	96.00
7	46.26	1.24	35.18	1.36	0.00	0.83	0.01	0.70	10.18	96.20
average	47.46	1.14	35.60	1.51	0.00	0.87	0.01	0.54	8.54	95.91
2	48.53	1.08	35.63	1.73	0.10	1.11	0.00	0.38	7.97	96.61
6	47.77	0.94	34.46	2.01	0.02	1.11	0.00	0.15	8.55	95.14
8	46.59	0.92	35.48	1.41	0.01	0.76	0.00	0.97	10.18	96.46
9	46.98	0.79	33.92	2.02	0.14	1.05	0.01	0.66	10.21	96.12
10	46.70	0.99	34.31	1.41	0.02	0.89	0.02	0.38	10.82	95.66
11	46.77	1.01	33.84	1.93	0.09	0.96	0.01	0.20	10.51	95.47
12	46.83	0.98	34.83	1.50	0.00	0.79	0.04	0.47	10.16	95.75
average	47.17	0.96	34.64	1.71	0.06	0.95	0.01	0.46	9.77	95.89

late-magmatic (H_2O-saturated), and non-magmatic (subsolidus) growth (Fig. 2.15). The problem of differentiating between these different generations of muscovite is further complicated by late-magmatic and post-magmatic textural modifications (e.g., deformation) that affect granitoid rocks.

The main petrogenetic interest in recognizing the presence of unequivocal magmatic muscovite concerns the possibility that muscovite may crystallize from a magma over a greater range of pressure and temperature than previously thought possible (Miller et al., 1981; Zen, 1988). For the purpose of this study, every attempt to fully characterize the paragenesis of PMP muscovite is required as this is the phase of interest in $^{40}Ar/^{39}Ar$ geochronology.

2.5.2 Textural and chemical criteria for recognizing magmatic muscovite

A variety of textural and chemical criteria have been proposed to help distinguish between magmatic ("primary") and non-magmatic ("secondary") muscovite (Table 2.13). Miller et al. (1981) used the textural criteria in Table 2.13 to distinguish between magmatic and non-magmatic muscovite in a group of 16 North American plutons. These authors found that texturally-looking magmatic muscovite (see Table 2.13 for characteristics of magmatic muscovite) was consistently higher in TiO_2 than texturally-looking non-magmatic muscovite. Further workers noted a similar distinction which led Zen (1988) to suggest that the difference in TiO_2 contents between magmatic and non-magmatic muscovite is real and can be used to distinguish between the two. Muscovite with a TiO_2 content >0.60 wt% is likely to be of magmatic origin (Zen 1988). One reason that Ti is a useful indicator of a magmatic origin may be that it does not readily undergo

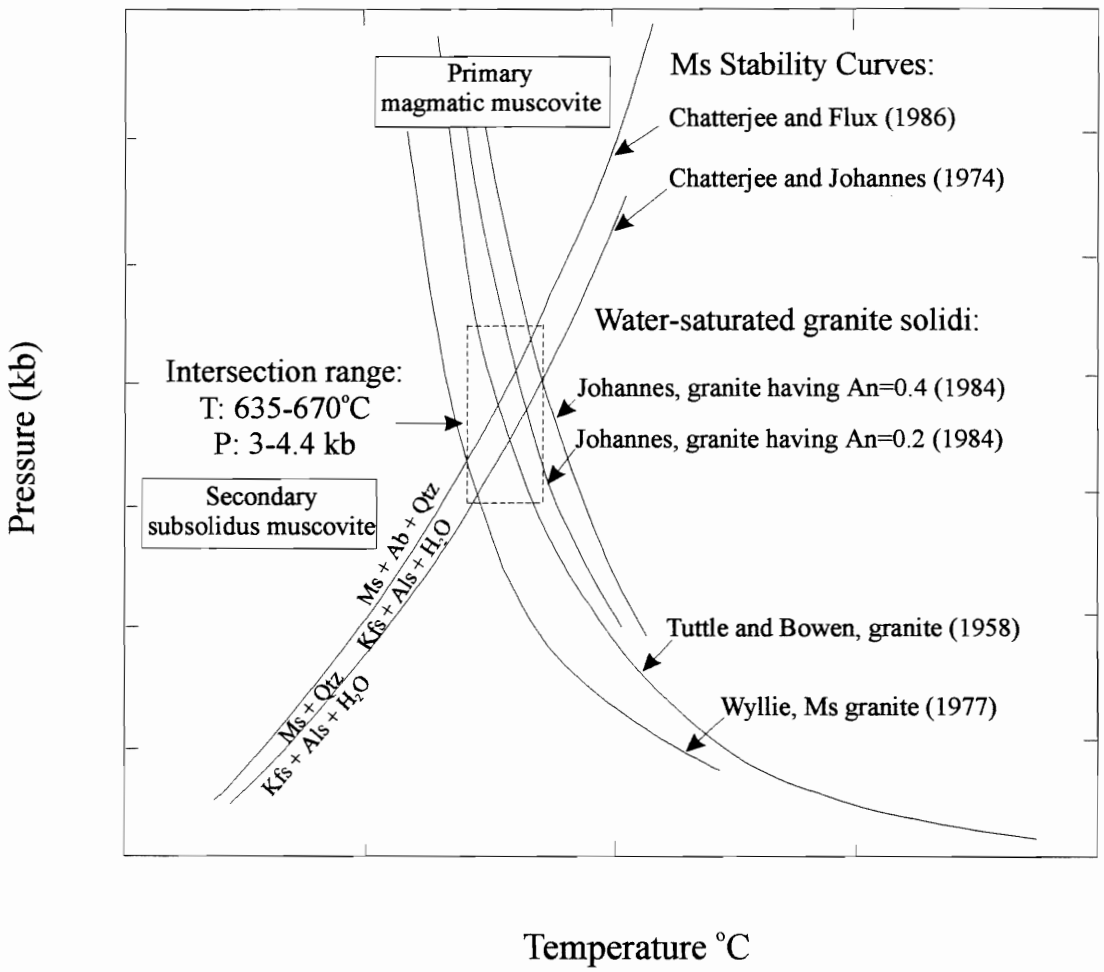

Figure 2.15. Compilation of P-T plots of muscovite equilibrium and granite solidi. Muscovite can grow over a wide range of pressure and temperature conditions, incorporating magmatic, late-magmatic, and sub-solidus (non-magmatic) growth. Modified from Zen (1988).

Table 2.13. Textural and chemical criteria used to distinguish magmatic muscovite from non-magmatic muscovite in the PMP. Criteria adapted from Miller et al. 1981; Speer 1984; Ham and Kontak 1988; Zen 1988; Roycroft 1991; and this study.

Textural criteria	
Primary magmatic muscovite	**Secondary post-magmatic muscovite**
Muscovite must be: 1: of coarse grain size, comparable to other magmatic phases, especially biotite 2: subhedral or euhedral in habit, with sharp, well-defined grain edges 3: not enclosed by, or enclose, a mineral from which it may have formed, e.g., plagioclase 4: relatively abundant, in a clean, unaltered granitoid rock 5: optically zoned in a manner identical to other magmatic minerals, specifically plagioclase 6: When intergrown with biotite, contacts between the two minerals should be well defined, euhedral, and both minerals should have different cleavage orientations.	1: Muscovite may be subhedral or euhedral in shape and of comparable grain size to other magmatic phases, but is normally enclosed within minerals from which it has formed. 2: Muscovite altering plagioclase or K-feldspar, usually takes the form of a fine-grained dense mass concentrated in the core of the host mineral; subhedral-euhedral grains along cleavage traces or in fractures; and, larger isolated subhedral grains with sharp or spongy grain edges, typically in the core of plagioclase. 3: Muscovite replacing biotite usually takes the form of fine-grained clusters or subhedral grains, enclosing or enclosed within larger biotite grains, or mantling the edges of the biotite. 4: Inclusions of groundmass minerals are common, and grains should have ragged outlines.
Chemical criteria	
Primary magmatic muscovite	**Secondary post-magmatic muscovite**
Magmatic muscovite may have TiO_2 >1 wt%, be richer in Al_2O_3, and Na_2O, and poorer in SiO_2 and MgO, compared to obvious secondary muscovite, such as that replacing plagioclase or biotite. Na/(Na + K) > 0.06	TiO_2 contents <1 wt% are considered typical of non-magmatic muscovite, which also have higher SiO_2, FeO, and MgO contents than their primary equivalents. Na/ (Na + K) < 0.06

subsolidus exchange or oxidation reactions as do Mg, Fe, and the alkali cations (Zen 1988).

Miller et al. (1981) found that their magmatic and non-magmatic muscovite could be further distinguished using several other major element indicators. Primary-looking muscovite had higher Al and Na contents than secondary-looking muscovite, which had higher Si and Mg contents. Monier et al. (1984) used Na/(Na+K) ratios to succesfully differentiate between magmatic (Na/(Na+K)>0.06) and non-magmatic (Na/(Na+K)<0.06) muscovite. Several workers have used the equilibrium distribution of trace elements between muscovite and magmatic biotite to distinguish between magmatic and non-magmatic muscovite (e.g., de Albuquerque 1975; Ham and Kontak 1988).

Any distinction between different types of muscovite based on chemical criteria, first requires a distinction based on textural criteria. Although each textural criterion can be challenged in isolation (Zen 1988), together, and in conjunction with real chemical differences between muscovite types, they provide the only means of distinguishing between magmatic and non-magmatic muscovite. Several studies have shown that the textural and chemical criteria of Table 2.13 are not always adequate to distinguish between different generations of muscovite. Ham and Kontak (1988) found no difference in TiO_2 contents between magmatic and non-magmatic muscovite from the South Mountain Batholith. Speer (1984) distinguished between magmatic and non-magmatic muscovite from 59 Acadian and Alleghanian plutons based on TiO_2 content, but found significant overlap in FeO, MgO, Al_2O_3, and Si_2O contents.

Clearly the proposed criteria do not suffice for all occurrences of plutonic muscovite. Our inability to distinguish between muscovite types based on chemical

parameters may result from our inability to distinguish between magmatic and non-magmatic muscovite based on textural criteria alone (Miller et al. 1981). Chemical zoning analogous to that shown by unequivocal magmatic minerals such as plagioclase, may provide the only sure way of recognizing magmatic muscovite (Roycroft 1991), as magmaticaly-zoned muscovite can have low TiO_2 contents considered characteristic of non-magmatic muscovite (Ding 1995). Because of these uncertainties, any distinction based on the criteria in Table 2.13 will be to some extent subjective.

Despite this ambiguity, the textural and chemical data for muscovite from the PMP appears to suggest that it may be possible to distinguish between different generations of muscovite for this pluton.

2.5.3 Magmatic versus non-magmatic muscovite in the PMP

In general, muscovite from undeformed samples conforms to the textural criteria in Table 2.13, and on this basis would appear to be magmatic. TiO_2 contents $\geq$0.97 wt % for muscovite from all undeformed samples (except 96-3) support a magmatic origin (Table 2.4). Minor overlap in the chemical composition of texturally magmatic and non-magmatic muscovite from the PMP (Fig. 2.10; Table 2.8) suggests that established chemical criteria are not entirely adequate in distinguishing between these two types of muscovite.

Texturally, the subhedral-anhedral habit, large size, and inclusions suggest that the largest muscovites from deformed samples (Fig. 2.7) may not be part of the original magmatic assemblage. Muscovite of comparable size is absent from undeformed

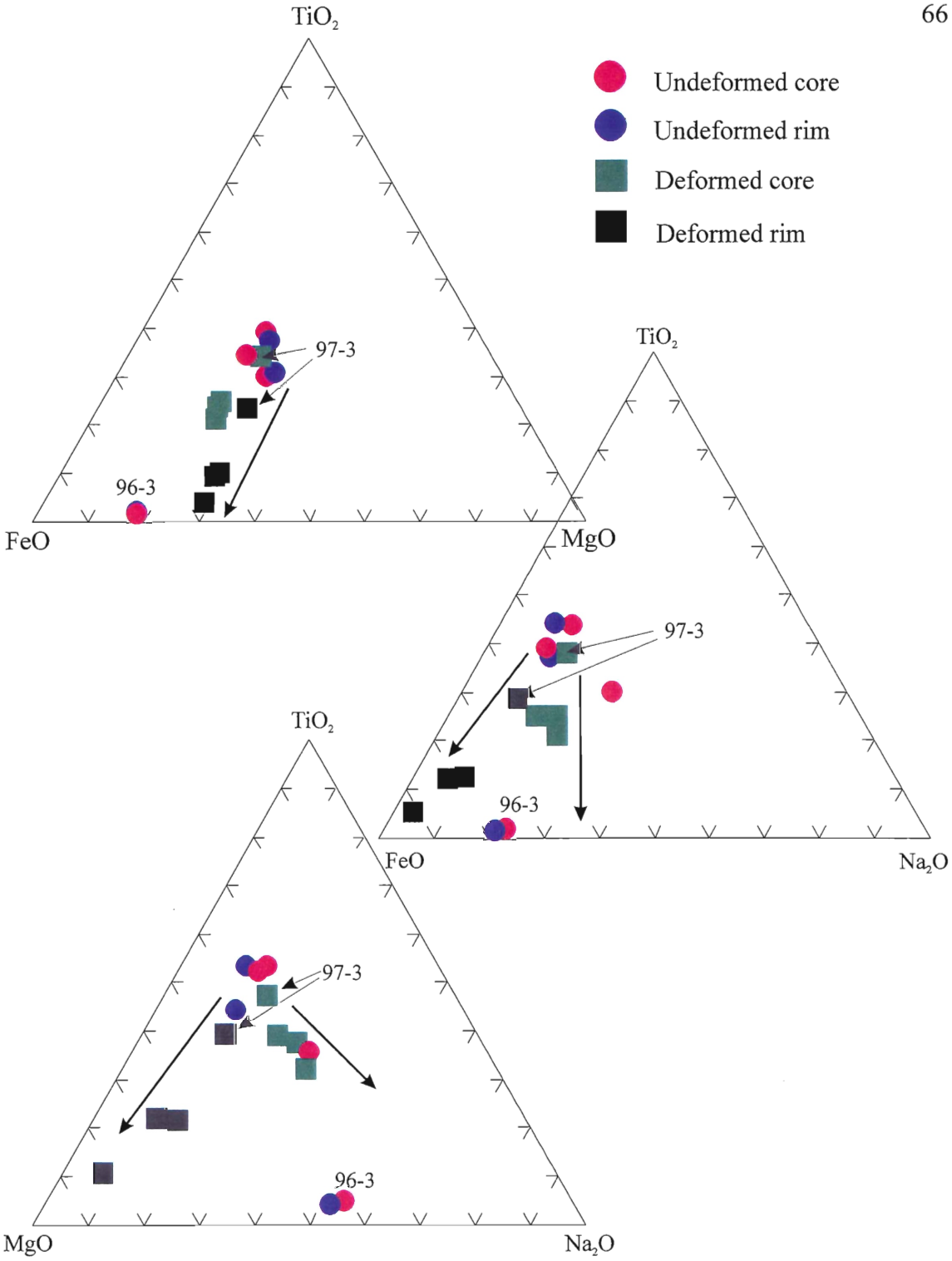

Figure 2.16. Ternary plots illustrating chemical differences between muscovite from deformed and undeformed samples. Undeformed cores and rims generally cluster together and have high values of TiO_2. Cores of muscovite from deformed samples have lower TiO_2, and higher FeO, MgO, and Na_2O than undeformed cores. Rims from deformed muscovite are distinctly enriched in FeO and MgO. Deformed sample **97-3** and undeformed sample **96-3** are explained in the text.

Table 2. 14. Structural formulae for muscovite data from **Tables 2.5** and **2.6** based on 11 atoms of oxygen.

a) Undeformed

	556 cores	556 rims	97-14 cores	97-14 rims	97-9 cores	96-3 cores	96-3 rims
Si	3.101	3.109	3.135	3.109	3.098	3.085	3.087
^{iv}Al	0.899	0.895	0.869	0.895	0.905	0.915	0.915
^{vi}Al	1.826	1.818	1.810	1.778	1.854	1.929	1.925
Ti	0.071	0.075	0.048	0.059	0.065	0.005	0.002
Fe^{2+}	0.076	0.080	0.075	0.087	0.085	0.102	0.105
Mn	0.005	0.003	0.002	0.005	0.005	0.001	0.002
Mg	0.085	0.095	0.085	0.109	0.075	0.040	0.045
Ca	0.000	0.000	0.000	0.000	0.000	0.000	0.000
Na	0.055	0.041	0.115	0.055	0.045	0.069	0.062
K	0.765	0.755	0.801	0.865	0.725	0.755	0.780
Na/(Na+K)	0.067	0.055	0.125	0.059	0.058	0.091	0.070

b) deformed

	96-1 cores	96-1 rims	97-16a cores	97-16a rims	97-17 cores	96-17 cores	97-3 cores	97-3 rims
Si	3.090	3.231	3.115	3.215	3.101	3.185	3.109	3.146
^{iv}Al	0.910	0.769	0.887	0.788	0.899	0.816	0.891	0.855
^{vi}Al	1.885	1.694	1.865	1.781	1.887	1.805	1.849	1.805
Ti	0.034	0.015	0.038	0.022	0.027	0.025	0.059	0.047
Fe^{2+}	0.053	0.227	0.098	0.165	0.053	0.140	0.080	0.115
Mn	0.003	0.007	0.003	0.005	0.003	0.005	0.000	0.002
Mg	0.060	0.176	0.070	0.135	0.058	0.118	0.085	0.108
Ca	0.000	0.000	0.000	0.000	0.000	0.000	0.000	0.000
Na	0.069	0.021	0.063	0.030	0.073	0.038	0.061	0.047
K	0.757	0.792	0.723	0.718	0.765	0.765	0.715	0.749
Na/(Na+K)	0.085	0.025	0.085	0.045	0.087	0.047	0.078	0.059

samples, further supporting this conclusion. Core compositions of large muscovites are distinctly different from muscovite from undeformed samples, being enriched in FeO and MgO, but depleted in TiO_2 (Fig. 2.16; Table 2.5; Table 2.13). These chemical differences suggest that muscovite from undeformed and deformed samples are of different origins.

Deformed sample 97-3 has core TiO_2, FeO, and MgO contents similar to muscovite from undeformed samples and may be of comparable origin. The large muscovites of deformed samples 96-1, 97-16a, and 97-17 are less obvious in this sample. Also, sample 97-3 was collected north of Highway 103 (Fig. 2.1), whereas the remaining deformed samples (96-1, 97-16a, and 97-17) all come from Wobamkek Beach (Fig. 2.1).

Muscovite from deformed samples shows a marked core-rim major element variation (Table 2.5; Table 2.14; Fig. 2.12; Fig. 2.16). Compared to cores, rims are markedly lower in Ti, Al, and Na, and higher in Si, Fe, and Mg, consistent with a non-magmatic origin (Table 2.13). Figure 2.17 shows muscovite compositions for all samples (data from Table 2.14) plotted in terms of Si, Al, and other octahedral cations (Fe+Mg+Mn+Ti). Although muscovite is close to end-member compositions, it is not ideal in composition. In contrast to Figure 2.16, some overlap between undeformed muscovite and the cores of deformed muscovite is evident from this diagram. Rim compositions from deformed samples show a trend toward a celadonitic composition (Fig. 2.17). Miller et al. (1981) suggested that magmatic muscovite is closer to ideal muscovite than secondary muscovite, although Anderson and Rowley (1981) reported the opposite conclusion.

Hames and Cheney (1997) noted similar core-rim variation in muscovite porphyroclasts from deformed polymetamorphic rocks and related the chemical variation

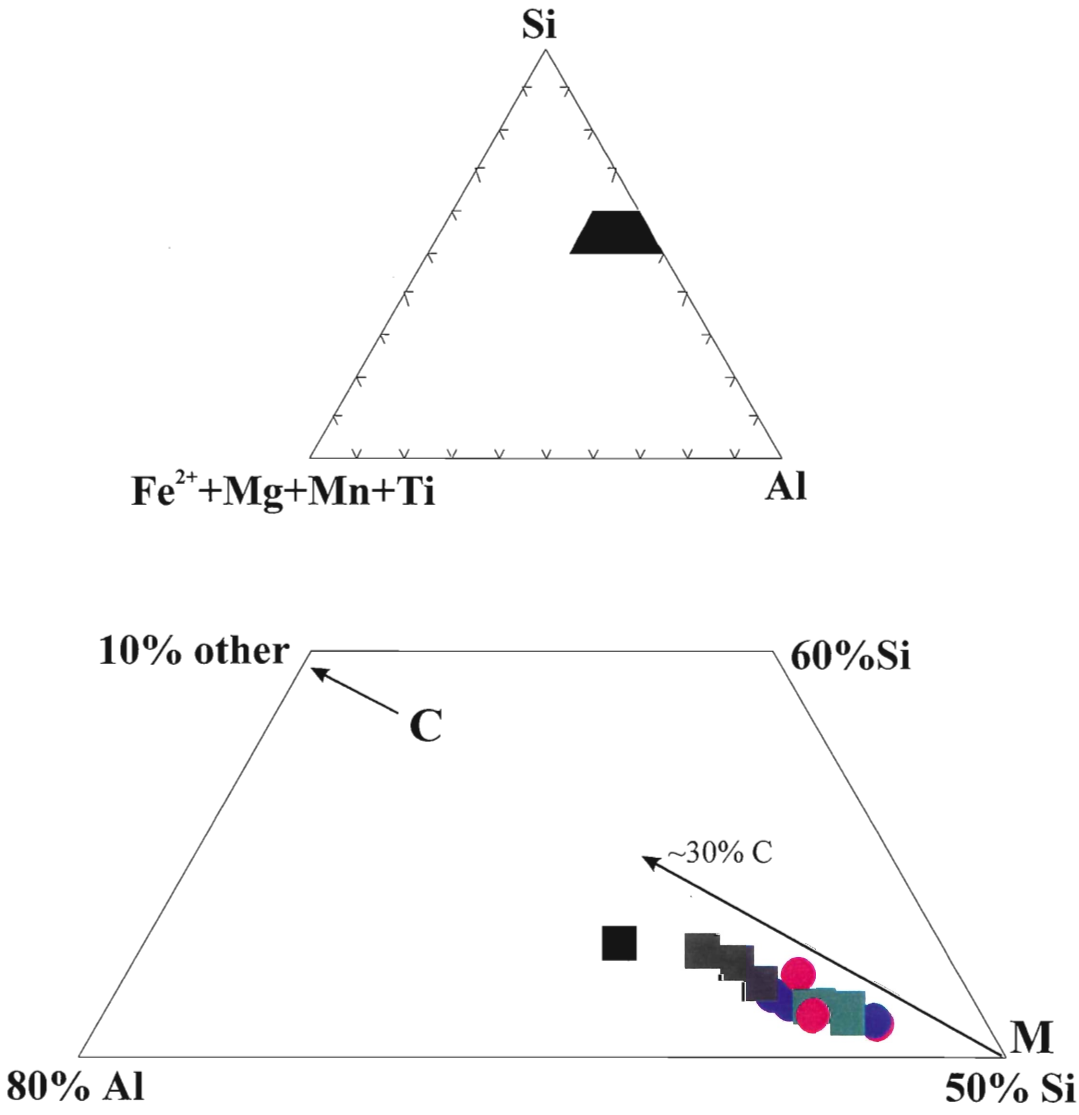

Figure 2.17. Mean muscovite compositions for undeformed and deformed samples plotted in the ternary diagram Si-Al-(Fe+Mg+Mn+Ti). M is end-member muscovite, $KAl_3Si_3O_{10}[OH]_2$. C is celadonite, $K[Mg,Fe]AlSi_4O_{10}[OH]_2$. Muscovite from all samples is close to end-member composition, but rims of muscovite from deformed samples display a clear trend toward celadonitic enrichment.

Table 2.15. Classification of PMP muscovite.

		TEXTURE	
		MAGMATIC	**NON-MAGMATIC**
CHEMISTRY	**MAGMATIC**	Undeformed samples: **556** **97-9** **97-14** Magmatic muscovite	Deformed sample: (Hwy 103) **97-3** Magmatic muscovite with post-magmatic textural modification
	NONMAGMATIC	Undeformed sample: (single grain) **97-14** Magmatic muscovite with post-magmatic chemical modification	Deformed samples: (Wobamkek Beach) **96-1** **97-16a** **97-17** Non-magmatic muscovite with post-magmatic chemical modification

to recrystallization during deformation. Deformation of large muscovite grains is largely restricted to their margins where significant grain size reduction has produced a thin mantle of fine-grained recrystallized muscovite (Fig. 2.12). Backscattered electron imaging of deformed muscovite shows that chemically altered zones are restricted to the very edges of grains (Fig. 2.12). This pattern suggests that the chemical variation is related to the deformation of the muscovite grain edges.

2.6 Summary

Based on the textural and chemical criteria outlined above, muscovite from the PMP can be classified as either magmatic or non-magmatic in origin (Table 2.15). Textural and chemical criteria suggest that the majority of muscovite from undeformed samples is of magmatic origin and has experienced minor post-magmatic textural and chemical modification. Muscovite from deformed rocks is distinctly different and shows core-rim chemical variation resulting from post-magmatic textural modification. Although Ti contents of these micas overlap values normally quoted for magmatic muscovite, the textural and chemical data from the PMP suggest that they are probably non-magmatic.

CHAPTER 3

U-Pb GEOCHRONOLOGY

3.1 Introduction

Precise crystallization ages from granitoid rocks underpin many tectonic models because they constrain the high-temperature parts of thermal histories. Uranium-bearing accessory minerals are useful for this purpose because they exhibit relatively strong retention of Pb at elevated temperatures (> 500°C), thus having the potential to date magmatic crystallization. Mica $^{40}Ar/^{39}Ar$ ages can also provide this information, but only in rapidly cooled terrains that have not experienced subsequent thermal disturbance above ca. 400°C.

The minerals most widely used for U-Pb geochronology in rocks from mid- to high-grade metamorphic terrains are zircon, monazite, and titanite. The vast majority of U-Pb studies on granitoid rocks have used zircon because of its abundance, high-retention temperature for lead (ca. 800°C), and relatively well understood U-Pb systematics. However, zircons from peraluminous granitoids tend to be complicated by inheritance and also by Pb loss at low temperatures, making interpretation of results difficult in many cases (Parrish 1990).

Although inheritance in monazite has been documented (Copeland et al. 1989), it is much less common than in zircon because the retention temperature for Pb diffusion in monazite (ca. 725°C) is less than the solidus temperature for most granitoid magmas (Parrish 1990). Also in contrast with zircon, in which low-temperature Pb loss is nearly ubiquitous, Pb loss in monazite is much less common (Parrish 1990). Monazite has

become the standard mineral for use in U-Pb geochronology of peraluminous granitoids and provides the best opportunity to determine the crystallization ages of these rocks (Hawkins and Bowring 1997).

3.2 Restatement of problem

As noted in Chapter 1, previous attempts to date the PMP relied on $^{40}Ar/^{39}Ar$ dating of micas and hornblende. Reynolds et al. (1987), Woodend-Douma (1988), and Keppie and Dallmeyer (1995) reported ages > 350 Ma, with the majority of ages between 340 and 300 Ma (Fig. 1.2 and Table 1.3). Reynolds et al. (1987) attributed $^{40}Ar/^{39}Ar$ mica ages of ca. 340-300 Ma to thermal resetting, whereas Keppie and Dallmeyer (1995) attributed a 340 Ma muscovite plateau age to moderately rapid post-crystallization cooling. In the absence of reliable crystallization ages for the main intrusive phases of the PMP, the pre - 350 Ma history of the PMP remains unclear. I undertook U-Pb geochronology of monazite to constrain the crystallization histories of the main intrusive phases.

3.3 Sample details and analytical procedures

I selected one sample of Early Stage tonalite (96-2), three samples of Middle Stage monzogranite (96-1, 97-9, 97-14), and one sample of Late Stage pegmatite (96-3) for U-Pb geochronology. Two large samples of Late Stage pegmatite failed to yield any monazite, and only poor quality zircon not suitable for precise age determination. One

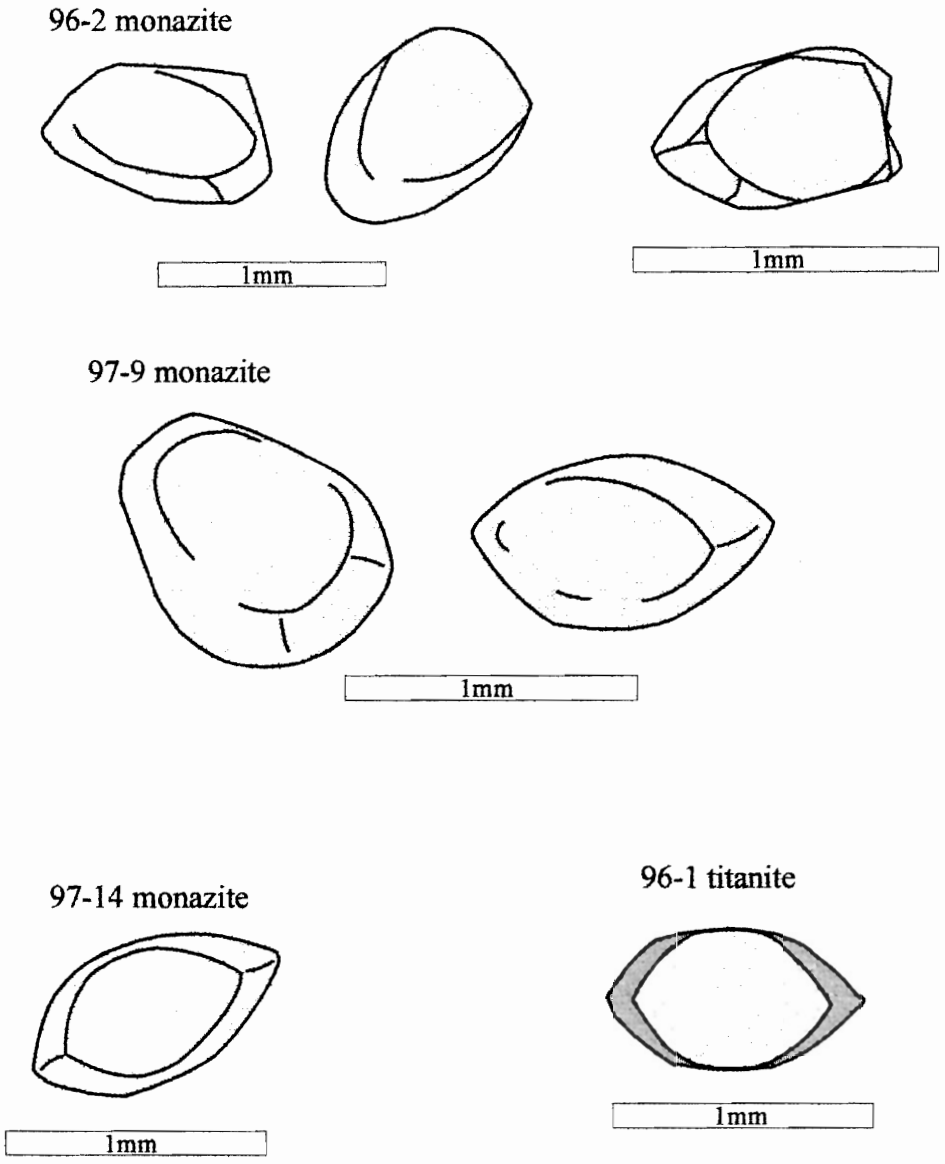

Figure 3.1. Monazite and titanite morphologies picked from samples dated in this study. Monazite from all samples is similar in size, shape, and color. Monazites are typically small, euhedral, well-faceted, pear-shaped grains, straw yellow in color, and transparent. Titanite from deformed sample **96-1** has distinct overgrowths.

Table 3.1. Fraction descriptions for monazite and titanite samples.

	96-1-2 Titanite	96-2-1/96-2-2 Monazite	97-9-1 Monazite	97-14-1 Monazite
Color	Brownish yellow, with dark brown rims; turbid, cloudy cores, no visible inclusions; obvious core-rim components	Yellow, turbid grains	Pale yellow grains; generally cloudy with few visible inclusions; possible faint zoning	Pale yellow grains; high-medium transparency; some tiny inclusions
Size	largest: 1.8 mm x 1.2mm; smallest: 0.7 x 0.8 mm; average ~1mm in diameter	1.0 mm-1.5 mm in diameter	0.7-0.8 x 0.4-0.5 mm	0.5-0.7 x 0.9-1.0 mm
Habit	Subhedral grains with quasi-equant faces; some have subrounded appearance	Subrounded-subangular grains, some possible fragments of larger grains	Euhedral with quasi-equant faces; some grains have subrounded appearance	Subhedral w/ quasi-equant faces
Magnetic Fraction	1.0A	0.5A	0.5A	0.4A

sample of Middle Stage monzogranite (96-1) did not contain any monazite or zircon, but did yield several titanite grains. Figure 3.1 illustrates some typical monazite and titanite morphologies and Table 3.1 contains fraction details. Appendix B describes the analytical procedures used in this study.

3.4 Results

3.4.1 Monazite

Table 3.2 presents monazite results for samples 96-2, 97-9, and 97-14; Figure 3.2 shows the corresponding concordia diagram. Monazite from all samples contains abundant U and very high Th (Table 3.2). High U contents meant that only a few grains were needed for a precise analysis. A first fraction from the Early Stage tonalite (96-2-1) has similar $^{206}Pb/^{238}U$, $^{207}Pb/^{235}U$, and $^{207}Pb/^{206}Pb$ ages (Table 3.2) and overlaps concordia (Fig. 3.2). A second fraction of Early Stage tonalite (96-2-2) is reversely discordant and plots just above concordia (Fig. 3.2), but yields similar $^{206}Pb/^{235}U$ and $^{207}Pb/^{238}U$ ages to the first fraction (Table 3.2). Two fractions from different Middle Stage monzogranites (97-9-1 and 97-14-1) also show reverse discordance, plotting just above concordia (Fig. 3.2), with 97-14-1 the more discordant. Although fraction 96-2-1 overlaps concordia, the large analytical uncertainty means that the presence of reverse discordance in this sample cannot be dismissed.

Table 3.2. U-Pb monazite data for the Port Mouton Pluton.

	Composition					Isotopic ratios				Ages (Ma)			
Fractions[a]	U (ppm)	Th[b] (ppm)	Pb_{tot}[c] (ppm)	Th/U[d]	Pb_{com}[e] (pg)	$^{206}Pb/^{204}Pb$[f]	$^{206}Pb/^{238}U$[g]	$^{207}Pb/^{235}U$[g]	$^{207}Pb/^{206}Pb$[g]	$^{206}Pb/^{238}U$	$^{207}Pb/^{235}U$	$^{207}Pb/^{206}Pb$	%disc.[h]
Early Stage Tonalite													
96-2-1, 3M, 25 ug	5362	40396	965	7.53	20	30504	0.0595±4	0.444±3	0.05406±4	372.8±2.4	372.9±2.1	373.6±1.8	0.22
96-2-2, 4M, 43 ug	3226	28082	639	8.70	25	23597	0.0598±1	0.445±1	0.05395±4	374.5±0.8	373.7±0.8	368.9±1.7	-1.5
Middle Stage Monzogranite													
97-9-1, 5M, 31 ug	8738	55888	1384	6.40	26	39087	0.0598±2	0.444±1	0.05383±3	374.2±1.0	372.8±0.9	364.1±1.4	-2.9
97-14-1, 6M, 22 ug	3337	49695	989	14.89	23	11986	0.0600±1	0.445±1	0.05380±4	375.8±0.7	373.9±0.7	362.6±1.8	-3.7

[a] Sample name (e.g., 96-2) followed by fraction number, number of grains analyzed (3M= 3 monazite grains), and weight in micrograms ug.
[b,d] Th concentration and Th/U ratio calculated from radiogenic ^{208}Pb.
[c] Pb_{tot} is total lead in each analysis.
[e] Pb_{com} is the calculated common lead in each analysis.
[f] Measured ratio corrected for fractionation and spike.
[g] Pb/U isotopic ratios corrected for fractionation, spike, blank, and initial common lead; quoted errors are absolute 1σ uncertainty in last digit(s).
[h] Percentage discordance in $^{207}Pb/^{206}Pb$ ages.

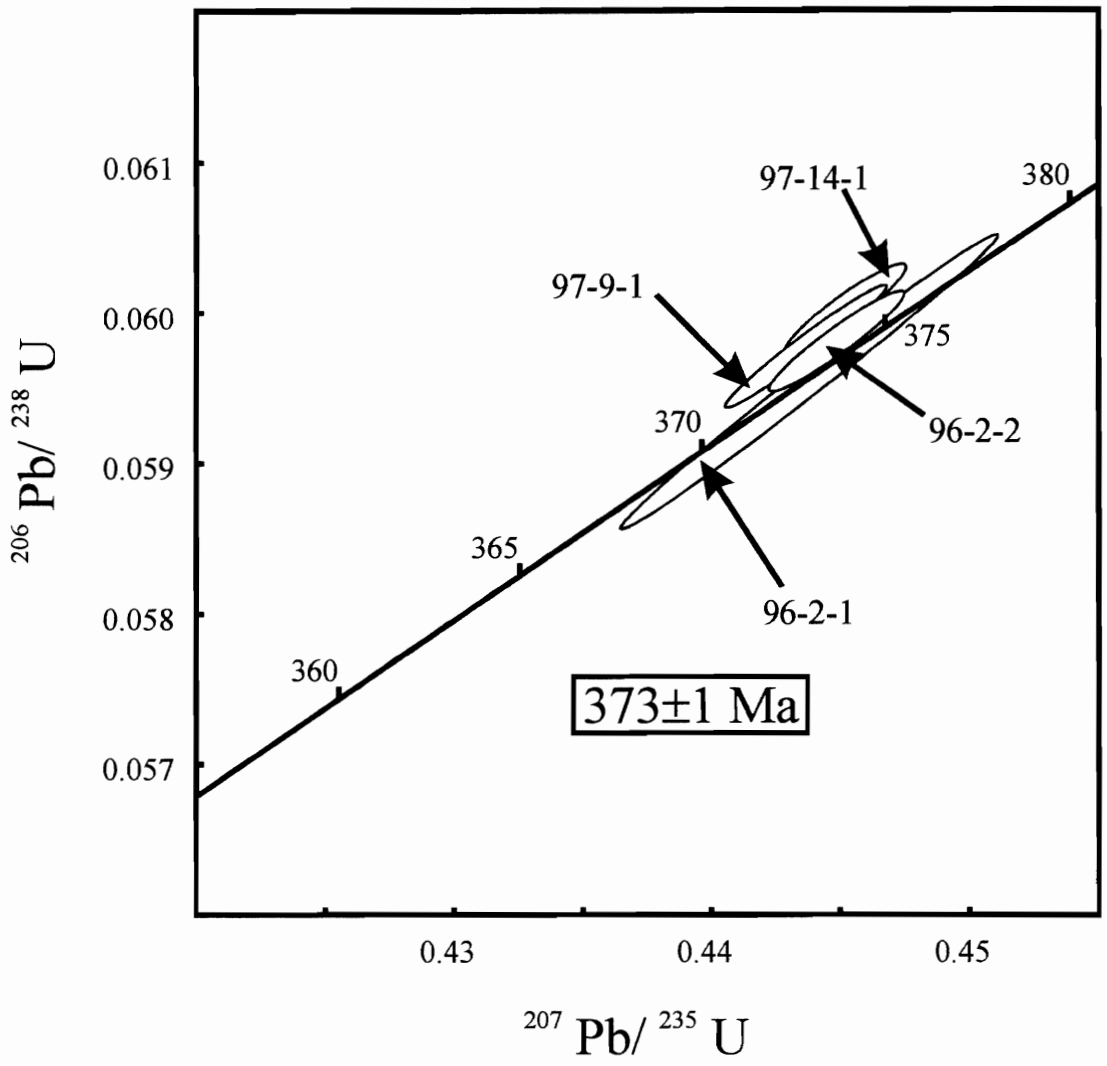

Figure 3.2. U-Pb concordia diagram for monazite fractions separated from the Port Mouton Pluton.

3.4.2 Discussion

Schärer (1984) attributed reverse discordance in monazite to excess ^{206}Pb produced from the in-situ decay of ^{230}Th, an intermediate daughter isotope in the ^{238}U decay chain. The effect of excess ^{206}Pb is to produce anomously old $^{206}Pb/^{238}U$ ages (Parrish 1990). The amount of excess ^{206}Pb in all fractions may be minor because: (i) $^{206}Pb/^{238}U$ ages are either identical to, or 1-2 Ma older than the $^{207}Pb/^{235}U$ ages (Table 3.2); and (ii) for monazite older than ca. 200 Ma, the amount of excess ^{206}Pb produced by decay of ^{230}Th is negligible (Parrish 1990). In rocks containing monazite with excess ^{206}Pb, the $^{207}Pb/^{235}U$ age is considered the best estimate of the time of crystallization (Parrish 1990). The $^{207}Pb/^{235}U$ ages for all four fractions are identical within error (Table 3.2); the mean age is 373 ± 1 Ma. I consider this to be the best estimate for the crystallization age of the main intrusive phases.

3.4.3 Titanite

I selected only a single fraction of titanite for analysis. Table 3.3 presents titanite results for sample 96-1; Figure 3.3 shows the corresponding concordia diagram. The titanite fraction has moderate to high U contents, low $^{206}Pb/^{204}Pb$ ratios, and high common Pb contents (Table 3.3). The discordance of this fraction (Fig. 3.3) reflects the uncertainty in the initial common Pb composition.

Table 3.3. U-Pb titanite data for the Port Mouton Pluton.

	Composition					Isotopic ratios				Ages (Ma)			
Fractions[a]	U (ppm)	Th[b] (ppm)	Pb_{tot}[c] (ppm)	Th/U[d]	Pb_{com}[e] (pg)	$^{206}Pb/^{204}Pb$[f]	$^{206}Pb/^{238}U$[g]	$^{207}Pb/^{235}U$[g]	$^{207}Pb/^{206}Pb$[g]	$^{206}Pb/^{238}U$	$^{207}Pb/^{235}U$	$^{207}Pb/^{206}Pb$	%disc.[h]
Middle Stage Monzogranite													
96-1-2, 2T, 16 ug	499	66	63	0.13	700	48	0.0407±3	0.316±16	0.0565±28	257±2	279±12	471±100	46.3

[a] Sample name (e.g., 96-1) followed by fraction number, number of grains analyzed (1T= 1titanite grain), and weight in micrograms ug.
[b,d] Th concentration and Th/U ratio calculated from radiogenic ^{208}Pb.
[c] Pb_{tot} is total lead in each analysis.
[e] Pb_{com} is the calculated common lead in each analysis.
[f] Measured ratio corrected for fractionation and spike.
[g] Pb/U isotopic ratios corrected for fractionation, spike, blank, and initial common lead; quoted errors are absolute 1σ uncertainty in last digit(s).
[h] Percentage discordance in $^{207}Pb/^{206}Pb$ ages.

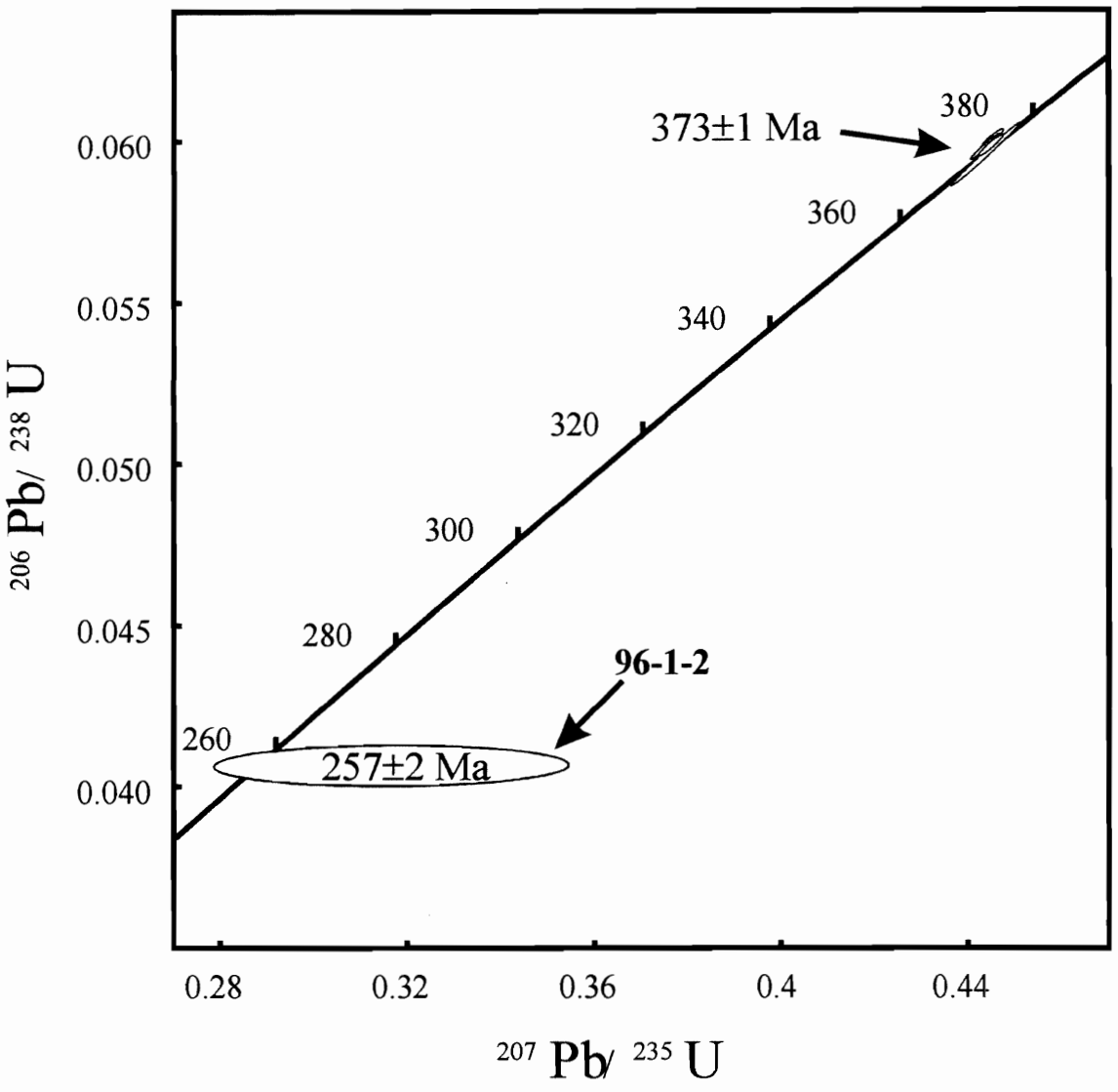

Figure 3.3. U-Pb concordia diagram for titanite separated from sample **96-1**.

3.4.4 Discussion

The titanite data are difficult to interpret, particularly with only a single reliable analysis. Without knowledge of the exact initial common Pb composition, the high common Pb contents preclude a precise age determination. Fraction 96-1-2 yielded a $^{206}Pb/^{238}U$ age of 257 ± 2 Ma. The $^{206}Pb/^{238}U$ age is least sensitive to the common Pb correction.

Visible core and rim components (Fig. 3.1) suggest multiple titanite growth events in this sample. The $^{206}Pb/^{238}U$ age of 257 ± 2 Ma probably reflects the average age of a mixed (core and rim) age population and does not date titanite growth in this sample. Because titanite is unlikely to crystallize from monazite-bearing peraluminous magmas, titanite may have initially grown in the subsolidus. Several workers (Gromet 1991; Ketchum et al. 1998; Timmerman 1998) have suggested that titanite growth in the presence of a late fluid phase can occur at temperatures below the estimated retention temperature for titanite of ca. 600°C (Heaman and Parrish 1991), particularly in deformed rocks. The presence of chloritized biotite in this sample, as well as secondary biotite along the cleavage of deformed muscovite porphyroclasts (Fig. 2.12), suggests that breakdown of magmatic biotite could provide a source of Ti for titanite growth.

3.5 Summary

The U-Pb monazite data reported here constrain the crystallization age of the PMP to ca. 373 Ma, and establish the pluton as Late Devonian in age. This age provides a benchmark against which all subsequent $^{40}Ar/^{39}Ar$ ages can be interpreted. The young

titanite age suggests the possibility of Permian thermal activity, which can be further evaluated with $^{40}Ar/^{39}Ar$ data. The next chapter presents new $^{40}Ar/^{39}Ar$ muscovite and K-feldspar age spectra for the PMP, and reports the first $^{40}Ar/^{39}Ar$ laserprobe data from Meguma Zone plutons.

CHAPTER 4

$^{40}Ar/^{39}Ar$ GEOCHRONOLOGY

4.1 Introduction

Incremental heating studies of single crystals or multigrain samples of micas and K-feldspar with a resistance furnace have traditionally been used to determine the intermediate-to-low-temperature thermal histories of plutonic and metamorphic terranes. Prior to the introduction of high-resolution laserprobes, $^{40}Ar/^{39}Ar$ geochronologists deduced the nature of argon isotopic gradients in minerals from the morphology of incremental heating spectra. With knowledge of the distribution of radiogenic ^{40}Ar within a geological sample, it is possible to construct its thermal history (McDougall and Harrison 1988).

Recent investigations into the behavior of hydrous minerals during incremental heating experiments (Lee et al. 1991) have shown that the morphologies of many release spectra (particularly those from slowly cooled or reset samples) do not provide accurate information about the distribution of argon isotopes within mineral grains. Consequently, many release spectra cannot be used to model thermal histories (Hames and Bowring 1995). The development of laserprobes eliminates the need to use release spectra to determine radiogenic ^{40}Ar gradients within minerals. Recent studies (Hodges et al. 1994) have demonstrated the value of laserprobe studies in regions that have experienced either slow cooling or thermal resetting, where incremental heating spectra can give misleading results.

In an effort to clarify the complex post-intrusive thermal history of the PMP, this study combines conventional incremental heating methods and laserprobe studies of single grains, allowing comparisons between the two techniques. This chapter presents the results of conventional incremental heating analysis of muscovite and K-feldspar, as well as the first high-resolution laserprobe data for single muscovite grains from Meguma Zone plutons.

4.2 Analytical procedures

4.2.1 Grain selection

I separated muscovite dated in this study in one of two ways. I separated muscovite from samples 96-1, 96-3, 97-9, and 97-14 following removal of monazite and titanite for U-Pb geochronology. The monazite separation process involved intense sample pulverization in a jaw-crusher and disk-mill resulting in significant grain-size reduction of constituent minerals. The crushing process yielded thin transparent muscovite grains that are clearly not complete grains, but consist of several cleavage fragments.

I attempted to pick only the most euhedral muscovite grains to avoid the effects of grain fragmentation. I picked all grains from a 0.85mm size fraction to yield the largest grains (generally > 1mm). Large muscovite is more suitable for $^{40}Ar/^{39}Ar$ laserprobe spot analysis and large grains are less likely to be grain fragments. I picked high-purity muscovite fractions under a binocular microscope. I dated muscovite separated using this

process using incremental heating analysis, laserprobe total fusion analysis, and laserprobe spot fusion analysis of single grains.

I separated muscovite from remaining samples (97-16a, 97-17, 477, 487 and 556, as well as several grains from samples 97-3 and 97-9) following crushing of a small piece of sample in a jaw-crusher and ring-mill for less than 10 seconds. I used this alternative procedure to preserve as much of the original grain size and morphology as possible. This less destructive separation process yielded euhedral, thicker, less transparent grains, which were used for laserprobe total fusion analysis and laserprobe spot fusion analysis of single grains. I picked all muscovite from a 0.85mm size fraction to ensure recovery of the largest grains possible. I washed muscovite separates in an ultrasonic bath of distilled water, rinsed them in methanol, and left them to evaporate to dryness. I hand-picked final high-purity muscovite fractions under a binocular microscope. I selected only high-quality, euhedral, inclusion-fee grains for analysis. I picked some muscovite from sample 97-3 following limited crushing with a geological hammer. This procedure yielded mostly small (< 1mm), poor-quality, anhedral grains, that had adhering matrix material (quartz, feldspar, and biotite). This material remained following a 15-minute ultrasonic treatment.

4.2.2 Incremental heating analysis

Procedures used in this study are described in detail elsewhere (Hicks 1996). McDougall and Harrison (1988) described the principles and method of $^{40}Ar/^{39}Ar$ dating.

4.2.3 Laserprobe $^{40}Ar/^{39}Ar$ analysis

The laser system operated at Dalhousie University is a Quantronix 117 Nd-YAG laser, operated in TEM 00 mode at the rated output of 17 Watts. The laser has a wavelength of 1064 nm and allowed spots with a diameter of approximately 75 microns to be produced in muscovite. The elements of a laser system such as that used in this study are illustrated in Figure 4.1 and described in detail by Hodges (1996). The grains to be analyzed are fitted into shallow machined holes of various shapes and sizes, which are custom-drilled into circular aluminum holders. After irradiation, the holders each containing several grains, are placed into the target chamber ready for analysis (Fig. 4.1).

The beam emitted from the laser is regulated using a calcite attenuator in the beam delivery device. During analysis of an individual muscovite grain, rims are normally analyzed first. The beam is first located away from the sample. The grain to be analyzed is then moved over the determined beam location by means of a motorized stage. The grain is hit several times with rapid bursts of energy, each burst having a frequency of approximately 200 Hz, the entire process lasting a few seconds. Although individual spots vary in size and shape, surface melting of samples typically takes the form of circular melt pits that have the form of an impact crater in cross-section.

On examination after analysis, these pits have glassy centers (representing quenched melt) surrounded by a discolored and deformed halo that varies in size, but is typically several times larger than the original laser spot. The halo probably represents localized structural damage of the mineral lattice, but could also represent peripheral heating (and presumably argon loss) from the grain (Hodges 1996). Using the laser in

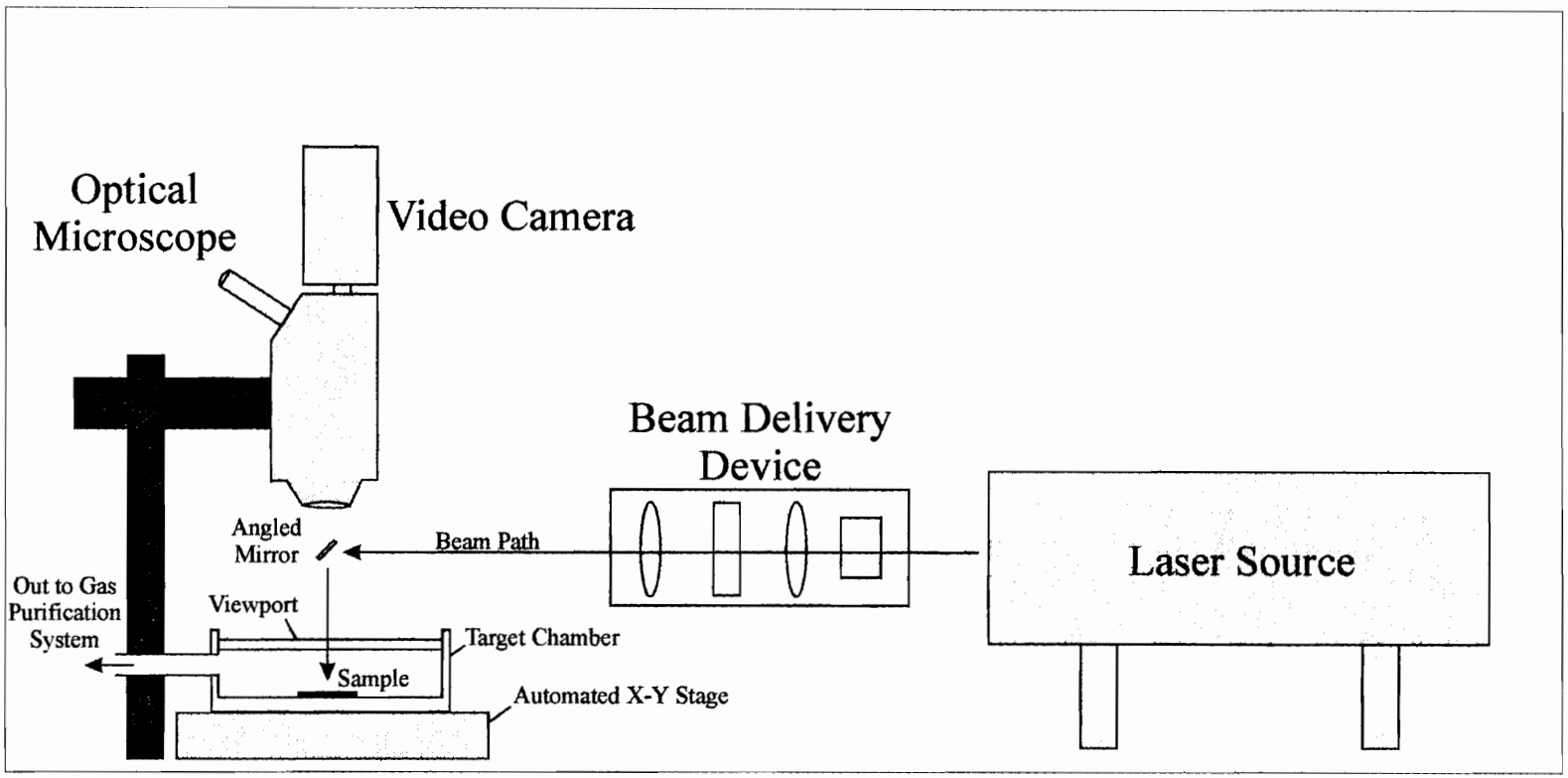

Figure 4.1. Schematic side view of a simple laser system, such as that used in this study.

pulsed mode delivers higher energy in a shorter period of time, allowing small melt pits to be produced. With each successive laser pulse, the melt pit gets deeper and the associated halo becomes wider.

During analysis, the degree of coupling between sample and laser beam varied greatly among samples. The amount of beam energy absorbed by a sample was apparently influenced by several factors, such as grain thickness, transparency, and orientation within the sample holder. Some grains required less heating than others to extract sufficient gas for analysis. In general, thinner grains required more heating over a wider area to extract enough gas for analysis. In this case, the grain was moved about under the laser beam producing a larger melt pit.

For laser total fusion analysis of single grains, the laser is operated in continuous mode and the beam is defocused from ca. 75 microns to ca. 1-2 mm in diameter. During analysis, the entire grain is heated under the laser beam. Power is slowly increased until the grain melts. During analysis grains typically undergo a series of structural changes prior to fusion. First, delamination of (001) planes occurs and the grain appears to move around under the beam. Next, the grain appears to "sweat", before finally, following total fusion, leaving behind a small glass bead. Following each individual total fusion or spot analysis, the evolved gas is extracted and analyzed in the mass spectrometer.

4.3 Results: Muscovite

I present muscovite data first, followed by feldspar data. The muscovite dataset for undeformed and deformed samples includes incremental heating spectra, laserprobe total fusion of single grains, and laserprobe spot mapping of single grains. Feldspar data consists of incremental heating spectra for three Late Stage pegmatite samples. Appendix C contains all corresponding analytical data.

4.3.1 Muscovite incremental heating spectra

Five samples were selected for incremental heating analysis: three undeformed samples and two deformed samples.

Undeformed samples

Sample 97-14 is characterized by the least disturbed spectrum (Fig. 4.2a), and yields the oldest age. Fourteen increments (775°C-1250°C) define a mean age of 359 ± 2 Ma. Sample 97-9 produced a mildly discordant age spectrum (Fig. 4.2b). The first four increments (650°C-825°C) record the youngest ages (ca. 336-350 Ma). The remaining fourteen increments (850°C-1250°C) define a mean age of 353 ± 2 Ma. A relatively flat age spectrum characterizes sample 96-3 (Fig. 4.2c). Fifteen increments (750°C-1200°C) record a mean age of 349 ± 2 Ma.

a) 97-14 muscovite

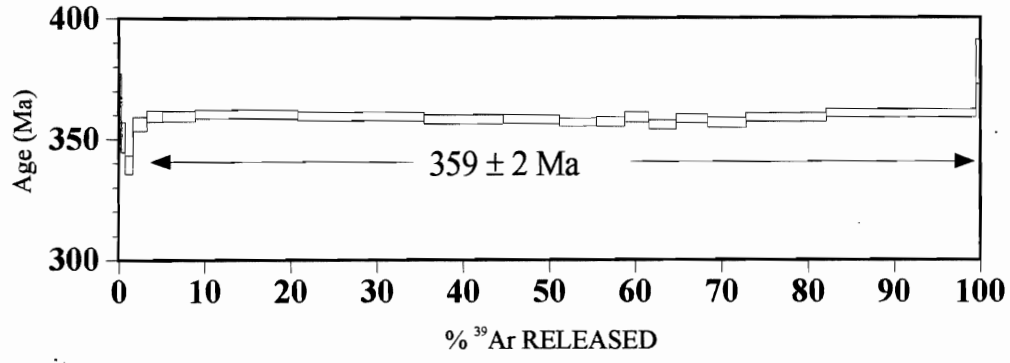

b) 97-9 muscovite

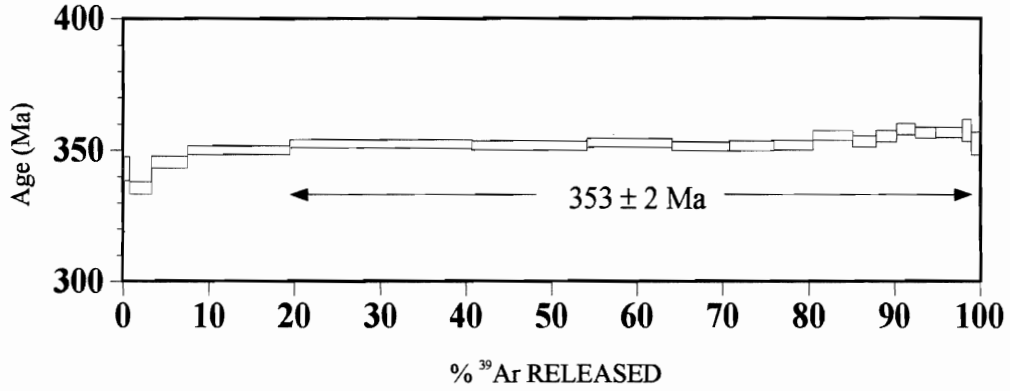

c) 96-3 muscovite

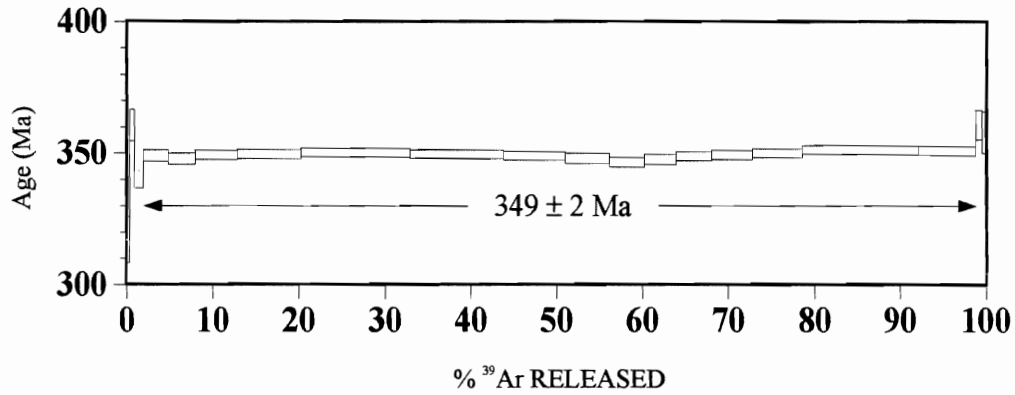

Figure 4.2. Incremental heating spectra for undeformed samples. Mean ages are shown for the number of increments indicated.

Deformed samples

The spectrum for sample 96-1 shows only minor discordance (Fig. 4.3a) and is similar in overall shape to spectra from undeformed samples 97-9 and 96-3. Eight intermediate increments (775°C-950°C) define a mean age of 349 ± 2 Ma; seven high-temperature increments (1075°C-1450°C) define a mean age of 357 ± 2 Ma. Sample 97-3 is characterized by a discordant age spectrum in which apparent ages systematically increase from ca. 310-347 Ma in the first seven increments (Fig. 4.3b). The following eleven increments (850°C-1200°C) record a mean age of 349 ± 2 Ma.

4.3.2 Total fusion data

Several total fusion ages were obtained for single muscovite grains from selected samples (Fig. 4.4). The total fusion method allows large numbers of single grains to be dated in a short period of time. Total fusion ages do not give important information concerning the distribution of ^{40}Ar within grains. Consequently, few grains were analyzed using this technique. Samples that yielded poor quality muscovite unsuitable for spot analysis were generally selected for total fusion analysis. Figure 4.4 shows that total fusion ages fall between 370 Ma and 340 Ma, possibly indicating the absence of any significantly younger ages within grains.

Undeformed samples usually yielded older ages than deformed samples, although some overlap occurs (Fig. 4.4). Undeformed samples 97-14 and 97-9 yielded the oldest ages. Total fusion ages from these samples are highly variable, ranging from 377 Ma to 355 Ma. Only a single total fusion age for undeformed sample 556 was obtained, but this

a) 96-1 muscovite

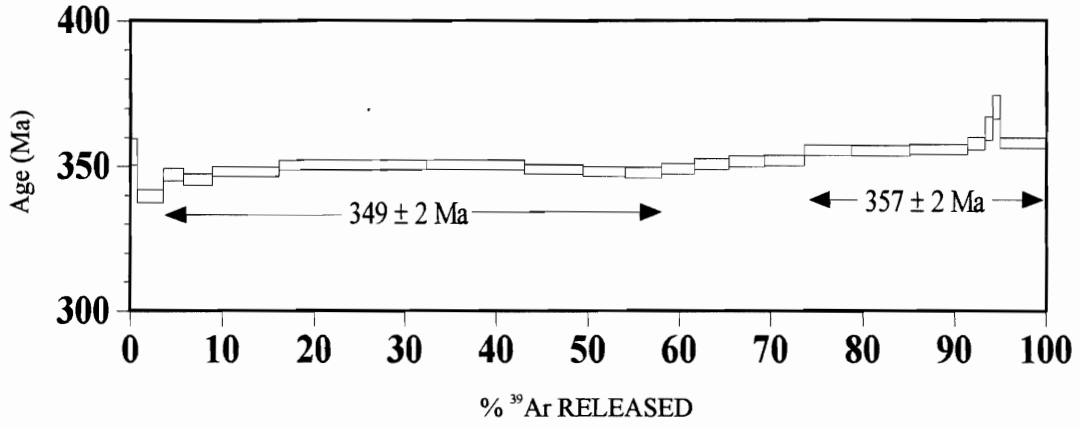

b) 97-3 muscovite

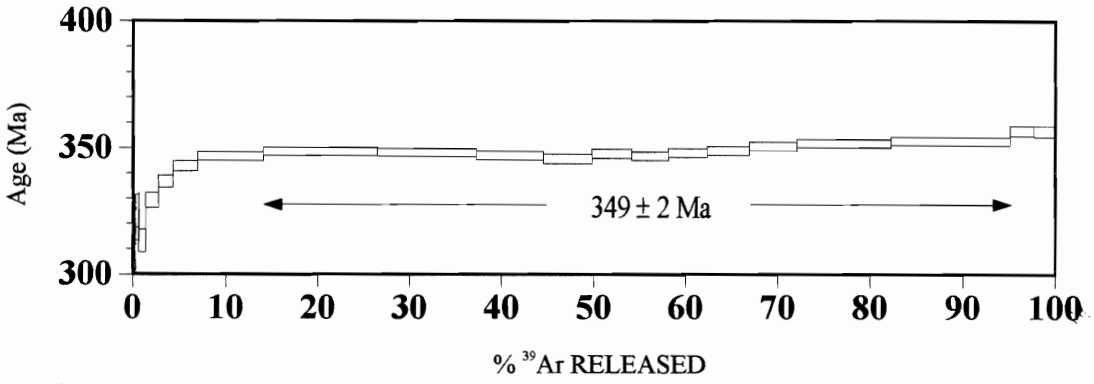

Figure 4.3. Incremental heating spectra for deformed samples. Mean ages are shown for the number of increments indicated.

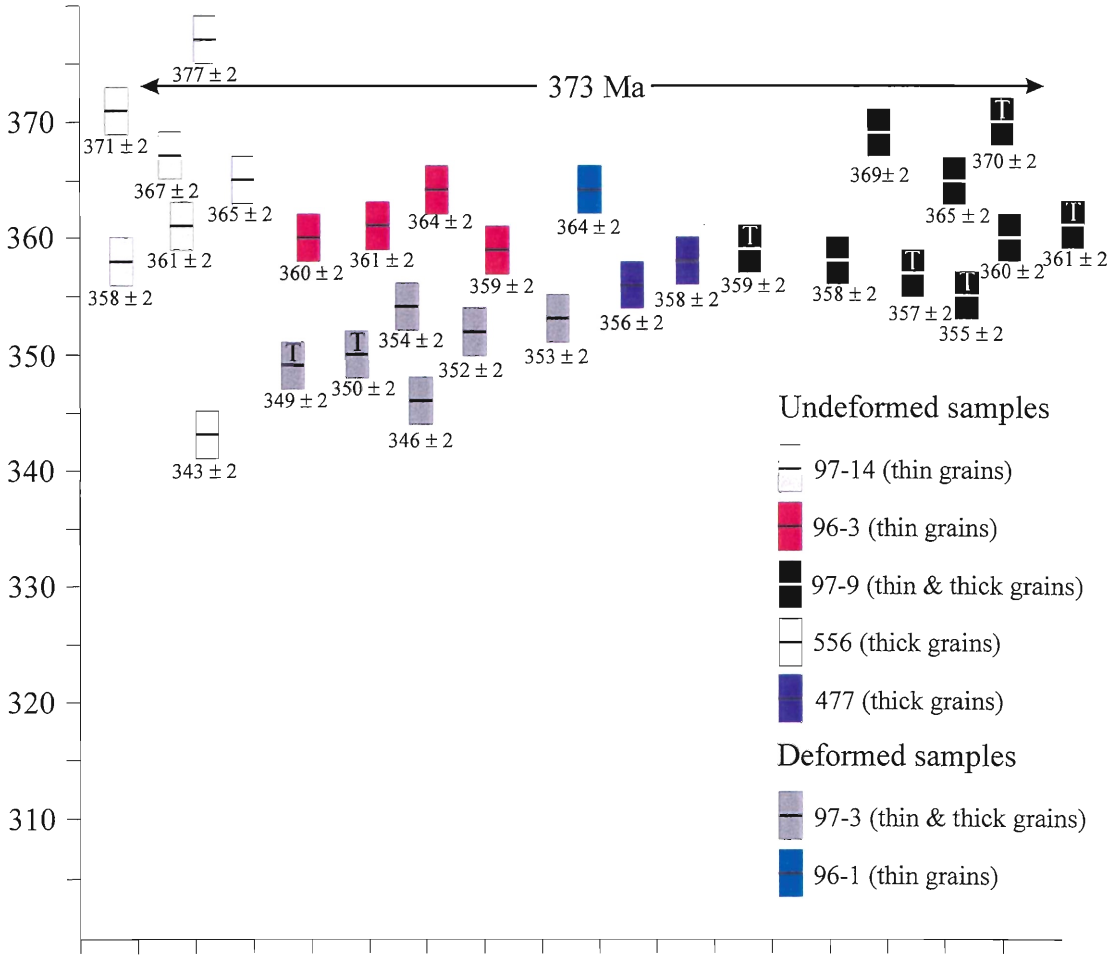

Figure 4.4. Total fusion data for undeformed and deformed samples. The horizontal line in each rectangle represents the age; the error (2σ) is represented by the colored rectangle. T denotes thick in samples **97-9** and **97-3**.

analysis is the youngest, at 343 ± 2 Ma. Undeformed sample 96-1 yielded a single total fusion age of 364 ± 2 Ma. Deformed sample 97-3 yielded several total fusion ages of ca. 350 Ma. Two types of muscovite grain were analyzed from undeformed sample 97-9 and deformed sample 97-3. Thin grains, separated following intense sample pulverization, and thicker grains, picked from samples subjected to only limited crushing. In general, the oldest total fusion ages were obtained from thin grains, although there is some overlap (Fig. 4.4)

4.3.3 Laserprobe spot mapping

Several grains from various undeformed and deformed samples were selected for $^{40}Ar/^{39}Ar$ laserprobe spot analysis. I discuss each sample individually. The aims of laserprobe spot mapping were: (i) to identify age gradients within single grains; (ii) to see if undeformed and deformed samples were characterized by different age gradients; and (iii) to relate these age gradients to known or suspected geological events.

Undeformed samples

97-14: Middle Stage granodiorite

The oldest spot ages are from the cores of grains (Figs. 4.5-4.8). The oldest core age is 376 ± 2 Ma (grain Y58-4), and the youngest 371 ± 2 Ma (grain Y58-1). The oldest rim age is 377 ± 5 Ma (grain Y58-4), comparable to the oldest core age. The youngest rim age is 365 ± 4 Ma (grain Y58-9), identical within error to the youngest core age. The average core age is 374 ± 1 Ma, and the average rim age is 369 ± 3 Ma.

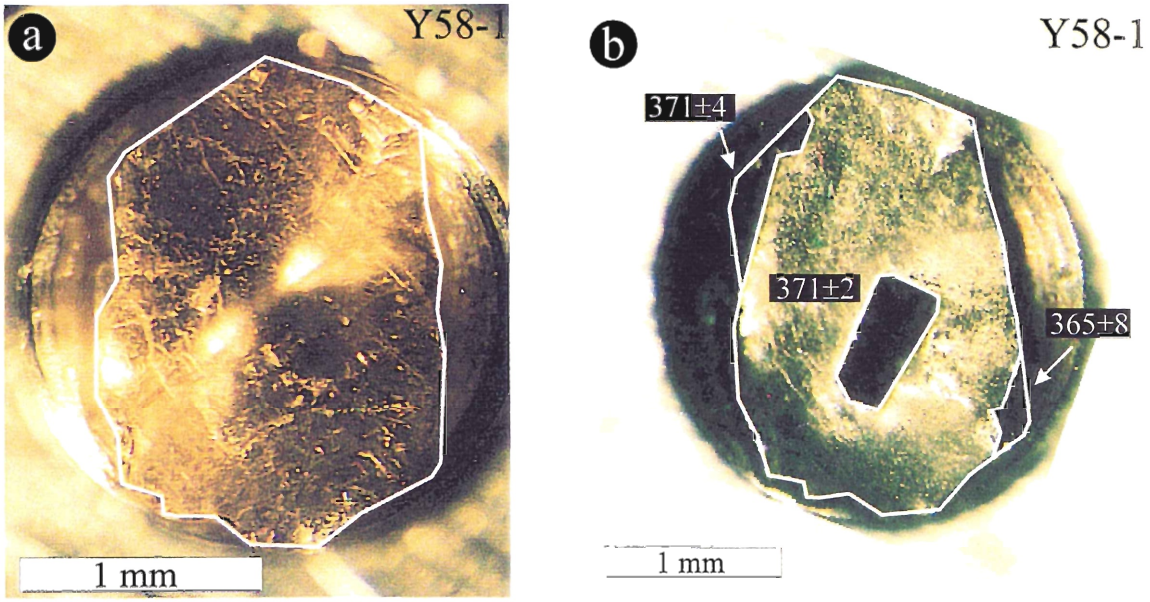

Figure 4.5. Spot data for euhedral muscovite **Y58-1** from undeformed sample **97-14**. a) Before fusion. b) After fusion. Note the absence of a significant difference between core and rim ages.

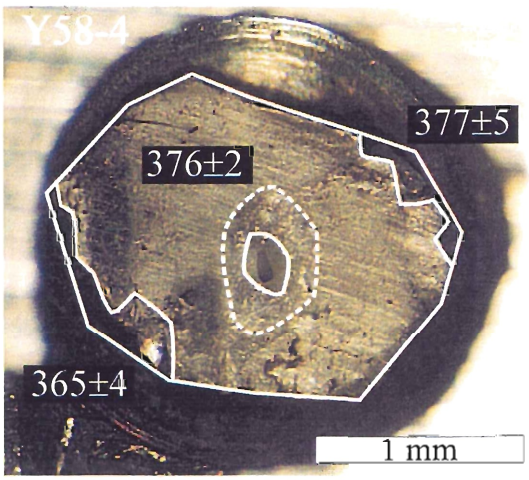

Figure 4.6. Grain **Y58-4** from undeformed sample **97-14**, after fusion. Core and rim ages are comparable in age.

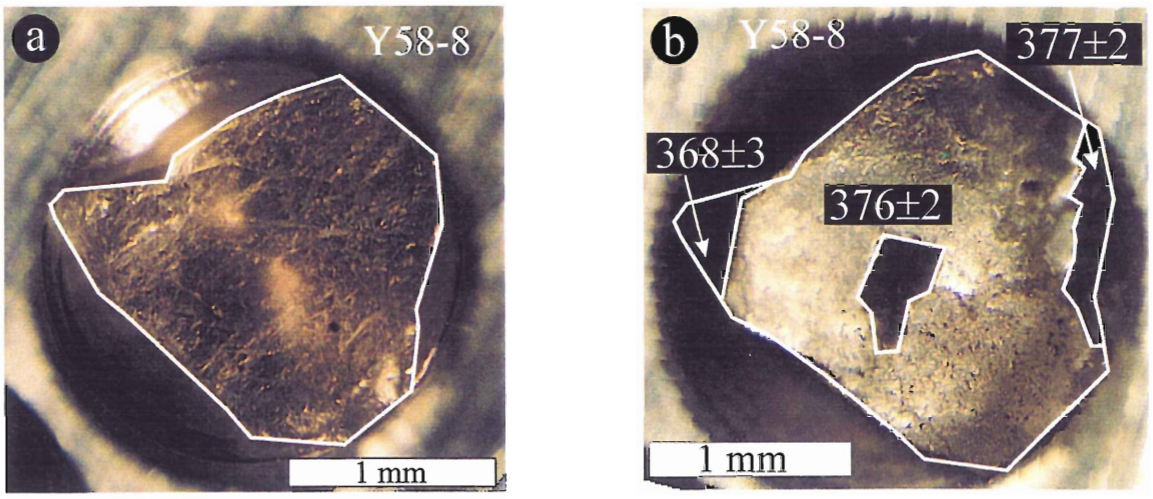

Figure 4.7. Grain **Y58-8** from undeformed sample **97-14**. a) Before fusion. b) After fusion. The distribution of ages is similar to grain **Y58-4**.

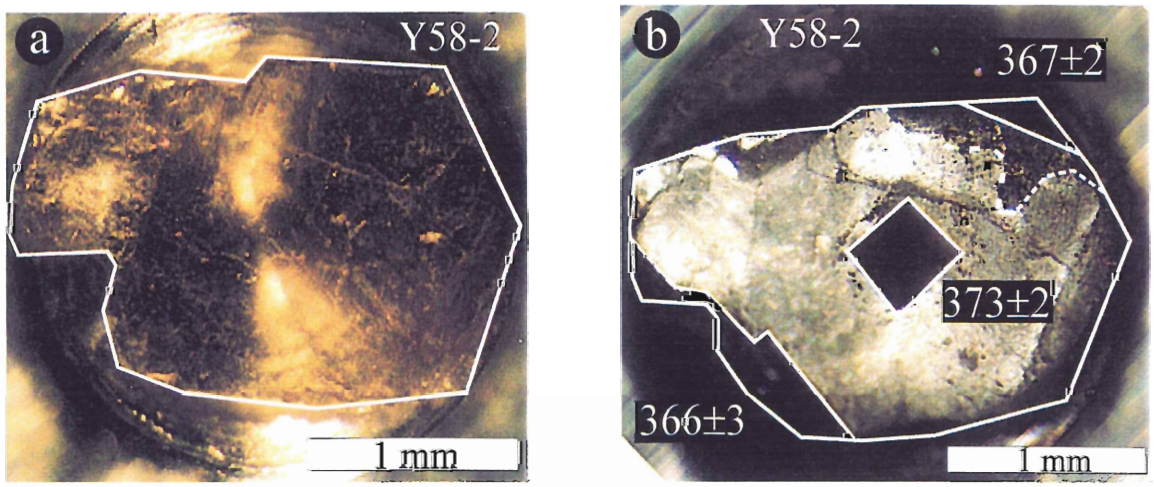

Figure 4.8. Grain **Y58-2** from undeformed sample **97-14**. a) Before fusion. b) After fusion. The core spot has the oldest age and is at most 2 Ma older than the rims, suggesting a steep core-rim age gradient.

Grain Y58-1 shows no apparent age difference between core and rim (Fig. 4.5). All other grains have rim ages similar to core ages, or rim ages 2-4 Ma younger than the core age. Sample 97-14 is notable for the clear spatial distinction between core and rim spots, with each analysis apparently incorporating little if any gas from intermediate parts of the grains.

96-3: Late Stage pegmatite

Two large grains from this sample were analyzed (Figs. 4.9-4.10). As in sample 97-14, core ages are mostly older than rim ages. The oldest core age is 371 ± 1 Ma (grain Y56-4), with the youngest 355 ± 5 Ma (grain Y56-3). The youngest rim age (343 ± 5 Ma) and the oldest rim age (372 ± 3 Ma) both come from grain Y56-4 (Fig. 4.10). The average age of a core spot is 362 ± 2 Ma and the average age of a rim spot is 356 ± 2 Ma.

Grains Y56-4 and Y56-3 exhibit different age distributions. Spot ages for Y56-4 are uniformly older than for Y56-3 (Fig. 4.10). Although rim ages are on average younger than core ages, no systematic decrease in spot ages from core to rim is evident, suggesting that no significant age gradients exist within these grains (see discussion for further explanation). Except for a single rim analysis of ca. 343 Ma, all core and rim spots for grain Y56-3 have identical ages of ca. 360 Ma (Fig. 4.9). Similarly, core and rim ages from grain Y56-4 are the same, ca. 370 Ma, except for one rim age of ca. 344 Ma (Fig. 4.10).

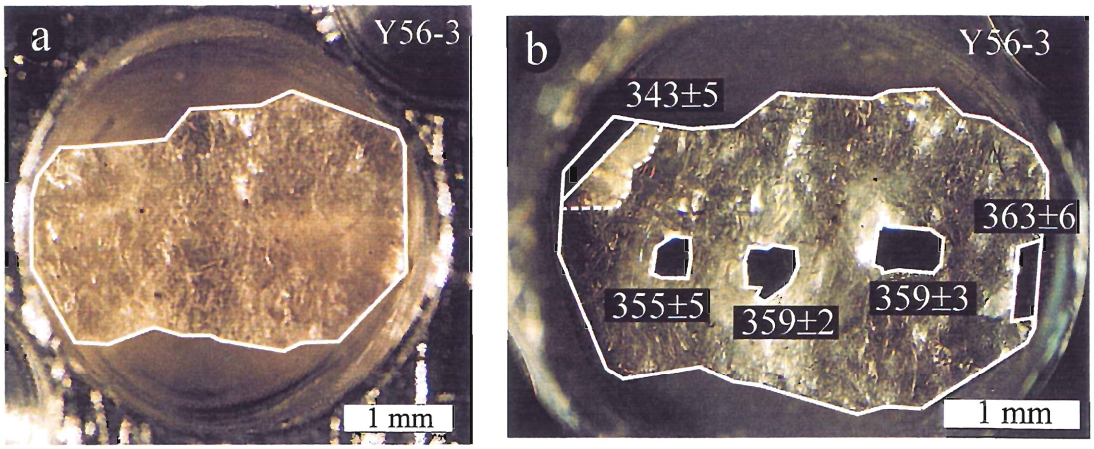

Figure 4.9. Large musovite **Y56-3** from Late Stage pegmatite **96-3**. a) Before fusion. b) After fusion. Core and rim ages are similar, ca. 360 Ma, except for a single rim of ca. 345 Ma. This pattern of ages suggests that systematic core-rim age gradients are absent from this grain.

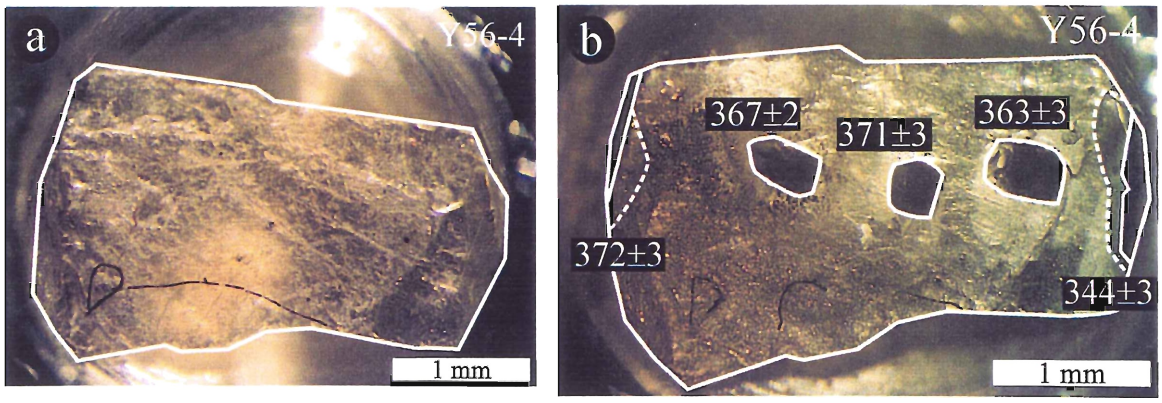

Figure 4.10. Large muscovite grain from Late Stage pegmatite sample **96-3**. The pattern of ages is identical to grain **Y56-3**, except that core and rim ages are older, ca. 370 Ma.

556: Middle Stage Monzogranite

As in previous samples, the majority of core ages are older than rim ages. Sample 556, however, is distinguished from samples 97-14 and 96-3 by significantly younger ages for both cores and rims (Figs. 4.11-4.14). The oldest core age is only 355 ± 5 Ma (grain Y72-6), with ages as young as 338 ± 2 Ma (Y72-6). The average age of a core spot is only 348 ± 2 Ma, compared to samples 97-14 (374 ± 1 Ma) and 96-3 (362 ± 2 Ma). The oldest rim age is 350 ± 5 Ma (grain Y72-2), with ages as low as 326 ± 2 Ma (grain Y72-5). The average age of a rim spot is 338 ± 2 Ma, significantly younger than samples 97-14 (369 ± 3 Ma) and 96-3 (356 ± 2 Ma).

Grain Y72-5 has three core spots with similar ages, ca. 345-350 Ma. Younger rims, ca. 325 Ma, suggest the possibility of steep age gradients in this grain (Fig. 4.12). Grain Y72-6 shows a similar pattern of ages (Fig. 4.13). The youngest core age (338 Ma) is identical to rim ages. This spot is very close to the grain rim and may have incorporated some rim gas thus lowering the age (see discussion for further explanation). Grain Y72-2 shows significant overlap between core and rim ages, with no obvious age gradient from core to rim (Fig. 4.11). Core ages from all three grains are similar, ca. 350 Ma.

97-9: Middle Stage granodiorite.

Muscovite grains from this sample were very small and unsuitable for precise $^{40}Ar/^{39}Ar$ laserprobe spot analysis. Only two core ages, 354 ± 2 Ma and 350 ± 2 Ma, were obtained for this sample.

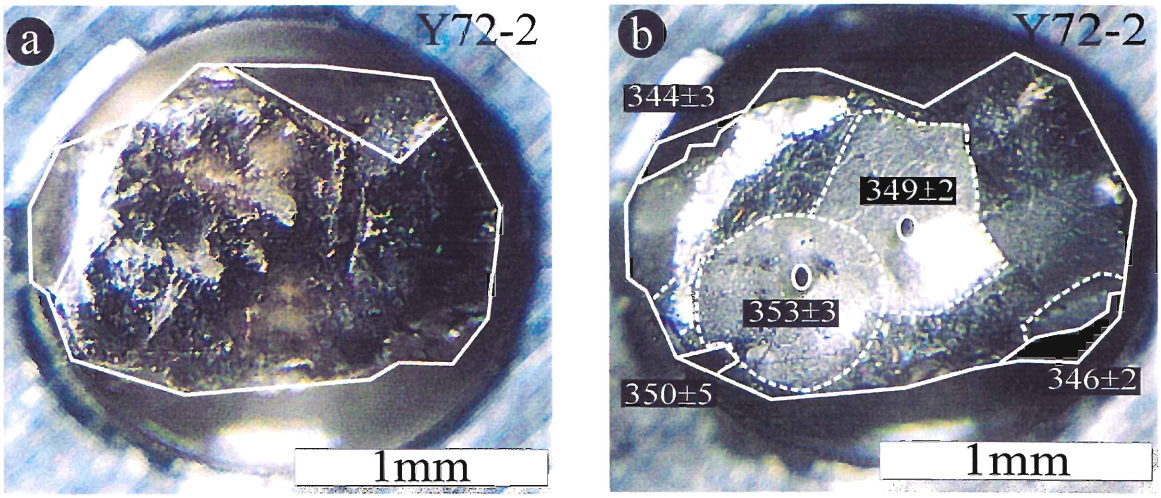

Figure 4.11. Grain **Y72-2** from undeformed sample **556**. a) Before fusion. b) After fusion. Although core ages are older than rim ages, there is some overlap, suggesting the absence of significant age gradients in this muscovite grain.

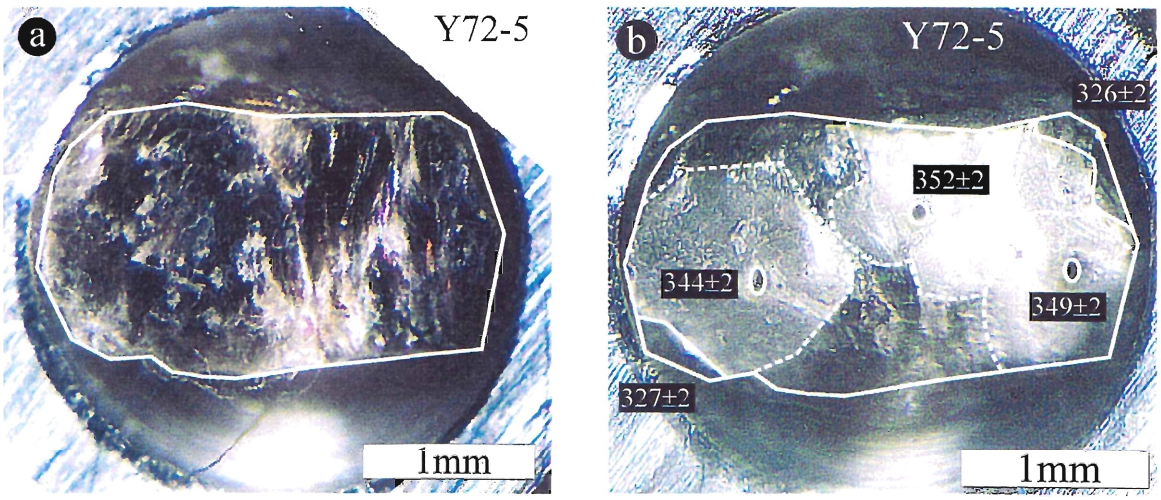

Figure 4.12. Grain **Y72-5** from undeformed sample **556**. a) Before fusion. b) After fusion. The three core ages are similar in age, and have large halos that overlap younger rims.

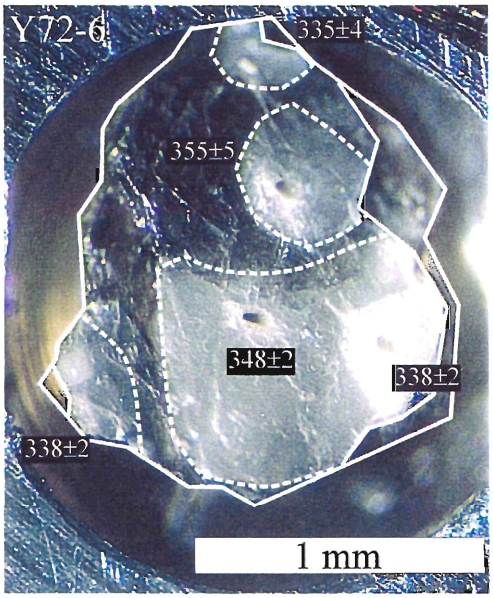

Figure 4.13. Grain **Y72-6** from undeformed sample **556**, after fusion. The variation in core ages may be related to the location of individual spots. The youngest core age (338 ± 2 Ma) may reflect a mix of core and rim gas, with the rim component dominant. The core age with the largest halo may have incorporated some younger near-rim gas, lowering its age (348 ± 2 Ma). The core age with the smallest halo does not overlap the rim and has the oldest age (355 ± 5 Ma).

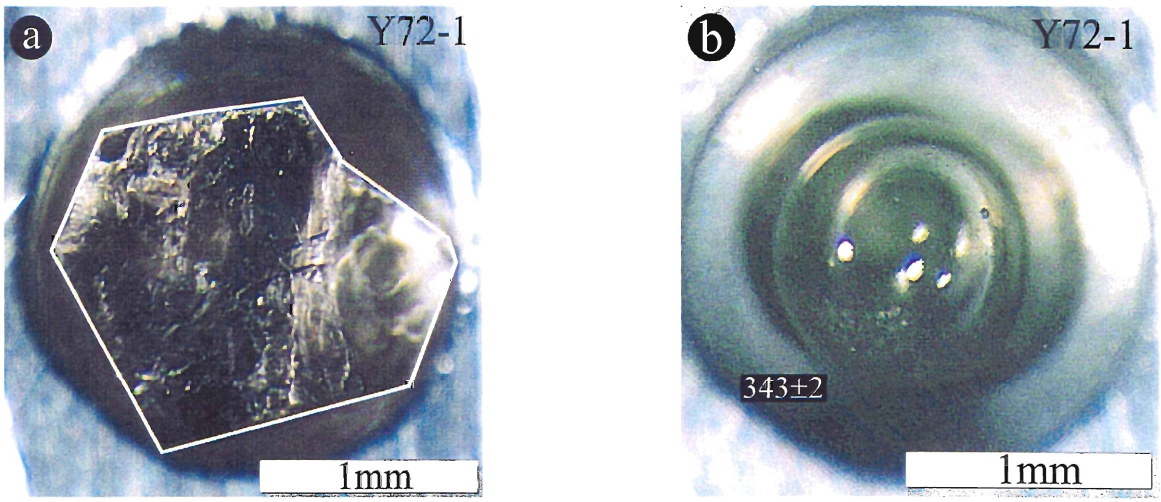

Figure 4.14.Total fusion analysis of grain **Y72-1** from undeformed sample **556**. a) Before fusion. b) After fusion. The entire grain is heated under a defocussed laser beam, producing a small glass bead. The total fusion age of this muscovite is 343 ± 2 Ma.

477: Middle Stage monzogranite.

Two grains from this sample were analyzed. As in previous samples, core ages are normally older than rim ages. The oldest core age is 359 ± 2 Ma (grain Y71-1), with the youngest 349 ± 2 Ma (Y71-2). The oldest rim age is only 335 ± 2 Ma (grain Y71-2) with the youngest being 326 ± 2 Ma (grain Y71-2). The average core age is 354 ± 1 Ma, with the average rim age 332 ± 1 Ma. Grain Y71-1 shows no significant difference between core and rim ages (Fig. 4.15b); however, the gas yields (mV Ar 39) for the two rim spots are very high, suggesting that these analyses may be core-rim mixtures. Grain Y71-2 shows the greatest difference between core and rim ages.

487: Early Stage tonalite

A single grain was analyzed from this sample (Fig. 4.16). The average core age is 349 ± 2 Ma, similar to samples 477 and 556. The youngest rim age is 337 ± 3 Ma. Although core ages are generally older than rim ages, some overlap may occur resulting from mixing of core and rim gas. Rim analyses 2-2 and 2-4 contain more gas that a normal rim analysis, possibly resulting from input from the interior of the grain.

Deformed samples

96-1: Middle Stage monzogranite

As in undeformed samples, core ages are consistently older than rim ages. The oldest core age is 370 ± 2 Ma (grain Y57-9) and the youngest core age is 350 ± 2 Ma

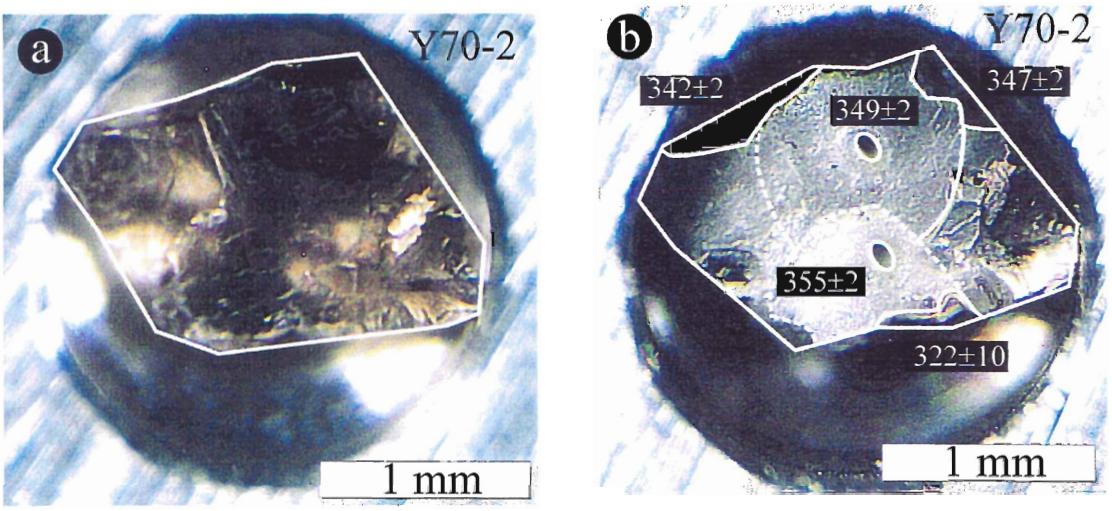

Figure 4.15. Grain **Y70-2** from undeformed sample **487**. a) Before fusion. b) After fusion. Although core ages are older than rim ages, there is some overlap. Also, some variation is evident among rim ages, suggesting a heterogeneous distribution of ^{40}Ar.

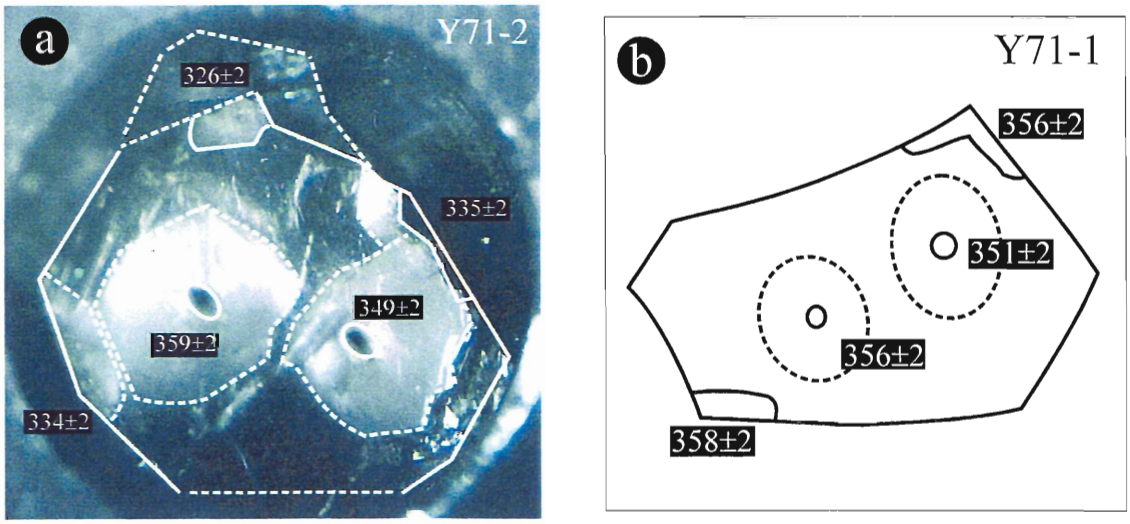

Figure 4.16. a) Grain **Y71-2** from undeformed sample **477** (after fusion) shows a clear distinction between old core ages (ca. 360-350 Ma) and younger rims (ca. 330-335 Ma). The younger core age may have incorporated some rim gas, lowering its age. b) Grain **Y71-1** (after fusion) exhibits similarly old core ages. The old rim ages are most likely a result of input from older core gas-the gas yields are too high for these spots to be true rims.

(grain Y61-6). The oldest rim age is 369 ± 10 Ma (grain Y57-9), comparable to the oldest core age. The youngest rim age is 320 ± 2 Ma (grain Y61-6). The average age of a core spot is 364 ± 5 Ma, compared with 352 ± 5 Ma for a rim spot.

No obvious relationship between the location of a core spot and its age is apparent from these data, although it is difficult to tell because of some imprecise analyses, e.g., grain Y57-6. Grain Y57-9 is notable for its very old rim ages, ca. 370 Ma (Fig. 4.20). The distribution of ages suggests the presence of very steep age gradients within this grain. Although the core analyses are imprecise, the distribution of ages within grain Y57-2 also suggests the possibility of a very steep age gradient (Fig. 4.18). In this grain, a large core of ca. 370 Ma age is rimmed by a zone of much younger age, ca. 340 Ma. Grain Y57-1 has core ages ca. 10 Ma younger than other grains from this sample (Fig. 4.17).

97-17: Middle Stage monzogranite

Two large grains were analyzed from this sample. In this sample, core ages are uniformly older (mean 355 ± 2 Ma) than rim ages (mean 329 ± 2 Ma). The oldest core age is 363 ± 2 Ma (grain Y68-1), with the youngest 349 ± 2 Ma (grain Y68-2). The oldest rim age is only 346 ± 2 Ma (grain Y68-1), and the youngest (most precise) only 318 ± 2 Ma (grain Y68-2).

Grain Y68-2 has a large uniformly old core, ca. 350 Ma, with younger rims of ca. 320 Ma, suggesting the possibility of steep age gradients (Fig. 4.21). The youngest core age (spot 2-5) is closest to the rim, but the age of this core spot is identical to the other two core spots, and does not overlap the rim as much. The pattern of ages in grain Y68-1

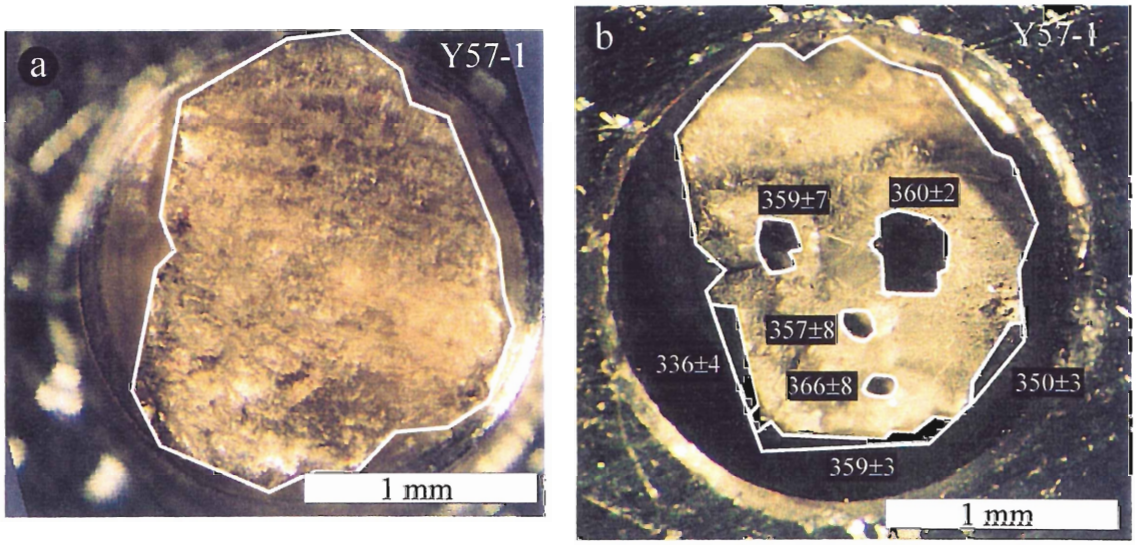

Figure 4.17. Subhedral grain **Y57-1** from deformed sample **96-1**. a) Before fusion. b) After fusion. This grain was welded to its holder at the top of the picture. Note the large halo that spreads out from this point.The four core spots have similar ages, ca. 360 Ma, although one may have an age >370 Ma. The three rim spots have different ages; one is the same age as the core (360 Ma), another is slightly younger (350 Ma), and another younger still at ca. 340 Ma.

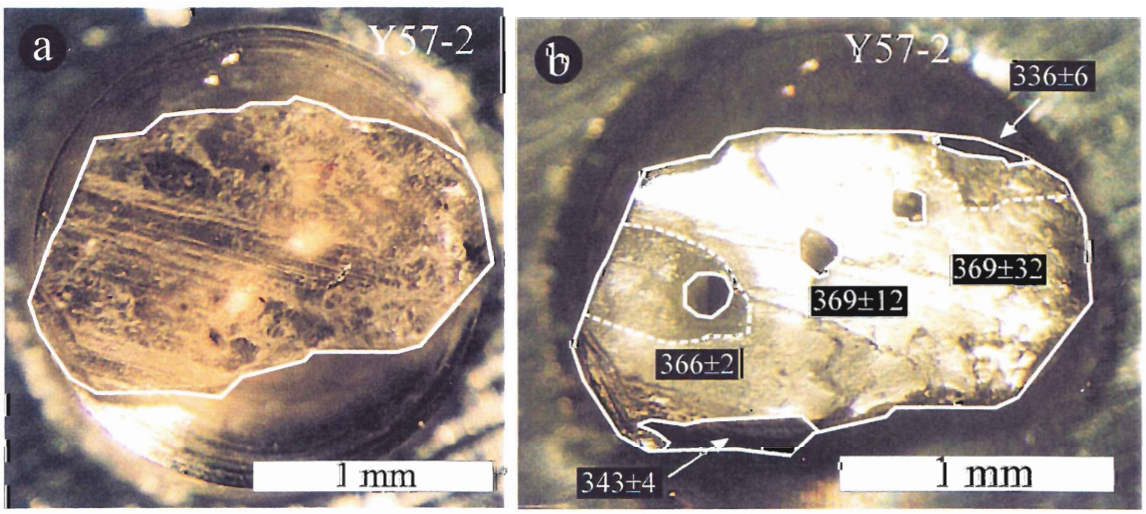

Figure 4.18. Euhedral grain **Y57-2** from deformed sample **96-1**. a) Before fusion. b) After fusion. The three core spots in this grain have similar ages of ca. 370 Ma. The youngest core spot could have incorporated some younger rim gas. The two rim spots have the same age of ca. 340 Ma.The distribution of spot ages in this grain suggests the presence of steep age gradients.

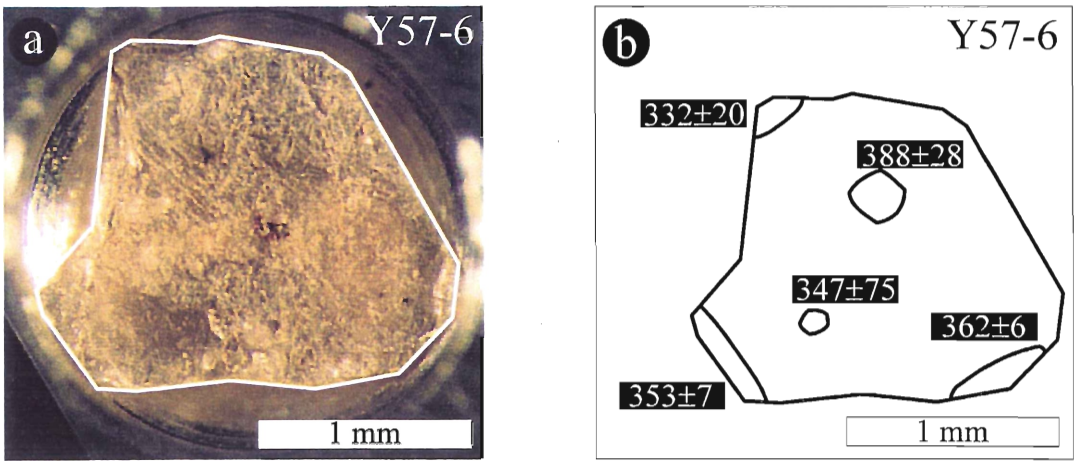

Figure 4.19. Subhedral grain **Y57-6** from deformed sample **96-1**. a) Before fusion. b) After fusion. It is difficult to identify core-rim age gradients from this sample because of the large errors associated with some analyses. However, considering other grains from this sample, the two core ages are probably old, ca.370 Ma, whereas rims are ca. 355 Ma.

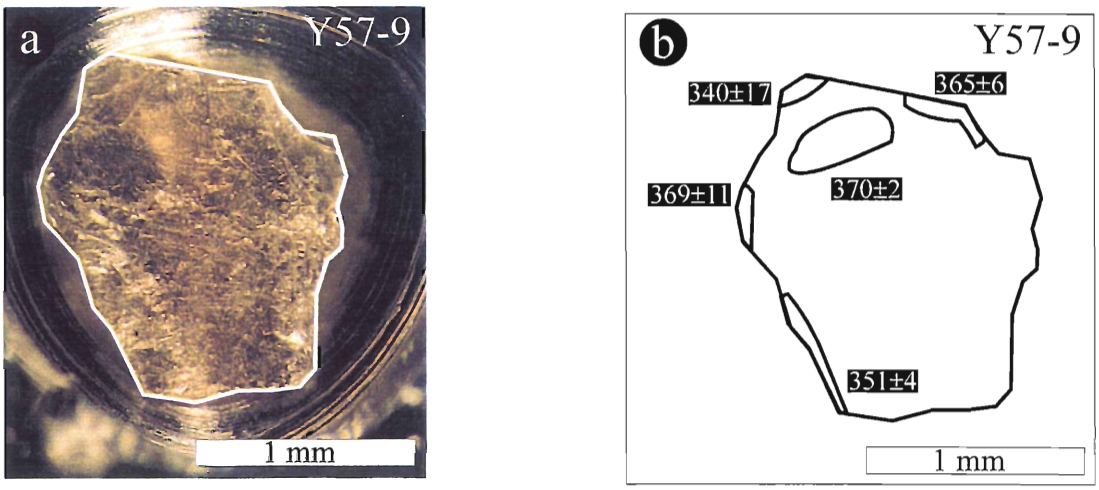

Figure 4.20. Subhedral grain **Y57-9** from deformed sample **96-1**. a) Before fusion. b) After fusion. The youngest ages occur along the rim of this grain. Some rim ages are comparable in age to the core. The proximity of old core and rim ages to the youngest rim ages, suggests the presence of very steep age gradients in this grain.

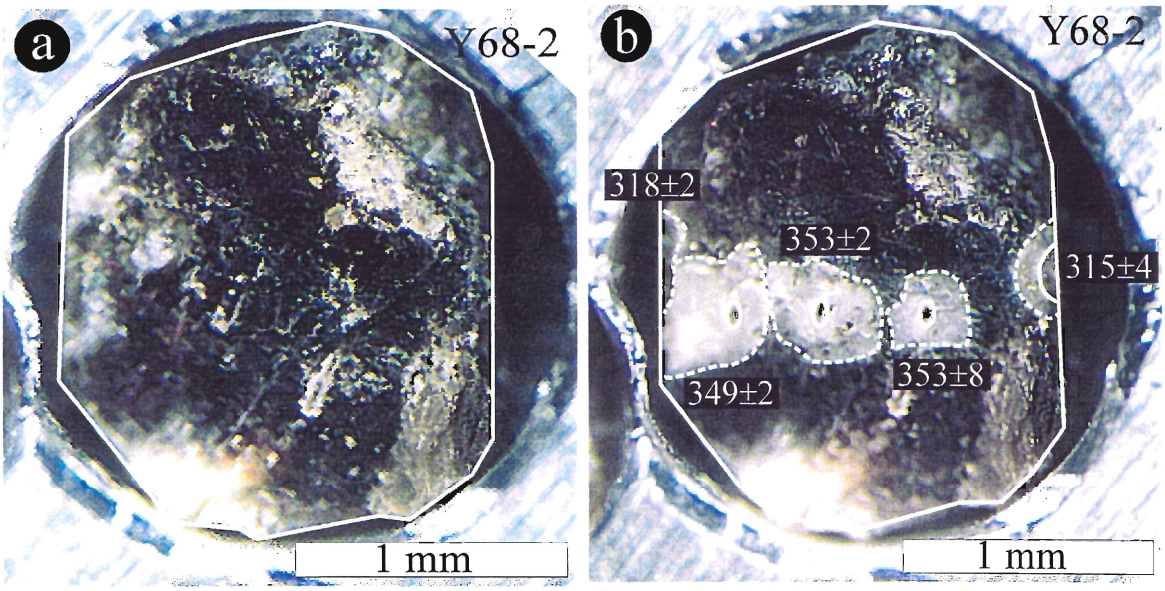

Figure 4.21. Euhedral grain **Y68-2** from deformed sample **97-17**. a) Before fusion. b) After fusion. Core ages are ca. 355 Ma. Rim ages are ca. 320 Ma. The youngest core spot (ca. 350 Ma) may reflect input from the younger rim which it overlaps. The distribution of ages suggests a broad core region with ages of ca. 355 Ma, and a narrow rim of younger ages of ca. 320 Ma.

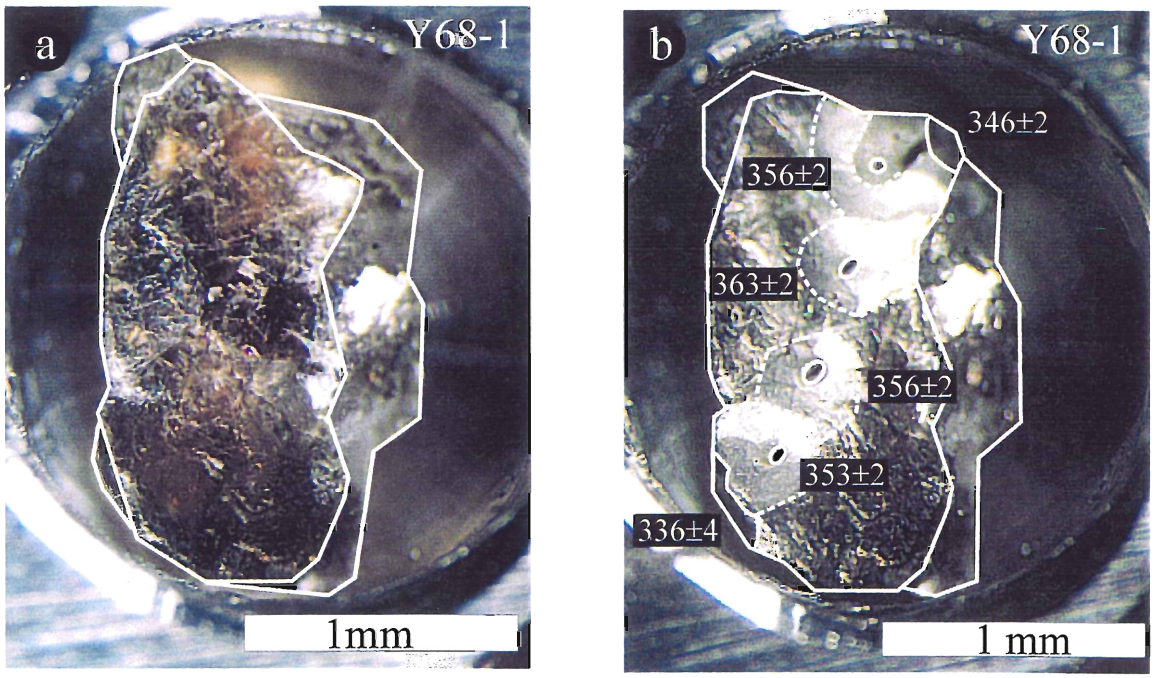

Figure 4.22. Subhedral grain **Y68-1** from deformed sample **97-17**. a) Before fusion. b) After fusion. Variable core ages may reflect different degrees of input from younger rims. Core ages are generally ca. 360-355 Ma. Rim ages vary from ca. 335-345 Ma.

is similar, with a large core of ca. 360-350 Ma surrounded by younger rims of ca. 340 Ma (Fig. 4.22). The presence of younger core ages close to the rim of this grain may suggest the presence of a more gradual age gradient in this sample, although I favour contamination from younger rims (see Section 4.4 for further discussion).

97-16a: Middle Stage monzogranite

In all but one case, core ages (mean 358 ± 1 Ma) are older than rim ages (mean 344 ± 1 Ma). The oldest core age is 370 ± 2 Ma (grain Y67-1), and the youngest is 350 ± 2 Ma (grain Y67-6). The oldest rim age is 358 ± 2 Ma (grain Y67-1), with the youngest 315 ± 2 Ma (grain Y67-2). All three grains analyzed from this sample show a different age distribution. Grain Y67-1 appears to preserve a relatively steep age gradient from an old core (ca. 370 Ma) to relatively old rims (ca. 360-355 Ma) (Fig. 4.24). In contrast, grain Y67-6 preserves no apparent age gradient, with core and rim ages identical within error at ca. 350 Ma (Fig. 4.23). Grain 67-2 has two rim spots of different age. One rim spot has an age identical to the core spot (ca. 360 Ma), whereas the other is significantly younger (ca. 320 Ma), suggesting either a non-uniform age gradient in this grain or contamination by younger rim gas.

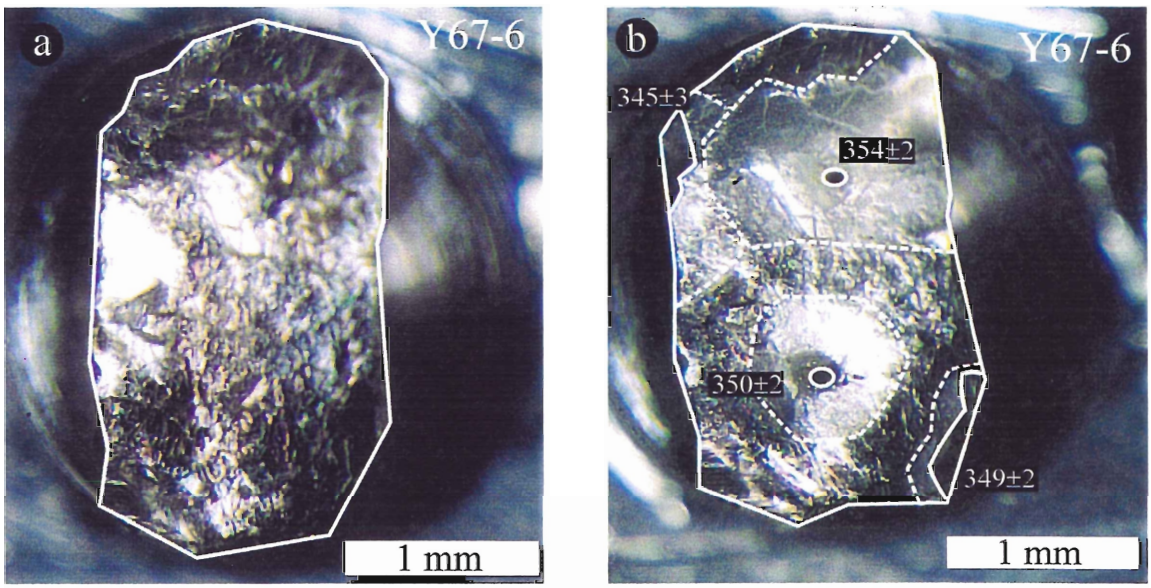

Figure 4.23. Muscovite **Y67-6** from deformed sample **97-16a**. a) Before fusion. b) After fusion. Core and rim spots are similar in age. The core spot with the largest halo overlaps the rim of the grain yet has the same age as the other core spot that does not overlap the rim, suggesting that no significant core-rim age gradient exists in this grain.

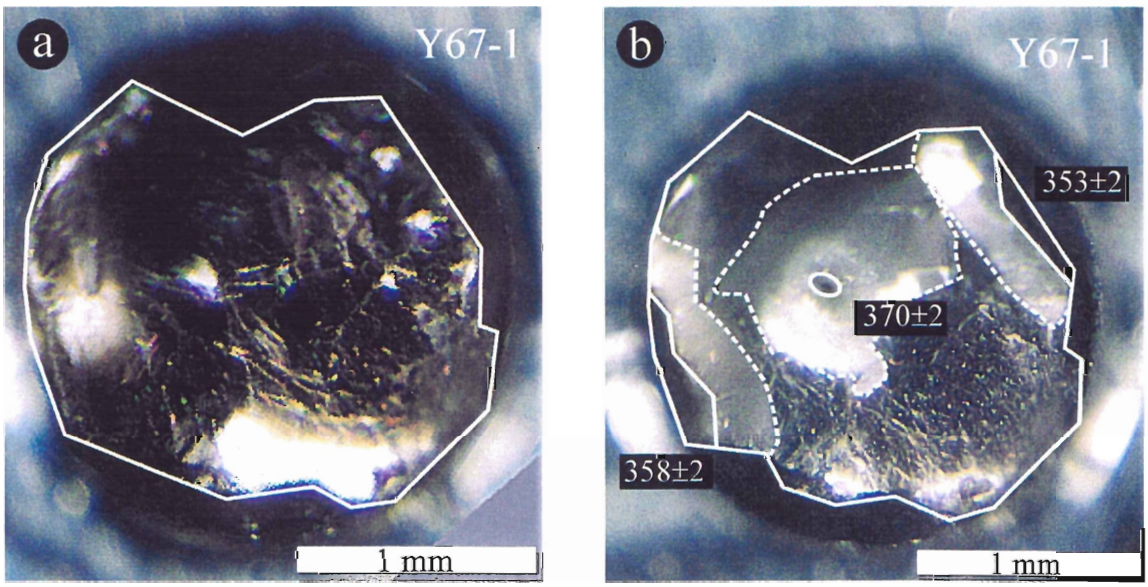

Figure 4.24. Muscovite grain **Y67-1** from deformed sample **97-16a**. a) Before fusion. b) After fusion. The core age of this grain is old and approaches the U-Pb monazite age of 373 Ma. Rims ages are older than the majority of rims from deformed samples, ca. 350-360 Ma.

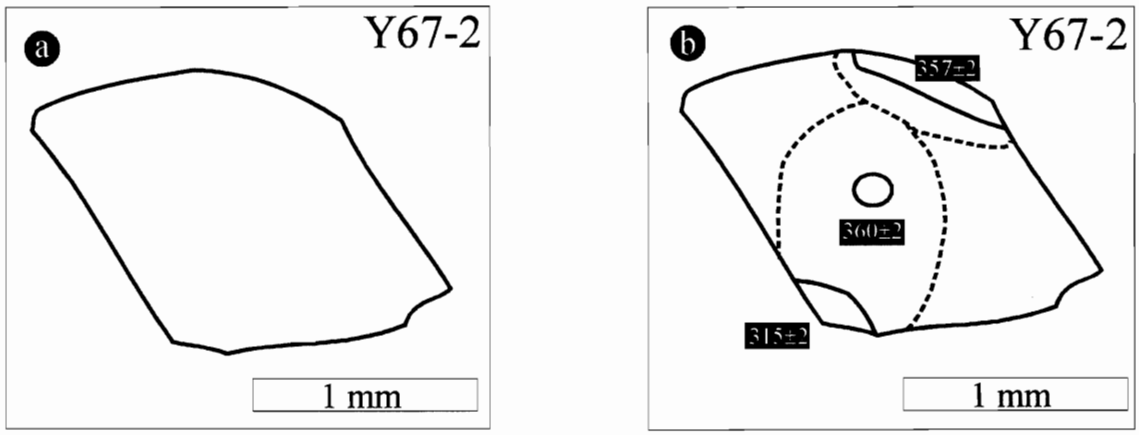

Figure 4.25. Subhedral grain **Y67-2** from deformed sample **97-16a**. a) Before fusion. b) After fusion. The grain is of similar size to Y67-1, but has a different age distribution. The core spot has an age of 360 Ma, but also a large halo that overlaps both rims. The two rim ages differ by ca. 40 Ma. The oldest rim most likely incorporated some core gas-the gas yield is significantly higher than the younger rim spot.

4.4 Discussion

4.4.1 Muscovite incremental heating and total fusion data

The muscovite age spectra and mean ages reported here are markedly different from previously published data (Fig. 1.2). The majority of previously published muscovite spectra yielded mean ages of ca. 330-315 Ma. The youngest mean age reported here is 350 Ma. Undeformed samples produced the least discordant spectra, although all spectra show a similar overall shape and record similar mean ages. The oldest mean age is 360 Ma (undeformed sample 97-14). This age suggests cooling through the muscovite retention temperature (ca. 350°-400°C) 10 to 15 Ma years following initial crystallization. Only deformed sample 97-3 gives an indication of younger ages, possibly suggesting argon loss at ca. 300 Ma. Total fusion ages from all samples are highly variable, possibly reflecting the complex age gradients preserved within PMP muscovite.

4.4.2 $^{40}Ar/^{39}Ar$ laserprobe data

Argon loss mechanisms

Several mechanisms can promote ^{40}Ar loss and produce apparent age gradients in minerals. Loss of ^{40}Ar from a mineral can occur by volume diffusion during slow cooling or superimposed thermal events (Hodges et al. 1994; Hodges and Bowring 1995). Mechanical deformation and chemical recrystallization are important mechanisms for accelerating ^{40}Ar loss from mineral grains (West and Lux 1993; Kirschner et al. 1996; Hames and Cheney 1997; Heizler et al. 1997). Age gradients can also develop from

complex combinations of these mechanisms (Hames and Cheney 1997). Consequently, independent constraints provided by sample petrology and regional geology are often required to place constraints on the conditions of ^{40}Ar loss.

Apparent age gradients in PMP muscovite

The apparent age profiles preserved in PMP muscovite can be divided into three types:

1) *No age gradients.*

   In this type of age profile (Fig. 4.26), no age difference exists between grain core and grain rim. Core and rim ages are identical within error. Core ages may be old (ca. 373 Ma) (Fig. 4.26a) or younger (ca. 350 Ma) (Fig. 4.26b).

2) *Age gradients with grain cores older than grain rims.*

   In this second type of age profile, a clear difference in age exists between grain core and grain rim. The age difference between core and rim may be small, only 2-3 Ma, as in undeformed sample 97-14 (Fig. 4.27a). Some muscovite grains preserve an age gradient from old cores (ca. 370 Ma) to young rims (ca. 340-350 Ma) (Fig. 4.27b). More commonly, muscovite preserves a gradient from a relatively younger core (ca. 350-360 Ma) to a younger rim (ca. 320-340 Ma) (Fig. 4.27c).

3) *Age gradients with variable rim ages.*

   In this third type of age profile, some rim ages are the same as core ages, whereas some are significantly younger. A few muscovite grains preserve old core and rim

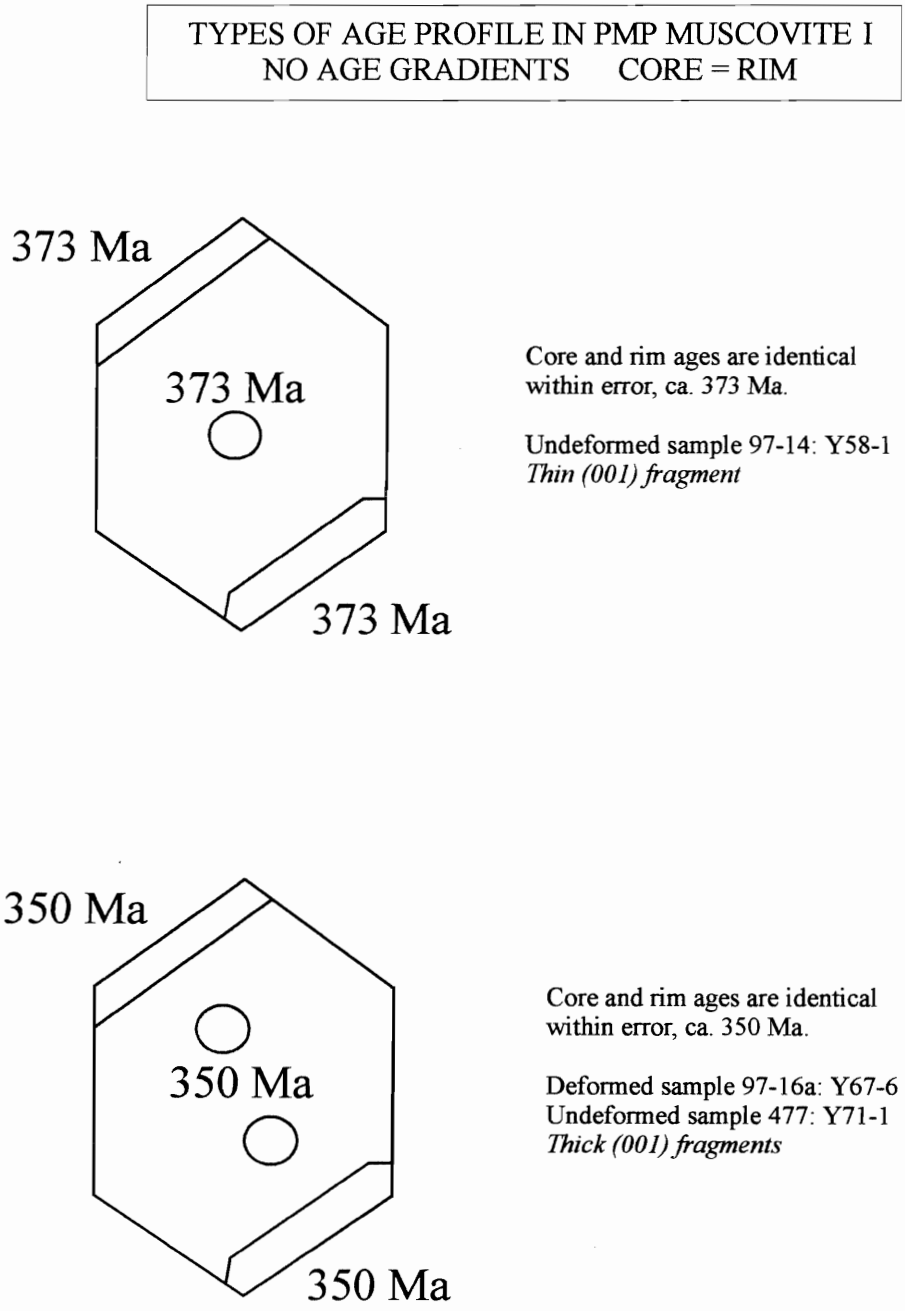

Figure 4.26. Types of age profile in PMP muscovite I. Age profiles with core spots and rim spots of similar age. Diagrams are highly simplified and only serve to illustrate the possible age-ranges preserved within grains.

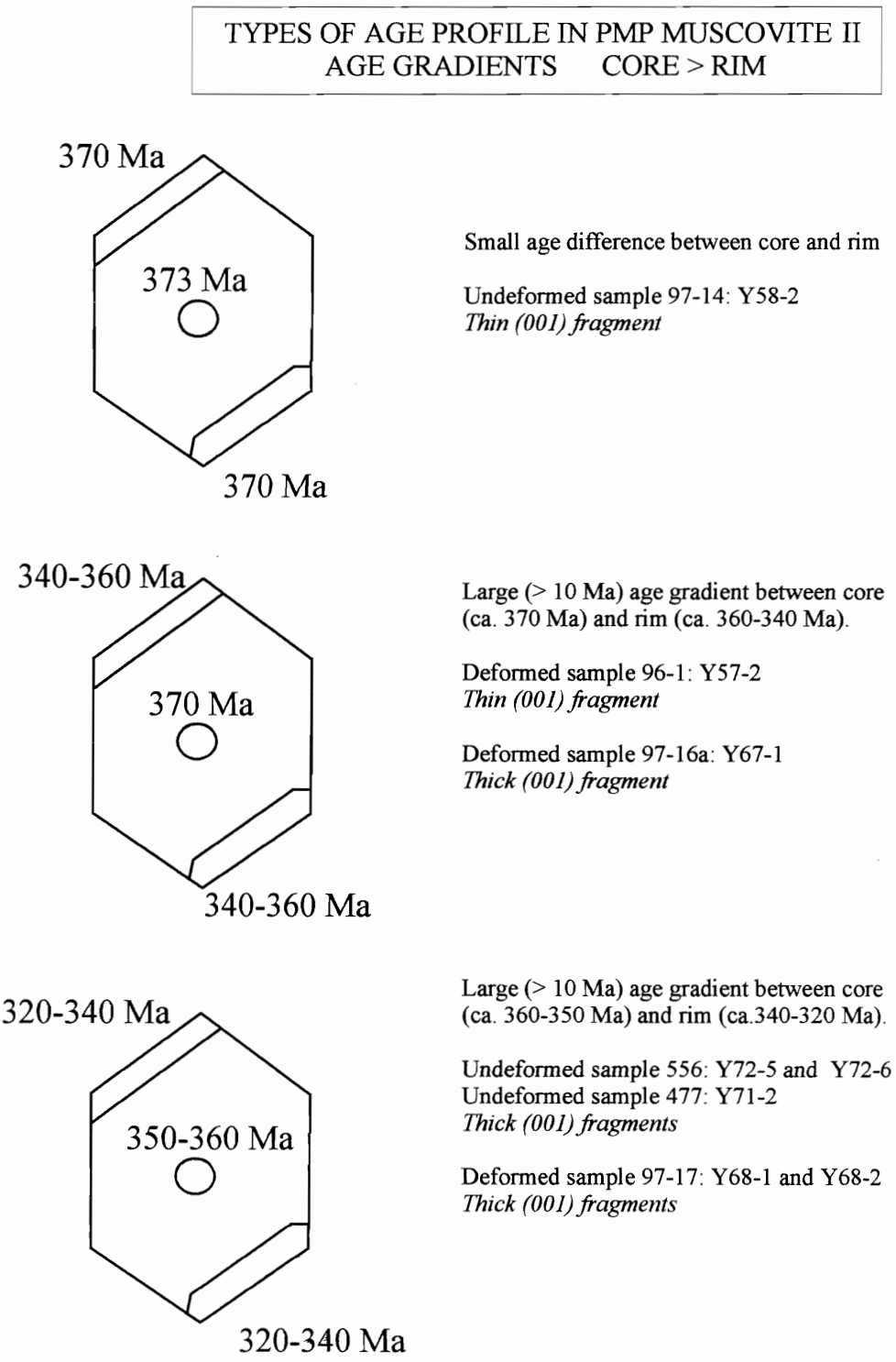

Figure 4.27. Types of age profile in PMP muscovite II. Muscovite has core ages older than rim ages.

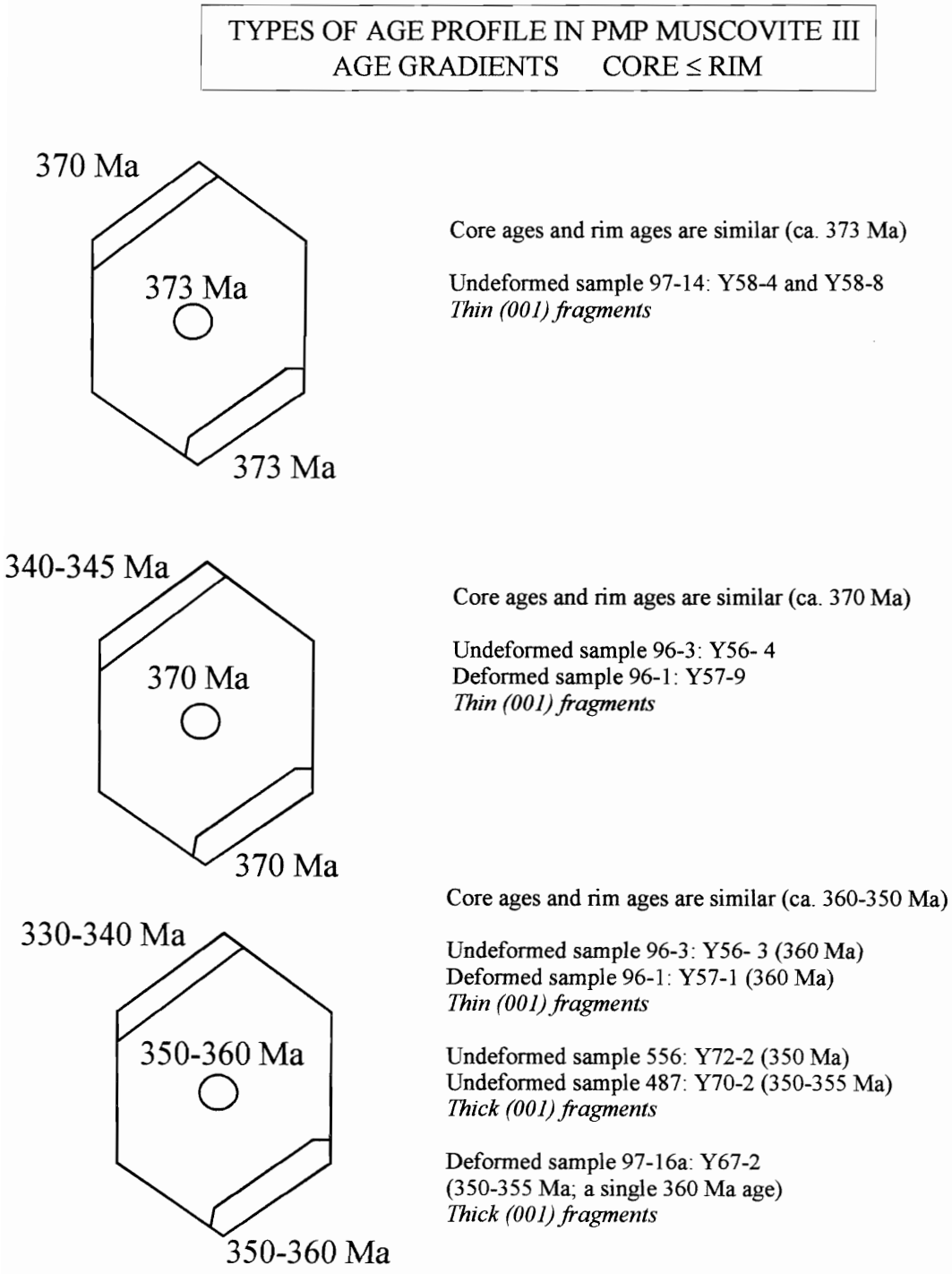

Figure 4.28. Types of age profile in PMP muscovite III. Muscovite with variable rim ages.

ages (ca. 373 or 370 Ma) (Fig. 4.28a, b). The majority of muscovite shows younger core ages (ca. 350 Ma) (Fig. 4.28c).

The three types of apparent age gradients illustrated in Figures 4.26 – 4.28 can be further subdivided into two groups: muscovite with old core ages (ca. 373-370 Ma) and muscovite with younger core ages (ca. 360-350 Ma). These two age groups can be correlated with grain thickness.

As discussed under *Analytical procedures,* muscovite dated in this study was separated from samples in one of two ways:

1) *As a by-product of U-Pb monazite separation.*

   This process involved intense sample pulverization and grain size reduction, producing thin highly transparent cleavage fragments.

2) *Following limited sample crushing in a ring-mill or with a hammer.*

   During analysis, the laser beam did not couple well with thin cleavage fragments. As a result, larger spot sized were needed to extract sufficient gas for analysis. In an effort to reduce spot size, a second set of muscovite grains were picked from samples subjected to brief sample pulverization. This process yielded thicker, less transparent grains that coupled better with the laser beam, reducing spot size.

Thin muscovite grains yield the oldest core ages. The only exception is a single 370 Ma core age from deformed sample 97-16a. All other core ages from this thick sample are 360-350 Ma. Ages of ca. 360-350 Ma are associated with thicker muscovite

grains. Although two thin samples (undeformed sample 96-1, grain Y56-3, and deformed sample 96-1, grain Y57-1) have ca. 360 Ma core ages, thicker muscovite grains generally have younger core ages, ca. 350-355 Ma. An exception is deformed sample 97-16a, which yielded a single 360 Ma core age. All other cores ages from this sample are 350-353 Ma. I discuss the influence of grain thickness on apparent age in detail below.

Evidence for rapid cooling of PMP muscovite

The apparent age gradients from undeformed sample 97-14 suggest rapid post-crystallization cooling of the PMP. Grain Y58-1 from this sample preserves no core-rim age gradient (Fig. 4.5). Core and rim ages are identical to the U-Pb monazite age of 373 Ma. Other grains dated from this sample (Y58-2, Y58-4, and Y58-8) preserve only a small age difference between cores (ca. 373 Ma) and rims (ca. 370 Ma), also suggesting rapid post-crystallization cooling. Both types of age profile suggest magmatic muscovite growth at ca. 373 Ma was followed by rapid cooling to below retention temperatures for radiogenic ^{40}Ar in muscovite (ca. 350-400 °C; Hames and Bowring 1994).

Rapid cooling of the PMP is consistent with previous studies in the Meguma Zone. Geochronological and stratigraphic constraints from the central Meguma Zone suggest that the Late Devonian granitoids and overlying sedimentary cover experienced rapid uplift during Latest Devonian time (Clarke et al. 1993; Martel et al.1993). Rapid cooling eliminates slow cooling following crystallization (as proposed by Keppie and Dallmeyer, 1995) as a cause of the apparent age gradients.

Deformation and chemical reaction as argon loss mechanisms

An alternative (to slow cooling) explanation for the variable ages of the PMP muscovite is that argon loss occurred during superimposed events. Two mechanisms likely to induce argon loss from muscovite during brief resetting events are volume diffusion (thermal) and deformation (mechanical) (Hames and Cheney 1997; Hames 1998). Recent studies (Hames and Cheney 1997) showed that argon loss via lattice diffusion during relatively brief thermal events is unlikely to induce significant argon loss from the muscovite lattice. According to Hames and Cheney (1997), nearly complete resetting of mm-diameter muscovite (95% loss) would require more than 70 million years of heating at ca. 350°C.

Evidence of low temperature deformation (ca. 350-400°C) in some PMP samples (Chapter 2), suggests that argon loss from deformed samples was related to post-crystallization deformation. Deformation may be the principal mechanism for promoting argon loss from muscovite in polymetamorphic rocks (Hames and Cheney 1997). Muscovite from deformed samples is characterized by undulose extinction and kinking of cleavage planes. In these rocks, deformation of muscovite involved recrystallization along grain edges and the generation of chemically distinct rims on earlier muscovite. Changes in the composition of muscovite porphyroclasts are also evident along cracks and cleavage planes.

If deformation and chemical reaction were the principal mechanisms of argon loss from muscovite, then we could expect apparent age gradients to mirror the steep chemical gradients observed in the majority of deformed muscovite porphyroclasts. Figure 4.29

shows a schematic illustration of this model whereby the youngest ages produced from argon loss occur only at the edges of porphyroclasts. The cores of muscovite grains remain relatively unaffected by argon loss. A steep age gradient from ca. 373-330 Ma occurs close to the rim, over a relatively short distance.

Although the resolution of the laser used in this study does not allow this model to be rigorously tested (by producing sufficient spots to accurately map the distribution of ages within grains), the data obtained are broadly consistent with this model. Several grains preserve steep core-rim age gradients similar to that illustrated in Figure 4.29, e.g., undeformed sample 97-14, grain Y57-9, and deformed sample 96-1, grain Y57-2. In some samples, younger core ages occur intermediate between the oldest core ages and younger rims ages, suggesting the presence of broader age gradients (e.g., Fig. 4.9 and 4.10). Previous laserprobe studies have suggested that the discolored halos which typically surround a spot could represent peripheral heating, thereby contributing some ^{40}Ar gas to the analysis, and lowering its age. The contribution of peripheral heating to the age of individual spots is difficult to quantify. Halos may represent only localized structural damage of the muscovite lattice with minimal argon loss. Microprobe traverses across these halos in micas (Hames and Hodges 1993) demonstate that they have been extensively devolatilized and indicate that the laser produced peripheral heating (and presumably argon loss) across a substantially larger volume than the focused spot size. This present study provides strong evidence that the laser beam can produce peripheral heating and argon loss around a substantially larger volume than the focused spot size. Grain Y72-6 from undeformed sample 556 illustrates how the age of a core spot might be

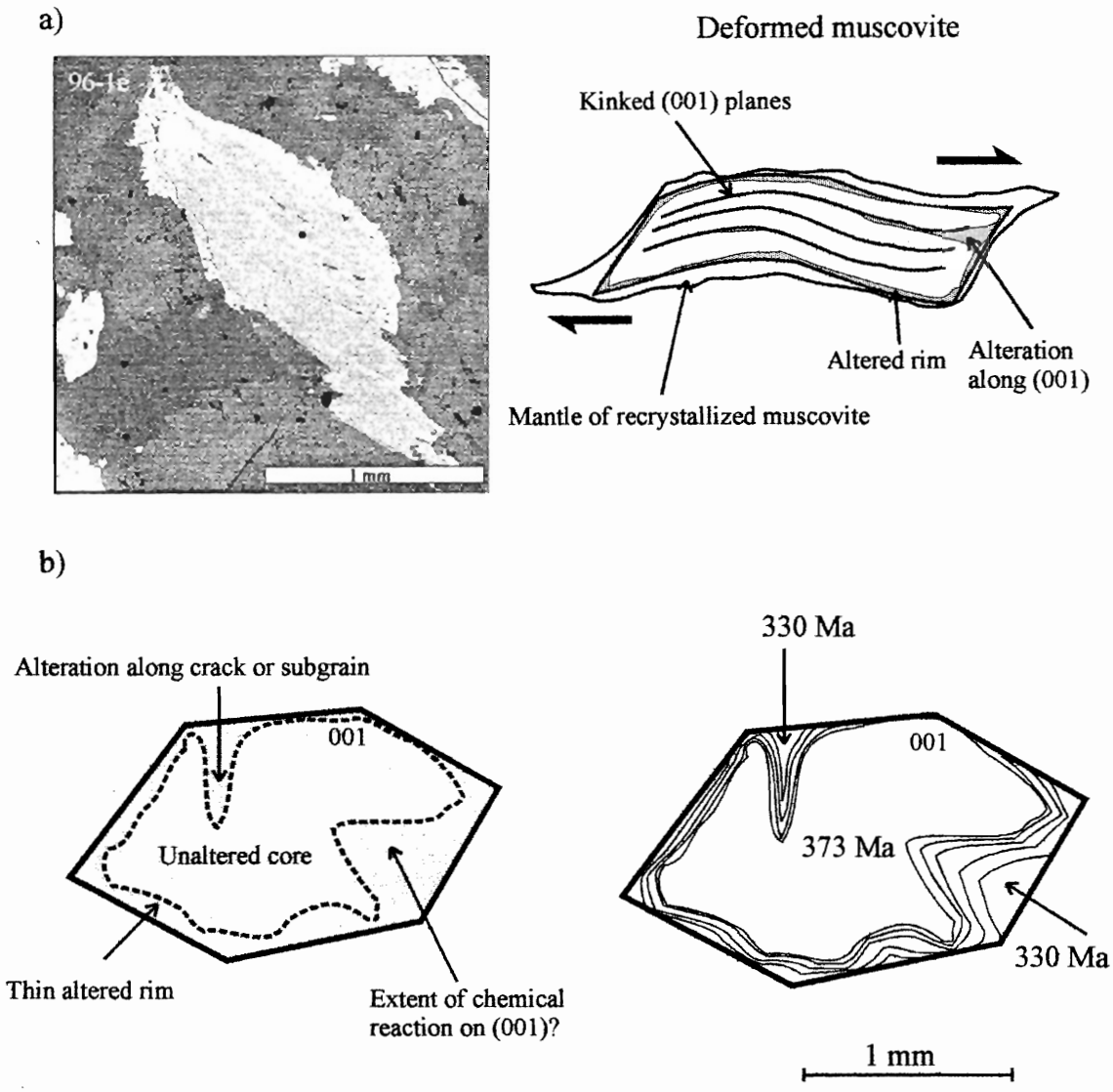

Figure 4.29. Schematic illustration of deformed muscovite crystal. a) Deformation causes kinking of (001) planes and the development of chemically distinct rims on crystals as a result of grain-edge recrystallization. b) Hypothetical age distribution in muscovite following isotopic disturbance at ca. 330 Ma; the crystal originally grew at ca. 373 Ma. If deformation and chemical reaction were the principal mechanisms of argon loss, then an age gradient similar to that shown might be expected. Argon loss is concentrated along grain edges producing a steep age gradient. The core of the crystal remains relatively unaffected and retains most of its original radiogenic argon. See text for further discussion.

influenced by the position of the spot relative to the rim, as well as the areal extent of its associated halo (Fig. 4.13).

If deformation and reaction mechanisms were the only causes of argon loss from muscovite, then we could reasonably expect the cores of muscovite porphyroclasts to have escaped significant, if any, argon loss. Most of the muscovite grains analyzed in this study, including undeformed samples, have core ages of ca. 350-360 Ma, significantly younger than the assumed crystallization age of 373 Ma. Considering the highly retentive nature of large (mm-diameter) muscovite crystals to argon loss, these younger ages are not easily explained.

Influence of grain thickness on apparent age

Tables 4.1 and 4.2 contain the relevant analytical data and Figure 4.30 presents all spot data from both undeformed and deformed samples. The following points can be noted from this diagram:

1) Thin muscovite grains from both undeformed and deformed samples yielded the oldest ages (core and rim).
2) Undeformed sample 97-14 yielded the oldest ages, overlapping the U-Pb crystallization age of 373 ± 1 Ma. The youngest age from this sample is only 365 ± 4 Ma.
3) A marked difference in age exists between thick and thin grains from undeformed samples. The average age of a core spot ranges from 348 Ma to

Table 4.1. Summary of argon data for undeformed samples

Sample	Spot #	mV 39	Age (Ma)±1σ	% Atm	37/39	36/40	39/40	Core/Rim
97-14 thin	Y58-1-3	45.6	371.1 ± 1.8	.5	0	.000019	.010007	C
97-14 thin	Y58-4-3	100.4	376 ± 1.7	1.1	0	.000039	.009806	C
97-14 thin	Y58-8-3	94.4	376.3 ± 1.8	1	0	.000036	.009805	C
97-14 thin	Y58-2-3	83.8	373.1 ± 1.8	.8	0	.000027	.009925	C
97-14 thin	Y58-1-1	12.4	371.1 ± 4.1	19.9	.01	.000675	.008057	R
97-14 thin	Y58-1-2	3.8	365.5 ± 7.7	3.7	.02	.000127	.009849	R
97-14 thin	Y58-4-1	9.6	365.1 ± 3.7	3.9	0	.000133	.009845	R
97-14 thin	Y58-4-2	6.1	376.7 ± 5.1	1.1	.01	.000037	.009791	R
97-14 thin	Y58-8-1	24.3	366.7 ± 2.5	5.8	0	.000196	.009608	R
97-14 thin	Y58-8-2	15.9	368.5 ± 3	7.7	.01	.000262	.009359	R
97-14 thin	Y58-2-1	16.1	366.1 ± 2.7	2.4	.01	.000081	.009971	R
97-14 thin	Y58-2-2	33.4	367.3 ± 2	.9	0	.000033	.010082	R
96-3 thin	Y56-3-3	6.8	355 ± 5.1	8.7	0	.000296	.009705	C
96-3 thin	Y56-3-4	22.7	359 ± 2.5	4.1	0	.00014	.010068	C
96-3 thin	Y56-3-5	13.9	358.8 ± 3	2.9	0	.000099	.010204	C
96-3 thin	Y56-4-2	40.2	367.4 ± 1.9	2.1	0	.000073	.010018	C
96-3 thin	Y56-4-3	11.6	371.2 ± 3.3	2.6	0	.000091	.00985	C
96-3 thin	Y56-4-4	14.6	363 ± 2.7	5.9	0	.000202	.009759	C
96-3 thin	Y56-3-1	4.9	363.4 ± 6.3	4.9	0	.000166	.009854	R
96-3 thin	Y56-3-2	6.9	342.7 ± 4.6	6.3	.01	.000213	.010358	R
96-3 thin	Y56-4-1	13.1	371.7 ± 3.4	10.4	0	.000351	.009058	R
96-3 thin	Y56-4-5	15.2	343.8 ± 2.9	9.1	0	.000309	.010012	R
556 thick	Y72-5-3	16.4	344.2 ± 2	2.9	0	.000099	.010407	C
556 thick	Y72-5-4	32.3	351.8 ± 1.7	.9	0	.000032	.010367	C
556 thick	Y72-5-5	24.3	349.1 ± 1.8	1.1	0	.00004	.010433	C
556 thick	Y72-2-4	7.2	352.7 ± 3.1	7.9	.01	.000269	.009604	C
556 thick	Y72-2-5	8.6	348.7 ± 2.3	1.5	0	.000054	.010402	C
556 thick	Y72-6-3	3.3	355.4 ± 5	7.2	0	.000246	.009595	C
556 thick	Y72-6-4	29.8	347.5 ± 1.9	8.7	0	.000297	.009679	C
556 thick	Y72-6-5	22.4	337.8 ± 1.8	.4	0	.000016	.010891	C
556 thick	Y72-3-1	27	348.1 ± 1.8	3.3	0	.000111	.01024	C
556 thick	Y72-4-1	67.3	347.5 ± 1.6	1.3	0	.000045	.010467	C
556 thick	Y72-5-1	9.2	325.8 ± 2.4	3.2	0	.000109	.011018	R
556 thick	Y72-5-2	18.5	327.2 ± 2	8.1	.01	.000276	.010408	R
556 thick	Y72-2-1	14.2	345.5 ± 2.2	5.3	0	.00018	.010108	R
556 thick	Y72-2-2	2.9	349.8 ± 5.2	2.1	.01	.000072	.010304	R
556 thick	Y72-2-3	8.4	344.2 ± 2.5	3.3	0	.000111	.010366	R
556 thick	Y72-6-1	5.3	335 ± 3.6	11.2	0	.000379	.009806	R
556 thick	Y72-6-2	14.4	337.6 ± 2.2	9.2	0	.000314	.009936	R
97-9 thick	Y73-4-2	178.3	354.3 ± 1.6	.3	.01	.000011	.010327	C
487 thick	Y70-2-3	37.1	348.6 ± 1.6	.9	0	.000031	.010509	C
487 thick	Y70-2-1	1.6	322.1 ± 9.5	16.1	0	.000546	.009688	R
487 thick	Y70-2-4	15.2	347.2 ± 2.1	.8	.01	.000028	.010564	R
487 thick	Y71-1-3	36.3	356.4 ± 1.7	.2	0	.000006	.010312	C
487 thick	Y71-1-4	67.2	351.4 ± 1.7	.1	.01	.000004	.010483	C
487 thick	Y71-2-4	74.9	358.7 ± 1.8	6	0	.000203	.009645	C
487 thick	Y71-2-5	33.3	349.4 ± 1.8	.4	0	.000013	.01052	C
487 thick	Y71-2-1	8.6	325.9 ± 2.7	6.6	.03	.000225	.010641	R
487 thick	Y71-2-2	9.4	334.4 ± 2.6	6.5	.01	.00022	.010362	R
487 thick	Y71-2-3	16.3	334.7 ± 2	2.2	0	.000075	.010828	R

Table 4.2. Summary of argon data for deformed samples

Sample	Spot #	mV 39	AgeE (Ma)±1σ	% Atm	37/39	36/40	39/40	Core/Rim
96-1 thin	Y57-9-6	23.3	369.9 ± 2.2	1.7	0	.000059	.009949	C
96-1 thin	Y57-1-4	4.4	366.1 ± 7.7	4.9	.01	.000167	.009735	C
96-1 thin	Y57-1-5	4.3	357 ± 7.8	8	.02	.00027	.009689	C
96-1 thin	Y57-1-6	3.8	358.9 ± 7.4	1.7	.01	.000058	.010289	C
96-1 thin	Y57-1-7	49.9	360.4 ± 2	1.3	0	.000046	.010279	C
96-1 thin	Y57-2-4	2.3	369.1 ± 11.6	3.3	.01	.000114	.009802	C
96-1 thin	Y57-2-5	172.7	365.8 ± 1.8	.8	0	.00003	.010163	C
96-1 thin	Y57-9-3	3.1	368.9 ± 10.5	7.5	.02	.000256	.009386	R
96-1 thin	Y57-6-1	6.7	361.8 ± 5.6	13.3	.01	.000451	.008993	R
96-1 thin	Y57-6-2	5.5	353.4 ± 6.7	5.6	.01	.000191	.010047	R
96-1 thin	Y57-9-4	9.9	350.9 ± 3.5	3.4	0	.000115	.010369	R
96-1 thin	Y57-9-5	5.6	364.6 ± 5.8	3.9	0	.000134	.009881	R
96-1 thin	Y57-1-1	16.6	349 ± 2.9	3.1	0	.000108	.010455	R
96-1 thin	Y57-1-2	16.2	358.6 ± 2.9	3.9	0	.000132	.01007	R
96-1 thin	Y57-1-3	9.2	335.5 ± 3.4	1.8	0	.000062	.011067	R
96-1 thin	Y57-2-1	7.9	343 ± 4.3	6.1	0	.000207	.010332	R
96-1 thin	Y57-2-2	6.2	336.5 ± 5.6	3.2	.02	.000109	.010872	R
96-1 thick	Y61-1-1	128.9	355.3 ± 1.6	1.6	0	.000056	.010316	C
96-1 thick	Y61-4-5	64.2	360.1 ± 1.7	1.4	0	.000047	.010195	C
96-1 thick	Y61-6-5	23.2	355.7 ± 1.8	.3	0	.00001	.010448	C
96-1 thick	Y61-6-6	74.9	364.3 ± 1.7	.1	0	.000004	.010194	C
96-1 thick	Y61-5-4	28.2	362.4 ± 1.7	1.1	.01	.00004	.010144	C
96-1 thick	Y61-2-4	15.3	361.5 ± 2.3	3.7	0	.000126	.009908	C
96-1 thick	Y61-6-1	11.2	337.3 ± 2.2	2.2	0	.000075	.010861	R
96-1 thick	Y61-6-3	14.3	326 ± 1.9	1.4	.02	.00005	.011361	R
96-1 thick	Y61-5-1	6.6	344.4 ± 3.2	4	0	.000137	.010417	R
96-1 thick	Y61-5-2	42.5	352.8 ± 1.7	3.2	0	.000108	.010236	R
96-1 thick	Y61-5-3	4	297.9 ± 3.1	2.6	.01	.000088	.012386	R
96-1 thick	Y61-2-2	21.9	352.6 ± 1.9	1.9	0	.000066	.010372	R
9716a thick	Y67-1-3	15.7	369.9 ± 2	2.4	0	.000084	.009765	C
9716a thick	Y67-6-3	10.2	353.9 ± 2.3	5.2	0	.000176	.009969	C
9716a thick	Y67-6-4	30.7	350.3 ± 1.7	3.3	0	.000113	.010277	C
9716a thick	Y67-2-3	114.8	359.6 ± 1.7	.1	0	.000005	.010316	C
9716a thick	Y67-1-1	13.8	357.7 ± 2.4	6.5	0	.00022	.009716	R
9716a thick	Y67-1-2	19.5	353.1 ± 1.9	.7	0	.000027	.010457	R
9716a thick	Y67-6-1	17.2	349.2 ± 2	6	0	.000204	.010026	R
9716a thick	Y67-6-2	8.6	345.1 ± 2.5	2.7	0	.000091	.010517	R
9716a thick	Y67-2-1	12	314.9 ± 2	2.3	0	.000078	.011672	R
97-17 thick	Y68-1-3	25.7	353.4 ± 2.3	10.8	0	.000368	.009354	C
97-17 thick	Y68-1-4	15.5	356.3 ± 2	3.4	0	.000116	.010043	C
97-17 thick	Y68-1-5	19.2	363.1 ± 2	3	0	.000101	.00988	C
97-17 thick	Y68-1-6	33.9	356.2 ± 1.7	1	.03	.000034	.010297	C
97-17 thick	Y68-2-2	6.9	352.6 ± 7.8	47.4	0	.001605	.005528	C
97-17 thick	Y68-2-3	16.4	352.9 ± 2.1	7.9	0	.000267	.009678	C
97-17 thick	Y68-2-5	16.6	349.4 ± 1.8	.8	0	.000028	.010537	C
97-17 thick	Y68-1-1	7.2	336.4 ± 3.8	18.9	0	.00064	.008981	R
97-17 thick	Y68-1-2	15.9	345.9 ± 2.2	10.2	.03	.000346	.009643	R
97-17 thick	Y68-2-1	10.8	315.2 ± 4.2	34.2	0	.001159	.00782	R
97-17 thick	Y68-2-4	12.7	317.9 ± 2	7.2	0	.000245	.010929	R

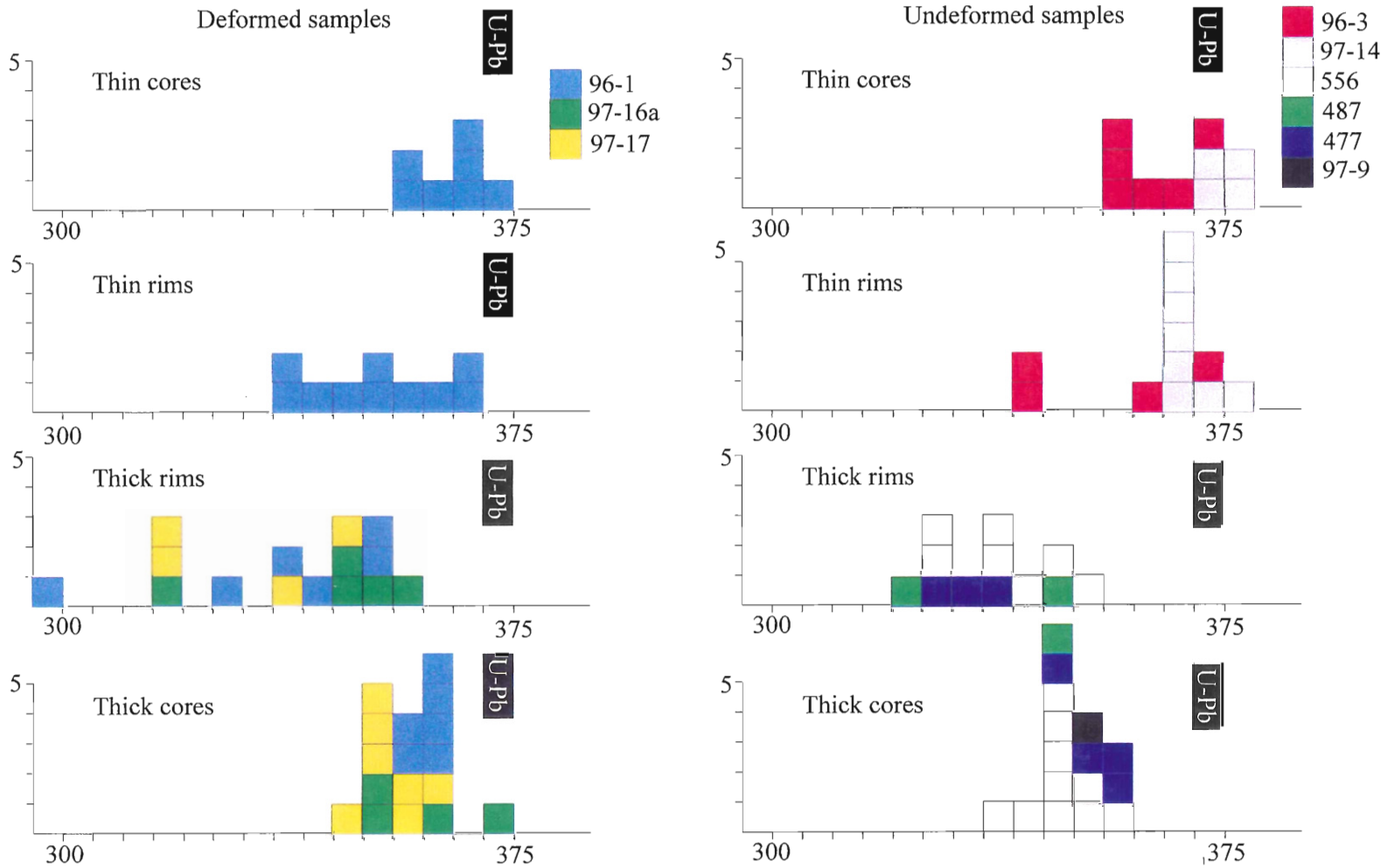

Figure 4.30. Histograms illustrating the range of laserprobe spot ages from undeformed and deformed samples. Samples can be divided into two groups based on grain thickness. In general, thin muscovite grains yielded the oldest ages. The interval is 5 Ma. See text for further discussion.

only 354 Ma for thick grains (Table 4.3), significantly younger than for thin grains.

4) The difference in age between thick and thin grains is mirrored by deformed samples, although the contrast is less pronounced. Minor overlap may reflect more severe argon loss amongst muscovite from deformed samples as a whole. Deformed sample 96-1 is the only sample to have ages from both thin and thick grains. Table 4.2 Shows that the actual ages from thin grains are consistently older than for thick grains.
5) Figure 4.30 shows significant overlap in the ages of thick muscovite from both undeformed and deformed samples.

Figure 4.31 illustrates the possible influence of grain thickness on apparent age. In deformed samples, the increased grain thickness may inhibit the laser beam from sampling the true core of the muscovite grain. Consequently, core ages are younger because the real core is not sampled, just the altered and deformed outer parts of grains. How far the laser penetrates in every muscovite analyzed is difficult to evaluate. Even if the laser beam does penetrate to the core of a grain, the resulting "core" age will still reflect a mixing of older core gas and younger rim gas, producing a false core age (Fig. 4.31). Either case could explain younger core ages from deformed samples.

What is the effect of thinner grains in producing older ages? The intense crushing and grain size reduction during monazite separation breaks muscovite crystals into

Table 4.3. Average laserprobe spot ages for cores and rims. Numbers in parentheses indicate number of analyses for individual samples.

Sample	Age	
	Core	**Rim**
Undeformed Thin		
97-14	374 ± 1 (4)	369 ± 3 (8)
96-3	362 ± 2 (6)	356 ± 2 (4)
Undeformed Thick		
556	348 ± 2 (4)	338 ± 2 (3)
487	349 ± 2 (1)	335 ± 3 (2)
477	354 ± 1 (7)	332 ± 1 (10)
Deformed Thin		
96-1	364 ± 5 (6)	352 ± 5 (6)
Deformed Thick		
96-1	360 ± 1 (6)	335 ± 1 (7)
97-17	355 ± 2 (7)	329 ± 2 (4)
97-16a	358 ± 1 (4)	344 ± 1 (5)

cleavage fragments parallel to (001). The probability of picking and dating true cores, as opposed to the outer, altered younger edges, is far higher as a result (Fig. 4.31b). Conversely, the probability of dating true rims is lower. This assumption is reasonable because the first batch of samples yielded ages identical or close to the U-Pb crystallization age. Figure 4.31 shows only two end-member possibilities (youngest rim and oldest core). Following the crushing and picking process, cleavage fragments from any part of the muscovite crystal can be dated. Undeformed sample 96-3 illustrates this possibility. Two thin grains were dated from this sample, both with very different ages. Grain Y56-4 (Fig. 4.10) has the oldest ages, and may have originated closer to the real core of a muscovite grain prior to crushing.

Additional argon loss mechanisms

The model illustrated in Figure 4.31 can account for the apparent age gradients observed from deformed samples. Younger core ages from thicker grains reflect averaging of younger rim gas and an older core component. However, muscovite from undeformed samples has experienced only minor deformation and chemical reaction, yet samples 556, 487, and 477 have markedly younger ages, comparable to muscovite from deformed samples (Fig. 4.30; Table 4.1). What mechanism of argon loss can account for these younger ages? Argon loss (via cylindrical diffusion) from near-surface regions is not considered important (Hames and Bowring 1994) and could not produce the observed gradients.

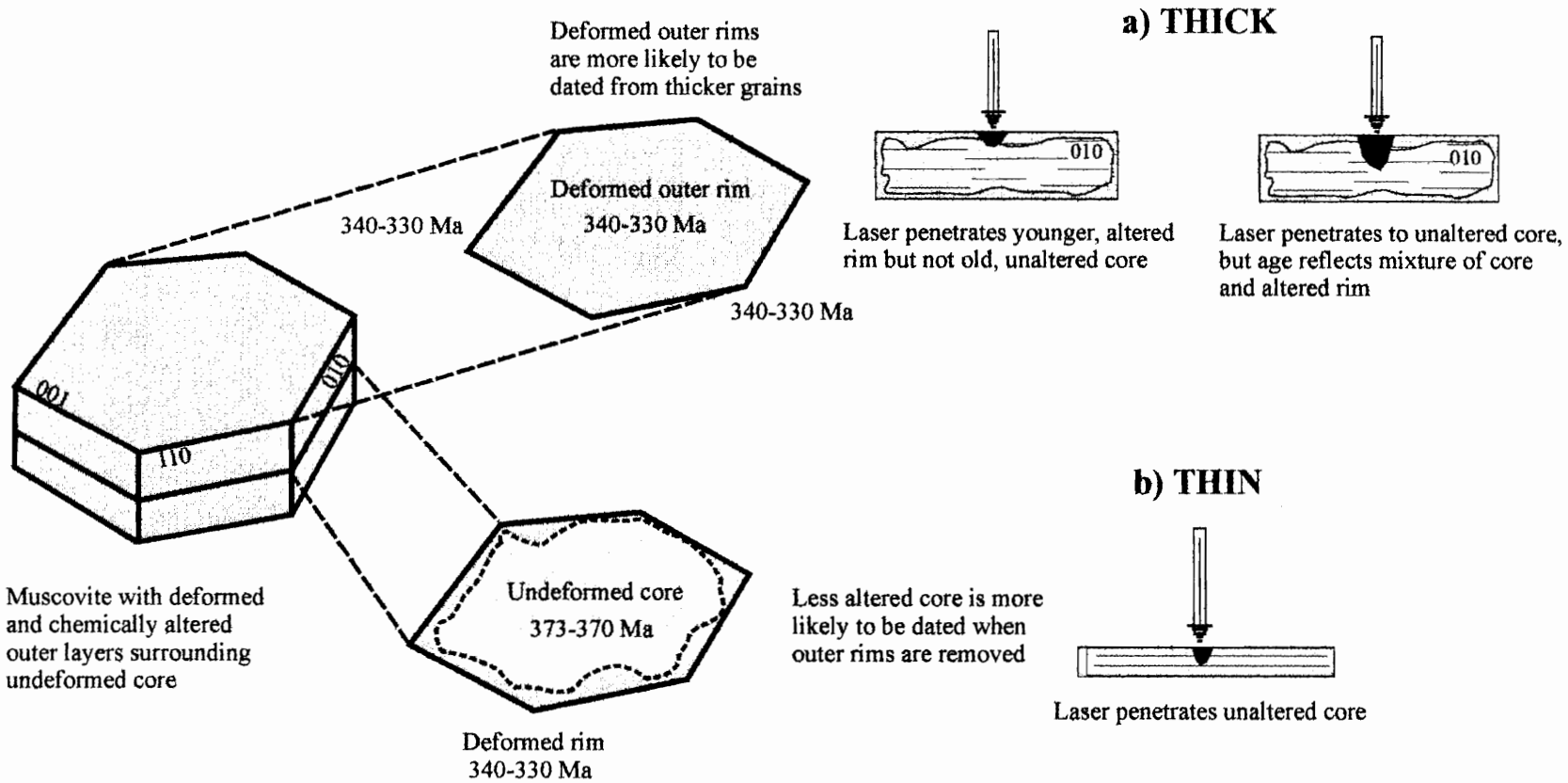

Figure 4.31. Possible effect of grain thickness on laserprobe analysis. a) In thicker grains, the laser beam may only sample the outer (001) layers, which have experienced the most severe argon loss. Alternatively, the laser could penetrate to the unaltered core which has retained most of its accumulated radiogenic argon. In this case, the apparent age produced reflects mixing of older core gas and younger rim gas. b) Older core ages from thinner grains can be explained by the fact that crushing produces (001) cleavage fragments. Consequently, the outer, more altered edges of muscovite crystals are less likely to be selected for spot analysis.

Several studies have shown that argon loss from muscovite can be accommodated by lattice defects such as kink planes, sub-grain boundaries, or cracks (Hames and Hodges 1993; Lee 1995; Hodges and Bowring 1995). This type of argon loss has been called short-circuit diffusion (Lee 1995) and may complement reaction and deformation mechanisms in promoting argon loss from deformed (and undeformed?) rocks. Evidence of lattice defects in muscovite from these samples includes undulose extinction and kinking. Consequently, argon loss from muscovite grains could be explained by a combination of reaction and deformation mechanisms and short-circuit diffusion.

Young ages from thicker muscovite from undeformed samples (556, 477, and 487) suggest the possibility that argon loss was controlled by mechanisms not readily observed in thin section. Young ages from undeformed samples imply also that argon loss is essentially unrelated to the degree of mechanical deformation to which a sample is subjected.

Timing of argon loss

Previous studies in the southwestern Meguma Zone have reported deformation-related argon loss at various times between ca. 330 and 300 Ma (Chapter 1). It is generally accepted that the southwestern Meguma Zone experienced a period of heightened tectono-thermal activity at this time, possibly associated with the Carboniferous-Permian Alleghanian Orogeny. The data from this study are consistent with this interpretation. Argon loss associated with low temperature brittle-ductile deformation at ca. 330-320 Ma could produce the apparent age gradients observed in

PMP muscovite. The absence of significantly younger ages appears to eliminate any further argon loss from PMP muscovite.

Evidence for pre-370 Ma deformation

The presence of large undeformed muscovite in some deformed samples, apparently overgrowing a matrix of polygonal quartz (Fig. 2.7e, f), provides evidence of an early phase of deformation that affected the PMP. Muscovite separated from deformed samples 96-1, 97-16a, and 97-17 is chemically and texturally distinct from magmatic muscovite from undeformed samples (Chapter 2). The oldest core ages from these large muscovites are generally ca. 370 Ma (cf. ages > 370 Ma from undeformed samples), consistent with a post-magmatic origin.

If undeformed muscovite from sample 96-1 is also ca. 370 Ma, then the deformation that it overgrows occurred between 373 Ma and 370 Ma. It is likely that the PMP experienced minor subsolidus deformation at temperatures sufficient to induce polygonization of quartz and some ductile deformation of micas.

Comparisons with age spectra and total fusion data

The laserprobe results provide a wealth of information not available from conventional incremental heating analysis and, to a lesser extent, total fusion analysis. Laserprobe spot fusion of the same muscovite suggests a much different thermal evolution for the PMP. Significantly, the incremental heating data did not reveal the apparent age gradients preserved in these samples. The age spectrum from deformed

sample 97-3 does reveal a subtle indication of the extent of argon heterogeneity within muscovite. More importantly, the incremental heating data give no indication of ca. 373 ages for undeformed sample 97-14. The variability in total fusion ages (within and between samples) clearly reflects the heterogeneous distribution of argon within muscovite from these samples. Although the total fusion data did yield older ages than conventional incremental heating analysis, only a single age older than ca. 370 and no ages younger than ca. 343 were obtained.

4.5 Results: K-feldspar incremental heating spectra

Four samples were selected for incremental heating analysis: three samples of Late Stage pegmatite (96-3, 97-4, and 98-4) and one sample of undeformed Early Stage tonalite (484) from MacLeods Cove (Fig. 2.3). X-ray diffraction analysis of each sample was undertaken prior to irradiation, to confirm the presence of K-feldspar. Results showed that sample 484 contained no K-feldspar, but rather a mixture of plagioclase and white mica, probably sericite. Thin section observations revealed that this sample contains abundant sericitized plagioclase. X-ray diffraction confirmed that feldspar picked from samples 96-3, 97-4, and 98-4 was microcline. The two fractions (B1 and B2) are duplicates of sample 96-3 located several cm apart on the same large K-feldspar crystal.

The spectrum for sample 97-4 is discordant, with ages increasing gradually from 212 ± 2 Ma for the first step, to 276 ± 2 Ma for the final step (Fig. 4.32a). Fractions B1

a) 97-4 microcline

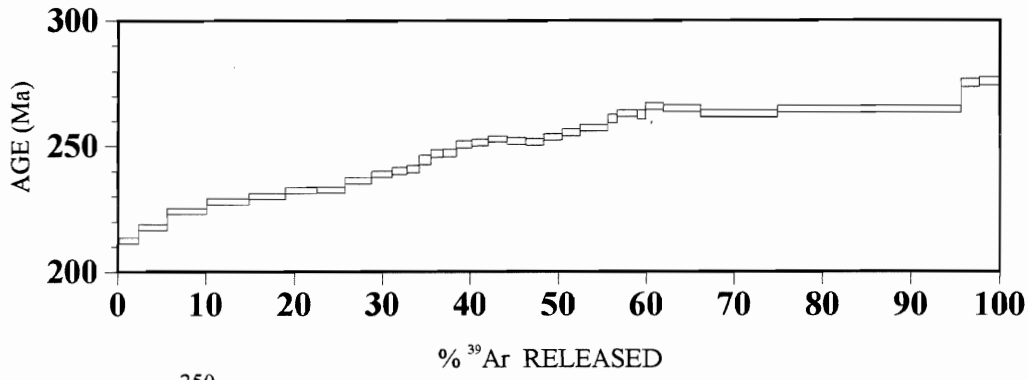

b) 98-4 microcline

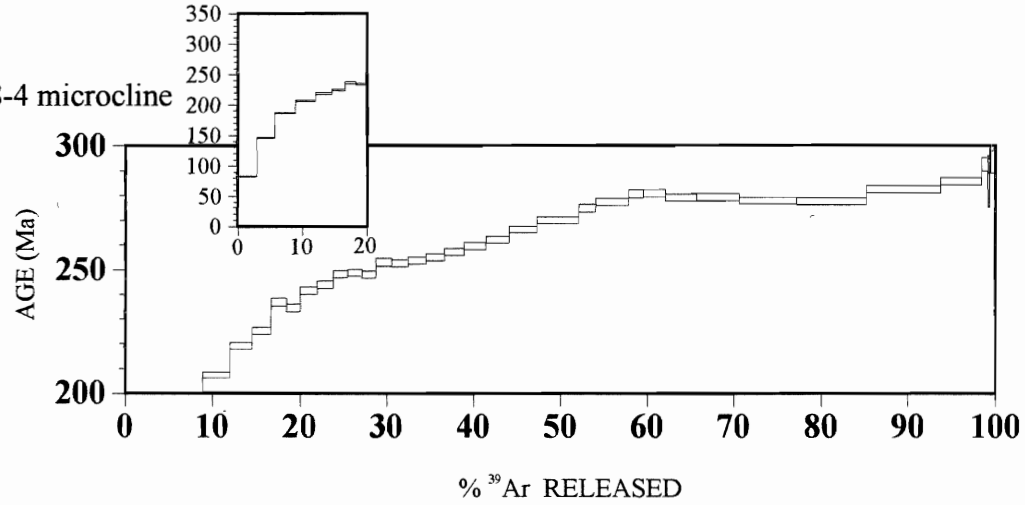

c) 484 sericite

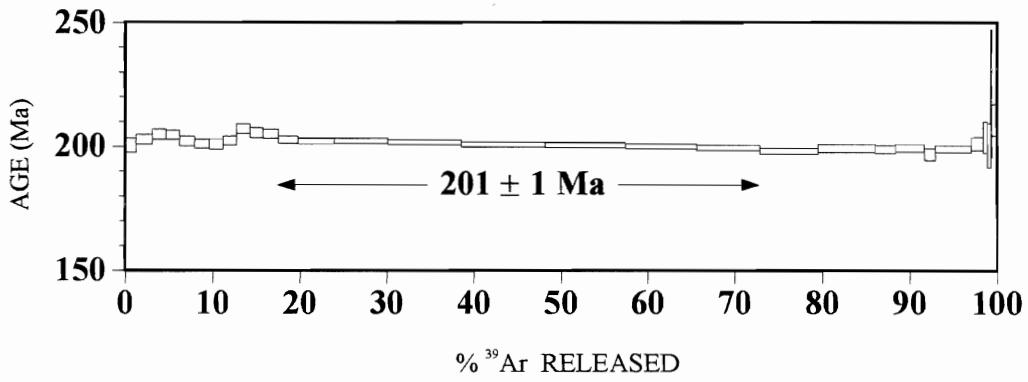

Figure 4.32. Incremental heating spectra for Late Stage pegmatite samples **97-4**, **98-4**, and Early Stage tonalite sample **484**. a) Spectrum is similar in age and overall shape to sample **96-3**. b) Sample **98-4** has a comparable high-temperature history to other microcline samples, but is distinguished by anomalously young ages for the lowest increments (inset). c) Spectrum for sample **484**: probably dominated by sericite from the cores of altered plagioclase grains.

and B2 from sample 96-3 yielded identical spectra with a similar overall shape to the spectrum for sample 97-4 (Fig. 4.32a,b). Initial ages of ca. 230 ± 1 Ma increase gradually to ca. 285 Ma for the final steps. Remarkably young ages for initial low-temperature steps characterizes sample 98-4, although the overall shape of this spectrum is similar to samples 97-4 and 96-3 (Fig. 4.32b). Initial ages of ca. 83 ± 1 Ma increase rapidly to ages of ca. 250 Ma over a period of about 10 steps, and then more gradually to ca. 280 ± 2 Ma over the remaining increments (Fig. 4.32b). The spectrum from sample 484 is remarkably flat over its entire length (Fig. 4.32c). Eight successive increments (850°C-1025°C) record a mean age of ca. 200 Ma. The Ar release pattern for this sample is more characteristic of a white mica such as sericite.

4.6 Discussion

The K-feldspar data can be interpreted in terms of a multi-domain diffusion model (Lovera et al. 1989; Lovera et al. 1991). According to this model, argon loss in K-feldspars is controlled by microstructural domains of variable size, rather than by whole-grain-scale diffusion. Thus, K-feldspar crystals consist of distinct diffusion domains of variable size, retention temperature, and age (Fig. 4.33b). With retention temperatures estimated at ca. 350°C-400°C, the largest domains are the most retentive of accumulated argon (Lovera et al. 1991). The smallest domains have estimated retention temperatures of ca. 150°C.

During cooling (or resetting), different parts of a K-feldspar crystal will close (or open) to argon loss at different times, depending on domain size. The largest (most

a) 96-3/B1 microcline

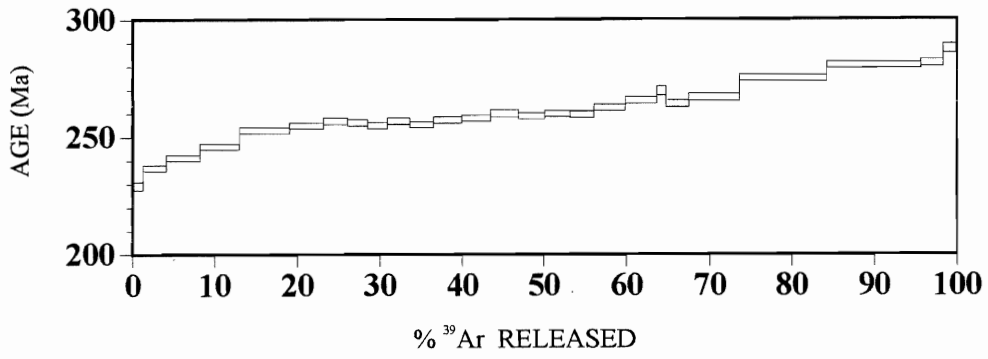

b) 96-3/B2 microcline

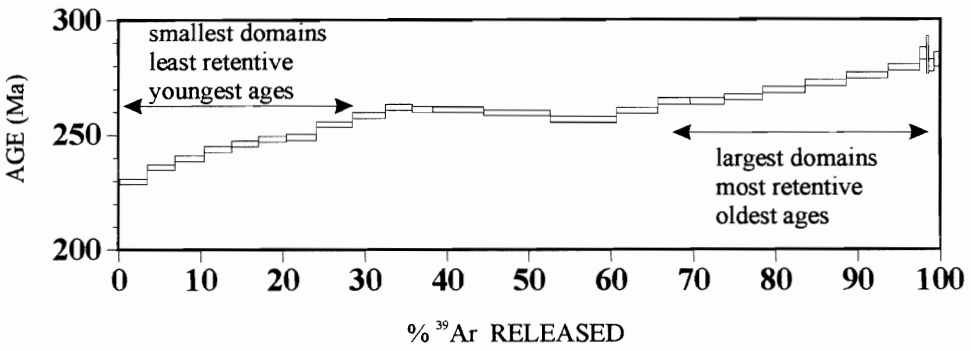

c) 96-3/B1and B2 microcline

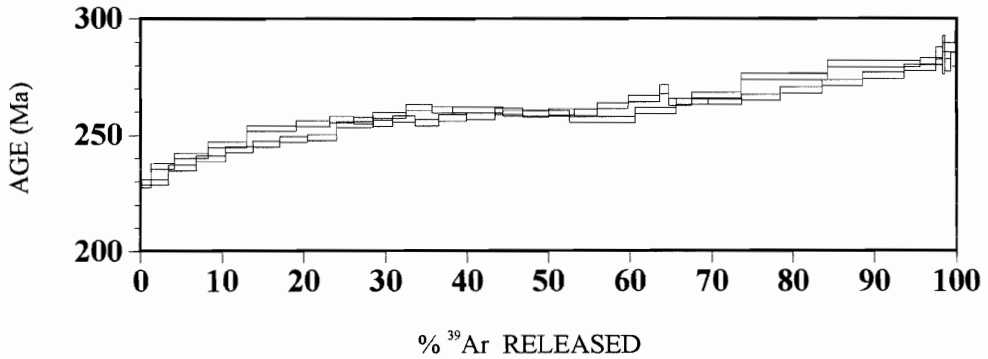

Figure 4.33. Incremental heating spectra for microcline from Late stage pegmatite sample **96-3**. a) Spectrum for fraction **B1**. b) Detail of spectrum for fraction **B2** showing possible sub-spectra corresponding to large and small domains. The largest domains are the most retentive of ^{40}Ar and are outgassed at the highest temperatures yielding the oldest ages. c) Fractions **B1** and **B2** produced identical age spectra.

retentive) domains close (or open) first and preserve the oldest ages. It follows that a K-feldspar spectrum is a composite spectrum in which increasing ages reflect argon loss from different domains. Low temperature increments reflect argon loss from the smallest microstructural domains, whereas the higher temperature parts of a spectrum record argon retention ages following argon loss from the most retentive domains.

The feldspar incremental heating data presented in this study provide additional information on the thermal history of the PMP. The oldest ages (ca. 280 Ma) from Late Stage pegmatite samples 96-3, 97-4, and 98-4 are significantly younger than the youngest age recorded from muscovite (a single 300 Ma laserprobe age). This difference in age suggests that the maximum retention temperature for argon loss in these K-feldspars is less than that of muscovite (< ca. 350-400°C). These maximum ages could record slow cooling following resetting at ca. 330-315 Ma (or 300 Ma), or a distinct resetting event at ca. 280 Ma. Evidence of possible titanite growth at ca. 260 Ma suggests a separate reheating event at ca. 280-260 Ma.

Younger ages recorded in the initial increments suggest another distinct reheating event at ca. 230-210 Ma, possibly related to the early stages of rifting associated with continental breakup. An age of ca. 200 Ma for sericite from Early Stage tonalite sample 484, is essentially identical to recent $^{40}Ar/^{39}Ar$ biotite ages (203 ± 1 Ma) from the Shelburne dyke (Dunn et al. 1998). An age of 200 Ma correlates well with the timing of rifting that eventually produced the North Atlantic Ocean during Late Triassic / Early Jurassic time.

4.7 Summary

The muscovite and K-feldspar data presented here provide a detailed record of the post-crystallization history of the PMP. In Chapter 5, I discuss the complete U-Pb and $^{40}Ar/^{39}Ar$ dataset in terms of an integrated model for the thermal history of the PMP in particular, and also discuss the implications of these data for Meguma Zone geochronology in general.

CHAPTER 5

SUMMARY, IMPLICATIONS, AND RECOMMENDATIONS

5.1 Introduction

The age data presented in this thesis represent the entire thermal evolution of the PMP over a period of approximately 350 My, from crystallization at 373 Ma to possible recent argon loss. This extensive coverage derives from using several geochronological techniques on a variety of minerals with different retention temperatures. These new data clarify the previously complex thermal history of the PMP in particular, and advance our understanding of Meguma Zone geochronology in general.

5.2 Summary of age data and interpretation

To constrain the thermal history of the PMP, I utilized several techniques: conventional U-Pb geochronology of monazite and titanite; conventional $^{40}Ar/^{39}Ar$ incremental heating (spectral) analysis of muscovite and K-feldspar; $^{40}Ar/^{39}Ar$ laserprobe total fusion of single muscovite grains; and $^{40}Ar/^{39}Ar$ laserprobe spot fusion of single muscovite grains. To establish the relationship between deformation and argon loss, I selected a variety of undeformed and deformed samples for study.

U-Pb dating of monazite constrains the crystallization age of main intrusive units to 373 Ma. Although no U-Pb age was obtained for Late Stage lithologies, $^{40}Ar/^{39}Ar$ laserprobe muscovite ages (ca. 373 Ma) from a Late Stage pegmatite confirm that all three intrusive phases crystallized ca. 373 Ma.

Magmatic muscovite ages of ca. 373 Ma from undeformed samples are the same as the U-Pb monazite crystallization age of 373 Ma suggesting that, following initial crystallization, the PMP cooled very rapidly to temperatures below that necessary for the retention of argon in muscovite (ca. 350°C-400°C). The majority of laserprobe ages (particularly those from deformed samples) fall into the range ca. 360 Ma to 345 Ma, with core ages generally older than rim ages. The apparent age gradients in muscovite reflect partial loss of accumulated argon from muscovite. Non-magmatic muscovite from deformed samples typically has recrystallized grain margins and shows core-rim element variation suggesting that argon loss from these samples occurred by a combination of reaction and deformation mechanisms. Ages of ca. 360-345 Ma from some undeformed samples suggest that other mechanisms may have contributed to argon loss from these samples.

Several studies from southwest Nova Scotia have identified an argon loss event between ca. 330 Ma and 300 Ma:

1) Reynolds et al. (1987) and Muecke et al. (1988) associated discordant mica spectra with resetting at ca. 320-300 Ma. These authors suggested that migration of hydrothermal fluids along Alleghanian shear zones caused argon loss at this time.
2) Kontak et al. (1995) reported variably reset muscovite ages of ca. 330-300 Ma from a sample of East Kemptville leucogranite. Granitoid rocks in this area are cut by narrow brittle-ductile faults and shear zones that are thought to have acted as conduits for heated fluids which facilitated argon loss at this time.

3) Keppie and Dallmeyer (1995) presented evidence of a pervasive 300 Ma overprint recorded in whole-rock slate-phyllite samples from the Goldenville formation at East Kemptville. Also, muscovite ages of ca. 330-300 Ma from plutons in southwestern Nova Scotia reflect variably reset argon systems associated with migration of heated (magmatic?) fluids along dextral shear zones that cut plutons in this region. These authors related dextral shearing to NW-SE compression associated with the Carboniferous-Permian Alleghanian Orogeny.
4) Culshaw and Reynolds (1997) obtained ca. 320 Ma ages from neoblastic muscovite from two Alleghanian shear zones in southwest Nova Scotia. The shear zones lie within a wide zone (ca. 30 km) of D2 (Alleghanian) deformation that overprinted D1 (Acadian) fabrics and reactivated F1 (Acadian) fold structures between the shear zones (Culshaw and Liesa 1997). Alleghanian deformation was accompanied by greenschist facies metamorphism that variably overprinted earlier Acadian metamorphic assemblages (Culshaw and Reynolds 1997).

The laserprobe data presented here are consistent with an argon loss event at ca. 330-300 Ma. However, it is not possible to distinguish between two separate argon loss events at ca. 330-315 Ma and 300 Ma, a single protracted event over a period of ca. 30 My, or a single argon loss event at ca. 300 Ma. Alleghanian ages in southwestern Nova Scotia are associated with minor plutonism, widespread dextral shearing, and reactivation of Acadian fold structures. Alleghanian deformation in the Meguma Zone reflects reactivation of Acadian structures "when Gondwana collided with Laurentia (D2

deformation) along a suture distant from present-day Nova Scotia" (Culshaw and Liesa 1997, p.845).

The muscovite incremental heating spectra generally yielded ages of ca. 360-350 Ma and did not show the apparent age gradients revealed by laserprobe spot fusion analysis. Total fusion ages from all samples are highly variable, possibly reflecting the complex age gradients preserved within PMP muscovite.

K-feldspar data provide information on the post-300 Ma thermal history of the PMP. The oldest ages recorded in the highest-temperature increments of K-feldspar spectra may suggest a distinct reheating event at ca. 280 Ma; however, ages of ca. 280 Ma could record cooling following thermal resetting at ca. 300 Ma. Younger ages recorded in low-temperature increments suggest reheating at ca. 230-210 Ma. K-Ar and $^{40}Ar/^{39}Ar$ ages of ca. 230-220 Ma from several mafic dykes in New England and Atlantic Canada (including southwestern Nova Scotia) suggest that mafic magmatism (related to the initial rifting of the North Atlantic) was widespread at this time (Pe-Piper and Reynolds, in prep. and references therein). Elevated temperatures during intrusion of these Late Triassic dykes could have reset some K-feldspar ages.

Fission track data combined with vitrinite reflectance data from the Maritimes Basin of eastern Canada (Ryan and Zentilli 1993) suggest that, following initial rapid cooling and exposure of the granitoids, the Meguma Zone was subsequently buried by up to 4 km of Carboniferous and Permian strata (ca. 348 Ma, the age of the overlying Windsor group). Organic maturation data, and apatite fission track modelling (Ryan and Zentilli 1993), indicate that exhumation took place from 280 Ma to 200 Ma. These data

suggest that a combination of Carboniferous-Permian burial and fluid migration along localized brittle-ductile fracture zones may have contributed to the resetting of some K-feldspar samples.

An age of 200 Ma from sericitized feldspar is similar to recent $^{40}Ar/^{39}Ar$ biotite ages (203 ± 1 Ma) from the Shelburne dyke, a prominent Late Triassic mafic dyke which extends along the southwestern coast of Nova Scotia (outcropping north of the PMP) for a distance of 140 km (Dunn et al. 1998). The incremental heating spectrum from pegmatite sample 98-4 suggests that argon loss from the least retentive K-feldspar domains occurred fairly recently, and probably at ambient temperatures. An alternative explanation suggests a link between initial ages of ca. 83 Ma for this sample and widespread Cretaceous reheating of basin strata from offshore Nova Scotia. Li et al. (1995) estimated that this reheating event occurred at paleotemperatures of about 80-110°C at some time during the interval 110-40 Ma. Figure 5.1 summarizes the thermal history of the PMP.

5.3 Implications for Meguma Zone geochronology

The results of this study have important implications for the interpretation of Meguma Zone geochronology.

1) Rapid cooling following initial intrusion was likely a terrane-wide event that affected both Central and Peripheral plutons. Variable mica ages between central and eastern parts of the Meguma Zone and the southwestern part of the Meguma Zone do not reflect diachronistic cooling.

Figure 5.1. Timescale of events in the evolution of the Port Mouton Pluton, southwest Meguma Zone.

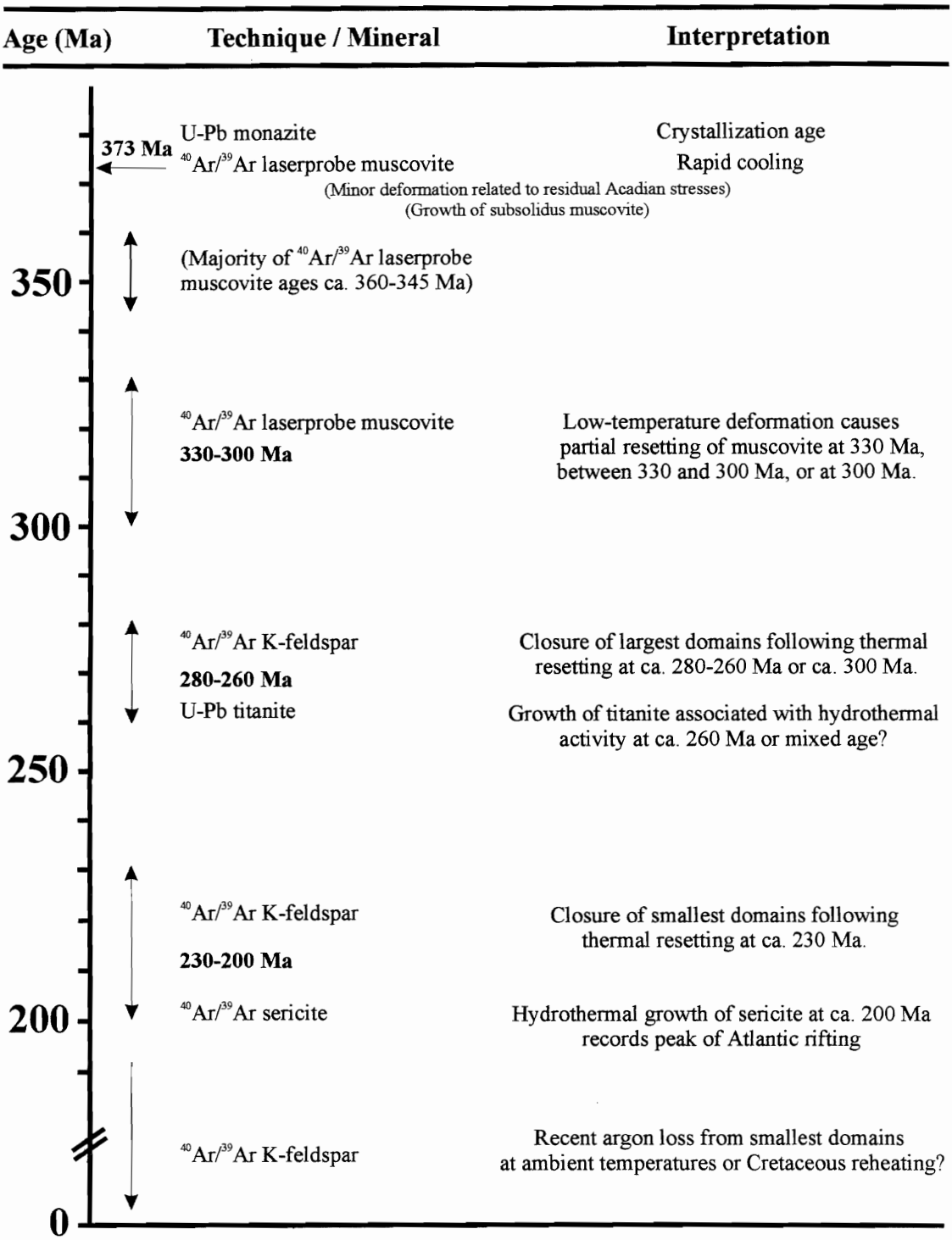

2) Laserprobe muscovite data provide additional evidence of a widespread argon loss event between ca. 330-315 Ma (possibly extending to ca. 300 Ma).
3) Muscovite that has experienced argon loss is likely to develop significant age gradients which may not be revealed by conventional incremental heating analysis. Age spectra produced in this way are potentially misleading and should be interpreted with caution.

5.4 Implications for laserprobe $^{40}Ar/^{39}Ar$ geochronology

This study has shown that grain thickness has a potentially crucial role in influencing the apparent age obtained from grains that have developed significant age gradients (as a result of argon loss). Depending on how grains are separated from samples, the apparent ages obtained may be different, suggesting different thermal histories for samples. Careful separation of mineral grains from samples by direct picking, without significant crushing, may actually result in misleading age information. In minerals that have experienced deformation, only the very centers of grains may preserve all of the originally accumulated argon and yield the correct age.

5.5 Recommendations for future work

Further work investigating the relationship between deformation and chemical reaction and argon loss from muscovite is required. In particular, information regarding the extent of chemical reaction on (001) cleavage fragments may have important implications for the degree of argon loss from minerals. Microprobe analysis of separated

cleavage fragments (instead of conventional polished thin-sections) will provide this information. An investigation of defects in muscovite crystals, possibly involving high-resolution imaging techniques, would provide information on the scales of argon loss in mineral grains, particularly those that are not obviously deformed.

The influence of grain thickness on apparent age may have important implications for $^{40}Ar/^{39}Ar$ laserprobe studies of deformed rocks. Further experiments investigating the relationship between grain thickness and apparent age are required, preferably involving the samples used in this study. Although the Nd-YAG laser used in this study revealed apparent age gradients in muscovite, problems of resolution prevented a precise determination of the timing of argon loss. Frequency-quadrupled Nd-YAG lasers are ideal for high spatial-resolution work because the resultant ultraviolet beam (266 nm) can be focused to an extremely small spot size (10 microns or less in diameter) (Kelly et al. 1994; Hodges 1996). Ultraviolet lasers are also preferable for this type of study because they couple better with felsic silicate minerals such as muscovite, allowing smaller spot sizes to be maintained. The use of a UV laserprobe could overcome the problems of resolution and coupling encountered in this study and may provide a precise age for the timing of argon loss from muscovite in plutons from southwestern Nova Scotia.

A detailed study of structural fabrics developed in the PMP would provide important information on the extent of deformation affecting these rocks, particularly pre-370 Ma deformation. The aims of such a study should be to identify multiple phases of deformation and place them in a regional (Acadian) or local (PMP) context.

APPENDIX A

Microprobe data for muscovite from undeformed and deformed samples

Undeformed samples:

97-14: Middle stage granodiorite

556: Middle Stage monzogranite (1 image)

97-9: Middle Stage granodiorite

96-3: Late Stage pegmatite (5 images)

Deformed samples:

96-1: Middle Stage monzogranite (4 images)

97-16a: Middle Stage monzogranite (2 images)

97-17: Middle Stage monzogranite (2 images)

97-3: Middle Stage monzogranite (2 images)

Microprobe data for muscovite from undeformed sample 97-14

Point	SiO_2	TiO_2	Al_2O_3	FeO	MnO	MgO	CaO	Na_2O	K_2O	Cr_2O_3	Cl	BaO	F	Total
CORES														
1	45.76	0.87	34.99	1.23	0.07	0.88	0.00	0.58	10.90	0.04	0.00	0.19	0.00	95.51
4	46.17	1.37	34.24	1.36	0.08	1.00	0.03	0.54	10.94	0.05	0.03	0.08	0.00	95.89
5	45.81	1.23	34.82	1.24	0.00	0.83	0.03	0.63	10.42	0.05	0.01	0.00	0.00	95.08
7	45.84	0.97	34.70	1.36	0.04	0.93	0.04	0.53	10.86	0.00	0.01	0.03	0.00	95.32
9	46.71	1.26	34.67	1.65	0.06	0.99	0.01	0.37	9.62	0.11	0.00	0.00	0.00	95.44
10	47.50	0.92	36.12	1.35	0.00	0.83	0.00	0.44	8.46	0.03	0.02	0.12	0.00	95.79
11	45.98	0.95	34.94	1.33	0.00	0.89	0.03	0.55	10.47	0.11	0.00	0.04	0.00	95.27
12	47.38	1.03	36.06	1.49	0.05	0.80	0.01	0.51	9.44	0.00	0.01	0.00	0.00	96.77
13	46.90	0.94	35.76	1.44	0.05	0.74	0.00	0.41	9.47	0.12	0.04	0.17	0.00	96.03
14	47.80	1.06	34.92	1.68	0.02	1.23	0.00	0.33	8.74	0.00	0.00	0.12	0.00	95.90
16	48.75	0.61	34.76	1.55	0.00	1.43	0.04	0.10	8.47	0.04	0.00	0.11	0.00	95.88
17	47.15	0.95	35.93	1.38	0.05	0.75	0.00	0.36	8.32	0.00	0.01	0.00	0.00	94.90
19	46.12	0.75	35.23	1.23	0.03	0.79	0.08	0.25	8.92	0.00	0.00	0.00	0.00	93.40
20	45.98	1.09	35.19	1.33	0.13	0.81	0.01	0.58	10.88	0.02	0.00	0.09	0.00	96.12
21	64.47	0.01	23.38	0.00	0.00	0.03	4.14	8.95	0.04	0.02	0.00	0.00	0.00	101.04
22	45.91	1.15	34.57	1.38	0.00	0.80	0.00	0.64	11.01	0.01	0.00	0.03	0.00	95.51
23	46.57	0.87	35.77	1.42	0.12	0.87	0.03	0.58	10.94	0.08	0.02	0.13	0.00	97.40
24	45.84	0.97	34.80	1.61	0.00	0.85	0.01	0.61	10.61	0.00	0.01	0.16	0.00	95.47
25	45.87	1.06	34.80	1.51	0.00	0.88	0.00	0.37	10.80	0.03	0.03	0.14	0.00	95.49
26	45.95	1.31	33.52	1.50	0.01	1.09	0.00	0.35	10.80	0.02	0.00	0.20	0.00	94.76
Average	47.42	0.97	34.46	1.35	0.04	0.87	0.22	0.88	9.51	0.04	0.01	0.08	0.00	95.85
RIMS														
2	45.34	0.98	34.71	1.55	0.00	0.85	0.00	0.56	10.74	0.06	0.00	0.15	0.00	94.93
3	46.68	1.34	32.18	1.71	0.09	1.37	0.00	0.35	11.01	0.00	0.00	0.31	0.00	95.04
6	46.94	1.32	34.07	1.58	0.00	1.10	0.00	0.38	10.49	0.06	0.02	0.29	0.00	96.25
18	48.28	1.12	35.46	1.43	0.07	1.10	0.00	0.32	8.47	0.00	0.02	0.00	0.00	96.28
Average	46.81	1.19	34.10	1.57	0.04	1.10	0.00	0.40	10.18	0.03	0.01	0.19	0.00	95.62

Microprobe data for muscovite cores from undeformed sample 556

Point	SiO_2	TiO_2	Al_2O_3	FeO	MnO	MgO	CaO	Na_2O	K_2O	Cr_2O3	NiO	P_2O_5	Cl	BaO	SrO	ZrO_2	Total
CORES																	
556a																	
2	47.11	1.41	35.39	1.44	0.00	0.93	0.00	0.40	9.13	0.00	0.00	0.08	0.00	0.14	0.00	0.01	96.04
3	47.14	1.56	35.23	1.32	0.00	0.82	0.00	0.42	8.91	0.05	0.06	0.00	0.04	0.33	0.00	0.00	95.86
4	46.94	1.44	35.19	1.39	0.02	0.86	0.01	0.51	9.50	0.00	0.04	0.00	0.02	0.02	0.00	0.03	95.97
5	47.01	1.45	35.53	1.58	0.00	0.82	0.00	0.42	9.11	0.02	0.24	0.00	0.00	0.00	0.00	0.00	96.20
8	47.25	1.36	35.00	1.28	0.04	0.68	0.04	0.38	9.22	0.00	0.03	0.04	0.02	0.24	0.00	0.00	95.58
9	47.42	1.46	35.29	1.19	0.05	0.79	0.00	0.32	9.49	0.05	0.11	0.00	0.02	0.05	0.00	0.07	96.31
10	47.29	1.31	34.91	1.28	0.04	0.78	0.00	0.55	8.97	0.05	0.00	0.05	0.00	0.31	0.00	0.00	95.56
11	47.12	1.40	35.26	1.36	0.09	0.87	0.00	0.48	9.13	0.05	0.00	0.00	0.00	0.20	0.04	0.02	96.02
556b																	
1	47.28	1.47	35.08	1.35	0.00	0.78	0.04	0.38	8.66	0.04	0.00	0.05	0.01	0.11	0.00	0.00	95.25
4	47.42	1.43	35.53	1.42	0.00	0.81	0.01	0.44	8.42	0.02	0.14	0.00	0.00	0.20	0.00	0.10	95.95
7	47.19	1.33	35.08	1.61	0.09	0.89	0.05	0.33	9.06	0.01	0.00	0.00	0.00	0.22	0.00	0.00	95.84
8	47.31	1.60	35.31	1.44	0.05	0.88	0.00	0.55	8.71	0.00	0.04	0.00	0.01	0.16	0.00	0.00	96.06
Average	47.21	1.44	35.23	1.39	0.03	0.82	0.01	0.43	9.03	0.02	0.05	0.02	0.01	0.16	0.00	0.02	95.89

Microprobe data for muscovite rims from undeformed sample 556

Point	SiO_2	TiO_2	Al_2O_3	FeO	MnO	MgO	CaO	Na_2O	K_2O	Cr_2O_3	NiO	P_2O_5	Cl	BaO	SrO	ZrO_2	Total
RIMS																	
556a																	
1	47.32	1.69	35.41	1.50	0.13	0.93	0.01	0.47	9.04	0.00	0.00	0.00	0.02	0.00	0.00	0.06	96.56
6	47.16	1.29	35.42	1.25	0.05	0.88	0.00	0.43	9.18	0.02	0.00	0.10	0.05	0.19	0.00	0.00	96.01
7	47.79	1.33	35.73	1.52	0.08	0.80	0.00	0.23	9.13	0.02	0.17	0.12	0.01	0.32	0.00	0.00	97.24
12	47.85	1.00	34.89	1.57	0.00	1.00	0.04	0.29	9.42	0.08	0.05	0.15	0.01	0.00	0.00	0.00	96.35
556b																	
2	46.43	1.58	34.36	1.33	0.07	0.78	0.00	0.39	8.58	0.11	0.05	0.00	0.00	0.00	0.00	0.00	93.67
3	46.33	1.65	34.26	1.50	0.05	0.97	0.07	0.18	8.68	0.05	0.00	0.00	0.01	0.00	0.00	0.00	93.76
5	47.43	1.42	34.33	1.49	0.00	1.11	0.00	0.23	9.07	0.02	0.00	0.00	0.00	0.00	0.00	0.03	95.15
Average	47.19	1.42	34.91	1.45	0.05	0.92	0.02	0.32	9.01	0.04	0.04	0.05	0.01	0.07	0.00	0.01	95.54

Backscattered electron image of muscovite from sample 556

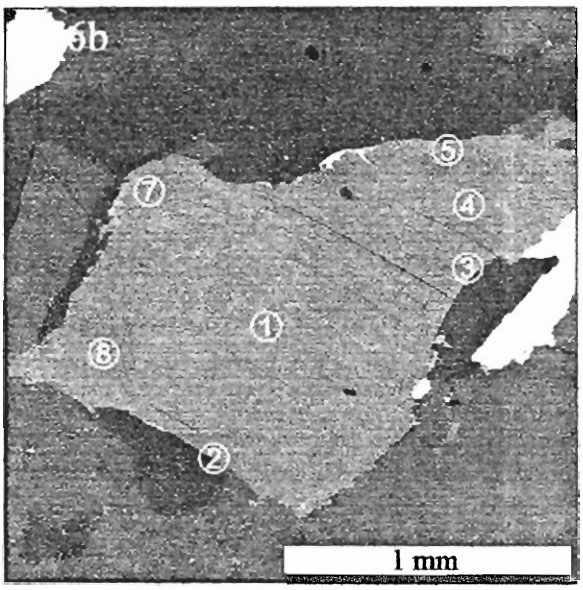

Microprobe data for muscovite from undeformed sample 97-9

Point	SiO_2	TiO_2	Al_2O_3	FeO	MnO	MgO	CaO	Na_2O	K2O	Cr_2O_3	Cl	BaO	F	Total
1	47.26	1.27	36.19	1.59	0.08	0.75	0.01	0.30	8.35	0.00	0.04	0.04	0.00	95.88
2	46.92	1.20	35.82	1.29	0.00	0.64	0.05	0.33	7.84	0.04	0.00	0.11	0.00	94.25
3	46.81	0.95	35.64	1.45	0.04	0.67	0.03	0.40	8.23	0.15	0.00	0.19	0.00	94.57
4	46.84	1.30	35.94	1.39	0.01	0.69	0.00	0.42	8.65	0.00	0.01	0.04	0.00	95.28
5	47.25	1.01	35.85	1.72	0.00	0.62	0.00	0.33	8.29	0.00	0.00	0.13	0.00	95.21
6	47.51	1.55	34.74	1.58	0.00	0.88	0.04	0.35	8.46	0.00	0.00	0.00	0.00	95.10
7	46.35	1.31	35.19	1.49	0.00	0.75	0.00	0.41	9.08	0.07	0.02	0.02	0.00	94.68
8	46.79	0.81	33.78	2.09	0.02	1.21	0.00	0.26	9.92	0.04	0.01	0.17	0.00	95.12
9	45.81	1.20	35.27	1.47	0.05	0.75	0.00	0.39	9.64	0.03	0.00	0.00	0.00	94.62
10	45.69	1.20	34.97	1.53	0.04	0.70	0.07	0.37	8.30	0.15	0.01	0.20	0.00	93.23
11	46.74	1.25	35.94	1.46	0.00	0.58	0.00	0.35	8.53	0.00	0.02	0.01	0.00	94.88
12	48.10	1.84	34.01	2.04	0.10	1.01	0.00	0.31	8.05	0.00	0.01	0.07	0.00	95.53
13	46.13	1.26	35.33	1.50	0.00	0.64	0.03	0.21	7.86	0.00	0.03	0.01	0.00	93.01
14	46.69	1.20	35.62	1.57	0.04	0.72	0.00	0.34	8.66	0.06	0.00	0.12	0.00	95.03
15	47.35	0.82	34.55	1.69	0.05	1.05	0.00	0.28	8.68	0.01	0.02	0.00	0.00	94.50
16	47.61	1.11	36.18	1.59	0.00	0.76	0.00	0.32	8.84	0.00	0.00	0.12	0.00	96.53
17	46.67	1.09	35.31	1.52	0.02	0.67	0.04	0.20	8.33	0.04	0.00	0.10	0.00	93.99
18	46.41	1.31	35.43	1.57	0.04	0.73	0.00	0.56	9.51	0.00	0.00	0.07	0.00	95.63
19	46.54	1.24	35.31	1.17	0.01	0.78	0.02	0.53	8.77	0.02	0.00	0.00	0.00	94.40
20	46.67	1.21	35.50	1.38	0.07	0.70	0.04	0.35	7.82	0.00	0.00	0.03	0.00	93.78
21	47.39	1.23	36.12	1.40	0.02	0.67	0.00	0.31	8.18	0.00	0.01	0.01	0.00	95.34
22	46.52	1.38	35.01	1.44	0.06	0.80	0.04	0.34	8.11	0.05	0.02	0.06	0.00	93.81
23	47.36	1.21	35.86	1.56	0.03	0.75	0.05	0.34	8.28	0.15	0.02	0.15	0.00	95.76
average	46.84	1.22	35.37	1.54	0.03	0.76	0.02	0.35	8.54	0.04	0.01	0.07	0.00	94.79

Microprobe data for muscovite cores from undeformed sample 96-3

Point	SiO_2	TiO_2	Al_2O3	FeO	MnO	MgO	CaO	Na_2O	K_2O	Cr_2O_3	Cl	BaO	F	Total
963a														
1	47.22	0.00	36.39	1.88	0.04	0.45	0.03	0.35	8.13	0.00	0.00	0.05	0.00	94.55
3	47.29	0.05	37.16	1.81	0.00	0.51	0.00	0.62	8.45	0.09	0.02	0.00	0.00	96.02
6	47.28	0.07	37.25	1.98	0.00	0.38	0.00	0.70	8.23	0.00	0.02	0.00	0.00	95.91
963b														
1	47.15	0.07	37.10	1.87	0.00	0.46	0.00	0.43	8.64	0.03	0.00	0.00	0.00	95.76
3	46.40	0.07	36.47	1.68	0.00	0.33	0.05	0.65	9.81	0.00	0.00	0.00	0.00	95.45
4	46.50	0.00	35.73	2.02	0.00	0.48	0.00	0.63	9.55	0.11	0.00	0.08	0.00	95.10
963c														
1	47.49	0.00	37.28	1.91	0.07	0.38	0.00	0.53	8.49	0.03	0.02	0.03	0.00	96.22
2	48.13	0.12	37.41	1.61	0.05	0.39	0.00	0.44	8.57	0.14	0.00	0.00	0.00	96.85
963d														
4	45.41	0.07	36.06	1.82	0.06	0.29	0.00	0.77	10.24	0.00	0.03	0.18	0.00	94.92
963e														
5	45.53	0.09	35.47	1.89	0.00	0.50	0.01	0.55	9.94	0.05	0.00	0.00	0.00	94.05
6	46.71	0.03	36.50	1.93	0.00	0.42	0.01	0.39	8.47	0.06	0.00	0.12	0.00	94.65
963f														
1	47.15	0.00	37.33	2.00	0.00	0.40	0.04	0.38	8.57	0.00	0.00	0.13	0.00	95.99
5	47.26	0.07	36.46	2.00	0.00	0.47	0.00	0.69	9.03	0.02	0.02	0.01	0.00	96.02
7	47.30	0.02	37.08	1.72	0.00	0.40	0.03	0.47	8.62	0.06	0.00	0.00	0.03	95.72
13	45.86	0.03	36.44	1.70	0.03	0.34	0.00	0.54	9.70	0.06	0.02	0.00	0.00	94.72
Average	46.85	0.05	36.68	1.85	0.02	0.41	0.01	0.54	8.96	0.04	0.01	0.04	0.00	95.46

Microprobe data for muscovite rims from undeformed sample 96-3

Point	SiO_2	TiO_2	Al_2O_3	FeO	MnO	MgO	CaO	Na_2O	K_2O	Cr_2O_3	Cl	BaO	F	Total
963a														
2	47.32	0.06	36.45	1.99	0.00	0.43	0.03	0.30	8.20	0.00	0.00	0.00	0.00	94.78
4	47.45	0.12	36.69	2.06	0.00	0.50	0.00	0.55	8.68	0.03	0.00	0.00	0.00	96.07
5	47.32	0.03	37.42	1.76	0.10	0.36	0.01	0.58	8.57	0.02	0.02	0.06	0.00	96.26
7	47.63	0.14	36.65	1.84	0.02	0.33	0.00	0.29	8.83	0.00	0.00	0.00	0.00	95.74
8	46.75	0.00	36.34	1.83	0.12	0.38	0.00	0.27	8.54	0.00	0.00	0.11	0.00	94.35
9	46.63	0.04	36.07	1.95	0.05	0.41	0.00	0.35	8.18	0.00	0.00	0.04	0.00	93.72
10	46.79	0.00	36.47	1.61	0.00	0.32	0.00	0.43	7.61	0.00	0.00	0.00	0.00	93.22
963b														
2	47.23	0.11	36.12	1.89	0.04	0.47	0.00	0.54	9.09	0.00	0.00	0.01	0.00	95.49
5	46.48	0.08	35.85	1.98	0.00	0.40	0.00	0.59	9.93	0.05	0.00	0.03	0.00	95.40
6	46.31	0.01	36.46	1.68	0.11	0.39	0.00	0.55	9.35	0.00	0.00	0.04	0.00	94.89
7	45.86	0.00	36.41	1.70	0.00	0.30	0.03	0.56	9.73	0.00	0.00	0.11	0.00	94.70
8	46.63	0.00	35.88	1.82	0.02	0.44	0.00	0.60	8.71	0.00	0.00	0.00	0.00	94.09
9	46.24	0.16	36.48	1.82	0.08	0.39	0.00	0.45	9.46	0.01	0.03	0.00	0.00	95.10
963d														
1	45.95	0.00	35.87	1.77	0.03	0.50	0.00	0.65	10.49	0.14	0.03	0.14	0.00	95.56
2	45.05	0.06	35.32	1.62	0.00	0.21	0.00	0.71	10.12	0.03	0.01	0.00	0.00	93.12
3	46.03	0.02	35.81	1.90	0.00	0.49	0.04	0.61	10.54	0.11	0.00	0.10	0.00	95.65
5	45.60	0.00	35.91	1.85	0.00	0.46	0.00	0.73	10.25	0.00	0.00	0.07	0.00	94.87
6	46.09	0.00	35.84	2.02	0.03	0.46	0.00	0.37	10.84	0.00	0.01	0.00	0.00	95.65
7	46.54	0.04	35.48	1.99	0.09	0.43	0.04	0.27	8.94	0.00	0.00	0.15	0.00	93.98
8	44.84	0.00	35.24	1.81	0.00	0.33	0.08	0.78	9.82	0.00	0.00	0.11	0.00	93.03
963e														
1	46.69	0.00	36.69	1.81	0.07	0.37	0.00	0.35	8.23	0.03	0.00	0.02	0.00	94.26
2	45.26	0.06	35.71	2.05	0.05	0.45	0.08	0.45	10.99	0.04	0.01	0.00	0.00	95.16
3	45.48	0.04	35.62	1.80	0.10	0.47	0.00	0.73	10.54	0.00	0.01	0.00	0.00	94.78
4	45.86	0.00	35.86	1.80	0.00	0.40	0.00	0.49	8.53	0.02	0.01	0.17	0.00	93.14
7	45.98	0.12	35.98	1.78	0.07	0.50	0.05	0.44	8.76	0.05	0.00	0.05	0.00	93.80
9	45.95	0.06	35.83	1.72	0.00	0.34	0.00	0.40	9.03	0.09	0.00	0.16	0.00	93.57
963f														
2	47.11	0.06	36.79	1.60	0.00	0.40	0.04	0.52	8.74	0.04	0.03	0.03	0.00	95.36
3	47.80	0.00	36.48	1.85	0.00	0.44	0.02	0.41	8.68	0.03	0.00	0.07	0.00	95.78
4	46.96	0.05	37.10	1.77	0.00	0.38	0.00	0.46	9.03	0.00	0.02	0.04	0.00	95.81
6	46.96	0.00	36.72	1.86	0.01	0.36	0.03	0.43	8.48	0.00	0.00	0.02	0.00	94.86
9	47.13	0.05	36.55	1.73	0.11	0.47	0.02	0.34	8.12	0.03	0.03	0.00	0.00	94.57
10	47.49	0.00	37.40	1.82	0.03	0.43	0.00	0.44	8.94	0.01	0.05	0.02	0.00	96.65
11	47.02	0.02	36.97	1.73	0.05	0.35	0.00	0.51	8.96	0.08	0.00	0.00	0.00	95.68
12	47.03	0.06	36.15	1.98	0.01	0.50	0.01	0.42	9.17	0.00	0.00	0.07	0.00	95.40
14	46.23	0.05	36.29	1.81	0.09	0.37	0.00	0.39	10.20	0.01	0.01	0.07	0.00	95.52
Average	46.51	0.04	36.25	1.83	0.04	0.41	0.01	0.48	9.21	0.02	0.01	0.05	0.00	94.86

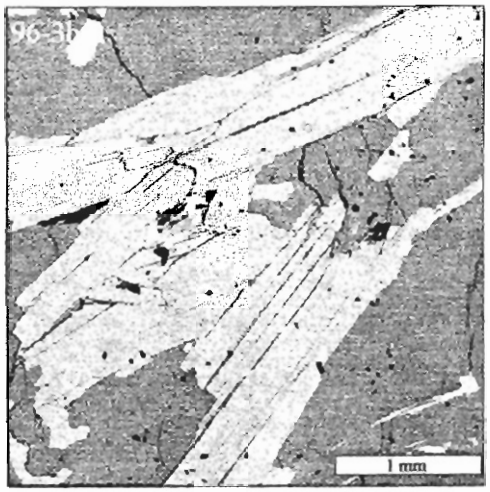
96-3b
1 mm

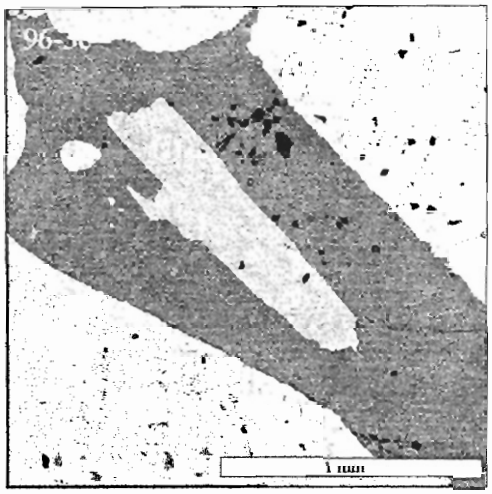
96-3c
1 mm

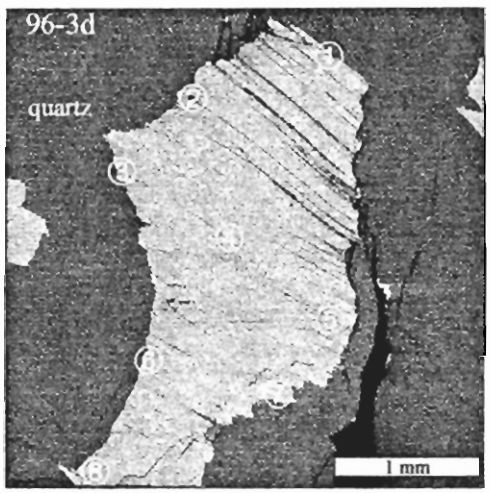
96-3d
quartz
1 mm

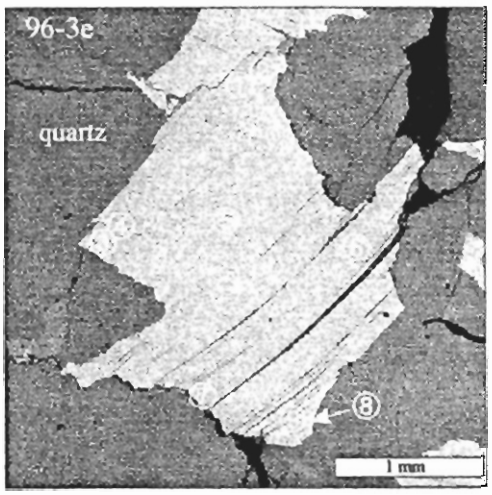
96-3e
quartz
1 mm

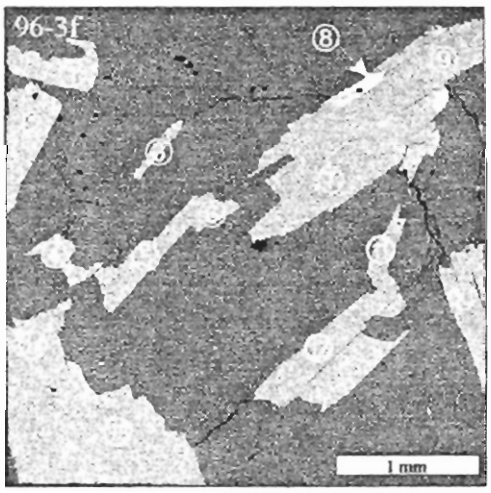
96-3f
1 mm

Microprobe data for muscovite cores from deformed sample 96-1

Point	SiO_2	TiO_2	Al_2O_3	FeO	MnO	MgO	CaO	Na_2O	K_2O	Cr_2O_3	Cl	BaO	F	Total
961a														
2	45.98	0.65	35.56	1.41	0.00	0.65	0.01	0.69	10.06	0.11	0.00	0.21	0.00	95.33
5	46.68	0.93	35.89	1.45	0.05	0.60	0.00	0.49	9.06	0.00	0.00	0.00	0.00	95.16
8	46.19	0.70	35.70	1.27	0.14	0.56	0.00	0.63	9.94	0.05	0.00	0.14	0.00	95.33
10	46.15	0.58	35.66	1.48	0.00	0.67	0.00	0.79	10.02	0.12	0.03	0.09	0.00	95.58
961b														
1	46.70	0.90	36.27	1.51	0.09	0.66	0.00	0.53	8.72	0.07	0.00	0.18	0.00	95.64
4	46.97	0.58	36.15	1.62	0.00	0.48	0.00	0.54	8.88	0.00	0.02	0.05	0.00	95.29
6	46.25	0.84	35.81	1.55	0.00	0.52	0.00	0.59	9.46	0.08	0.00	0.00	0.00	95.10
961c														
2	47.71	0.56	36.33	1.45	0.09	0.55	0.00	0.52	8.66	0.00	0.01	0.11	0.00	95.98
4	46.17	0.65	35.36	1.49	0.04	0.56	0.01	0.65	9.67	0.00	0.00	0.20	0.00	94.80
6	46.96	0.78	36.04	1.38	0.04	0.54	0.02	0.53	9.15	0.00	0.01	0.03	0.00	95.46
961d														
2	47.82	0.77	36.35	1.52	0.00	0.73	0.00	0.56	8.36	0.12	0.02	0.00	0.00	96.25
4	47.99	0.88	36.44	1.50	0.09	0.66	0.00	0.55	8.61	0.00	0.00	0.02	0.00	96.75
7	47.43	0.58	36.28	1.57	0.04	0.73	0.02	0.49	8.71	0.09	0.00	0.03	0.00	95.97
8	47.99	0.61	36.85	1.58	0.03	0.55	0.03	0.46	8.35	0.00	0.04	0.03	0.00	96.54
961e														
1	47.18	0.54	36.45	1.57	0.18	0.64	0.00	0.28	8.79	0.00	0.01	0.00	0.00	95.65
2	47.09	0.63	36.09	1.52	0.03	0.57	0.00	0.41	8.22	0.10	0.01	0.16	0.00	94.83
5	47.24	0.66	35.73	1.44	0.03	0.72	0.00	0.45	8.73	0.05	0.01	0.00	0.00	95.04
Average	46.97	0.69	36.06	1.49	0.05	0.61	0.01	0.54	9.02	0.05	0.01	0.07	0.00	95.57

Microprobe data for muscovite rims from deformed sample 96-1

Point	SiO_2	TiO_2	Al_2O_3	FeO	MnO	MgO	CaO	Na_2O	K_2O	Cr_2O_3	Cl	BaO	F	Total
961a														
1	46.71	0.42	30.16	5.04	0.02	1.95	0.00	0.19	10.58	0.04	0.01	0.00	0.00	95.12
3	47.93	0.24	30.24	4.15	0.08	1.95	0.02	0.15	8.50	0.05	0.00	0.00	0.00	93.31
4	48.56	0.17	30.53	4.00	0.15	1.90	0.00	0.23	9.16	0.05	0.00	0.00	0.00	94.75
6	46.86	0.21	30.90	4.02	0.10	1.66	0.00	0.15	10.02	0.00	0.01	0.00	0.00	93.94
7	46.72	0.49	31.08	4.04	0.08	1.72	0.00	0.17	10.40	0.02	0.02	0.00	0.00	94.74
9	47.34	0.23	30.62	4.14	0.07	1.75	0.07	0.14	10.38	0.08	0.00	0.00	0.00	94.81
11	46.20	0.78	35.59	1.36	0.00	0.63	0.00	0.50	10.09	0.04	0.00	0.00	0.00	95.20
12	47.28	0.28	30.11	4.37	0.03	1.80	0.08	0.17	10.94	0.04	0.01	0.01	0.00	95.12
13	47.19	0.32	30.28	3.67	0.07	1.66	0.00	0.07	11.01	0.00	0.01	0.00	0.00	94.28
961b														
2	48.49	0.18	31.71	3.24	0.13	1.70	0.00	0.13	9.14	0.00	0.01	0.14	0.00	94.89
5	49.29	0.12	30.73	3.74	0.09	1.72	0.00	0.04	9.08	0.05	0.00	0.00	0.00	94.86
7	47.81	0.29	30.99	3.62	0.18	1.63	0.00	0.15	10.36	0.11	0.00	0.00	0.00	95.13
961c														
1	48.77	0.16	32.74	3.35	0.06	1.55	0.00	0.22	8.62	0.10	0.01	0.03	0.00	95.60
3	48.40	0.22	31.69	3.89	0.12	1.84	0.05	0.18	8.81	0.01	0.02	0.01	0.00	95.24
5	48.17	0.02	30.53	4.13	0.18	1.83	0.03	0.14	9.95	0.02	0.00	0.00	0.00	95.00
961d														
5	47.49	0.08	30.44	4.65	0.19	1.82	0.00	0.15	8.42	0.00	0.00	0.00	0.00	93.23
6	48.61	0.09	31.61	4.39	0.10	1.75	0.01	0.14	8.53	0.00	0.00	0.08	0.00	95.32
9	46.98	0.19	31.57	4.73	0.21	1.77	0.04	0.13	8.28	0.00	0.03	0.02	0.00	93.94
961e														
3	50.07	0.17	31.13	3.98	0.24	1.95	0.06	0.07	8.42	0.01	0.00	0.00	0.00	96.10
4	47.68	0.10	30.61	4.41	0.15	2.01	0.08	0.09	8.85	0.07	0.03	0.19	0.00	94.27
6	49.52	0.25	31.28	4.32	0.28	1.92	0.00	0.09	8.38	0.00	0.03	0.00	0.00	96.06
7	48.28	0.23	31.43	4.37	0.22	1.84	0.00	0.25	7.99	0.00	0.06	0.00	0.00	94.67
8	49.06	0.22	30.97	4.12	0.11	1.76	0.01	0.19	8.38	0.00	0.00	0.17	0.00	94.97
9	48.65	0.19	30.57	4.49	0.11	1.86	0.00	0.11	8.43	0.00	0.00	0.00	0.00	94.41
10.00	50.36	0.04	30.87	4.72	0.08	2.06	0.00	0.06	8.32	0.00	0.00	0.13	0.00	96.65
Average	48.10	0.23	31.13	4.04	0.12	1.76	0.02	0.16	9.24	0.03	0.01	0.03	0.00	94.86

Backscattered electron images of muscovite from deformed sample 96-1

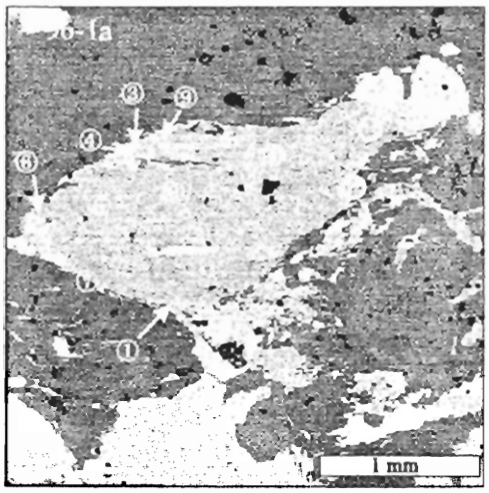

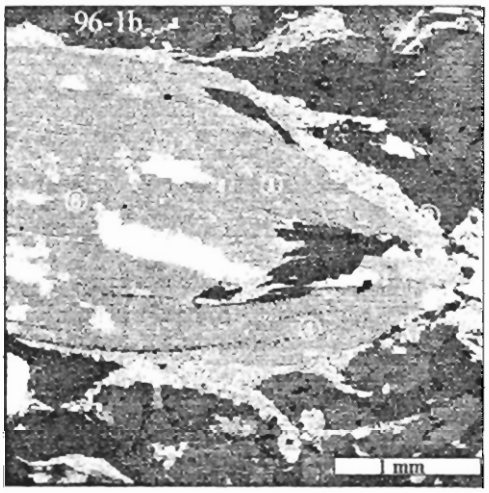

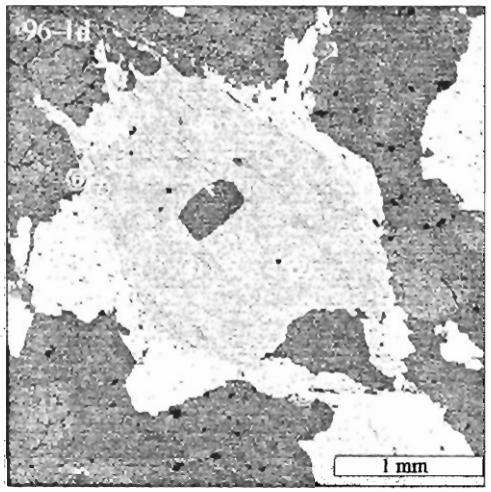

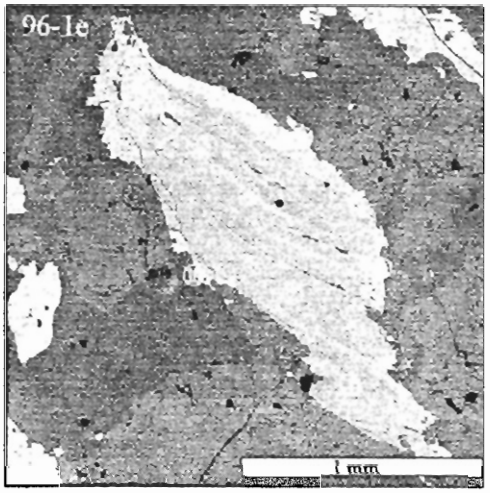

Microprobe data for muscovite from deformed sample 97-16a

Point	SiO_2	TiO_2	Al_2O_3	FeO	MnO	MgO	CaO	Na_2O	K_2O	Cr_2O_3	NiO	P_2O_5	Cl	BaO	SrO	ZrO_2	Total
97-16a1																	
1	47.12	0.74	35.50	1.56	0.00	0.59	0.04	0.58	8.82	0.01	0.16	0.03	0.02	0.19	0.00	0.00	95.36
4	47.18	0.59	35.96	1.67	0.00	0.70	0.00	0.54	8.67	0.09	0.00	0.08	0.05	0.14	0.00	0.00	95.68
7	46.13	0.88	35.19	1.50	0.02	0.65	0.00	0.44	8.47	0.05	0.02	0.05	0.00	0.04	0.00	0.01	93.44
8	47.51	0.87	35.90	1.52	0.10	0.77	0.01	0.49	8.28	0.06	0.03	0.04	0.03	0.02	0.00	0.00	95.62
9	47.38	0.72	31.80	3.35	0.11	1.20	0.03	0.17	8.72	0.00	0.00	0.06	0.04	0.01	0.00	0.00	93.60
97-16a2																	
1	47.09	0.75	36.20	1.54	0.01	0.62	0.06	0.51	8.52	0.00	0.12	0.09	0.00	0.09	0.00	0.00	95.58
2	47.06	0.91	35.57	1.73	0.05	0.59	0.03	0.49	8.36	0.04	0.17	0.02	0.01	0.00	0.00	0.00	95.02
5	47.26	0.69	36.14	1.67	0.11	0.71	0.00	0.48	8.79	0.04	0.00	0.17	0.00	0.00	0.02	0.00	96.08
8	46.45	0.70	35.23	1.51	0.11	0.60	0.03	0.52	8.62	0.07	0.02	0.05	0.01	0.04	0.00	0.00	93.96
9	46.91	0.88	35.65	1.79	0.03	0.63	0.00	0.69	8.33	0.03	0.09	0.06	0.05	0.00	0.00	0.03	95.17
Average	47.01	0.77	35.31	1.78	0.05	0.71	0.02	0.49	8.56	0.04	0.06	0.07	0.02	0.05	0.00	0.00	94.95

Microprobe data for muscovite rims from deformed sample 97-16a.

Point	SiO_2	TiO_2	Al_2O_3	FeO	MnO	MgO	CaO	Na_2O	K_2O	Cr_2O_3	NiO	P_2O_5	Cl	BaO	SrO	ZrO_2	Total
97-16a1																	
2	47.55	0.21	30.09	4.11	0.23	1.89	0.00	0.37	8.84	0.04	0.13	0.00	0.41	0.00	0.00	0.00	93.87
3	49.22	0.54	32.04	3.30	0.03	1.48	0.00	0.08	9.33	0.01	0.09	0.01	0.00	0.00	0.00	0.00	96.11
5	48.21	0.19	29.85	3.93	0.09	1.77	0.00	0.08	8.66	0.04	0.08	0.04	0.03	0.09	0.00	0.00	93.08
6	47.16	0.47	35.64	1.57	0.04	0.69	0.00	0.36	8.80	0.09	0.15	0.01	0.00	0.00	0.00	0.00	94.97
10	50.47	0.42	30.60	3.94	0.14	1.95	0.00	0.16	9.00	0.00	0.00	0.00	0.03	0.05	0.00	0.00	96.75
97-16a2																	
3	46.18	0.56	35.58	1.37	0.04	0.53	0.05	0.22	8.58	0.00	0.09	0.00	0.00	0.17	0.00	0.00	93.39
4	47.62	0.46	32.34	2.58	0.10	1.32	0.00	0.31	8.44	0.11	0.00	0.02	0.05	0.10	0.01	0.03	93.48
6	47.78	0.50	34.51	2.81	0.00	0.97	0.03	0.19	6.06	0.00	0.00	0.61	0.17	0.00	0.16	0.00	93.80
10	46.81	0.68	35.01	1.70	0.00	0.85	0.05	0.35	8.45	0.01	0.00	0.00	0.00	0.15	0.00	0.00	94.04
11	48.98	0.41	30.46	3.87	0.10	1.86	0.05	0.19	7.89	0.00	0.00	0.12	0.02	0.02	0.00	0.00	93.97
Average	48.00	0.44	32.61	2.92	0.08	1.33	0.02	0.23	8.41	0.03	0.05	0.08	0.07	0.06	0.02	0.00	94.35

Backscattered electron images of muscovite from deformed sample 97-16a

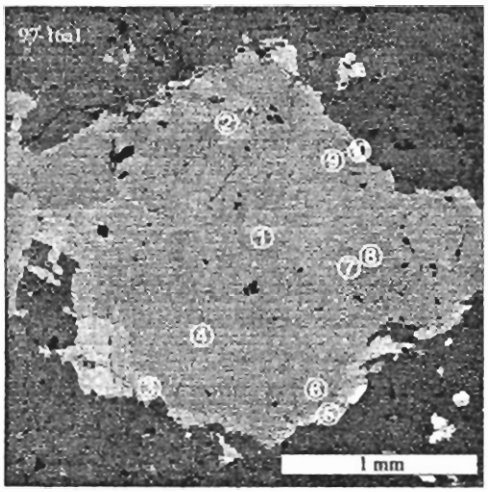

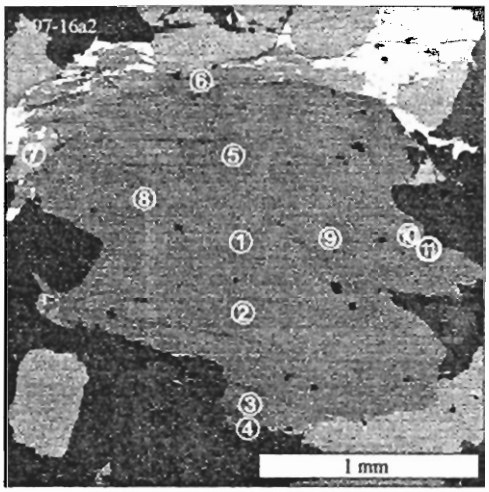

Microprobe data for muscovite from deformed sample 97-17

Point	SiO_2	TiO_2	Al_2O_3	FeO	MnO	MgO	CaO	Na_2O	K_2O	Cr_2O_3	NiO	P_2O_5	Cl	BaO	SrO	ZrO_2	Total
CORES																	
97-17a																	
1	46.79	0.60	35.82	1.26	0.09	0.55	0.00	0.57	8.92	0.00	0.04	0.01	0.03	0.07	0.00	0.00	94.75
2	46.82	0.67	35.98	1.34	0.00	0.57	0.00	0.69	9.10	0.00	0.00	0.00	0.02	0.07	0.00	0.00	95.27
3	46.62	0.45	35.47	1.49	0.03	0.56	0.00	0.47	9.16	0.04	0.05	0.00	0.04	0.02	0.00	0.00	94.40
4	47.38	0.39	35.76	1.62	0.08	0.68	0.00	0.43	9.18	0.23	0.00	0.03	0.00	0.22	0.00	0.00	96.01
97-17b																	
1	46.94	0.68	35.75	1.60	0.07	0.60	0.00	0.66	8.94	0.03	0.02	0.00	0.01	0.04	0.00	0.15	95.49
8	47.27	0.49	36.26	1.48	0.03	0.59	0.06	0.64	8.96	0.00	0.03	0.08	0.04	0.12	0.00	0.00	96.04
Average	46.97	0.55	35.84	1.47	0.05	0.59	0.01	0.57	9.04	0.05	0.02	0.02	0.02	0.09	0.00	0.03	95.32
RIMS																	
97-17a																	
5	45.92	0.40	27.84	4.30	0.15	2.11	3.42	0.08	8.52	0.00	0.00	2.89	0.03	0.00	0.00	0.00	95.66
6	49.08	0.24	31.34	3.51	0.16	1.92	0.00	0.22	9.12	0.01	0.00	0.00	0.01	0.08	0.00	0.00	95.69
7	48.14	0.40	34.79	1.84	0.20	0.92	0.02	0.25	9.37	0.00	0.06	0.07	0.05	0.00	0.00	0.00	96.11
9	47.88	0.54	35.87	1.58	0.01	0.71	0.00	0.36	8.59	0.00	0.00	0.15	0.02	0.03	0.00	0.00	95.74
10	49.18	0.29	32.23	2.91	0.10	1.51	0.00	0.17	9.30	0.00	0.00	0.07	0.01	0.00	0.00	0.00	95.76
97-17b																	
2	49.27	0.47	31.46	4.04	0.00	1.75	0.00	0.20	9.07	0.05	0.05	0.00	0.00	0.00	0.00	0.00	96.35
3	47.53	0.41	35.57	1.70	0.06	0.60	0.00	0.48	9.24	0.04	0.00	0.00	0.04	0.08	0.00	0.00	95.75
4	47.25	0.52	36.31	1.51	0.06	0.59	0.00	0.51	9.00	0.00	0.00	0.09	0.00	0.13	0.00	0.00	95.97
5	47.50	0.40	36.71	1.46	0.04	0.72	0.00	0.59	8.85	0.02	0.00	0.00	0.00	0.00	0.00	0.10	96.40
6	47.29	0.56	35.75	1.39	0.00	0.62	0.00	0.36	9.05	0.00	0.00	0.00	0.01	0.00	0.00	0.02	95.06
7	49.48	0.33	31.06	3.63	0.09	1.72	0.00	0.07	8.87	0.00	0.09	0.18	0.00	0.06	0.00	0.00	95.60
Average	48.05	0.42	33.54	2.53	0.08	1.20	0.31	0.30	9.00	0.01	0.02	0.31	0.02	0.03	0.00	0.01	95.83

Backscattered electron images of muscovite from deformed sample 97-17

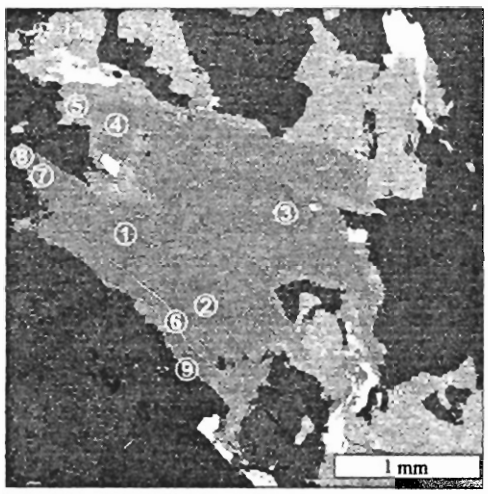

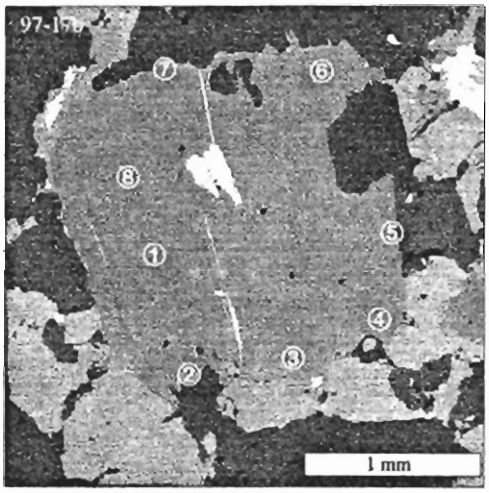

Microprobe data for muscovite cores from deformed sample 97-3

Point	SiO_2	TiO_2	Al_2O_3	FeO	MnO	MgO	CaO	Na_2O	K_2O	Cr_2O_3	Cl	BaO	F	Total
973a														
1	47.05	1.18	34.86	1.57	0.00	0.81	0.00	0.41	9.35	0.07	0.00	0.00	0.03	95.33
973b														
4	46.76	1.28	35.25	1.21	0.00	0.89	0.00	0.51	7.40	0.04	0.00	0.05	0.09	93.49
10	47.38	1.19	35.27	1.50	0.00	0.75	0.01	0.39	8.37	0.00	0.02	0.00	0.02	94.91
11	47.29	1.27	35.50	1.37	0.03	0.84	0.00	0.46	8.65	0.07	0.02	0.00	0.00	95.49
973c														
3	47.92	1.08	35.66	1.64	0.00	0.92	0.01	0.36	7.79	0.00	0.03	0.04	0.09	95.54
4	48.21	1.10	35.95	1.53	0.00	0.88	0.00	0.55	7.65	0.00	0.00	0.13	0.01	96.00
7	46.26	1.24	35.18	1.36	0.00	0.83	0.01	0.70	10.18	0.00	0.00	0.00	0.44	96.20
Average	47.27	1.19	35.38	1.45	0.00	0.85	0.01	0.48	8.49	0.03	0.01	0.03	0.10	95.28

Microprobe data for muscovite rims from deformed sample 97-3

Point	SiO_2	TiO_2	Al_2O_3	FeO	MnO	MgO	CaO	Na_2O	K_2O	Cr_2O_3	Cl	BaO	F	Total
973a														
2	48.90	0.64	30.77	3.06	0.04	1.77	0.00	0.12	8.38	0.07	0.02	0.03	0.06	93.85
3	47.62	0.95	35.77	1.42	0.04	0.83	0.00	0.42	8.51	0.00	0.00	0.00	0.00	95.57
4	49.97	0.99	29.00	4.71	0.12	2.23	0.03	0.18	8.31	0.06	0.00	0.00	0.07	95.66
5	47.90	1.02	35.63	1.66	0.02	1.02	0.00	0.34	8.29	0.00	0.00	0.00	0.03	95.93
6	48.11	0.96	34.38	2.17	0.08	1.18	0.00	0.22	8.47	0.00	0.01	0.00	0.09	95.66
973b														
3	47.29	1.15	34.87	1.72	0.00	0.91	0.00	0.33	7.77	0.13	0.00	0.07	0.00	94.24
6	47.38	1.00	35.23	1.70	0.01	0.95	0.00	0.29	7.94	0.00	0.03	0.12	0.02	94.68
7	48.03	0.92	34.62	1.84	0.00	1.02	0.01	0.44	7.88	0.00	0.01	0.04	0.05	94.86
9	48.12	1.01	34.90	1.99	0.00	1.06	0.00	0.33	8.66	0.00	0.00	0.14	0.04	96.25
973c														
2	48.53	1.08	35.63	1.73	0.10	1.11	0.00	0.38	7.97	0.01	0.01	0.08	0.00	96.61
6	47.77	0.94	34.46	2.01	0.02	1.11	0.00	0.15	8.55	0.00	0.03	0.00	0.10	95.14
8	46.59	0.92	35.48	1.41	0.01	0.76	0.00	0.97	10.18	0.00	0.14	0.00	0.00	96.46
9	46.98	0.79	33.92	2.02	0.14	1.05	0.01	0.66	10.21	0.00	0.20	0.12	0.00	96.12
10	46.70	0.99	34.31	1.41	0.02	0.89	0.02	0.38	10.82	0.06	0.00	0.06	0.01	95.66
11	46.77	1.01	33.84	1.93	0.09	0.96	0.01	0.20	10.51	0.00	0.02	0.10	0.01	95.47
12	46.83	0.98	34.83	1.50	0.00	0.79	0.04	0.47	10.16	0.00	0.00	0.05	0.10	95.75
Average	47.72	0.96	34.23	2.02	0.04	1.10	0.01	0.37	8.91	0.02	0.03	0.05	0.04	95.49

Backscattered electron images for muscovite from deformed sample 97-3

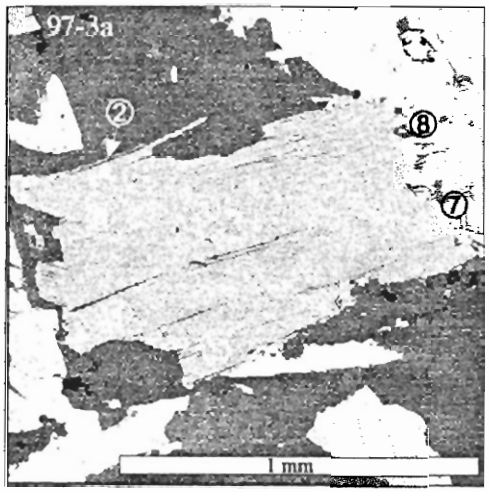

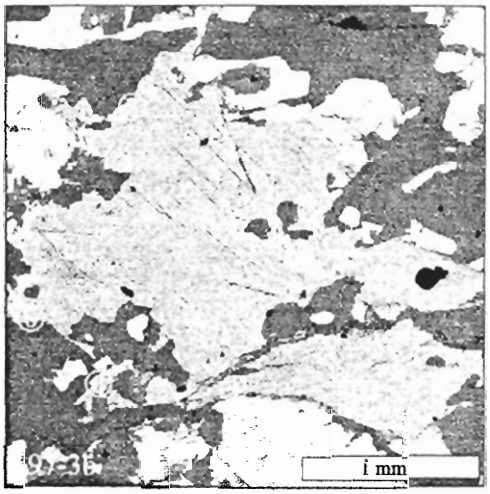

APPENDIX B

Analytical procedure for U-Pb geochronology

All analytical work was carried out at the U-Pb Geochronology Laboratory, University of Alberta, Edmonton. Stringent laboratory procedures for equipment and sample cleanliness were followed at all times to minimize the possibility of contamination.

Samples were reduced to a fine powder in a jaw crusher and disk mill which was divided into heavy and light mineral concentrates on a Wilfley Table. The heavy mineral concentrates were sieved through a 70 mesh screen prior to removal of strongly magnetic particles (e.g., magnetite) using a free-fall magnetic separation technique. Feldspar and quartz were removed from concentrates by a heavy liquid (MI or TBE) separation. The separates were passed 3-4 times at successively higher field strengths through a Franz isodynamic separator at 15° side-tilt to remove mica, garnet, and other matrix phases.

All material for dating was hand picked with tweezers under a binocular microscope from separates immersed in ethyl alcohol. Monazite was picked from initial Franz magnetic splits at 0.4A and 0.5A. Titanite was chosen from initial Franz magnetic split 1.0A. In all cases, multi grain fractions were selected based on similarities in grain morphology, size, color, and transparency. Were possible, grains with cracks, alteration, inclusions, core-rim relationships, and other irregularities were avoided.

Monazite was washed in 4N nitric acid, rinsed in high-purity water, weighed accurately on an electric Cann balance in disposable aluminum boats, and dissolved in 6.2N HCl in sealed, screw-cap PFA Teflon capsules at 150°C for approximately 60

hours. A precise amount of mixed ^{205}Pb-^{235}U tracer was added prior to dissolution so that isotopic concentrations could be determined by isotope dilution. Titanite fractions were prepared in a similar way, except titanite was dissolved with a mixture of concentrated HF and 7N HNO_3 (15:1). Isolation of Pb and U by anion exchange chromatography followed the approach for zircon as described by Heaman and Machado (1991). U and Pb were extracted from titanite using and HBr technique (Heaman and Machado 1991). The total blanks for these procedures are typically 3 pg Pb and 0.5 pg U for monazite, and 8 pg Pb and 0.5 pg for titanite.

Uranium and lead were combined in a silica gel-H_3PO_4 mixture and loaded on single outgassed Re filaments. Isotopic ratios were determined at 1440-1630°C with a VG-354 thermal ionization mass spectrometer in single collector mode. A Faraday collector was used for all ratio measurements except those involving ^{204}Pb and other low intensity signals, which were measured using a Daly photomultiplier. All isotopic data were corrected for mass discrimination by a factor of 0.088%/amu (Pb) and 0.155%/amu (U), based on repeated analysis of the NIST SRM 981 Pb and U500 standards.

Initial common Pb corrections were made by subtracting the amount and isotopic composition of procedural blank Pb from the measured Pb/U and Pb/Pb ratios (already corrected for fractionation and the ^{205}Pb-^{235}U spike). The remaining ^{204}Pb was applied to isotopic ratios for common lead calculated with the model of Stacy and Kramers (1975) at the estimated time of initial Pb retention. This allowed amounts of common ^{206}Pb, ^{207}Pb, and ^{208}Pb incorporated during mineral growth to be estimated and corrected for. Calculation of data for plotting on standard concordia diagrams and error propagation

were done using custom in-house software. The U decay constants and isotopic abundance ratio used were: $^{238}U = 1.55125 \times 10^{-10}$ yr^{-1}, $^{235}U = 9.8485 \times 10^{-10}$ yr^{-1}, and $^{238}U/^{235}U = 137.88$ (Steiger and Jäger 1977).

APPENDIX C

ANALYTICAL DATA FOR $^{40}Ar/^{39}Ar$ GEOCHRONOLOGY

Muscovite incremental heating data

97-14: Undeformed Middle Stage granoriotite

97-9: Undeformed Middle Stage granoriotite

96-3: Undeformed Late Stage pegmatite

96-1: Deformed Middle Stage monzogranite

97-3: Deformed Middle Stage monzogranite

Muscovite laserprobe (total fusion and spot mapping) data

97-14: Undeformed Middle Stage granoriotite

556: Undeformed Middle Stage monzogranite

487: Undeformed Early Stage tonalite

96-3: Undeformed Late Stage pegmatite

477: Undeformed Middle Stage monzogranite

97-9: Undeformed Middle Stage granoriotite

96-1: Deformed Middle Stage monzogranite

97-16a: Deformed Middle Stage monzogranite

97-17: Deformed Middle Stage monzogranite

97-3: Deformed Middle Stage monzogranite

Feldspar incremental heating data

97-4: Late Stage pegmatite

98-4: Late Stage pegmatite

484: Late Stage pegmatite

96-3: Late Stage pegmatite

97-14 MUSCOVITE ARGON SUMMARY

T°C	mV 39	% 39	Age (Ma)±1σ	% Atm	37/39	36/40	39/40	% IIC
600	6.7	.2	364.7 ± 12.4	7.9	.04	.00027	.009411	0
650	10.6	.4	350.7 ± 6.2	8.9	.02	.000302	.009726	0
700	22.3	.8	339.3 ± 3.8	10.8	.01	.000365	.009883	0
750	40.3	1.6	356.2 ± 2.8	10.3	0	.000349	.009421	0
775	44	1.7	359.3 ± 2.3	6.2	0	.00021	.009757	0
800	97.1	3.9	359.4 ± 2	6	0	.000204	.009773	0
825	296.6	11.9	360.1 ± 1.7	2.4	0	.000081	.010131	0
850	364.3	14.6	359.3 ± 1.6	.8	0	.000029	.010317	0
875	228.1	9.1	358.1 ± 1.8	.4	0	.000014	.0104	0
900	162.4	6.5	358.2 ± 1.7	.5	0	.000019	.010382	0
925	108.8	4.3	357 ± 1.7	.8	0	.000029	.01039	0
950	79.7	3.1	357.1 ± 1.9	1	0	.000036	.010362	0
975	71	2.8	358.9 ± 2	1	0	.000036	.010304	0
1000	80.4	3.2	355.8 ± 1.9	1	0	.000035	.010406	0
1025	90.1	3.6	358.3 ± 1.7	1	0	.000037	.010322	0
1050	109.9	4.4	356.8 ± 2.1	.8	0	.000029	.010395	0
1100	230.8	9.2	358.8 ± 1.6	.7	0	.000025	.010343	0
1250	434.1	17.4	360.5 ± 1.6	.8	0	.000028	.010281	0
1450	13.1	.5	381.6 ± 9.1	34.2	.08	.001157	.006401	.01

Total gas age = 358.8 ± 2.5 Ma

Mean age (775°C-1250°C) = 358.9 ± 1.9 Ma (2σ uncertainty including error in J)

J = .002273 ± .0000114 (.5 %)

37/39, 36/40, and 39/40 Ar ratios are corrected for mass spectrometer discrimination, interfering isotopes and system blanks

% IIC – Interfering isotopes correction

97-9 MUSCOVITE ARGON SUMMARY

T°C	mV 39	% 39	Age (Ma) ± 1σ	% Atm	37/39	36/40	39/40	% IIC
650	15.5	.7	343 ± 4.5	10.2	0	.000347	.009815	0
750	51.5	2.5	335.7 ± 2.3	9.9	0	.000336	.01009	0
800	87.4	4.2	345.5 ± 2.1	5.4	0	.000182	.010267	0
825	247.4	12	350 ± 1.6	2.8	0	.000095	.0104	0
850	434.8	21.1	352.5 ± 1.6	1.6	0	.000056	.010443	0
875	277.2	13.4	351.7 ± 1.6	.9	0	.000033	.010539	0
900	204.9	9.9	352.8 ± 1.6	1	0	.000034	.0105	0
925	137.2	6.6	351.4 ± 1.6	1	0	.000036	.010539	0
950	106	5.1	351.6 ± 1.7	1.1	0	.000039	.010524	0
975	93.3	4.5	351.9 ± 1.8	1.1	0	.000038	.010518	0
1000	94.3	4.5	355.6 ± 1.8	1	0	.000034	.010409	0
1025	55.8	2.7	353.3 ± 2.1	1.4	0	.000049	.010437	0
1050	49.1	2.3	355.3 ± 2.2	1.1	0	.000037	.01041	0
1075	46	2.2	358 ± 2.1	.8	0	.000029	.010347	0
1100	49	2.3	356.7 ± 2	.9	0	.00003	.010385	0
1150	64.3	3.1	356.7 ± 1.9	.9	0	.000032	.010378	0
1250	22.5	1	357.5 ± 4.1	5.5	0	.000188	.00987	0
1450	21.2	1	352.5 ± 4.2	20.3	.01	.000687	.008456	0

Total gas age = 351.88 ± 2.4 Ma

Mean age (850°C-1250°C) = 353 ± 2 Ma (2σ uncertainty including error in J)

J = .002271 ± .0000113 (.4 %)

37/39, 36/40, and 39/40 Ar ratios are corrected for mass spectrometer discrimination, interfering isotopes and system blanks

% IIC – Interfering isotopes correction

96-3 MUSCOVITE ARGON SUMMARY

T°C	mV 39	% 39	Age (Ma) ± 1σ	% Atm	37/39	36/40	39/40	% IIC
600	7.8	.3	317 ± 8.7	8.2	0	.000279	.010951	0
650	12	.5	360.6 ± 6	6.5	.01	.00022	.009691	0
700	24.7	1	339.9 ± 3.3	11	0	.000374	.009842	0
750	65.8	2.8	349.1 ± 2.1	4.3	0	.000148	.01028	0
775	73	3.1	347.8 ± 2	2.4	0	.000082	.010531	0
800	114.2	4.9	349.3 ± 1.7	2.7	0	.000091	.010454	0
825	168.4	7.3	349.7 ± 1.7	2.9	0	.0001	.010412	0
850	291.7	12.6	350.1 ± 1.6	2	0	.000069	.010495	0
875	249.8	10.8	349.5 ± 1.6	.6	0	.000023	.010664	0
900	167.5	7.2	349 ± 1.6	.8	0	.000028	.010664	0
925	117	5	348 ± 1.8	1.2	0	.000043	.01065	0
950	93.8	4	346.6 ± 1.8	1.2	0	.000042	.0107	0
975	86.5	3.7	347.6 ± 1.8	1.1	0	.000039	.010675	0
1000	95	4.1	348.9 ± 1.7	1	0	.000034	.010649	0
1025	107.4	4.6	349.3 ± 1.7	.9	0	.00003	.010648	0
1050	134.3	5.8	350 ± 1.6	.8	0	.00003	.010625	0
1100	311.1	13.5	351.1 ± 1.6	.7	0	.000024	.010606	0
1200	152.8	6.6	350.9 ± 1.6	1.1	0	.000039	.010567	0
1300	16.9	.7	360.9 ± 5.5	9.4	0	.00032	.00938	0
1450	12.4	.5	357.9 ± 7.9	28.5	0	.000965	.007472	0

Total gas age = 349.5 ± 2.4 Ma

Mean age (750°C-1200°C) = 349.5 ± 1.8 Ma (2σ uncertainty including error in J)

J = .002275 ± .0000114 (.5 %)

37/39, 36/40, and 39/40 Ar ratios are corrected for mass spectrometer discrimination, interfering isotopes and system blanks

% IIC – Interfering isotopes correction

96-1 MUSCOVITE ARGON SUMMARY

T°C	mV 39	% 39	Age (Ma) ± 1σ	% Atm	37/39	36/40	39/40	% IIC
650	18.3	.7	355 ± 4.5	8.5	.01	.00029	.009658	0
750	69.9	2.7	339.8 ± 2.2	10	0	.000338	.009978	0
775	55.5	2.2	347.1 ± 2.1	4.9	0	.000166	.010299	0
800	79.2	3.1	345.4 ± 1.9	4.5	0	.000154	.010394	0
825	181.9	7.2	348.2 ± 1.6	2.8	0	.000097	.010485	0
850	405.5	16.1	350.4 ± 1.6	1.5	0	.000053	.010554	0
875	267.9	10.6	350.4 ± 1.7	.7	0	.000023	.010646	0
900	162.4	6.4	348.7 ± 1.6	.8	0	.000029	.010687	0
925	116.6	4.6	348 ± 1.6	.9	0	.000032	.010698	0
950	97.9	3.9	347.6 ± 1.8	1.1	0	.00004	.010686	0
975	91.5	3.6	348.9 ± 1.8	1	0	.000034	.010664	0
1000	93.6	3.7	350.6 ± 1.7	.8	0	.000028	.010624	0
1025	98.1	3.9	351.5 ± 1.8	.7	0	.000025	.010605	0
1050	109.1	4.3	351.8 ± 1.7	.6	0	.000022	.010603	0
1075	125.5	5	355.2 ± 1.7	.4	0	.000015	.010512	0
1100	161.1	6.4	355.1 ± 1.6	.3	0	.000011	.010529	0
1125	157.7	6.2	355.6 ± 1.6	.1	0	.000006	.010528	0
1150	48.8	1.9	357.6 ± 2.2	.1	0	.000006	.010463	0
1200	19.9	.7	362.7 ± 4	7.4	0	.000252	.009548	0
1250	20	.7	370.1 ± 4.1	5.4	.01	.000185	.009536	0
1450	127.7	5	357.8 ± 1.8	3.8	0	.00013	.010074	0

Total gas age = 351.1 ± 2.4 Ma

Mean age (1075°C-1450°C) = 356.6 ± 2.2 Ma (2σ uncertainty including error in J)

J = .002278 ± .0000114 (.5 %)

37/39, 36/40, and 39/40 Ar ratios are corrected for mass spectrometer discrimination, interfering isotopes and system blanks

% IIC – Interfering isotopes correction

97-3 MUSCOVITE ARGON SUMMARY

T°C	mV 39	% 39	Age (Ma) ± 1σ	% Atm	37/39	36/40	39/40	% IIC
600	5.2	.2	309.5 ± 11.7	9.3	.03	.000317	.011066	0
650	10.2	.3	325 ± 6.4	4.5	.01	.000153	.011062	0
700	20	.7	313.2 ± 4.5	9.2	.01	.000312	.010956	0
750	35.4	1.3	329.3 ± 2.9	7.2	0	.000244	.010606	0
775	38.9	1.5	336.7 ± 2.3	1.8	0	.000063	.010945	0
800	69.2	2.6	342.7 ± 1.9	2	0	.000069	.010716	0
825	181.6	7	346.7 ± 1.6	.9	0	.000032	.010699	0
850	321.7	12.4	348.5 ± 1.6	.2	0	.000008	.010718	0
875	276.7	10.7	348.1 ± 1.6	.1	0	.000004	.010744	0
900	185.7	7.2	346.9 ± 1.6	.1	0	.000005	.010781	0
925	136.3	5.2	345.6 ± 1.8	.2	0	.000007	.010819	0
950	111.9	4.3	347.7 ± 1.7	.1	0	.000005	.010753	0
975	102.7	3.9	346.7 ± 1.6	.1	0	.000005	.010788	0
1000	108.1	4.2	347.9 ± 1.7	.1	0	.000005	.010745	0
1025	117.9	4.5	348.8 ± 1.6	0	0	.000002	.010725	0
1050	134.7	5.2	350.6 ± 1.7	0	0	.000002	.010667	0
1100	259.8	10	351.7 ± 1.6	0	0	.000002	.010629	0
1200	331.1	12.8	352.6 ± 1.6	.2	0	.000008	.010577	0
1300	67.8	2.6	356.7 ± 2	1.5	0	.000051	.01031	0
1450	59.2	2.3	356.5 ± 2.2	8.5	0	.00029	.009579	0

Total gas age = 348.3 ± 2.4 Ma

Mean age (850°C-1200°C) = 349.1 ± 1.9 Ma (2σ uncertainty including error in J)

J = .002269 ± .0000113 (.4 %)

37/39, 36/40, and 39/40 Ar ratios are corrected for mass spectrometer discrimination, interfering isotopes and system blanks

% IIC – Interfering isotopes correction

97-14L MUSCOVITE ARGON SUMMARY

T°C	mV 39	% 39	Age (Ma) ± 1σ	% Atm	37/39	36/40	39/40	% IIC
Total fusion								
3-1	103.2	9	371 ± 1.8	2.6	0	.000089	.009979	0
7-1	125.1	10.9	376.8 ± 1.8	.8	0	.000028	.00999	0
9-1	53.4	4.6	361.1 ± 2	.7	0	.000026	.010478	0
5-1	175	15.2	366.9 ± 1.7	3.1	0	.000105	.009886	0
6-1	126.3	11	358.4 ± 1.7	1.4	0	.000049	.010316	0
10-1	116	10.1	364.9 ± 1.8	2.6	0	.000089	.009996	0
Laserprobe								
1-1	12.4	1	371.1 ± 4.1	19.9	.01	.000675	.008202	0
1-2	3.8	.3	365.5 ± 7.7	3.7	.02	.000127	.010027	0
1-3	45.6	3.9	371.1 ± 1.8	.5	0	.000019	.010187	0
4-1	9.6	.8	365.1 ± 3.7	3.9	0	.000133	.010023	0
4-2	6.1	.5	376.7 ± 5.1	1.1	.01	.000037	.009968	0
4-3	100.4	8.7	376 ± 1.7	1.1	0	.000039	.009982	0
8-1	24.3	2.1	366.7 ± 2.5	5.8	0	.000196	.009781	0
8-2	15.9	1.3	368.5 ± 3	7.7	.01	.000262	.009528	0
8-3	94.4	8.2	376.3 ± 1.8	1	0	.000036	.009982	0
2-1	16.1	1.4	366.1 ± 2.7	2.4	.01	.000081	.010151	0
2-2	33.4	2.9	367.3 ± 2	.9	0	.000033	.010264	0
2-3	83.8	7.3	373.1 ± 1.8	.8	0	.000027	.010104	0

Total gas age = 369.2 ± 2.5 Ma

J = .0023 ± .0000161 (.7 %)

37/39, 36/40, and 39/40 Ar ratios are corrected for mass spectrometer discrimination, interfering isotopes, and system blanks.

% IIC – interfering isotopes correction

556 MUSCOVITE ARGON SUMMARY

T°C	mV 39	% 39	Age (Ma) ± 1σ	% Atm	37/39	36/40	39/40	% IIC
Total fusion								
7-1	413.2	37.2	348.5 ± 1.6	1.7	0	.000058	.010728	0
Laserprobe								
5-1	9.2	.8	325.8 ± 2.4	3.2	0	.000109	.011313	0
5-2	18.5	1.6	327.2 ± 2	8.1	.01	.000276	.010687	0
5-3	16.4	1.4	344.2 ± 2	2.9	0	.000099	.010686	0
5-4	32.3	2.9	351.8 ± 1.7	.9	0	.000032	.010644	0
5-5	24.3	2.1	349.1 ± 1.8	1.1	0	.00004	.010712	0
2-1	14.2	1.2	345.5 ± 2.2	5.3	0	.00018	.010379	0
2-2	2.9	.2	349.8 ± 5.2	2.1	.01	.000072	.010581	0
2-3	8.4	.7	344.2 ± 2.5	3.3	0	.000111	.010644	0
2-4	7.2	.6	352.7 ± 3.1	7.9	.01	.000269	.009861	0
2-5	8.6	.7	348.7 ± 2.3	1.5	0	.000054	.010681	0
6-1	5.3	.4	335 ± 3.6	11.2	0	.000379	.010069	0
6-2	14.4	1.2	337.6 ± 2.2	9.2	0	.000314	.010202	0
6-3	3.3	.3	355.4 ± 5	7.2	0	.000246	.009853	0
6-4	29.8	2.6	347.5 ± 1.9	8.7	0	.000297	.009938	0
6-5	22.4	2	337.8 ± 1.8	.4	0	.000016	.011182	0
3-1	27	2.4	348.1 ± 1.8	3.3	0	.000111	.010569	0
1-1	384.7	34.6	342.5 ± 1.6	.9	0	.000031	.010968	0
4-1	67.3	6	347.5 ± 1.6	1.3	0	.000045	.010803	0

Total gas age = 345.4 ± 2.7 Ma

J = .002255 ± 1.5785E-05 (.7 %)

37/39, 36/40, and 39/40 Ar ratios are corrected for mass spectrometer discrimination, interfering isotopes, and system blanks.

% IIC – interfering isotopes correction

487 MUSCOVITE ARGON SUMMARY

T°C	mV 39	% 39	Age (Ma) ± 1σ	% Atm	37/39	36/40	39/40	% IIC
2-1	1.6	1	322.1 ± 9.5	16.1	0	.000546	.010003	0
2-2	25.3	15.9	342.2 ± 1.7	1.4	0	.000049	.011008	0
2-3	37.1	23.3	348.6 ± 1.6	.9	0	.000031	.010846	0
2-4	15.2	9.5	347.2 ± 2.1	.8	.01	.000028	.010903	0
2-5	79.9	50.1	354.8 ± 1.6	.2	0	.000009	.010706	0

Total gas age = 350.3 ± 2.9 Ma

J = .002262 ± 1.5834E-05 (.7 %)

37/39, 36/40, and 39/40 Ar ratios are corrected for mass spectrometer discrimination, interfering isotopes, and system blanks.

% IIC – interfering isotopes correction

96-3 MUSCOVITE ARGON SUMMARY

T°C	mV 39	% 39	Age (Ma) ± 1σ	% Atm	37/39	36/40	39/40	% IIC
Total fusion								
1-1	350.2	18.8	361 ± 1.6	1.7	0	.000057	.010265	0
5-1	666.2	35.7	364.4 ± 1.7	4.4	0	.000149	.009878	0
9-1	198.1	10.6	364.2 ± 1.7	4.4	0	.00015	.00988	0
6-1	251.5	13.5	358.6 ± 1.6	2	0	.00007	.0103	0
7-1	245.9	13.2	360 ± 1.7	1.9	0	.000066	.010269	0
Laserprobe								
3-1	4.9	.2	363.4 ± 6.3	4.9	0	.000166	.009854	0
3-2	6.9	.3	342.7 ± 4.6	6.3	.01	.000213	.010358	0
3-3	6.8	.3	355 ± 5.1	8.7	0	.000296	.009705	0
3-4	22.7	1.2	359 ± 2.5	4.1	0	.00014	.010068	0
3-5	13.9	.7	358.8 ± 3	2.9	0	.000099	.010204	0
4-1	13.1	.7	371.7 ± 3.4	10.4	0	.000351	.009058	0
4-2	40.2	2.1	367.4 ± 1.9	2.1	0	.000073	.010018	0
4-3	11.6	.6	371.2 ± 3.3	2.6	0	.000091	.00985	0
4-4	14.6	.7	363 ± 2.7	5.9	0	.000202	.009759	0
4-5	15.2	.8	343.8 ± 2.9	9.1	0	.000309	.010012	0

Total gas age = 362.1 ± 2.7 Ma

J = .002314 ± 1.6198E-05 (.7 %)

37/39, 36/40, and 39/40 Ar ratios are corrected for mass spectrometer discrimination, interfering isotopes, and system blanks.

% IIC – interfering isotopes correction

477 MUSCOVITE ARGON SUMMARY

T°C	mV 39	% 39	Age (Ma) ± 1σ	% Atm	37/39	36/40	39/40	% IIC
Total fusion								
1-1	412.3	53.3	355.9 ± 1.6	.8	.02	.000029	.010261	0
1-2	114.7	14.8	357.9 ± 1.6	.4	0	.000013	.010243	0
Laserprobe								
1-3	36.3	4.6	356.4 ± 1.6	.2	0	.000006	.010312	0
1-4	67.2	8.6	351.4 ± 1.6	.1	.01	.000004	.010483	0
2-1	8.6	1.1	325.9 ± 2.1	6.6	.03	.000225	.010641	0
2-2	9.4	1.2	334.4 ± 2.1	6.5	.01	.00022	.010362	0
2-3	16.3	2.1	334.7 ± 1.7	2.2	0	.000075	.010828	0
2-4	74.9	9.6	358.7 ± 1.7	6	0	.000203	.009645	0
2-5	33.3	4.3	349.4 ± 1.7	.4	0	.000013	.01052	0

Total gas age = 354.8 ± 2.9 Ma

J = .002258 ± 1.5806E-05 (.7 %)

37/39, 36/40, and 39/40 Ar ratios are corrected for mass spectrometer discrimination, interfering isotopes, and system blanks.

% IIC – interfering isotopes correction

97-9 MUSCOVITE ARGON SUMMARY

T°C	mV 39	% 39	Age (Ma) ± 1σ	% Atm	37/39	36/40	39/40	% IIC
Total fusion								
9-1	46.4	5.3	368.9 ± 2.4	2.8	0	.000095	.009817	0
8-1	87.4	10	365.4 ± 1.9	4.4	0	.00015	.009754	0
3-1	111.3	12.7	357.7 ± 1.7	2.1	0	.000073	.010225	0
2-1	134.3	15.4	360.3 ± 1.9	1.9	0	.000065	.010165	0
1-1	65.5	7.5	356.8 ± 1.8	1.5	0	.000051	.01041	0
4-1	79	9	360.8 ± 1.9	2.7	0	.000094	.010152	0
5-1	144.5	16.5	355 ± 1.7	1.6	0	.000056	.010453	0
7-1	100.4	11.5	359 ± 1.8	2.4	0	.000082	.010243	0
8-1	101.4	11.6	370.2 ± 1.9	1.6	0	.000056	.009981	0

Total gas age = 360.9 ± 2.6 Ma

J = .002293 ± 1.6051E-05 (.7 %) (9-1 to 1-1)

J = .002250 ± 1.575E-05 (.7 %) (4-1 to 8-1)

37/39, 36/40, and 39/40 Ar ratios are corrected for mass spectrometer discrimination, interfering isotopes, and system blanks.

% IIC – interfering isotopes correction

96-1L MUSCOVITE ARGON SUMMARY

T°C	mV 39	% 39	Age (Ma) ± 1σ	% Atm	37/39	36/40	39/40	% IIC
Total fusion								
5-1	171.7	32.6	364.4 ± 2.3	2	0	.000068	.010272	0
Laserprobe								
6-1	6.7	1.2	361.8 ± 5.6	13.3	.01	.000451	.009156	0
6-2	5.5	1	353.4 ± 6.7	5.6	.01	.000191	.010229	0
6-3	1.3	.2	332.2 ± 20.2	11.5	.03	.00039	.010257	0
6-4	.3	0	347.2 ± 74.8	32.4	.21	.001093	.007462	.03
6-5	1	.1	387.8 ± 28.2	8.2	.07	.000279	.008969	0
9-2	1.6	.3	340.2 ± 17	10.8	.06	.000366	.010076	.01
9-3	3.1	.6	368.9 ± 10.5	7.5	.02	.000256	.009557	0
9-4	9.9	1.8	350.9 ± 3.5	3.4	0	.000115	.010557	0
9-5	5.6	1	364.6 ± 5.8	3.9	0	.000134	.01006	0
9-6	23.3	4.4	369.9 ± 2.2	1.7	0	.000059	.010128	0
1-1	16.6	3.1	349 ± 2.9	3.1	0	.000108	.010644	0
1-2	16.2	3	358.6 ± 2.9	3.9	0	.000132	.010252	0
1-3	9.2	1.7	335.5 ± 3.4	1.8	0	.000062	.011267	0
1-4	4.4	.8	366.1 ± 7.7	4.9	.01	.000167	.009912	0
1-5	4.3	.8	357 ± 7.8	8	.02	.00027	.009865	0
1-6	3.8	.7	358.9 ± 7.4	1.7	.01	.000058	.010476	0
1-7	49.9	9.5	360.4 ± 2	1.3	0	.000046	.010464	0
2-1	7.9	1.5	343 ± 4.3	6.1	0	.000207	.010519	0
2-2	6.2	1.1	336.5 ± 5.6	3.2	.02	.000109	.011069	0
2-3	.8	.1	368.7 ± 32	14	.06	.000474	.008889	0
2-4	2.3	.4	369.1 ± 11.6	3.3	.01	.000114	.009982	0
2-5	172.7	32.8	365.8 ± 1.8	.8	0	.00003	.010346	0

Total gas age = 362.4 ± 3.1 Ma

J = .002306 ± 1.6142E-05 (.7 %)

37/39, 36/40, and 39/40 Ar ratios are corrected for mass spectrometer discrimination, interfering isotopes, and system blanks.

% IIC – interfering isotopes correction

96-1L(B) MUSCOVITE ARGON SUMMARY

T°C	mV 39	% 39	Age (Ma) ± 1σ	% Atm	37/39	36/40	39/40	% IIC
1-1	128.9	14.1	355.3 ± 1.7	1.6	0	.000056	.010502	0
1-4	12	1.3	323.6 ± 1.9	1.2	.03	.00004	.01169	0
1-5	36.2	3.9	351.9 ± 1.7	.9	.01	.00003	.010697	0
1-6	35.9	3.9	353.6 ± 1.7	.7	0	.000026	.010655	0
1-7	18.9	2	345 ± 1.9	1.5	.01	.000051	.010864	0
1-8	9.4	1	350.4 ± 2.2	.1	.01	.000004	.010834	0
1-9	25.9	2.8	358.6 ± 1.8	.9	0	.000032	.010472	0
4-1	24.2	2.6	333 ± 1.8	5.2	.01	.000178	.010863	0
4-2	124.5	13.7	358.4 ± 1.8	4.1	0	.000141	.010138	0
4-3	17	1.8	327.4 ± 1.8	.6	0	.000023	.011603	0
4-4	19.9	2.1	344.5 ± 1.9	2.3	0	.000077	.010797	0
4-5	64.2	7	360.1 ± 1.7	1.4	0	.000047	.010379	0
6-1	11.2	1.2	337.3 ± 2.3	2.2	0	.000075	.011057	0
6-2	132.8	14.6	348.1 ± 1.6	.5	0	.000018	.010864	0
6-3	14.3	1.5	326 ± 2	1.4	.02	.00005	.011566	0
6-4	11.5	1.2	332.6 ± 2.1	.8	.01	.000029	.011382	0
6-5	23.2	2.5	355.7 ± 1.8	.3	0	.00001	.010637	0
6-6	74.9	8.2	364.3 ± 1.7	.1	0	.000004	.010378	0
5-1	6.6	.7	344.4 ± 3.5	4	0	.000137	.010605	0
5-2	42.5	4.6	352.8 ± 1.8	3.2	0	.000108	.01042	0
5-3	4	.4	297.9 ± 3.5	2.6	.01	.000088	.01261	0
5-4	28.2	3.1	362.4 ± 1.8	1.1	.01	.00004	.010327	0
2-2	21.9	2.4	352.6 ± 1.9	1.9	0	.000066	.010559	0
2-3	4	.4	345.8 ± 4	2.1	0	.000072	.010768	0
2-4	15.3	1.6	361.5 ± 2.4	3.7	0	.000126	.010087	0

Total gas age = 352.4 ± 2.4 Ma

J = .002285 ± 1.5995E-05 (.7 %)

37/39, 36/40, and 39/40 Ar ratios are corrected for mass spectrometer discrimination, interfering isotopes, and system blanks.

% IIC – interfering isotopes correction

97-16A MUSCOVITE ARGON SUMMARY

T°C	mV 39	% 39	Age (Ma) ± 1σ	% Atm	37/39	36/40	39/40	% IIC
1-1	13.8	3.1	357.7 ± 2.4	6.5	0	.00022	.009977	0
1-2	19.5	4.5	353.1 ± 1.9	.7	0	.000027	.010737	0
1-3	15.7	3.6	369.9 ± 2	2.4	0	.000084	.010026	0
6-1	17.2	3.9	349.2 ± 2	6	0	.000204	.010294	0
6-2	8.6	1.9	345.1 ± 2.5	2.7	0	.000091	.010799	0
6-3	10.2	2.3	353.9 ± 2.3	5.2	0	.000176	.010236	0
6-4	30.7	7	350.3 ± 1.7	3.3	0	.000113	.010552	0
2-1	12	2.7	314.9 ± 2	2.3	0	.000078	.011985	0
2-2	191.1	44	357.1 ± 1.6	.7	0	.000024	.010612	0
2-3	114.8	26.4	359.6 ± 1.7	.1	0	.000005	.010592	0

Total gas age = 355.8 ± 2.8 Ma

J = .00228 ± 1.596E-05 (.7 %)

37/39, 36/40, and 39/40 Ar ratios are corrected for mass spectrometer discrimination, interfering isotopes, and system blanks.

% IIC – interfering isotopes correction

97-17 MUSCOVITE ARGON SUMMARY

T°C	mV 39	% 39	Age (Ma) ± 1σ	% Atm	37/39	36/40	39/40	% IIC
1-1	7.2	3.9	336.4 ± 3.8	18.9	0	.00064	.009222	0
1-2	15.9	8.7	345.9 ± 2.2	10.2	.03	.000346	.009902	0
1-3	25.7	14.1	353.4 ± 2.3	10.8	0	.000368	.009605	0
1-4	15.5	8.5	356.3 ± 2	3.4	0	.000116	.010312	0
1-5	19.2	10.5	363.1 ± 2	3	0	.000101	.010145	0
1-6	33.9	18.7	356.2 ± 1.7	1	.03	.000034	.010573	0
2-1	10.8	5.9	315.2 ± 4.2	34.2	0	.001159	.008029	0
2-2	6.9	3.8	352.6 ± 7.8	47.4	0	.001605	.005676	0
2-3	16.4	9	352.9 ± 2.1	7.9	0	.000267	.009937	0
2-4	12.7	7	317.9 ± 2	7.2	0	.000245	.011222	0
2-5	16.6	9.2	349.4 ± 1.8	.8	0	.000028	.010819	0

Total gas age = 348.7 ± 2.7 Ma

J = .002272 ± 1.5904E-05 (.7 %)

37/39, 36/40, and 39/40 Ar ratios are corrected for mass spectrometer discrimination, interfering isotopes, and system blanks.

% IIC – interfering isotopes correction

97-3 MUSCOVITE ARGON SUMMARY

T°C	mV 39	% 39	Age (Ma) ± 1σ	% Atm	37/39	36/40	39/40	% IIC
Total fusion								
2-1	486.1	20.9	353.7 ± 1.6	1.2	0	.000041	.010416	0
1-1	242.8	10.4	353.2 ± 1.6	.1	0	.000006	.010544	0
4-1	181.2	7.8	351.9 ± 1.6	.3	0	.00001	.010573	0
5-1	474.4	20.4	346.4 ± 1.6	.2	0	.000008	.010763	0
6-1	207.7	8.9	350.1 ± 1.6	.2	0	.000007	.010641	0
8-1	487.5	20.9	349.1 ± 1.6	.6	0	.000022	.010408	0
7-1	242.3	10.4	350.2 ± 1.6	.7	0	.000025	.010366	0

Total gas age = 345.8 ± 2.6 Ma

J = .002238 ± 1.5995E-05 (.7 %) (2-1 to 6-1)

J = .002238 1.5666E-05 (.7 %) (8-1 and 7-1)

37/39, 36/40, and 39/40 Ar ratios are corrected for mass spectrometer discrimination, interfering isotopes, and system blanks.

% IIC – interfering isotopes correction

97-4 FELDSPAR ARGON SUMMARY

T°C	mV 39	% 39	Age (Ma) ± 1σ	% Atm	37/39	36/40	39/40	% IIC
550	112.4	2.3	212.4 ± 1.2	.9	0	.000031	.017883	0
575	159.8	3.3	217.8 ± 1.1	.5	0	.000017	.017485	0
600	216.8	4.4	224.2 ± 1.1	.3	0	.000011	.016991	0
625	229.4	4.7	228 ± 1.1	.2	0	.000007	.016709	0
650	197.5	4	230.1 ± 1.1	.2	0	.000006	.016548	0
675	171.6	3.5	232.4 ± 1.1	.2	0	.000007	.016372	0
700	153.3	3.1	232.6 ± 1.2	1.5	0	.000053	.016134	0
725	144.3	2.9	236.4 ± 1.2	.2	0	.000007	.016073	0
750	113.5	2.3	239 ± 1.2	.4	0	.000013	.015862	0
775	81.5	1.6	240.3 ± 1.3	.3	0	.000012	.015772	0
800	66.6	1.3	241.1 ± 1.4	.3	.01	.000012	.015718	0
825	64.5	1.3	244.7 ± 1.8	.3	.01	.00001	.01548	0
850	65.6	1.3	247.2 ± 1.4	.5	.01	.000017	.01528	0
875	74	1.5	247.4 ± 1.5	.6	.02	.000022	.015245	0
900	83.2	1.7	250.8 ± 1.4	.6	.02	.000023	.015024	0
925	92.4	1.9	251.6 ± 1.3	.8	.02	.000027	.014952	0
950	101.1	2	253 ± 1.3	1.2	.02	.000042	.014798	0
975	101.6	2.1	252.2 ± 1.3	.7	.02	.000026	.014915	0
1000	99.3	2	251.9 ± 1.3	.6	.03	.00002	.014964	0
1025	98	2	253.8 ± 1.3	.5	.03	.000016	.014859	0
1050	98.4	2	255.6 ± 1.3	.5	.04	.00002	.014732	0
1051	150.7	3.1	257.3 ± 1.2	.8	.04	.000029	.014588	0
1075	54.4	1.1	261 ± 1.6	.7	.05	.000025	.014378	.01
1076	109.5	2.2	263.1 ± 1.3	1.2	.06	.000043	.014185	.01
1100	45.2	.9	262.6 ± 1.8	1.3	.08	.000046	.014197	.01
1150	99.9	2	266 ± 1.3	1.7	.08	.000058	.013953	.01
1200	202.3	4.1	265.2 ± 1.3	2.6	.09	.00009	.013865	.01
1250	422.3	8.7	263 ± 1.3	3.8	.06	.00013	.013815	.01
1300	999	20.7	264.7 ± 1.3	4.7	.04	.00016	.013599	0
1350	97.3	2	275.1 ± 1.5	4.9	.37	.000168	.013014	.06
1450	112.8	2.3	275.8 ± 1.5	9.5	1.71	.000323	.012352	.28
1500	.5	0	-73.5 ± -969.1	101	2.44	.003421	.000674	.86

Total gas age = 250.2 ± 1.7 Ma

J = .002217 ± 1.5519E-05 (.7 %)

37/39, 36/40, and 39/40 Ar ratios are corrected for mass spectrometer discrimination, interfering isotopes, and system blanks.

% IIC – interfering isotopes correction

98-4 FELDSPAR ARGON SUMMARY

T°C	mV 39	% 39	Age (Ma) ± 1σ	% Atm	37/39	36/40	39/40	% IIC
550	105.5	2.9	82.8 ± .6	14.2	0	.000483	.040682	0
575	96.1	2.7	146.6 ± .9	3.7	0	.000126	.025345	0
600	114.1	3.2	187 ± 1	2.9	0	.0001	.019801	0
625	110	3	207.4 ± 1.1	3.4	0	.000117	.01766	0
650	90.8	2.5	219.3 ± 1.4	4.4	0	.000149	.016483	0
675	73.8	2	225.2 ± 1.4	4.9	0	.000168	.015928	0
700	62.9	1.7	236.9 ± 1.6	6.2	0	.000209	.014901	0
725	56.8	1.5	234.5 ± 1.6	2.5	0	.000085	.015651	0
750	69.3	1.9	241.5 ± 1.4	1.4	0	.000047	.01534	0
775	66.7	1.8	243.9 ± 1.4	1.3	0	.000044	.015198	0
800	58	1.6	248.2 ± 1.4	.6	0	.000023	.015008	0
825	58	1.6	248.7 ± 1.5	.7	0	.000025	.014962	0
850	56.9	1.6	248 ± 1.5	.6	0	.00002	.015037	0
875	66.2	1.8	253.2 ± 1.6	.7	0	.000026	.014683	0
900	66.5	1.8	252.7 ± 1.4	.6	0	.00002	.014736	0
925	73.3	2	253.8 ± 1.4	.5	0	.000017	.014682	0
950	76.9	2.1	255 ± 1.3	.4	0	.000015	.014617	0
975	80.5	2.2	257.1 ± 1.3	.4	0	.000015	.014492	0
1000	87.6	2.4	259.5 ± 1.3	.5	0	.000018	.014333	0
1025	96.1	2.7	262.1 ± 1.4	.6	0	.000021	.014168	0
1050	111.8	3.1	266.3 ± 1.3	.8	0	.000028	.013899	0
1051	170.4	4.7	269.8 ± 1.3	1	0	.000033	.01368	0
1075	70.6	1.9	274.8 ± 1.5	.8	0	.00003	.013427	0
1076	134.6	3.7	277.4 ± 1.3	1.2	0	.00004	.013253	0
1100	61.1	1.7	280.6 ± 1.6	1	0	.000034	.013115	0
1125	89.3	2.5	281 ± 1.5	1.3	0	.000046	.013048	0
1150	126	3.5	279.1 ± 1.4	1.6	0	.000056	.013103	0
1175	175.9	4.9	279.2 ± 1.3	1.8	0	.000063	.01307	0
1200	233.6	6.5	277.9 ± 1.3	2.3	0	.000078	.013079	0
1225	286.4	8	277.5 ± 1.3	2.3	0	.00008	.01309	0
1250	300.3	8.4	282.3 ± 1.3	2.1	0	.000074	.012876	0
1275	166.9	4.6	285.6 ± 1.4	1.9	0	.000067	.01274	0
1300	27.3	.7	292.4 ± 2.6	3.7	0	.000126	.012194	0
1325	6.6	.1	285.5 ± 10.3	13.2	.02	.000448	.011256	0
1350	4	.1	286 ± 19.1	25.9	.03	.000875	.009586	0
1450	18.7	.5	293.3 ± 4.5	22.1	.02	.000748	.00983	0
1500	1	0	393.3 ± 236	86.7	.01	.002931	.00121	0

Total gas age = 254.2 ± 1.7 Ma

J = .00221 ± 1.547E-05 (.7 %)

37/39, 36/40, and 39/40 Ar ratios are corrected for mass spectrometer discrimination, interfering isotopes, and system blanks.

% IIC – interfering isotopes correction

484 FELDSPAR-SERICITE ARGON SUMMARY

T°C	mV 39	% 39	Age (Ma) ± 1σ	% Atm	37/39	36/40	39/40	% IIC
550	30.6	1.2	200.4 ± 2.9	24.5	.01	.000829	.014466	0
600	47.7	1.8	202.7 ± 1.9	17.2	.02	.000584	.015665	0
625	39	1.5	204.9 ± 2	10.3	.02	.000349	.016793	0
650	39.1	1.5	204.7 ± 1.8	6.6	.02	.000225	.017499	0
675	43.6	1.7	202.1 ± 1.9	11.9	.03	.000405	.016721	0
700	41.3	1.6	201 ± 1.9	10.8	.05	.000366	.017042	.01
725	39.5	1.5	200.9 ± 2	15	.06	.00051	.016236	.01
750	38.7	1.5	202.4 ± 1.8	9.5	.07	.000321	.017164	.01
775	37.6	1.4	207.2 ± 2	12.3	.07	.000416	.01623	.01
800	37.6	1.4	205.5 ± 2.1	14.8	.06	.0005	.015904	.01
825	43.2	1.7	205 ± 1.8	10.6	.05	.000359	.016722	.01
850	57.3	2.2	202.7 ± 1.4	6.4	.03	.000218	.017717	0
875	105.2	4.1	202.1 ± 1.1	5.4	.02	.000183	.017969	0
900	154.4	6.1	202.3 ± 1	3.3	.01	.000111	.018356	0
925	212.8	8.4	201.7 ± 1	3.4	0	.000115	.018399	0
950	240.8	9.5	200.7 ± 1	4	0	.000137	.018371	0
975	233.5	9.2	200.4 ± 1	5.1	.01	.000175	.018183	0
1000	206.6	8.2	200 ± 1	6.5	.01	.00022	.017965	0
1025	182.9	7.2	199.4 ± 1.1	8.1	.02	.000276	.017703	0
1050	166.7	6.6	198.1 ± 1.1	10	.03	.000341	.017452	0
1051	164.2	6.5	199 ± 1.5	11.1	.04	.000378	.017153	.01
1075	57.2	2.2	198.7 ± 1.5	12.1	.06	.000412	.016988	.01
1076	83	3.3	199.2 ± 1.4	14	.08	.000474	.016595	.01
1100	32.3	1.2	196.6 ± 2.3	15.1	.1	.000511	.016597	.02
1150	102.7	4	198.9 ± 1.4	16.3	.12	.000554	.016158	.02
1200	34.8	1.3	201 ± 2.7	21.9	.34	.000742	.014914	.07
1250	12.5	.5	203.6 ± 6.2	29.7	.64	.001005	.013241	.13
1300	8.2	.3	200.4 ± 8.8	30.9	.35	.001046	.013223	.07
1350	3.5	.1	221.4 ± 25.9	46.1	.33	.001556	.009281	.06
1450	15.3	.6	210.7 ± 6.3	44.2	.36	.001498	.010127	.07
1500	.3	0	2119.7 ± 656	68	.36	.0023	.000321	.02

Total gas age = 201.4 ± 1.5 Ma

Mean age (850°C-1025°C)= 200.9 ± 1.2 Ma (2σ uncertainty including error in J)

J = .002214 ± .0000111 (.5 %)

37/39, 36/40, and 39/40 Ar ratios are corrected for mass spectrometer discrimination, interfering isotopes, and system blanks.

% IIC – interfering isotopes correction

96-3/B1 FELDSPAR ARGON SUMMARY

T°C	mV 39	% 39	Age (Ma) ± 1σ	% Atm	37/39	36/40	39/40	% IIC
550	66.8	1.2	229.2 ± 1.6	1.2	0	.000042	.016262	0
600	149.1	2.8	236.8 ± 1.2	1.2	0	.000041	.015718	0
650	213.9	4.1	241.1 ± 1.2	.5	0	.000018	.01552	0
700	247.5	4.7	245.8 ± 1.2	1	0	.000036	.015121	0
750	316.3	6	252.8 ± 1.2	.6	0	.000021	.014737	0
775	215.7	4.1	255 ± 1.2	.4	0	.000016	.014625	0
800	150.5	2.8	256.8 ± 1.3	.6	0	.000023	.014485	0
825	128.7	2.4	256.3 ± 1.4	.5	0	.000019	.014535	0
850	122.7	2.3	255.1 ± 1.3	.6	0	.000021	.014602	0
875	140.8	2.7	257 ± 1.3	.9	0	.000032	.014438	0
900	152.5	2.9	255.4 ± 1.3	1.2	0	.000042	.014491	0
925	178.4	3.4	257.4 ± 1.3	1.4	0	.000049	.014339	0
950	183.9	3.5	258.2 ± 1.3	1.4	0	.000047	.0143	0
975	178.2	3.4	260.2 ± 1.4	1.3	0	.000044	.014193	0
1000	167.2	3.2	259.1 ± 1.3	1.3	0	.000047	.014249	0
1025	161.6	3	260 ± 1.3	1.5	0	.000052	.014171	0
1050	148.2	2.8	259.7 ± 1.3	1.7	0	.000057	.014168	0
1051	197.4	3.7	262.6 ± 1.3	1.8	0	.000062	.013978	0
1075	199.7	3.8	265.7 ± 1.3	2.2	0	.000076	.013744	0
1100	56.4	1	269.8 ± 1.9	1.6	0	.000055	.013608	0
1150	146.1	2.8	264.2 ± 1.4	2.9	0	.000101	.013726	0
1200	317.9	6	267 ± 1.4	2.9	0	.000099	.013578	0
1250	553.7	10.6	275 ± 1.3	1.6	0	.000056	.013323	0
1300	591.7	11.3	280.6 ± 1.3	1	0	.000037	.013119	0
1350	140.3	2.6	281.6 ± 1.4	2.4	0	.000082	.012889	0
1450	87.1	1.6	287.6 ± 1.8	8.8	0	.000297	.011775	0
1500	1	0	774.9 ± 327	81.9	.03	.002769	.000751	0
1550	.9	0	1533.7 ± 478	77.1	.07	.00261	.00038	0

Total gas age = 262.6 ± 1.8 Ma

J = .002212 ± 1.5484E-05 (.7 %)

37/39, 36/40, and 39/40 Ar ratios are corrected for mass spectrometer discrimination, interfering isotopes, and system blanks.

% IIC – interfering isotopes correction

96-3/B2 FELDSPAR ARGON SUMMARY

T°C	mV 39	% 39	Age (Ma) ± 1σ	% Atm	37/39	36/40	39/40	% IIC
550	130.1	3.4	229.7 ± 1.1	.9	0	.000032	.016383	0
575	127.9	3.4	236 ± 1.2	.5	0	.000019	.01598	0
600	133.2	3.5	239.9 ± 1.2	.3	0	.000012	.015736	0
625	126.4	3.3	243.8 ± 1.2	.3	0	.000012	.015474	0
650	122.9	3.2	246 ± 1.2	.2	0	.000009	.015335	0
675	127.8	3.4	248.2 ± 1.2	.3	0	.000011	.015181	0
700	134.8	3.5	249 ± 1.3	1.4	0	.00005	.014957	0
725	166.9	4.4	254.5 ± 1.2	.3	0	.000013	.014771	0
750	150.7	4	258.5 ± 1.2	.4	0	.000015	.01452	0
775	120.5	3.2	262 ± 1.3	.7	0	.000026	.01426	0
800	95.3	2.5	261 ± 1.3	.3	0	.000013	.014378	0
900	233.7	6.2	260.8 ± 1.2	.7	0	.000025	.014334	0
1000	306.7	8.1	259.4 ± 1.2	.9	0	.000032	.01439	0
1050	302.1	8	256.6 ± 1.2	1.9	0	.000065	.014417	0
1100	188.9	5	260.4 ± 1.2	2.8	0	.000096	.014055	0
1125	146.5	3.8	264.4 ± 1.3	2.5	0	.000087	.013862	0
1150	153.8	4	264.5 ± 1.3	2.7	0	.000094	.013832	0
1175	177.9	4.7	266.3 ± 1.3	2.9	0	.000098	.013716	0
1200	193.6	5.1	269.4 ± 1.3	2.5	0	.000087	.013589	0
1225	188	5	272.5 ± 1.3	2	0	.000069	.013496	0
1250	193.3	5.1	275.5 ± 1.3	1.5	0	.000054	.013398	0
1275	141.6	3.7	279 ± 1.3	1.3	0	.000044	.013258	0
1300	32.2	.8	285 ± 2.6	2.6	0	.000088	.012783	0
1325	9	.2	284.4 ± 8.3	10.7	0	.000364	.01173	0
1350	25.7	.6	280 ± 2.6	6.5	0	.00022	.012506	0
1450	27.5	.7	282.4 ± 3	17.7	0	.0006	.010903	0
1500	.2	0	161.9 ± 1544	98	.13	.003315	.000454	.03

Total gas age = 259 ± 1.7 Ma

J = .002208 ± 1.5456E-05 (.7 %)

37/39, 36/40, and 39/40 Ar ratios are corrected for mass spectrometer discrimination, interfering isotopes, and system blanks.

% IIC – interfering isotopes correction

References cited

Anderson, J. L. and Rowley, M. C. 1981. Synkinematic intrusion of peraluminous and associated metaluminous granitic magmas, Whipple Mountains, California. Canadian Mineralogist, **19**: 83-101.

Benn, K., Horne, R. J., Kontak, D. J., Pignotta, G. S., and Evans, N. G. 1997. Syn-Acadian emplacement model for the South Mountain Batholith, Meguma Terrane, Nova Scotia: Magnetic fabric and structural analysis. Geological Society of America Bulletin, **109**: 1279-1293.

Brown, M. 1993. P-T-t evolution of metamorphic belts and the causes of regional metamorphism. Journal of the Geological Society, London, **150**: 227-241.

Chatterjee, A. K. and Cormier, R. F. 1991. A Rb-Sr geochronological study of the Davis Lake Pluton, South Mountain Batholith, southern Nova Scotia: evidence for a 374 Ma time of emplacement. *In* Nova Scotia Department of Mines and Energy Report of Activities 1990. *Edited by* D. R. MacDonald. Nova Scotia Department of Mines and Energy Report 91-A, p 19

Chatterjee, A. K. and Ham, L. J. 1991.U-Th-Pb systematics of the South Mountain Batholith, Nova Scotia. Atlantic Geoscience Society Annual Colloquium, Sackville, New Brunswick. Proceedings with Abstracts.

Clarke, D. B., Fallon, R., and Heanan, L. M. The Port Mouton Pluton, Meguma Zone, southwest Nova Scotia: interaction among upper crustal, lower crustal, and mantle materials. In preparation.

Clarke, D. B., MacDonald, M. A., Reynolds, P. H., and Longstaffe, F. J. 1993. Leucogranites from the eastern part of the South Mountain Batholith, Nova Scotia. Journal of Petrology, **34**: 653-679.

Clarke, D. B., MacDonald, M. A. and Tate, M. C. 1997. Late Devonian Mafic-Felsic Magmatism in the Meguma Zone, Nova Scotia. *In* The Nature of Magmatism in the Appalachian Orogen . Edited by A. K. Sinha, J. B. Whalen, and J. P. Hogan. Geological Society of America Memoir 191, pp. 107-127.

Copeland, P., Parrish, R., and Harrison, T. M. 1988. Identification of inherited Pb in monazite and its implications for U-Pb systematics. Nature, **333**: 760-763.

Cormier, R. F., Keppie, J. D., and Odom, A. L. 1988. U-Pb and Rb-Sr geochronology of The Wedgeport granitoid pluton, southwestern Nova Scotia. Canadian Journal of Earth Sciences, **25**: 255-261.

Culshaw, N. and Liesa, M. 1997. Alleghanian reactivation of the Acadian fold belt, Meguma Zone, southwest Nova Scotia. Canadian Journal of Earth Sciences, **34**: 833-847.

Culshaw, N. and Reynolds, P. 1997. $^{40}Ar/^{39}Ar$ age of shear zones in the southwest Meguma Zone between Yarmouth and Meteghan, Nova Scotia. Canadian Journal of Earth Sciences, **34**: 848-853.

Dallmeyer, R. D. and Keppie, J. D. 1987. Polyphase late Paleozoic tectonothermal Evolution of the southwestern Meguma Terrane, Nova Scotia: evidence from $^{40}Ar/^{39}Ar$ mineral ages. Canadian Journal of Earth Sciences, **24**: 1242-1254.

Daly, J. S., Cliff, R. A., and Yardley, B. W. D. 1989. Evolution of Metamorphic Belts. Geological Society Special Publication No. 43

De Albuquerque. 1975. Partition of trace elements on co-existing biotite, muscovite, and potassium feldspar of granitic rocks, northern Portugal. Chemical Geology, **16**: 89-108.

Ding, Yi. 1995. AFM minerals in the Halifax pluton. Unpublished MSc. Thesis, Dalhousie University, 191 pp.

Dunn, A. M., Reynolds, P. H., Clarke, D. B., and Ugidos, J. M. 1998. A comparison of The age and composition of the Shelburne dyke, Nova Scotia, and Messejana dyke, Spain. Canadian Journal of Earth Science, submitted.

Gromet, L. P. 1991. Direct dating of deformational fabrics. . *In* Applications of radiogenic isotope systems to problems in geology. *Edited by* L. M. Heaman and J. N. Ludden. Mineralogical Association of Canada, Short Course Handbook, 19, pp. 167-190.

Ham, L. J. and Kontak, D. J. 1988. A textural and chemical study of white mica in the South Mountain Batholith, Nova scotia: primary versus secondary origin. Maritime sedimets and Atlantic Geology, **24**: 111-121.

Hames, W. E. and Bowring, S. A. 1994. An empirical evaluation of the argon diffusion geometry in muscovite. Earth and Planetary Science Letters, **124**: 161-167.

Hames, W. E. and Cheney, J. T. 1997. On the loss of $^{40}Ar^*$ from muscovite during polymetamorphism. Geochimica et Cosmochimica Acta, **61**: 3863-3872.

Hames, W. E. and Hodges, K. V. 1993. Laser $^{40}Ar/^{39}Ar$ evaluation of slow cooling and episodic loss of ^{40}Ar from a sample of polymetamorphic muscovite. Science, **261**: 1721-1723.

Hanes, J. A. 1991. K-Ar and $^{40}Ar/^{39}Ar$ geochronology: methods and applications. *In* Applications of radiogenic isotope systems to problems in geology. *Edited by* L. M. Heaman and J. N. Ludden. Mineralogical Association of Canada, Short Course Handbook, 19, pp. 27-58.

Harper, C. L. 1988. On the nature of time in the cosmological perspective. Unpublished PhD. Thesis, Oxford University, 508 pp.

Hawkins, D. P. and Bowring, S. A. 1997. U-Pb systematics of monazite and xenotime: case studies from the Paleoproterozoic of the Grand Canyon, Arizona. Contributions to Mineralogy and Petrology, **127**: 87-103.

Heaman, L. M. and Parrish, R. 1991. U-Pb geochronology of accessory minerals. *In* Applications of radiogenic isotope systems to problems in geology. *Edited by* L. M. Heaman and J. N. Ludden. Mineralogical Association of Canada, Short Course Handbook, 19, pp. 59-102.

Heaman, L.M. and Machado, N. 1992. Timing and origin of mid-continent rift alkaline magmatism, North America: evidence from the Coldwell complex. Contributions to Mineralogy and Petrology, **110**: 289-303.

Heizler, M. T., Ralser, S., and Karlstrom, K. E. 1997. Late Proterozoic (Grenville?) deformation in central New Mexico determined from single-crystal muscovite $^{40}Ar/^{39}Ar$ age spectra. Precambrian Research, **84**: 1-15.

Hicks, R. J. 1996. Low-grade metamorphism in the Meguma Group, southern Nova Scotia. Unpublished MSc. Thesis, Dalhousie University, 352 pp.

Hicks, R. J., Jamieson, R. A., and Reynolds, P. H. 1998.Detrital and metamorphic $^{40}Ar/^{39}Ar$ ages from muscovite and whole-rock samples, Meguma Supergroup, southern Nova Scotia. Canadian Journal of Earth Sciences, in press.

Hill, J. D. 1991. Petrology, tectonic setting, and economic potential of Devonian peraluminous granitoid plutons in the Canso and Forest Hills areas, Eastern Meguma Terrane, Nova Scotia. Geological Survey of Canada Bulletin, v. 383, pp. 96

Hodges, K. V. 1996. $^{40}Ar/^{39}Ar$ using the Laser Microprobe. *In*: Applications of Microanalytical Techniques to Understanding Mineralizing Processes. *Edited by*: M. A. McKibben and W. C. Shanks. Society of Economic Geologists, Reviews in Economic Geology, vol. 7, in press.

Hodges, K. V. and Bowring, S. A. 1995. $^{40}Ar/^{39}Ar$ thermochronology of isotopically zoned micas: insights from the southwestern USA Proterozoic orogen. Geochimica et Cosmochimica Acta, **59**: 3205-3220.

Hodges, K. V., Hames, W. E., and Bowring, S. A. 1994. $^{40}Ar/^{39}Ar$ age gradients in micas from a high-temperature-low-pressure metamorphic terrain: evidence for very slow cooling and implications for the interpretation of age spectra. Geology, **22**: 55-58.

Kelly, S. P, Arnaud, N. O., and Turner, S. P. 1994. High spatial resolution $^{40}Ar/^{39}Ar$ investigations using an ultra-violet laser probe extraction technique. Geochimica et Cosmochimica Acta, **58**: 3519-3525.

Keppie, J. D. 1993. Synthesis of Palaeozoic deformational events and terrane accretion in the Canadian Appalachians. Geologische Rundschau, **82**: 381-431.

Keppie, J. D. and Dallmeyer, R. D. 1987. Dating transcurrent terrane accretion: and example from the Meguma and Avalon composite terranes in the northern Appalachians. Tectonics, **6**: 831-847.

Keppie, J. D., and Dallmeyer, R. D. 1995. Late Paleozoic collision, delamination, short-lived magmatism, and rapid denudation in the Meguma Terrane (Nova Scotia, Canada): constraints from $^{40}Ar/^{39}Ar$ isotopic data. Canadian Journal of Earth Sciences, **32**: 644-659.

Keppie, J. D., Dallmeyer, R. D., Krogh, T. E., and Aftalion, M. 1993. Dating mineralization using several isotopic methods: an example from the South Mountain Batholith, Nova Scotia, Canada. Chemical Geology (Isotope Geoscience Section), **103**: 251-270.

Keppie, J. D., Dallmeyer, R. D., Krogh, T. E., Cormier, R. F., and Halliday, A. N. 1985. Geochronological constraints for mineralization in the easternmost Meguma Terrane, Nova Scotia. Nova Scotia Department of Mines and Energy, Information series, no 9, 39-40.

Ketchum, J. W. F., Heaman, L. M., Krogh, T. E., Culshaw, N. G., and Jamieson, R. A. 1998. Timing and thermal influence of late orogenic extension in the lower crust: a U-Pb geochronological study from the southwest Grenville orogen, Canada. Precambrian Research, **89**: 25-45.

Kirschner, D. L., Cosca, M. A., Masson, H., and Hunziker, J. C. 1996. Staircase $^{40}Ar/^{39}Ar$ spectra of fine-grained white mica: timing and duration of deformation and empirical constraints on argon diffusion. Geology, **24**: 747-750.

Kontak, D. J. and Chatterjee, A. K. 1992. The East Kemptville tin deposit, Yarmouth County, Nova Scotia: a Pb-isotope study of the leucogranite and mineralized greisens-evidence for a 366 Ma metallogenic event. Canadian Journal of Earth Sciences, **29**: 1180-1196.

Kontak, D. J. and Cormier, R. F. 1991. Geochronological evidence for multiple tectono-thermal overprinting events in the East Kemptville muscovite-topaz leucogranite, Yarmouth County, Nova Scotia, Canada. Canadian Journal of Earth Sciences **28**: 209-224.

Kontak, D. J, Horne, R. J., and Ansdell, K. 1998. Results of mineral deposit studies at the granite-hosted Dunbrack (Zn-Pb-Cu-Ag) and Kinsac (Ba-F) localities, Central Meguma Terrane, Nova Scotia: possible implications for Carboniferous Zn-Pb-Cu-Ag- Ba-F metallogeny in the Meguma Zone. Atlantic Geoscience Society Annual Colloquium, Wolfville, Nova Scotia. Proceedings with Abstracts, p. 18.

Kontak, D. J., Farrar, E., McBride, S., and Martin, R. F. 1995. Mineral chemistry and $^{40}Ar/^{39}Ar$ dating of muscovite from the East Kemptville leucogranite, southern Nova Scotia: evidence for localized resetting of $^{40}Ar/^{39}Ar$ systematics in a shear zone. The Canadian Mineralogist **33**: 1237-1253.

Kontak, D. J. and Reynolds, P. H. 1994. $^{40}Ar/^{39}Ar$ dating of metamorphic and igneous rocks of the Liscomb complex, Meguma Terrane, southern Nova Scotia, Canada. Canadian Journal of Earth Sciences, **31**: 1643-1652.

Lee, J. K. W. 1995. Multipath diffusion in geochronology. Contributions to Mineralogy and Petrology, **120**: 60-82.

Lee, J. K. W., Onstott, T. C., Cashman, K. V.Cumbest, R. J. and Johnson, D. 1991. Incremental heating of hornblende in vacuo: implications for $^{40}Ar/^{39}Ar$ geochronology and the interpretation of thermal histories. Geology, **19**: 872-876

Lee, J. K. W., Onstott, T. C., and Hanes, J. A. 1990. An $^{40}Ar/^{39}Ar$ investigation of the contact effects of a dyke intrusion, Kapuskasing Structural Zone, Ontario. Contributions to Mineralogy and Petrology, **105**: 87-105.

Li, G., Ravenhurst, C. E., and Zentilli, M. 1995. Implications of apatite fission track analysis for the thermal history of the Scotian Basin, offshore Nova Scotia, Canada. Bulletin of Canadian Petroleum Geology, **43**: 127-144.

Lovera, O. M., Richter, F. M., and Harrison, T. M. 1989. The $^{40}Ar/^{39}Ar$ thermochronometry for slowly-cooled samples having a distribution of domain sizes. Journal of Geophysical Research, **94**: 17917-17930

Lovera, O. M., Richter, F. M., and Harrison, T. M. 1991. Diffusion domains determined by ^{39}Ar released during step heating. Journal of Geophysical Research, **96**: 2057-2069.

Martel, T. A., McGregor, C. D., and Utting, J. 1993. Stratigraphic significance of Upper Devonian and Lower Carboniferous miospores from the type area of the Horton Group, Nova Scotia. Canadian Journal of Earth Sciences, **30**: 1091-1098.

McDougall, I, and Harrison, T. M. 1988. Geochronology and Thermochronology by the $^{40}Ar/^{39}Ar$ method. Oxford Monographs on Geology and Geophysics No. 9, Oxford University Press, New York.

Miller, C. F., Stoddard, E. F., Bradfish, L. J., and Dollase, W. A. 1981. Composition of plutonic muscovite: genetic implications. Canadian Mineralogist, **19**: 25-34.

Monier, G., Mergoil-Daniel, J., and Labernardiere, H. 1984. Générations successives de muscovites et feldspaths potassiques dans les leucogranite du massif de Millevaches (Massif Central francais). Bulletin Minéralogie, **107**: 55-68.

Muecke, G. K., Elias, P., and Reynolds, P. H. 1988. Hercynian/Alleghanian overprinting of an Acadian terrane: $^{40}Ar/^{39}Ar$ studies in the Meguma Zone, Nova Scotia, Canada. Chemical Geology (Isotope Geoscience Section), **73**: 153-167.

Parrish, R. R. 1990. U-Pb dating of monazite and its application to geological problems. Canadian Journal of Earth Sciences, **27**: 1431-1450.

Pe-Piper, G. and Reynolds, P. H. Early Mezozoic alkaline dykes, southwest of Nova Scotia, Canada, and their bearing on Triassic-Jurassic magmatism. In preparation.

Reynolds, P. H., Elias, P., Muecke, G. K., and Grist, A. M. 1987. Thermal history of the southwestern Meguma zone, Nova Scotia, from an $^{40}Ar/^{39}Ar$ and fission track dating study of intrusive rocks. Canadian Journal of Earth Sciences, **24**: 1952-1965.

Reynolds, P.H., Zentilli, M., and Muecke, G. K. 1981. K-Ar and $^{40}Ar/^{39}Ar$ geochronology of granitoid rocks from southern Nova Scotia: its bearing on the geological evolution of the Meguma Zone of the Appalachians. Canadian Journal of Earth Sciences, **18**: 386-394.

Roycroft, P. 1991. Magmatically zoned muscovite from the peraluminous two-mica granites of the Leinster batholith, southeast Ireland. Geology, **19**: 437-440.

Ryan, R. J. and Zentilli, M. 1993. Allocyclic and thermochronological constraints on the evolution of the Maritimes Basin of eastern Canada. Atlantic Geology, **29**: 187-197.

Schärer, U. 1984. The effect of initial ^{230}Th disequilibrium on young U-Pb ages: the Mahalu case, Himalaya. Earth and Planetary Science Letters, **67**: 191-204.

Schenk, P. E. 1995. Meguma Zone. *In* Chapter 3 of Geology of the Appalachina-Caledonian Orogen in Canada and Greenland. *Edited* by H. Williams. Geological survey of Canada, Geology of Canada, no 6, pp. 261-277.

Simpson, C. 1985. Deformation of granitic rocks across the brittle-ductile transition. Journal of Structural Geology, **7**: 503-511.

Speer, J. A. 1984. Micas in igneous rocks. *In* Micas. *Edited by* S. W. Bailey. Mineralogical Society of America, Reviews in Mineralogy 13, pp 229-356.

Stacey, J. S. and Kramers, J. D. 1975. Approximation of terrestrial lead isotope evolution by a two-stage model. Earth and Planetary Science Letters, **26**: 207-221.

Steiger, R. H. and Jäger, E. 1977, Subcommision of geochronology: convention on the use of decay constants in geo- and cosmochronology. Earth and Planetary Science Letters, **36**: 359-362.

Tate, M. C. 1995. The relationship between late Devonian mafic intrusions and peraluminous granitoid generation in the Meguma Lithotectonic Zone, Nova Scotia, Canada. Unpublished PhD. Thesis, Dalhousie University, 528 pp.

Tate, M. C., Clarke, D. B., and Heaman, L. M. 1997. Progressive hybridisation between Late Devonian mafic-intermediate and felsic magmas in the Meguma Zone of Nova Scotia, Canada. Contributions to Mineralogy and Petrology, **126**: 401-415.

Timmerman, H. 1998. Geology, metamorphism, and U-PBS geochronology in the Central Gneiss Belt between Huntsville and Haliburton, southwest Grenville Provinve, Ontario. Unpublished PhD. Thesis, Dalhousie University, 401 pp.

Tomascak, P. B., Krogstad, E. J., and Walker, R. J. 1996. U-Pb monazite geochronology of granitic rocks from Maine: implications for Late Paleozoic tectonics in the Northern Appalachians. The Journal of Geology, **104**: 185-195.

West, D. P., Jr. and Lux, D. R. 1993. Dating mylonitic deformation by the $^{40}Ar/^{39}Ar$ method: an example from the Norumbega Fault Zone, Maine. Earth and Planetary Science Letters, **120**: 221-237.

Windley, B. F. 1995. The Evolving Continents. Third edition. Wiley.

Woodend-Douma, S. L. 1988. The mineralogy, petrology, and geochemistry of the Port Mouton Pluton, Nova Scotia, Canada. Unpublished MSc. Thesis, Dalhousie University, 324 pp.

Zeitler, P. K. 1989. The geochronolgy of metamorphic processes. *In* Evolution of Metamorphic Belts. *Edited by* J. S. Daly, R. A. Cliff, and B. W. D. Yardley. Geological Society Special Publication No. 43, pp. 131-148.

Zen, E-an. 1988. Phase relations of peraluminous granitic rocks and their petrogenetic implications, Annual Review of Earth and Planetary Sciences, **16**: 21-51

Zentilli, M. and Reynolds, P. H. 1985. $^{40}Ar/^{39}Ar$ dating of micas from the East Kemptville tin deposit, Yarmouth County, Nova Scotia. Canadian Journal of Earth Sciences, **22**: 1546-1548.